Strategies to Mitigate Electrolyte Degradation Processes in Potassium Batteries

Zur Erlangung des akademischen Grades eines

DOKTORS DER NATURWISSENSCHAFTEN

(Dr. rer. nat.)

von der KIT-Fakultät für Chemie und Biowissenschaften

des Karlsruher Instituts für Technologie (KIT)

genehmigte

DISSERTATION

von

M.Sc. Iurii Panasenko

1. Referent: Prof. Dr. Helmut Ehrenberg

2. Referent: Prof. Dr. Rolf Schuster

Tag der mündlichen Prüfung: 10.12.2024

Selbständigkeitserklärung

Hiermit versichere ich, dass ich die vorliegende Arbeit selbstständig verfasst habe, dass ich keine anderen als die angegebenen Quellen und Hilfsmittel benutzt habe, dass ich die wörtlich oder inhaltlich übernommenen Stellen als solche gekennzeichnet habe und dass ich die Satzung des KIT zur Sicherung guter wissenschaftlicher Praxis in der jeweils gültigen Fassung beachtet habe.

Karlsruhe, den

Panasenko Iurii

Abstract

The global demand for batteries is increasing in tandem with the growing need for renewable energy sources. However, the limited availability of key raw materials, such as lithium, and the toxicity of other elements, such as cobalt, are creating significant challenges in meeting this demand. As potassium is abundant in the earth's crust and relatively affordable, it has the potential to address the issue of material constraints. The use of potassium-ion batteries (KIBs) could help to reduce material costs and facilitate wider access to energy storage technologies.

The progression of KIB technology is currently hindered by a number of significant obstacles, mainly associated with high reactivity of potassium. Traditional approaches of material testing against metallic counter electrodes (so-called half-cells) struggle with the high reactivity of K-metal that gives rise to considerable interferences in the electrochemical or surface analysis of electrode processes at the electrode-electrolyte interphaces (EEI) from soluble degradation products. Therefore, it is crucial to identify methods that mitigate or supress these parasitic reactions and to develop a thorough understand of the underlying degradation processes. It is thus essential to perform reliable electrochemical investigations in three-electrode setups with stable, inert reference electrodes (RE), combined with detailed electrode surface analysis. This thesis employs advanced electrochemical methods and surface-sensitive techniques, such as X-ray photoelectron spectroscopy, to investigate electrolyte degradation and the effects of the electrolyte additive 1,3,2-dioxathiolane 2,2-dioxide (DTD) on graphite and $K_2Fe[Fe(CN)_6]$ (KFF, Prussian white) electrodes in both half and full-cells.

Within the scope of this thesis a 3-electrode setup was developed to illustrate the side reactions in presence of K-metal (as counter or reference electrode). A major observation was a self-discharge mechanism induced by soluble degradation products formed at potassium electrodes. The 3-electrode tests provide a more comprehensive and detailed analysis than previous studies, allowing accurate differentiation between reversible electrochemical processes and irreversible parasitic reactions. Furthermore, the it enables an in-depth investigation of the impact of the DTD additive on the electrochemistry of graphite negative and Prussian white positive electrodes. The findings demonstrate that DTD can effectively mitigate the crosstalk process in Prussian white half-cell experiments by passivation of the K-metal counter electrode. However, DTD shows poor compatibility with graphite anodes, as indicated by the formation of a dense surface film, which negatively affects the electrochemical performance of both anode half-cells and full-cells.

Although DTD did not result in an improvement in overall battery performance, this thesis offers valuable insights into the DTD degradation and passivation patterns in KIB systems. The surface analysis presented in the thesis provides a model for the fitting of PBA interphaces in future studies. Moreover, a combination of surface analysis and electrochemical techniques provides insight into the

formation of the EEI in the presence of the sulfur-based additive. The resulting knowledge will facilitate the design of additives, electrolytes and electrodes, and assist with optimisation of the latter, thereby providing more efficient working batteries. Such advancements could enable KIBs to achieve performance levels that are competitive with those of LIBs, thereby paving the way for their wider adoption as an alternative energy storage solution.

Kurzfassung

Die weltweite Nachfrage nach Batterien steigt parallel zum wachsenden Bedarf an erneuerbaren Energiequellen. Allerdings stellen die begrenzte Verfügbarkeit von Schlüsselrohstoffen wie Lithium und die Toxizität anderer Elemente wie Kobalt erhebliche Herausforderungen bei der Deckung dieser Nachfrage dar. Da Kalium in der Erdkruste reichlich vorhanden und relativ erschwinglich ist, hat es das Potenzial, das Problem der Materialknappheit zu lösen. Der Einsatz von Kalium-Ionen-Batterien (KIBs) könnte dazu beitragen, die Materialkosten zu senken und einen breiteren Zugang zu Energiespeichertechnologien zu ermöglichen.

Der Fortschritt der KIB-Technologie wird derzeit durch eine Reihe bedeutender Hindernisse gebremst, die hauptsächlich mit der hohen Reaktivität von Kalium zusammenhängen. Traditionelle Ansätze zur Materialprüfung gegen metallische Gegenelektroden (sogenannte Halbzellen) kämpfen mit der hohen Reaktivität von K-Metall, was zu erheblichen Interferenzen bei der elektrochemischen oder Oberflächenanalyse von Elektrodenprozessen an den Elektroden-Elektrolyt-Grenzflächen (EEI) durch lösliche Abbauprodukte führt. Daher ist es entscheidend, Methoden zu identifizieren, die diese parasitären Reaktionen mindern oder unterdrücken, und ein umfassendes Verständnis der zugrunde liegenden Abbauprozesse zu entwickeln. Es ist daher unerlässlich, zuverlässige elektrochemische Untersuchungen in Drei-Elektroden-Aufbauten mit stabilen, inertem Bezugselektroden (RE) durchzuführen, kombiniert mit einer detaillierten Oberflächenanalyse der Elektroden. Diese Dissertation verwendet fortschrittliche elektrochemische Methoden und oberflächensensitive Techniken wie die Röntgenphotoelektronenspektroskopie, um den Elektrolytabbau und die Auswirkungen des Elektrolytadditivs 1,3,2-Dioxathiolan-2,2-dioxid (DTD) auf Graphit- und $K_2Fe[Fe(CN)_6]$-Elektroden (KFF, Preußisch Weiß) sowohl in Halb- als auch in Vollzellen zu untersuchen.

Im Rahmen dieser Arbeit wurde ein Drei-Elektroden-Aufbau entwickelt, um die Nebenreaktionen in Anwesenheit von K-Metall (als Gegen- oder Bezugselektrode) darzustellen. Eine wesentliche Beobachtung war ein Selbstentladungsmechanismus, der durch lösliche Abbauprodukte an Kaliumelektroden verursacht wurde. Die Drei-Elektroden-Tests liefern eine umfassendere und detailliertere Analyse als frühere Studien, die eine genaue Unterscheidung zwischen reversiblen elektrochemischen Prozessen und irreversiblen parasitären Reaktionen ermöglichen. Darüber hinaus ermöglicht der Aufbau eine eingehende Untersuchung der Auswirkungen des DTD-Additivs auf die Elektrochemie von Graphitnegativ- und Preußisch-Weiß-Positiv-Elektroden.Die Ergebnisse zeigen, dass DTD den Crosstalk-Prozess in Preußisch-Weiß-Halbzellversuchen durch Passivierung der K-Metall-Gegenelektrode wirksam mindern kann. DTD weist jedoch eine geringe Verträglichkeit mit Graphitanoden auf, wie die Bildung eines dichten Oberflächenfilms zeigt, der die elektrochemische Leistung sowohl der Anodenhalbzellen als auch der Vollzellen negativ beeinflusst.

Obwohl DTD keine Verbesserung der Gesamtbatterieleistung bewirkte, liefert diese Arbeit wertvolle Erkenntnisse über die Abbau- und Passivierungsmuster von DTD in KIB-Systemen. Die in der Arbeit präsentierte Oberflächenanalyse bietet ein Modell für die Anpassung von PBA-Grenzflächen in zukünftigen Studien. Darüber hinaus bietet die Kombination aus Oberflächenanalyse und elektrochemischen Techniken Einblicke in die Bildung der EEI in Anwesenheit des schwefelbasierten Additivs. Das daraus resultierende Wissen wird die Gestaltung von Additiven, Elektrolyten und Elektroden erleichtern und zur Optimierung derselben beitragen, wodurch effizienter arbeitende Batterien entwickelt werden können. Solche Fortschritte könnten es KIBs ermöglichen, Leistungsniveaus zu erreichen, die mit denen von LIBs konkurrieren, und so den Weg für eine breitere Einführung als alternative Energiespeicherlösung ebnen.

“If I was an NBA player, I’d be
Dillon Brooks but worse”

Contents

List of Abbreviations

2-el	2-electrode
3-el	3-electrode
AgCI-RE	silver-silver chloride reference electrode
ASF	Atomic sensitivity factor
BE	binding energy
C.E.	coulombic efficiency,
CE	counter electrode
CEI	cathode electrolyte interphase
CMC-Na	carboxymethyl cellulose sodium salt
CV	cyclic voltammetry
DEC	diethyl carbonate
DECC	di-(2-ethoxycarbonyloxyethyl)carbonate)
DEDD	diethyl 2,5-dioxahexanedioate
DMC	dimethyl carbonate
DMDD	ethane-1,2-diyl dimethyl biscarbonate
DME	dimethoxyethane
DTD	1,3,2-Dioxathiolane-2,2-dioxide
E	electrochemical potential
EC	ethylene carbonate
EEI	electrode-electrolyte interphase
EMC	ethyl methyl carbonate
EMDD	ethane-1,2-diyl ethylmethyl biscarbonat
ES	ethylene sulfite
F	Faraday constant
FC	full-cell
Fc	ferrocene, iron(II) cyclopentadienide
Fc^+	ferrocenium, iron(III) cyclopentadienide
FEC	fluoroethylene carbonate
G	Gibbs energy
GCPL	galvanostatic cycling with potential limitation
GIC	graphite intercalation compound
Gr-WE	graphite working electrode
HC	half cell

HOMO	highest occupied molecular orbital
IMFP	inelastic mean free path
K-CE	potassium counter electrode
KFe2	potassium hexacyanoferrate (II)
KFe3	potassium hexacyanoferrate (III)
KFF	potassium iron (II) hexacyanoferrate (II)
KFF-RE	potassium iron hexacyanoferrate reference electrode
KFSI	potassium bis(fluorosulfonylimide)
KIB	potassium-ion battery
KPF_6	potassium hexafluorophosphate
K-RE	potassium metal reference electrode
KTFSI	potassium bis(trifluoromethane sulfonyl)imide
LIB	lithium-ion battery
Li-CE	lithium counter electrode
$LiPF_6$	lithium hexafluorophosphate
LUMO	lowest unoccupied molecular orbital
NIB	sodium-ion battery
NMP	*N*-methyl-2-pyrrolidone
OCV	open-circuit voltage
PAA	poly(acrylic acid)
PB	Prussian blue, potassium iron (II) hexacyanoferrate (III)
PBA	Prussian blue analogue
PC	propylene carbonate
PES	Photoelectron spectroscopy
PG	Prussian green, Iron (III) hexacyanoferrate
PS	1,3-Propane sultone
PVdF	poly(vinylidene difluoride)
Q	Charge, capacity
QRE	quasi-reference electrode
RE	Reference electrode
SEI	solid electrolyte interphase
SHE	standard hydrogen electrode
TBACl	tetrabutylammonium chloride
V	voltage

WE	working electrode
XPS	x-ray photoelectron spectroscopy

Acknowledgements

I would like to express my grateful appreciation to all those who offered their support during my doctoral studies.

Firstly, I would like to express my gratitude to Prof. Dr. Helmut Ehrenberg for giving me the opportunity to work in IAM-ESS.

I would like to acknowledge and thank my technical supervisor, Dr. Fabian Jeschull, for his invaluable patience and guidance throughout my PhD. I am certain that without his support, my work would have been turn into pure chaos.

I really grateful to Dr. Christian Njel and Vanessa Trouillet for the introduction into XPS analyses. It was a significant step for me in learning of the technique, which I was barely familiar. I would also like to express my gratitude to Liuda Mereacre for her invaluable assistance. Without her technical support for adjusting electrochemical measurements in glove box, I would not have been able to complete my PhD project.

And a big, heartfelt thank you to the "Potassium" group of IAM-ESS (Timofey, Ulf, Celine, Leonie, Anna, Monika, Ferdinand) for tolerating my bad jokes and engaging in a nice scientific discussion. Our meetings were a great help to me. I learned so much about how to present and discuss results there.

I am deeply appreciating the support from my friends: Alexandra, Tim, Ed, Mr. Deng, Anna, Cedric, Ramon, Francesco, Christopher from dragging me out from house and spending free time together. I am so lucky to have friends like that, even though I did have to deal with some pretty rough hangovers from time to time.

I'd like to say a big thanks to Danny Brown for "Atrocity Exhibition". It's such a lovely album. It helped me a lot during writing process, especially when I caught cold (twice).

And finally, I'd like to thank my wonderful parents, Vasilii and Olga, and my brother Alexander. They were there for me every step of the way, offering their unwavering support and love through this long and tough journey.

1 Introduction

Potassium-ion batteries (KIB) have emerged as a promising alternative to lithium-ion batteries (LIB), driven by the abundance and low cost of potassium compared to lithium. Potassium is not only widely available but also shares many similar electrochemical properties with lithium, such as a standard electrode potential and high ionic conductivity in various electrolytes. These advantages make KIBs a potentially viable solution for large-scale energy storage applications, particularly in the context of growing demand for sustainable and cost-effective battery technologies. Despite their potential, KIB face a number of significant challenges that currently impede their development and commercialisation.

One of the most significant challenges in KIB technology is the degradation of electrolytes during battery cycling. Electrolyte decomposition leads to the formation of unstable interphases at the electrodes, resulting in poor long-term stability and reduced cycle life. The larger ionic radius of potassium in comparison to lithium worsens these issues, as it causes increased strain on the electrode structure and accelerates side reactions at the electrode-electrolyte interphase (EEI). The KIBs EEI are less stable than their counterparts in LIB. These interphases degrade over time, allowing further electrolyte decomposition and decreasing the overall performance and safety of the battery. To address the issue of electrolyte degradation, researchers have explored various mitigation strategies. One effective approach is the use of electrolyte additives, which can help stabilize EEI layers. For instance, the additive 1,3,2-dioxathiolane 2,2-dioxide (DTD) was successfully utilised in stabilising both anode and cathode surfaces in LIB. DTD forms a passivation film that protects the electrode surface from excessive degradation, enabling better performance over multiple cycles. An alternative strategy for avoiding the use of reactive metals is optimisation of full-cell configurations.

Both of the aforementioned approaches require the use of advanced electrochemical techniques. In order to study battery performance, a three-electrode electrochemical setup is an essential tool. This setup allows for precise monitoring of electrochemical processes, which is crucial for optimising battery behaviour. The incorporation of a reliable reference electrode, further enhances the ability to track and assess reactions at both the anode and cathode. This provides invaluable insights into the stability and effectiveness of electrolyte additives like DTD.

To gain a full insight into the processes occurring within the battery, it is essential to complement electrochemical analysis with surface-sensitive techniques, such as X-ray photoelectron spectroscopy (XPS). The method enables the characterisation of the SEI and CEI layers and the effects of additives in great detail. Furthermore, XPS allows us to examine the chemical composition and evolution of these layers over time, thus providing a clearer understanding of the degradation processes at the electrode

surfaces. The combination of these analytical tools allows for a more comprehensive and precise characterisation of electrolyte degradation.

While previous studies have contributed to understanding the surface chemistry of KIB electrodes, there is still a need for a more comprehensive exploration of electrolyte additives in full-cell and half-cell configurations. The objective is to investigate the degradation processes in the KIB anode and cathode sides, with a particular focus on the impact of DTD as an electrolyte additive. From an electrochemical perspective, this thesis examines the utilisation of an AgCl reference electrode (AgCl-RE) to investigate the impact of DTD on both the positive and negative electrodes in a range of KIB cell configurations, thereby emphasising the importance of a reliable reference electrode. The AgCl-RE was employed to assess the impact of the electrolyte additive DTD on electrode reactions at the positive and negative electrodes in various cell configurations. From surface analysis, this work provides detailed XPS data for Prussian White ($K_2Fe[Fe(CN)_6]$ or KFF) electrodes, including reference peak positions and assignments for different electrode states—precursors, powders, and coated electrodes. This reference data will aid in the accurate analysis of cycled samples and support future research on KIB surface chemistry. Following the presentation of the referencing data for KFF, the thesis investigates the role of DTD in stabilising the anode and cathode surfaces in graphite/KFF KIB full and half-cells. A comparison was made between cells with and without 1 wt. % DTD.

The findings of the thesis contribute to the existing body of knowledge on the complex mechanisms governing electrolyte degradation in KIBs.

The combination of advanced surface characterisation techniques and detailed electrochemical testing provides a robust foundation for future research aimed at addressing remaining challenges in KIB technology.

2 Theoretical Background

This chapter covers the basics of electrochemistry as well as working principles and key parameters of KIB. Different KIB components such as cathode, anode, and electrolyte are detailed. In addition, it provides an overview of the theoretical foundations of XPS.

2.1 Potassium-Ion Batteries

As with sodium-ion batteries (NIBs)[1] and magnesium batteries (Mg batteries)[2], KIB exhibit the same advantages over LIB[3]. These include the abundance of battery materials and their electrochemical properties as carrier ions[4]. Potassium (2.09 %) is as abundant as Mg (2.33 %) and Na (2.36 %)[5]. In addition, K does not thermodynamically form intermetallic compounds with Al, thus enabling the use of aluminium foil as a negative electrode current collector[6], which is a further advantage over lithium. In fact, KIB are operating at higher voltages than NIB and LIB[7]. The electrode potential of K^+/K in the carbonate ester electrolytes is the lowest of the alkali metals[7].

Also KIB is capable to achieve high power densities[8]. This due to the high diffusion coefficient K^+ ions. Despite potassium's relatively large atomic radius (1.38 Å), K^+ has the smallest Stokes radius (3.6 Å) in propylene carbonate (PC), which results in reduced coulombic interactions[9]. Molecular dynamics simulations demonstrate that K^+ diffuses three times faster in ethylene carbonate (EC) than Li^+ and has the lowest solvation energy (397.5 kJ mol^{-1}), indicating superior rate capability compared to Li^+ and Na^+[10]. This series of advantages makes KIB a prospective alternative to LIB[11]. Concurrently, the emerging field of potassium-ion batteries is confronted with considerable obstacles related to safety, efficiency, and long-term stability. Addressing these issues requires advancements in electrode materials, electrolyte formulations, and a deeper understanding of the fundamental electrochemical processes at play. This chapter presents an overview of the most commonly used materials in KIB, along with a discussion of the fundamental operational principles and a comparison with other alkali systems.

The abundance and low cost of materials utilised in KIB, coupled with potassium's widespread availability, could significantly reduce the overall costs of battery production in the future[9]. Furthermore, these materials are composed of non-toxic elements, in contrast to LIB, which utilises Co and Ni[12]. For a comparison of the theoretical capacities and energy densities based on pure electrode materials for the most common materials used in alkali ion battery systems are presented in **Table 1**. The NIBs and KIBs electrode materials have comparable capacities, although KIBs typically demonstrate a higher average operational potential. (defined as the midpoint between the battery's open circuit voltage (OCV) when fully charged and the lower voltage limit when the battery is fully

discharged)[13]. This enables the KIB to achieve both higher specific energy density and the same energy density as the NIB (**Table 1**).

Table 1. Cell characteristics of alkali ions battery systems

Battery type	Specific capacities (mAh g^{-1}/ mAh cm^{-3})		Average operating potential	Energy densities		Ref.
	Anode	Cathode		Gravimetric (Wh kg^{-1})	Volumetric (Wh L^{-1})	
LIB	Graphite (372/818)	$LiCoO_2$ (140/700)	3.8	387	1434	[14]
		$LiFePO_4$ (170/612)	3.5	408	1226	
NIB	Hard carbon (335/450)	$NaMnO_2$ (244/816)	2.8	302	925	[15,16]
		$Na_{0.61}Fe[Fe(CN)_6]_{0.94}$ (150/270)	3.0	287	531	
KIB	Graphite (279/613)	$K_2Fe[Fe(CN)_6]$ (155/295)	3.8	378	831	[3]

KIB operate in accordance with the identical fundamental principles that govern LIB and NIB. A typical configuration for KIB employs a Prussian Blue Analogues (PBA) cathode and graphite as the anode electrode material[3,12]. A typical electrolyte solution is potassium hexafluorophosphate (KPF_6) dissolved in a mixture of EC and diethyl carbonate (DEC)[17]. The system is referred to as the 'rocking chair' battery due to the back-and-forth movement of the metal ions between the two electrodes, which is schematically presented in **Figure 1**. Potassium ions (K^+) act as the ionic charge carriers during cycling process. At charge stage, the ions migrate from the active material of the positive electrode (cathode) to the negative electrode (anode) through the electrolyte, typically intercalating into the anode material. During the charging process, the cathode material undergoes oxidation, while the anode material is reduced. However, in electrochemical terms, roles of the electrodes are reversed. The material typically referred to as the "cathode" functions as the anode, and the material referred to as the "anode" acts as the cathode. It is of important to distinguish between the battery's anode/cathode material and the anode/cathode as defined in the context of electrochemistry. Upon discharge, the potassium ions move in the opposite direction, from the anode material (deintercalation/oxidation) to the cathode material (which undergoes intercalation/reduction). During this phase, the cathode material functions as the cathode, and the anode material acts as the anode. As discharging (i.e. storing energy and releasing it back) is the primary operation of a battery, the

terminology for the electrodes is based on their function during this phase. The given redox reaction is as follows:

Anode:	K_xC_n	⇌	$x\ K^+ + n\ C + x\ e^-$	(1)
Cathode:	$K_2Fe[Fe(CN)_6]$	⇌	$Fe[Fe(CN)_6] + 2\ K^+ + 2\ e^-$	(2)
Full cell reaction:	$x\ Fe[Fe(CN)_6] + 2\ K_xC_n$	⇌	$x\ K_2Fe[Fe(CN)_6] + n\ C$	(3)

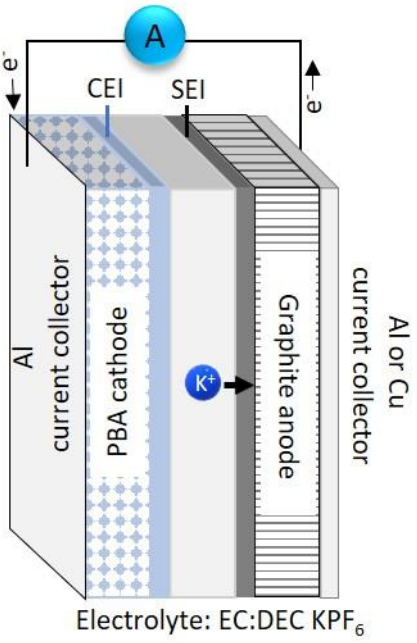

Figure 1. Schematic illustration of a potassium-ion battery

The battery cell configuration presented above (**Figure 1**) is referred to as a full-cell (FC). FC operates without a metallic electrode. When a metallic electrode (e.g., Li, Na, or K) which could act as an almost unlimited source of A^+ ions is present, the battery cell is classified as a half-cell (HC). If a metal acts as an anode, it is called a cathode half-cell, and vice versa if a metal acts as a cathode, it is called an anode half-cell. The aforementioned nomenclature will be employed in the subsequent text. In FC, the quantity of charge carriers is constrained by the capacity of the cathode. Consequently, one of the critical parameters is the coulombic efficiency (C.E.). In the case of LIB, C.E, can reach values close to 100 %[18], eliminating the need for metallic lithium supply and enabling lithium-metal-free LIB[19,20]. In comparison to LIB, KIB have not yet reached the same level of efficiency. At the moment, the highest C.E. for KIB is reported by the Komaba group with a PBA/graphite cell, with a discharge capacity of approximately 100 mA h g^{-1} and a 90 % coulombic efficiency[12].

2.2 Electrochemical background

2.2.1 Key parameters

Electrode potential

The electrode potential is defined as the free energy change divided by the electron charge, which represents the movement of an electron (and any associated ion/solvent movement/rearrangement) from a reference state (often a reference electrode) to the working electrode. It indicates the oxidising or reducing power of an electrode and is related to the Fermi level of electrons in the electrode. It is the driving force behind the flow of electrons between electrodes during the operation of a battery. Practically, electrode potentials are evaluated as a difference between two electrodes. The potential difference between two electrodes in a cell is defined as the cell voltage (E_{cell}, ΔE), and determined as the difference between redox potentials of each electrode ($\Delta E = E_{cathode} - E_{anode}$). The electrochemical potential is associated with the Gibbs energy in the following relationship:

$$\Delta E = -\frac{\Delta G}{nF} \tag{4}$$

where n is the stoichiometric number of electrons exchanged during the reaction and F is Faraday's constant.

The standard potential for a redox reaction is defined as the potential of a cell measured under in relation to the standard hydrogen electrode (*vs*. SHE). The SHE potential is defined as a zero. The SHE comprises a platinum electrode submerged in a 1 M solution of H^+ in water at 25 °C, with 1 atm of H_2 bubbled through the solution ('standard conditions').
In order to ascertain the electrode potential, it is necessary to employ the Nernst equation:

$$\mathrm{E} = \mathrm{E}^0 + \frac{\mathrm{RT}}{\mathrm{F}} \ln \frac{a_{Ox}}{a_{Red}} \tag{5}$$

Where E - potential to the standard potential of a species (E^0) and the relative activities of the oxidised (a_{Ox}) and reduced (a_{Red}) analyte in the system at equilibrium. In the equation, F is Faraday's constant, R is the universal gas constant, n is the number of electrons, and T is the temperature.

Battery Capacity

Battery capacity is defined as the maximum amount of electrical charge that a battery is capable of delivering or storing. When a constant current I is applied, the charge Q is proportional to the time t:

$$Q = I \cdot t \tag{7}$$

The battery capacity is typically reported per unit mass in Ah g^{-1} or mAh g^{-1}, whereas electronic devices specify the capacity in Ah or mAh. The theoretical maximum capacity that a material with molecular mass M can achieve is given by the theoretical capacity Q_{theor}:

$$Q_{theor} = \frac{znF}{M} \tag{8}$$

where n is the maximum amount of insertable or extractable charge carriers with valence number z, F is Faraday's constant.

Coulombic efficiency

Coulombic efficiency is defined as the ratio of the charge and discharge capacities, which serves to quantify the reversibility of the charging and discharging process.

$$C.E. = 100 \cdot \frac{Q_{charge}}{Q_{discharge}} \tag{9}$$

It can be concluded that fully reversible processes would be indicated by C.E. = 100 %. However, this is not achievable by a battery due to the loss of metal ions inventory.

Energy density

The gravimetric or specific energy density w_m is defined as the amount of energy stored in a given system per unit mass. A specific quantity always refers to the mass m_i of the components of the cell. The volumetric energy density w_v can be attributed to the electrical energy stored per unit volume V_i:

$$w_m = \frac{zF\Delta E}{\sum_i m_i}; w_v = \frac{zF\Delta E}{\sum_i V_i} \tag{10}$$

Furthermore, gravimetric and specific energies can be calculated by multiplying the capacity by the cell voltage and dividing the result by the mass of the anode and cathode:

$$w_m = \frac{QE_{cell}}{(m_{cathode} + m_{anode})} \tag{11}$$

An increase in gravimetric or specific energy density will result in a reduction in the weight of the storage device. An increase in volumetric energy density will decrease the size of the battery.

Power density

The terms gravimetric and volumetric power density are used to describe the power (i.e., time rate of energy transfer) that a battery is capable of delivering per unit mass or volume, respectively.:

$$p_m = \frac{I\Delta E}{\sum_i m_i}; p_v = \frac{I\Delta E}{\sum_i V_i} \quad (12)$$

High power densities are essential for high power applications, as they enable high charge and discharge currents. In contrast to energy density, which indicates the amount of energy that can be stored, power density is a measure of the rate at which energy is delivered.

2.2.2 2 electrode and 3-electrode configurations

The typical battery setup comprises of two electrodes, which are arranged in what is referred to as a two-electrode configuration (**Figure 2a**). In this case, the current flows between a counter electrode (CE) and a working electrode (WE). In the majority of cases, the WE properties are the primary subject of investigation. The objective of the CE is to provide a current of equal magnitude but opposite sign to the working electrode, with the aim of achieving this without interfering with the response of the working electrode. As it is only possible to measure electrode potential in relation to another electrode, a two-electrode configuration only provides the potential difference between WE and CE (cell voltage). In the event that CE exhibits minimal polarisation, i.e. a potential is only slightly affected by an applied current, for instance in the case of Li-CE, the potential of WE can be monitored with a high degree of precision. This is due to the fact that the potential differential between the CE and WE is largely influenced by the latter. In situations where the CE demonstrates high polarisation (for instance, in the case of a potassium metal CE) or is subjected to electrochemical reactions (such as those occurring in a FC configuration), the potentials can be monitored by introducing a third reference electrode (RE) into the cell (**Figure 2b**). So, potentials of WE and CE can determined relative to RE.

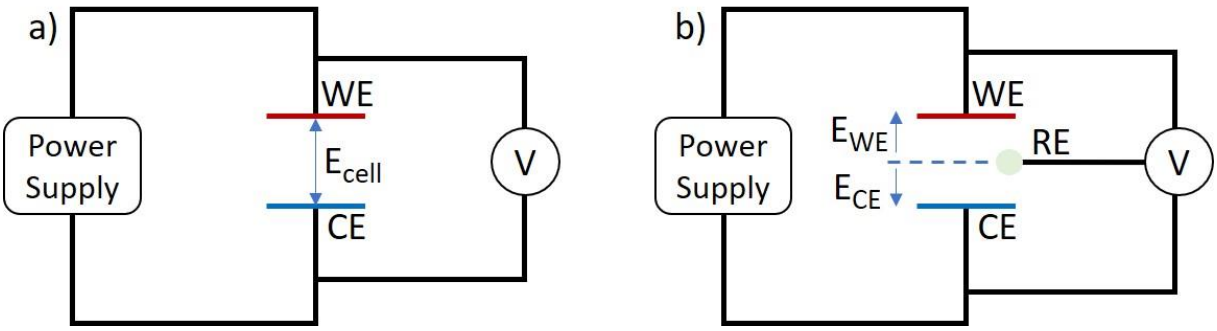

Figure 2. Schematic illustration of a) Two-electrode; b) Three-electrode cell configuration

It is vital that the RE maintains a constant potential throughout the experiment, thus ensuring stability over time. It is therefore essential that it should be capable of maintaining a known and consistent composition. Furthermore, the interfacial potential difference at the RE should remain unaltered when a current flows through the cell, and there should be no contamination between the reference and working sides. It is of particular importance that the potential is independent of current density, which necessitates that the electrode couple exhibits rapid kinetics. This requirement is more readily fulfilled in a three-electrode configuration In this configuration, the potentials of WE and CE are measured in relation to RE, through which current does not flow. Consequently, RE does not depend on current density.

2.3 Reference Electrodes

In order to provide an illustrative example of RE, it is helpful to analyse the characteristics of the Ag/AgCl aqueous reference electrode. This electrode is commonly used in aqueous electrochemistry. It consists of a silver wire coated with solid, low-soluble AgCl, immersed in a chloride-containing aqueous solution (typically 3 M KCl). The chemical reaction at the electrode is:

$$AgCl_{(s)}+e^{-} \rightarrow Ag_{(s)}+Cl^{-}_{(aq)},\ E^{o} = 0.222V\ \textit{vs.}\ SHE \tag{13}$$

Nernst equation for the Ag/AgCl electrode can be written as:

$$E = E^{0} - \frac{RT}{F}\ln\frac{[Ag][Cl^{-}]}{[AgCl]} \tag{14}$$

Given that the activities of pure solids are equal to 1, the equation can be simplified to:

$$E = E^{0} - \frac{RT}{F}\ln[Cl^{-}] \tag{15}$$

This expression demonstrates that the potential of the Ag/AgCl electrode is dependent upon the activity of the Cl^{-} ions, despite the fact that the Cl^{-} ions are not directly involved in the redox reaction. It illustrates that the activities of all species that are involved in the overall chemical reaction influence the electrode potential, and that this is not limited to the redox-active species.

2.3.1 Quasi references

If the reference electrode exhibits non-Nernst behaviour, i.e. its potential cannot be defined by the Nernst equation (see example above) due to the absence of thermodynamic equilibrium, for example Ag, Pt or alkali metal wires placed in the same solution as the working electrode become a so-called "quasi-" or "pseudo-" reference electrode[21]. The potential of a quasi-reference electrode (QRE) is dependent on the presence of a variety of compounds (most commonly Ag_2O or Pt_2O, alkali metal cation) on the metal surface. It should be noted that the precise concentration of the metal oxide molecules/cations is not a definitive quantity and therefore cannot be ascertained with absolute certainty. Thus, the potential of quasi-reference electrodes is influenced by: reactions with impurities, solvation of oxides on metal surfaces, polarization, and recent usage history. Such electrodes do not meet the strict requirements of reference electrodes because they do not have a constant, well-

defined potential and can change over time. However, it is essential to ensure that their potential remains stable over time in the specific system and that they are calibrated with a reliable reference during experiments. For example, the ferrocene/ferrocenium (Fc^+/Fc) couple can be used as a reliable external reference.

Despite these limitations, quasi-reference electrodes can be useful in many applications due to their ease of implementation, especially in systems where conventional reference electrodes are impractical. In the field of LIB, Li metal represents a viable option and is employed extensively, representing the simplest solution[22–24]. In the post-lithium technologies, quasi reference electrodes are confronted with major challenges. Even for the least reactive Na, there is an unstable interphase between the metal and the electrolyte, and partial dissolution of the solid electrolyte interphase (SEI) can affect the measurement in alkylcarbonate electrolytes[25–27]. However, it is possible to utilise Na metal for three-electrode measurements, despite the aforementioned instability[28,29]. Furthermore, K metal presents additional constraints.

Due to its high reactivity, it exhibits considerably elevated polarisation in comparison to Li and Na, even following preliminary treatment by forming a fresh surface through plating-stripping of potassium metals between CE and RE inside three-electrode cells[30]. The behaviour of metallic K is markedly influenced by electrolyte salts, solvents, and additives[3,30,31]. Furthermore, the soluble products that form at the potassium surface can affect the WE and CE performance, ("crosstalk" reactions). The aforementioned factors indicate that K-metal RE is an inadequate solution and that alternative options must be sought.

2.3.2 Alloys/Insertion electrode materials as reference electrodes

Several alloy-type reference electrodes, such as Li_xSn[32,33], Li_xAu[34–36], and Li_xBi[37], have been successfully used as RE for Li batteries. These electrodes are convenient because electrochemical alloying can usually be done inside the cell, simplifying the preparation process[38]. Additionally, these alloys can be made in the form of a wire, making it easier to position the RE within the cell[39,40]. While these electrodes provide a stable potential over short to intermediate periods, they often experience potential drift over longer periods (weeks) due to SEI growth or self-delithiation[32,34].

To date, there are reports about Sn-K[41],Sb-K[42], K-In[43] and K-Bi[44] alloys. The latter was successfully implemented as a RE in KIB[45]. It was demonstrated that the Bi-Bi_2K couple provides a stable potential with negligible drift (approximately 3 mV) within at least 100 hours[45]. The primary disadvantage of this RE system is the challenging preparation of the alloy, which requires a high temperature of over 600°C.

The utilisation of electrode materials (cathode as a rule) that exhibit a flat and stable voltage plateau represents an effective approach for reliable RE. These electrodes often can avoid SEI formation by having equilibrium potentials above the SEI-formation threshold. With a sufficiently flat discharge profile, these materials can be practically non-polarizable[24]. For example, $LiFePO_4$ (LFP) has a voltage plateau around 3.4 V and exhibits very small polarization compared to other common Li-based reference electrodes under current[46]. Similarly, $Li_4Ti_5O_{12}$ (LTO), with a voltage plateau at 1.5 V, is also suitable for Li batteries[47]. The requisite composition is typically achieved through electrochemical processes (electrochemical discharge and a subsequent partial charge) [24]. The potential use of electrode materials as reference electrodes for post-Li batteries has been explored. While several materials, such as Prussian blue analogues (PBA) and vanadium phosphates, exhibit a flat plateau in their potential curves[48,49], their application as reference electrodes remains challenging[38]. For example, the insertion material nickel hexacyanoferrate, $NaNiFe(CN)_6$ (a Prussian blue analogue), has been used as a reference electrode in Na-ion batteries, but significant potential drift was observed[50]. The development of reference electrode materials currently represents a knowledge gap in the post-Li battery field. A reliable RE would provide a valuable tool for studying the electrochemical behaviour of electrodes. This is particularly relevant in the case of a full-cell, where both electrodes contribute to the overall cell voltage, thereby making it challenging to isolate the behaviour of a single electrode. The use of RE allows an isolation of the anode or cathode performance, thereby providing more detailed insights into specific electrochemical reactions, such as electrode/electrolyte interphases formation, degradation, or capacity fade. RE enables the investigation of the influence of diverse electrolytes or additives on electrode performance, offering real-time insights into their impact on electrode potential and reactivity. This is a crucial aspect in the optimisation of electrolyte composition for enhanced performance and safety, a particularly pivotal objective in the context of KIB.

2.3.3 Ag|AgCl reference electrode in non-aqueous solutions

Silver-silver chloride (Ag/AgCl) electrodes are widely used as reference electrodes, particularly in aqueous systems, due to their stable potential and straightforward, cost-effective manufacturing process. They are also relatively non-toxic compared to alternatives like the saturated calomel electrode. However, using Ag/AgCl electrodes in non-aqueous media, such as organic solvents and ionic liquids, presents unique challenges and considerations.

The Ag/AgCl electrode is typically made by anodizing a silver wire in a chloride ion solution, forming an insoluble layer of AgCl on the wire's surface. This wire is then encased in a glass or plastic tube filled with KCl (usually 1–3 M or saturated), with a porous frit separating the reference electrode

compartment from the working electrode compartment. The frit allows ions to pass between the sample solution and the reference electrode's inner filling solution, maintaining charge balance during measurements. However, this frit poses significant limitations, including hindering miniaturization and allowing ions to leak in and out of the reference electrode compartment. Over time, silver and chloride ion leakage can significantly impact electrochemical measurements, especially in electrocatalytic studies.

To adapt Ag/AgCl electrodes for non-aqueous systems, modifications are necessary. The electrolyte inside the reference electrode compartment frequently differs from the main electrolyte, which can lead to contamination and unwanted responses at the working electrode. While a frit is used to slow electrolyte mixing times, challenges remain, such as increased impedance and changes in the liquid junction potential over time. In non-aqueous systems, traditional electrolytes salts like sodium and potassium chloride are not very soluble, leading to precipitation issues. As a result, alternatives such as sodium perchlorate and tetraethylammonium chloride are explored for their better solubility in non-aqueous media.

Ag/AgCl reference electrodes using 0.1 M tetrabutylammonium chloride (TBACl) in acetonitrile (MeCN) as the inner electrolyte have shown remarkable precision in absolute potential, high manufacturing accuracy, and stability[51]. Ag/AgCl RE is a straightforward and effective alternative to the commonly used anhydrous $AgNO_3$ RE. AgCl-RE are particularly well-suited for various electrochemical experiments, including cyclic voltammetry (CV), linear sweep voltammetry, electrochemical impedance spectroscopy, and controlled potential electrolysis, where potential stability and resistance to substrate contamination are crucial, and external potential calibration is sufficient.

When two electrolytes with different compositions (salt concentration and solvent) are in contact, for instance through a porous membrane, a potential difference is created. It can be due to the difference in salt concentration, which causes the liquid junction potential. Furthermore, if electrolytes have different solvents, different solvation leads to an additional contribution to the overall potential difference. These parameters should be considered in reference electrode systems that are placed in separate compartments. This is particularly relevant in the context of Ag/AgCl or Ag/Ag^+ systems discussed above. In general, the precise calculation or measurement of liquid junctions is hard to achieve due to the fact that there is no quantitative method for estimating the potentials at sides of membrane[52,53]. However, there are methods to minimize impact of these effects.

Utilizing the same solvent for the reference electrode compartment and the electrolyte solution in the cell compartment, as this reduces solvation effects consequently the potential difference. It is crucial to consider that electrode potentials can exhibit considerable variation in different solvents. This is reflected in the comparison of the K/K^+ potentials in different solvents, as briefly mentioned in **chapter 2.1**. The Li/Li^+ couple exhibits the most negative standard potential among alkali metals in water, while

the K/K^+ couple has a standard potential approximately 90 mV lower than Li/Li^+ in propylene carbonate[7].

Another way to reduce junction potential is the implementation of a salt bridge with an electrolyte containing ions of comparable mobilities, which serves to balance ion movement and thereby reduce the junction potential[54]. It should be noted that a small junction potential, the magnitude of which is unknown, is always present.

Nevertheless, in practice, the junction potential is frequently considered through internal calibration. This is especially crucial for Ag/Ag^+ RE and AgCl-RE due to the issue of reproducibility of absolute RE potential. Calibration enables an accurate assessment of absolute electrode potentials and can be achieved internally using standards, such as ferrocene.

2.4 Electrode Materials

In 2004, the possibility of designing a potassium secondary cell based on a $K_2Fe[Fe(CN)_6]$ cathode and potasium metal anode was demonstrated[55], and in 2010, work by Wang and Yoshio showed reversible K-ion intercalation in graphite[56]. These papers stimulated interest in KIB and the number of publications increased significantly, reaching more than 200 per year in 2019[3]. The special characteristics of K^+ ions described above (including elemental abundance, absence of Al-K intermetallic compound formation, *etc.*) have led to extensive research into electrode materials that can facilitate the generation of high voltage and power density capabilities.

2.4.1 Cathode materials

The positive electrode materials for KIB can be classified into four main categories, i.e. layered transition metal oxides, Prussian blue analogues (PBA) compounds, polyanionic compounds, and organic materials[57]. The typical average operation potential and capacity of the most commonly used cathode materials for KIB applications are presented in **Figure 3**. As can be observed, the general trend is that materials with a higher average operating potential exhibit a lower capacity value, and *vice versa*. Among these, Prussian blue analogues (PBA) demonstrate the most balanced properties. The following sections will present a discussion of the four material classes, before focusing on the main material of analysis of the presented thesis, namely PBA.

Organic Materials. A number of organic materials including 3,4,9,10-perylene–tetracarboxylicacid–dianhydride[58], copper-tetracyanoquinodimethane[59], carbonyl-based polyimide and polyquinoneimide[60] and poly(anthraquinonyl sulfide)[61] have been demonstrated to exhibit superior capacities and longer cyclability compared to other KIBs cathode materials. However, their redox activity at low operational voltages of around 2.0-2.5 V limits their specific energy[62]. Moreover, a considerable number of organic materials are afflicted by cathode material dissolution issues[3]. The synthesis of these electrodes typically occurs without the incorporation of potassium into their crystalline structure. Consequently, a chemical reduction is required prior to the first use, or alternatively, the use of pre-potassiated negative electrodes[60,63]. The structural flexibility of organic materials may offer researchers a potential pathway to the development of high-sustainability materials with high energy density in the future[63].

Layered Oxides. Layered oxides of the AMO_2 (A = alkali metal, M = 3d transition metals) type have been the subject of extensive investigation as positive electrodes for both LIB and NIB[64–67]. However, these materials, for example K_xCoO_2, have a number of challenges, including low reversible capacities, low operating potentials and stepwise voltage variations due to strong K^+–K^+ repulsion and multiple phase transitions[68–70]. The large ionic radius of K^+ limits the packing types in K_xMO_2

compounds, resulting in P-type stackings with larger interlayer distances[71]. This structural arrangement makes K-rich layered oxides thermodynamically unstable, causing them to degrade easily when exposed to air, which in turn leads to structural collapse and a decline in performance[72]. Nevertheless, these materials is the subject of ongoing research, and there have been instances of successful mitigation of some of the inherent limitations. To cite one example, the group of professors led by Myung achieved a notable degree of stability and capacity retention during the cycling process with the $K_{0.54}[Co_{0.5}Mn_{0.5}]O_2$/hard carbon full-cell. This cell demonstrated a 90 % C.E. and after 100 cycles, the discharge capacity was approximately 75 mA h g^{-1}[73], which is comparable to the best full-cell cycling performance achieved by the Komaba group (100 mA h g^{-1} and a 90 % coulombic efficiency)[12]. Given that the Komaba cell was operating at a higher voltage and in bigger potential window [2.0 V; 4.5 V] than the Myung cell [1.9 V; 3.9 V], and yet still exhibited a higher capacity, there is clearly room for further improvement.

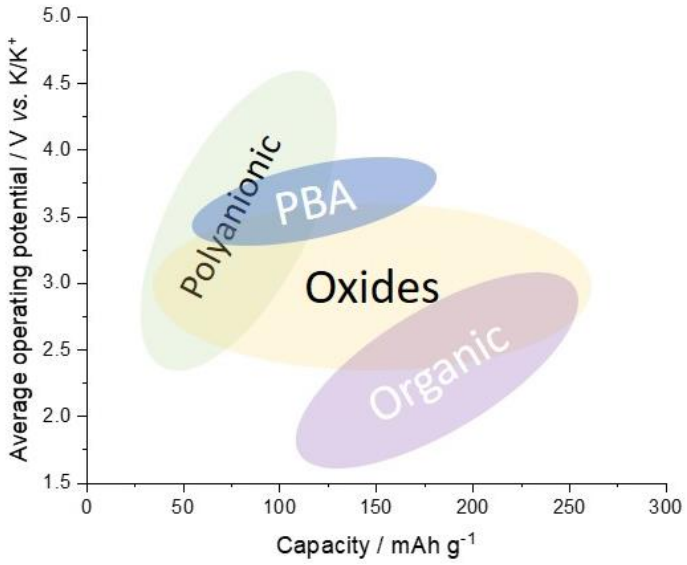

Figure 3. Average operational potential, specific capacity and energy of KIB cathode materials. Adapted and modified from ref[3]

Polyanionic Compounds. A different approach to developing a KIB cathode material would be the use of a range of polyanionic compounds. These compounds possess three-dimensional open framework structures comprising MO_x (M = transition metals, Fe,Ti or V) and $X_mO_n^{k-}$ (X – *p*-element, P, S, As, Si, Mo, and W) polyhedral[74]. The open 3-dimensional structure of these polyanionic compounds is advantageous for fast ionic diffusion in comparison with the 2-dimensional diffusion pathways observed in layered structures[75]. These materials are capable of achieving the highest average operating potential (up to 4.3 V and cut-off at 5V), which places significant demands on the electrolyte to be used in such a setup[76]. The elevated redox potential is attributed to the reduction in covalency of the M−O bonds, which is a consequence of the highly covalent X−O bond, which in turn is dependent

on the electronegativity of central *p*-element in polyhedral[77]. At this time, polyanionic materials are undergoing active development, with vanadium-based electrodes ($KVPO_4F$ and KVP_xO_y) representing a dominant area of research[78–80]. These electrodes have been shown to exhibit
the highest average potential and specific capacity, reaching up to 100 mAh g^{-1}[81–83]. Moreover, within KIB cathode materials this class of materials has demonstrated the highest capacity retention to date. For example, Liao et al. assembled $KVPO_4F/VPO_4$ full-cell with a capacity of 101 mAh g^{-1} (controlled by the cathode), operating voltage of 3.1 V, and a capacity retention of 86.8 % over 2000 cycles[81]. The relatively low average operating voltage is associated with a wide potential range of cycling, from 1.0 to 4.8 V. In order to achieve the full potential of the cathode materials under discussion, it is necessary to develop next-generation electrolytes that are capable of stable functioning in a wide voltage range, up to 5V[84].

Prussian Blue Analogues (PBA). Among the various cathode materials presented above, PBA exhibit the most balanced parameters, offering a high abundance of electrode materials, such as iron or manganese, a high operating potential, and a relatively high capacity (up to 150 mA g^{-1} for $K_2Mn[Fe(CN)_6$ [12]) compared to organic materials or some metal oxides[13,85,86]. Additionally, its synthesis is relatively straightforward[87].

The general chemical formular of Prussian Blue Analogues are expressed as $K_xM_1[M_2(CN)_6]y{\cdot}nH_2O$ ($0 \leq x \leq 2$, $y \leq 1$), where M_1 and M_2 represent different transition metals such as Fe[85,88], Mn[12,89,90], Co[91,92], Ni[91–93], Cu[49] and Zn[94]. The most common PBA ($K_xFe[Fe(CN)_6]$ undergoes a change from blue to white when the Fe^{3+} ions are completely reduced to Fe^{2+} (**Figure 4**). The fully reduced form, is referred to as Prussian White ($K_2Fe[Fe(CN)_6]$), while the partially reduced state is commonly referred to as Prussian blue ($KFe[Fe(CN)_6]$). The fully oxidised state PBA is called Prussian (or Berlin) green ($Fe[Fe(CN)_6]$). It is crucial to highlight that the aforementioned terminology is exclusively applicable to $K_xFe[Fe(CN)_6]$ and $K_xMn[Fe(CN)_6]$ PBAs.

Figure 4 illustrates the crystal structure of PBA in various charge states, demonstrating its three-dimensional open framework where octahedra are linked by cyano ligands. These frameworks create spacious 3D channels, facilitating the movement of large ions[95]. Typically, PBA have a cubic structure where the octahedra are arranged linearly[96]. However, depending on the guest cations and molecules, the octahedra can rotate cooperatively, leading to monoclinic (for K-rich PBAs, space group P21/n) or rhombohedral (typically space group R-3m, for expel for $K_2Mn[Fe(CN)_6]$) structures[97]. For $K_xFe[Fe(CN)_6]$ ($0 \leq x \leq 1$) the cubic structure is most stable, whereas for $K_2Fe[Fe(CN)_6]$ the rhombohedral phase is favoured[13]. In fully K-rich phases, monoclinic structures predominate, especially when water molecules occupy interstitial sites[98].

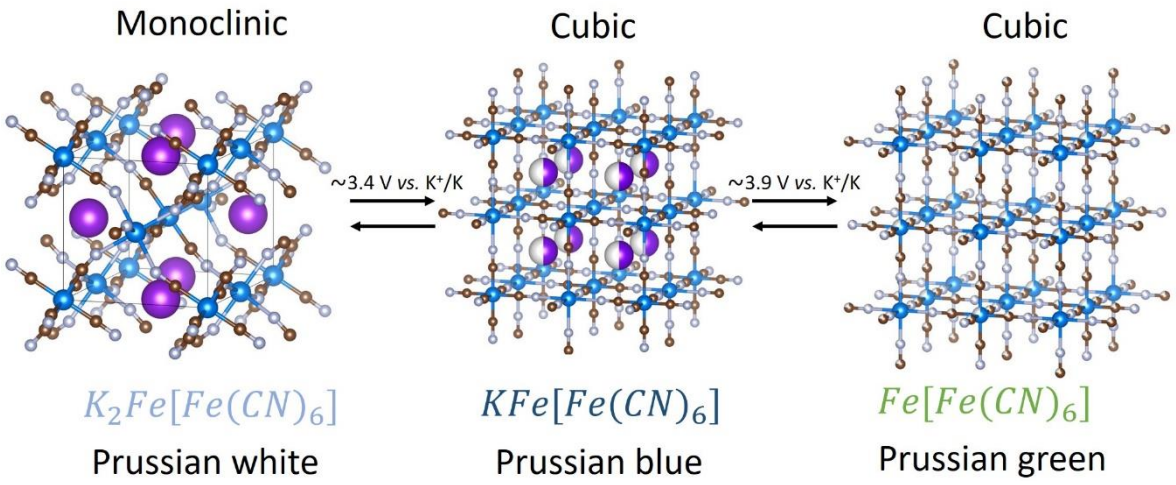

Figure 4. Structural evolution and colour change of PBA in different charge states

This behaviour differs from that of sodium-based PBA, as K-rich PBA always exhibit monoclinic structures regardless of the drying conditions[12,99]. This phenomenon is attributed to the larger ionic radii of K^+ ions, which increase Pauli repulsion in the lattice, preventing lattice shrinkage and favouring the formation of a rhombohedral phase with a smaller lattice volume compared to the monoclinic phase[100]. Given the size of PBA sites, it is possible for them to accumulate a considerable quantity of water[100,101]. To achieve a minimal amount of interstitial water, it is essential to dry the material at a temperature that allows for the removal of water while preventing the decomposition of the material. The optimal drying temperature is therefore around 150°C. [102]

2.4.2 Anode Materials

Currently, graphite is the most commonly utilized anode material for KIB. However, a variety of alternative materials, including non-graphitic carbonaceous materials, K-alloys, oxides, chalcogenides, polyanionic compounds, and organic materials, can be employed as negative electrode materials[103]. ***Non-graphitic anodes.*** Recent findings have indicated that a number of materials exhibit superior characteristics in comparison to graphite, particularly in terms of both C.E. and rate capabilities[104–106]. For instance, transition metal oxides (e.g. $K_2T_4O_9$ [106]), chalcogenides ($TiSe_2$[107]) and polyanionic compounds ($KTiPO_4F$ [80,107]) are well-suited for use as safe negative electrodes in KIB, given that their operating potentials exceed that of the K^+/K electrode deposition potential[107–109]. However, this material class exhibits a common drawback, namely a low capacity that is 2-3 times lower (around 100 mA h^{-1}) than that of graphite. Similarly to lithium and sodium systems, certain alloying materials demonstrate higher gravimetric and volumetric capacities in potassium cells than carbonaceous materials[110–112]. However, these materials display low cycling stability, due to high volume expansion, which in KIB is even more significant than that observed in LIB and NIB[113].

Certain organic materials, predominantly para-aromatic dicarboxylates, demonstrate comparable capacity (around 200 mAh g^{-1}) and superior cycling stability relative to carbonaceous anodes[114–116]. Among anode KIB materials, with the exception of graphite, hard carbon is the most extensively researched and employed[103]. It is a form of carbon that can be derived from a variety of precursors, including petroleum pitch, coal tar pitch, polymers, and biomass[117]. The highly disordered structure of hard carbon provides numerous active sites for alkali-ion storage, resulting in high capacity (reversible capacity 200-220[118,119]) and good cycling stability[120]. However, the use of it in KIB presents certain challenges. In comparison to graphite anodes, HC exhibits lower initial efficiency (50-60 % of hard carbon[119] *vs.* 80-90 % of graphite[6,121]) and a higher irreversible capacity, predominantly due to substantial losses in the initial cycles resulting from the formation of SEI. It is therefore crucial to understand these losses in order to optimise full-cell performance.

To the moment, aforementioned groups of materials require further investigation and still exhibit inferior overall performance compared to graphite[103,113,122]. Consequently, the presented work primarily focuses on graphite, which is still the most prevalent and widely utilised material in KIB[3].

Graphite as anode material. The graphite materials, which have been well-established in LIB and optimised for performance enhancement[123], appear to be promising options for KIB due to their favourable combination of low operating potential and high capacity, as well as their high cycling stability[124]. The third generation of LIB has led to the widespread adoption of graphite as a battery material[125]. It was spread extensively due to its high gravimetric and volumetric capacities, low operational potential, and high electronic conductivity[126]. However, the electrochemical intercalation behaviours of lithium, sodium and potassium into graphite at room temperature exhibit notable differences[127]. In lithium cells, the graphite electrode exhibits the highest reversible capacity, around 370 mAh g^{-1}, associated with the formation of LiC_6[128]. Conversely, in sodium cells, observed capacity is low due to the limited occurrence of electrochemical Na intercalation within defect-free graphite[129]. This is attributed to the unstable NaC_6 and NaC_8 structures, which are caused by the weak ionic binding between Na^+ ions and carbon planes[130]. In contrast to sodium, potassium can reversibly intercalate into graphite, yet exhibits a distinct structural configuration[131]. In general, among alkali metals, only NaC_6 has a positive formation energy, indicating instability. For cations larger than Na^+, the formation energy becomes more negative (more stable) as ion radius increases[129,132]. This is due to the decreasing electronegativity of alkali metals down the group, which increases the ionic character of the metal-carbon bond[133]. Conversely, smaller ions like Na^+ form weaker metal-carbon bonds, leading to positive formation energies. However, Li is an exception to this trend, with the formation energy becoming negative due to the presence of a covalent component in the binding energy, alongside ionic interaction[129].

It has been demonstrated that potassium can form stable graphite intercalation compound (GIC) as early as 1926[134] and 1954[135]. It exhibits reversible capacities within the range of 240–260 mAh g^{-1}, with a theoretical capacity of 279 mAh g^{-1}, which is associated with the formation of KC_8[136]. The volume expansion of graphite due to changes in interlayer distance is 59.7 % at full K intercalation, which is nearly six times greater than the ~10 % expansion observed with Li intercalation[121,137]. In contrast to alloy and conversion electrode materials, where substantial volume expansion has a detrimental impact on cycling stability and structural reversibility, the considerable volume change in graphite during potassiation can entirely come back its original layered structure after deintercalation[121]. Therefore, it can be concluded that graphite is an optimal anode material for KIB. Furthermore, the industrial knowledge and technologies accumulated for LIB graphite electrodes could be applied to KIB.

Graphite is composed of stacked graphene layers. These layers are linked together by weak van der Waals forces and π-π interactions of the delocalised electron orbitals[138]. Predominantly (~70 %) it is organised in an ABAB stacking sequence with an interlayer distance of 3.354 Å and hexagonal symmetry[139]. A smaller fraction of the layers (~30 %) are arranged in a less stable ABCABC stacking sequence with rhombohedral symmetry[140]. Upon intercalation of alkali metal ions, the stacking sequence can transform into an A|A configuration, leading to the formation of "stage n" GIC, where **n**th stage represents a number (n) of graphene layers between the two closest intercalated layers[141]. During electrochemical intercalation, potassium ions insert between the graphene layers, forming K-GICs that progress through stages 4, 3, 2, and 1[6]. Stage-1 K-GICs have a composition of KC_8, which differs from LiC_6. The interlayer distance in KC_8 is approximately 5.3 Å, which is longer than the 3.7 Å in LiC_6[6,142]. In a simplified representation: graphite→ graphite + disorderly stacked potassium (KC_{96}) → Stage-4 (KC_{48})→ Stage-3 (KC_{36})→Stage-2 (KC_{24}) → Stage-1 (KC_8)[121,141]. In the deintercalation process, all stages are reversed from KC_8 to graphite[6,121].

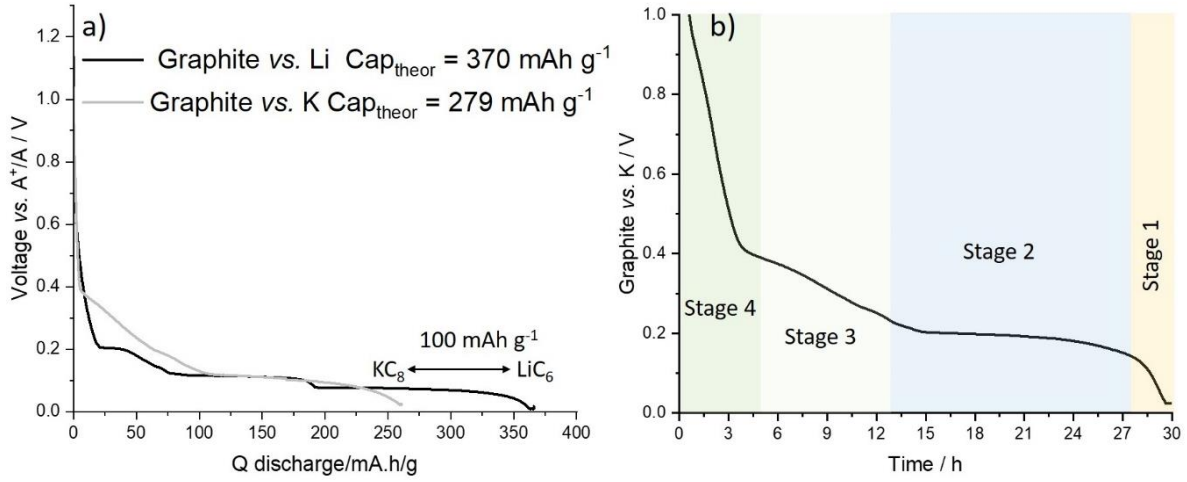

Figure 5. a) Comarison of electrochemical intercalation of Li^+ and K^+; b) Intercalition stages of potassium into graphite

Figure 5a demonstrates stepwise potential changes are observed in the galvanostatic charge-discharge curves for the K/graphite cell, with comparison of the Li/graphite cell. Each stepwise region indicates of the stage transformations of Li/K-GIC[143]. As could be seen in **Figure 5b**, the graphite electrode cycling curve exhibits three pronounced reduction peaks. The main redox peak of K^+ intercalation is observed at 0.14 V/0.29 V *vs.* K^+/K. The intercalation of Li demonstrates two major redox peaks at 0.10 V/0.12 and 0.07 V/0.08 V *vs*. Li^+/Li. It is therefore anticipated that the formation of the stage structures of K-GIC will differ from those of Li-GICs. The difference in ion size affects the stability and formation energies of the resulting GIC[129]. Additionally, research has highlighted the presence of Daumas–Hérold defects in K-GIC, which serve as domain boundaries and contribute to the formation of unique characteristics not observed in Li-GIC[144].

2.5 Electrolytes

The electrolyte plays a crucial role in battery performance[145]. The ionic conductivity of electrolytes affects reaction kinetics, while their electrochemical stability defines the working potential range and limits energy density[146]. Additionally, solvent co-intercalation reactions can occur and result in a reduction in battery performance[147]. The electrolyte properties, including solvation behaviours, steric configuration, and chain length, have a direct influence on the reversibility, working potential, and K-ion storage kinetics[148]. The formation, composition and stability of SEI are directly dependent on the electrolyte[149]. According to molecular orbital theory, the anodic and cathodic stability of the electrolyte can be influenced by the electronic states of the solvent and ion solvation (e.g., K^+)[150,151]. Furthermore, electrolytes must be compatible with electrodes to prevent adverse side reactions, rapid capacity fading, and to ensure high wettability, which reduces polarization in battery reactions[30,31,145].

To guarantee optimal functionality, reliability, and safety in KIB, electrolytes must satisfy a number of essential criteria. It is vital that the electrolyte remains stable across the entire operating voltage range of the battery. Instability at cathode voltages in excess of the optimal range or anode voltages below the optimal range can result in undesirable side reactions, capacity loss, or even safety hazards[152]. A broad electrochemical stability window is crucial, as it minimizes the risk of electrolyte decomposition across the battery's voltage range, thus reducing the occurrence of unwanted side reactions. For instance, when electrode materials were discussed, it was demonstrated that a voltage window of up to 5 V can be applied in a full-cell, if graphite is used as the anode and $KVPO_4F$ is used as the cathode. In the context of KIBs, it is of particular importance to have an electrolyte that is stable over a wide potential range. Unfortunately, at the moment, due to the necessity for a very wide potential window, conventional carbonate electrolytes are reaching their limits. Therefore, the optimal electrolyte for KIBs in the search process and it is one of great interest in the field.

A further crucial electrolyte attribute is the provision of high ionic conductivity. The electrolyte should facilitate the rapid and efficient movement of ions (such as Li^+, Na^+, or K^+) between the electrodes, thereby ensuring the expeditious completion of charge/discharge cycles[146]. This is typically achieved through the provision of high ionic conductivity, which is typically in excess of 1 mS cm^{-1}. The electrolyte should also exhibit low viscosity. A low viscosity enables enhanced ion mobility and thus improves the overall conductivity of the electrolyte, facilitating a faster ion transport between electrodes[148]. Furthermore, an optimal electrolyte should be non-flammable or exhibit low flammability in order to minimise the potential for fire hazards, particularly in circumstances involving elevated temperatures or instances of overcharging[153].

In general, two principal categories of electrolytes can be defined: liquid and solid-state. The first category includes organic, aqueous, gel polymeric, and ionic liquid systems, whereas the latter comprises inorganic solid electrolytes and polymer systems. In the field of liquid KIB electrolytes, the most prevalent combinations are EC:DEC and EC:DMC in combination with KPF_6[3]. For solid-state electrolytes, research is still relatively limited, especially regarding inorganic solid-state potassium ion conductors[3,145]. In terms of polymers, much of the focus has been on poly(ethylene oxide) (PEO)[154–156] and polymethyl methacrylate[157] as promising candidates for KIB applications.

2.5.1 Organic electrolytes

The current predominant utilisation of organic electrolytes in KIB is predicated upon their high ionic conductivity, satisfactory electrochemical stability and compatibility with electrode materials[17]. However, a major drawback of organic electrolytes is their safety risks, as they are flammable and volatile[158]. Moreover, the reaction between highly reactive potassium metal and carbonate-based electrolytes often results in formation of degradation products which cause decrease in performance of half-cell[159].

One alternative to traditional ester-based electrolytes is ether-based electrolytes, which have demonstrated certain advantages in improving the performance of KIB. For example, the use of triethyl phosphate (TEP) as a solvent in KIB has been shown to stabilize the layered structure of the cathode material, $K_{0.5}MnO_2$[160]. TEP-based electrolytes enable better cycling performance by preventing the co-intercalation of electrolyte molecules that would otherwise degrade the layered structure, as seen in the use of EC:DEC-based electrolytes. Additionally, TEP provides a high initial C.E. and low overpotential, making it a promising option for high-voltage KIB. Furthermore, the flame-retardant properties of the material address safety concerns[161].

Similarly, dimethoxyethane (DME)-based electrolytes have been shown to improve the cycling stability of organic electrode materials like anthraquinone[162] and alloy-based anodes (e.g., Sn, Bi, SnSb)[163,164]. DME promotes the formation of a SEI layer, resulting in higher C.E. and less polarization compared to ester-based solvents[164]. Moreover, DME-based electrolytes enhance K^+ diffusion and charge transfer kinetics in certain cathode materials, such as TiS_2[165].

While carbonate, such as EC, PC, and DEC, remain the most common solvents in KIB electrolytes due to their high electrochemical stability and ability to dissolve K salts[3], ether solvents offer promising alternatives. These solvents, including DME and DEGDME, provide benefits like lower viscosity, improved SEI formation, and enhanced electrode performance, though their reactivity and limited oxidation resistance present challenges that need to be addressed in future research[17].

Carbonate ester electrolytes. K^+ ions exhibit considerably weaker Lewis acidity in comparison to Li^+ and Na^+ ions, resulting in weaker interactions with Lewis bases, such as anions and solvents[166]. One of the disadvantages of KIB is that potassium salts solubility in non-aqueous solvents is lower than that of its Li and Na[166]. This phenomenon can be attributed to the lower solvation energies exhibited by these ions in comparison to others[167]. At this time, the most prevalent electrolytes in KIB are carbonate-based[168].Owing high electrochemical stability at high voltages and exceptional ability to dissolve alkali metal salts, carbonates have become as the predominant solvents for KIB[13,129]. To date, the most commonly used carbonate electrolytes are typically consisting of two classes of carbonate esters: cyclic carbonates (EC and PC) and linear carbonates (DMC, DEC, and EMC)[145]. The structure of the aforementioned carbonates is illustrated in **Figure 6**. The viscosity of linear carbonates is typically lower than that of their non-linear analogue, and they also have a lower dielectric constant. In contrast, ethylene carbonate has the highest dielectric constant, thereby demonstrating superior capacity to dissolve salts for the purpose of enhancing the overall performance of the electrolyte (such as ionic conductivity) and the stability of the SEI[3]. The primary disadvantage of EC is that it is solid at room temperature (melting point: 36 °C)[169]. Consequently, it should be utilized with linear carbonate. The decomposition of electrolytes based on EC results in the formation of a stable SEI. Furthermore, in addition to important role of EC in SEI formation, it has been demonstrated that EC is the key factor in suppressing electrolyte decomposition in LIB[170]. When employed as a co-solvent, EC forms a stable Li^+–EC solvation structure, which serves to prevent the decomposition of other linear carbonate solvents (such as DMC or DEC). The Li^+–EC pairing effect serves to stabilise the electrolyte system, thereby reducing the occurrence of unwanted side reactions[170].

Like $LiPF_6$ is most used lithium salt for electrolytes used in commercial LIB due to its outstanding compatibility with various cathode and anode materials. Similarly, KPF_6 has become the most used salt in battery research[31,121,171,172]. It is beneficial that in KPF_6, the solubility in carbonates is moderate, and the PF_6^- anion does not undergo any reaction with the aluminium current collector. However, they tend to form unstable SEI on the anode surface, leading to low coulombic efficiency. In contrast, electrolytes based on concentrated KFSI solutions offer more stable formation of SEI, resulting in greater cycling stability, but are susceptible to aluminium corrosion at higher voltages. One potential solution to the aluminium corrosion issue is the utilisation of highly concentrated KFSI electrolytes in conjunction with KFSI-containing ionic liquids. This represents an aspect worthy of further investigation, given that highly concentrated KFSI electrolytes have been shown to result in the formation of pronounced 'salt-derived' SEI compositions. Notwithstanding the disadvantages associated with KPF_6, including an unstable SEI and unsatisfactory thermal stability, it remains the most used K salt for KIBs[3,173]. KPF_6 has a number of advantages, including relatively high ionic conductivity, electrochemical stability, accessibility, and passivation of Al foils[173]. Consequently, the

EC:DEC/KPF_6 formulation is currently the most prevalent electrolyte formulation. Furthermore, some of the inherent disadvantages of the system, such as the formation of an unstable SEI, can be mitigated through the incorporation of electrolyte additives[174].

Electrolyte decomposition. In LIB, electrochemical testing is typically conducted in half-cell configurations to evaluate electrode performance. In the short term, it is evident that Li-metal has no significant effect on the behaviour of electrodes or electrolytes. Consequently, it is a valid approach to estimate electrode material performance in conditions of high excess of ion carriers. In case of KIB, half-cell configuration bear a lot of issues due to the extensive side reactions at the highly reactive metallic CE. The degradation of the counter electrode can also affect the working electrode through a phenomenon known as "cross-talk," where degradation products from the alkali metal electrode deposit on the working electrode, altering its surface layer properties[175].

These changes in surface layer composition and thickness, even during storage at open-circuit conditions, can be substantial. The chemical processes involved can interfere with electrochemical reactions, leading to increased cell resistance[176], voltage hysteresis[177], misleading voltage signatures, and potential drifts during cycling. The effects of cross-talk reactions at electrode surfaces will be further discussed in the following section on electrode interphaces and throughout this thesis. Here, the focus will be on the soluble and gaseous products of electrolyte degradation.

In carbonate-based electrolytes, the main products of electrolyte degradation, particularly those involved in cross-talk reactions, are dicarbonates (**Figure 6**)[159]. Depending on the electrolyte composition (whether a single carbonate or a mixture of several), dimerization of one of the electrolyte's carbonates or reactions between multiple carbonates can occur. The formation rate of dicarbonate coupling products decreases in the order of EC/DMC > EC/EMC > EC/DEC. Moreover, the presence of conducting salts has been shown to accelerate the formation of corresponding dicarbonates[159]. For instance, the detrimental effect of these products on cell performance was demonstrated by Hosaka *et al.*[178]. Their findings revealed that the formation of oligocarbonates (DEDD and DECC, **Figure 6**) due to the reaction of the electrolyte with the K-metal in KPF_6 EC:DEC electrolyte led to a significant decline in the performance of the cathode material ($K_2Mn[Fe(CN)_6]$). The product of electrolyte degradation reduced the reversible capacity of the cathode from 130 to 110 mA h g^{-1} caused a decline in the C.E. to approximately 20% (from 87-86 to 68 %).

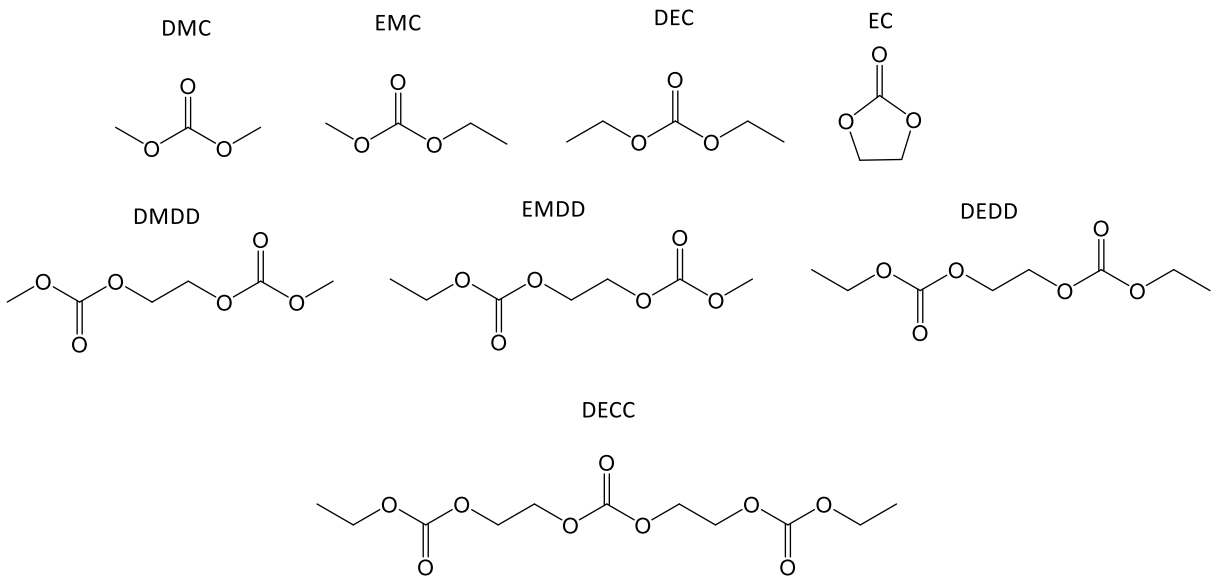

Figure 6. Linear organic carbonates (DMC, EMC, DEC), cyclic carbonates (EC), dicarbonates: DMDD (Ethane-1,2-diyl dimethyl biscarbonate), EMDD (Ethane-1,2-diyl ethylmethyl biscarbonate), DEDD (Ethane-1,2-diyl diethyl biscarbonate) and oligocarbonate: DECC (Di-(2-ethoxycarbonyloxyethyl)carbonate)

The high levels of electrolyte decomposition observed in KIBs are likely explained by the solvation structure of K^+ ions, which is determined by electrolyte composition (solvent chemistry, anion type, and salt concentration). K^+ donates an electron more readily to the solvent compared to Li^+ in a given metal-solvent pair. Among carbonates, the Li^+–EC pair is the most stable, which accounts for the higher solvent reduction seen with K^+. Additionally, for a given metal-solvent-anion complex, the closer the anion is to the metal ion, the higher the stability of the solvent.

It has been demonstrated in the literature that electrolyte additives can suppress the formation of dicarbonate derivatives by passivating alkali metals[179]. This enables the use of shorter-chain linear carbonates, some of which exhibit enhanced flow and solubility properties.

Nevertheless, the evidence of intensive electrolyte degradation was observed mainly in the half setup, whereas full-cell electrolyte degradation is significantly lower. This difference introduces additional challenges to KIB testing, as the majority of effects observed in the half-cell setup will not appear in the full-cell, and *vice versa*. Consequently, researchers must consider both the half and full-cells as distinct systems, in contrast to the approach typically employed in LIB practice.

2.6 The Electrolyte-Electrode Interphases

When the system operates above or below the potential window of the electrolyte, the latter decomposes (either reducing or oxidising), forming insoluble compounds on the electrode surfaces. (**Figure 7**). This irreversible decomposition results in various solid products, including insoluble inorganic salts and organic components, depositing or precipitating on the electrode surfaces[149]. These products form compact coatings at the electrode-electrolyte interphase. This deposition or precipitation process, occurring upon contact between the electrode and electrolyte or during the initial cycles[180]. Ideally, these compounds create a kinetic barrier that prevents further electrolyte decomposition and solvent co-intercalation in subsequent cycles[181]. The stability of electrode–electrolyte interphases (EEI) is crucial to battery performance. The formation of the EEI results in the consumption of electrolytes and active ions, which can lead to a reduction in both energy capacity and power output in batteries. The EEI should ideally form only once at the initial cycles and remain as a stable passivation layer throughout the battery's lifespan[181]. In practice, however, the EEI is undergoing significant changes as a result of the complex multistage electrochemical and chemical oxidation-reduction processes that occur within it. These changes affect the composition, structure, and function of the EEI, and they emerge and evolve dynamically throughout the cycling process. The dissolution, decomposition, or reforming of certain components of the EEI was observed to occur in the case of KIB, resulting in the continuous degradation of the electrolyte in response to the dynamic evolution of the EEI[17]. The interphases have a considerable impact on the overall performance of the battery cell, influencing the reversibility of redox reactions at the electrodes, the kinetics of cell processes, and the cell's safety[182]. The EEI fulfils a dual function, providing vital protection while simultaneously impeding ion transfer[183]. It is essential to achieve an optimal balance between these opposing effects through careful and meticulous management.

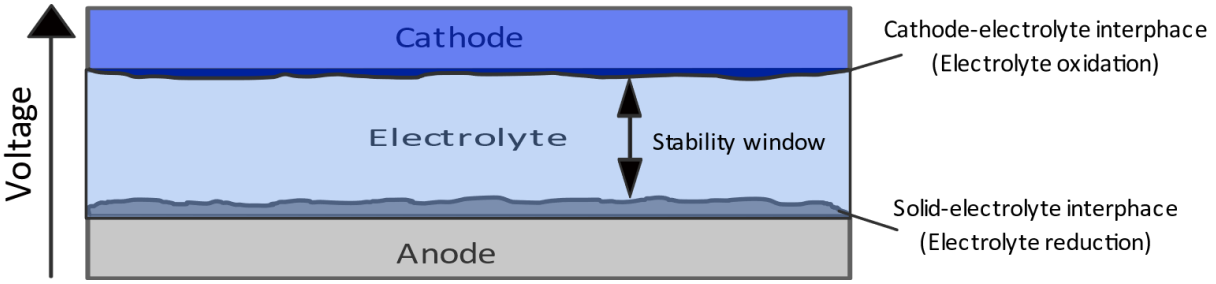

Figure 7. Electrode-electrolyte interphase formation at the negative and positive electrode surfaces due to electrolyte decomposition

2.7.1 Solid electrolyte interphase (SEI)

The SEI layer allows the diffusion of cations to maintain reaction kinetics and insulating the electronic contact between the electrode and electrolyte[184]. A robust SEI is a critical parameter for ensuring the stability and longevity of batteries as it prevents further electrolyte decomposition which effectively enhances the Coulombic efficiency and the reversible specific capacity of the battery[146,149,185]. The composition of the SEI, meaning the relative proportions of its compounds, is dependent on the reactivity of the electrolyte solvents used, as their reduction rate influences the growth rate of the surface deposit[172].

A well-designed SEI should have a high ionic conductivity (allowing rapid metal ion diffusion across the interphase). Additionally, it should be thin and elastic, preventing cracking[186]. Even in the case of LIB, where the volume expansion of graphite particles during lithium intercalation is relatively low (approximately 10 %), stress-induced cracking of the passivation layer can still occur[187]. This results in the continued occurrence of irreversible reactions, which, over time, consume a significant amount of lithium. It is evident that in KIB, where the expansion is significantly higher, the issue is even more critical[6]. Furthermore, the necessity for a thicker SEI layer to cover the entire surface area, due to the high surface area, further complicates the issue[188]. The use of small amounts of electrolyte additives, which are designed to decompose early, can help form thinner more stable SEI layers. Alternatively, the properties of the SEI can be enhanced through surface modifications or by creating an artificial SEI layer before operation[189].

Characteristics of SEI in Carbonate Electrolytes. The formation of the SEI is influenced by a range of factors, including the ion radius and the solvent's solvating power, which is associated with its dielectric constant[190]. In carbonates, the solvation of lithium ions is typically stronger than that of anions by solvent molecules[191]. Thus, SEI formation in the carbonate-based electrolyte derives from both cation-coordinated and free solvents, but not anions. Solvated lithium ions diffuse towards graphite surface edge sites, where reductive decomposition reactions occur (**Figure 8**)[192]. The solvation of lithium ions by anions or solvent molecules is crucial for the formation of a stable protective interphase, as the SEI is predominantly the result of the decomposition of solvents in the Li^+ solvation shell in close proximity to the electrode[193]. The rigidity of the solvation shell is key to ion mobility, as increased rigidity results in slower ionic transport due to greater drag on lithium-solvent complexes[194].

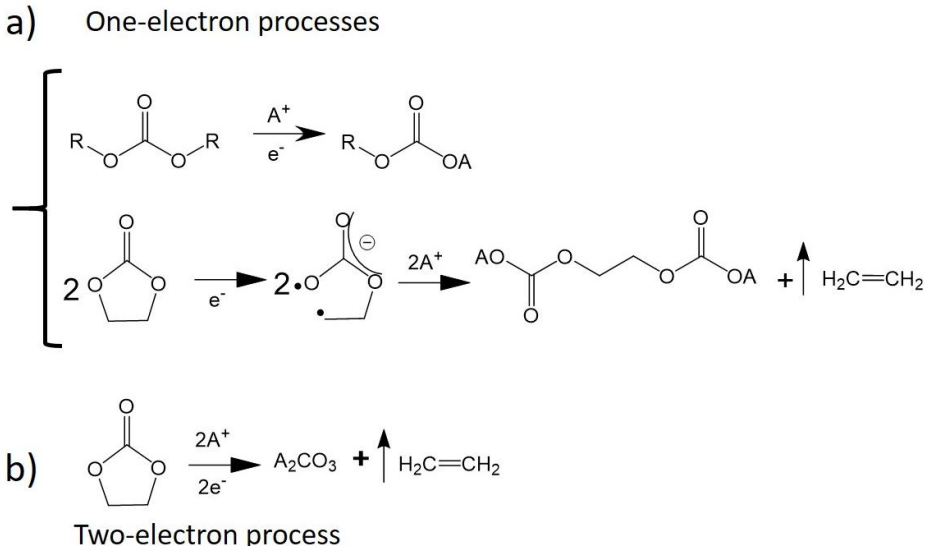

Figure 8. Main electrolyte decomposition reactions in SEI formation: The reduction of carbonate solvents a) one-electron b) two-electron process

The most spontaneous reaction occurs when desolvated lithium ions intercalate into graphene layers (**Figure 8a, b**) at a more negative potential than other competing reactions during cathodic polarization[195]. The reduction of carbonate solvents can follow either a one-electron (**Figure 8a**) or two-electron process (**Figure 8b**)[196]. The electrochemical reduction of EC at the graphite surface results in the formation of an intermediate radical anion[197]. This subsequently decomposes to form lithium ethylene dicarbonate (LEDC) and then reacts with trace water to produce Li_2CO_3[149]. It is proposed that EC undergoes a two-electron transfer reaction with Li^+ to form Li_2CO_3 and C_2H_4 (**Figure 8b)**[198]. Solvated lithium ions co-intercalate into graphene layers, forming GIC, which then reduce to form the SEI. Another pathway involves PF_6^- attacking EC, forming $CH_2FCH_2(O(C=O)O)PF_3O^-$ and PF_5[199]. The $LiPF_6$ salt is thermodynamically unstable and reacts with Li_2CO_3 to produce LiF, POF_3, and CO_2[200]. The presence of impurities, such as H_2O and CO_2, results in the reaction between Li^+ and the formation of Li_2CO_3, LiOH, and Li_2O, which are common components of the SEI[201]. These species can accumulate and crack due to thermal expansion differences. $LiPF_6$ also reacts with water, releasing HF and HPO_2F_2, which are harmful and reduce battery performance[200]. Therefore, keeping impurity levels in the electrolyte to a minimum is crucial.

As illustrated in **Figure 8**, the formation of SEI is often accompanied by the generation of gaseous products. In a publication by Caracciolo[202], it was shown that, in addition to soluble dicarbonates and insoluble carbonates and other products of electrolyte degradation, CO, CO_2 and C_2H_4 gases are formed in a KIB half-cell. Furthermore, the addition of conductive salt, as in case formation of soluble products, was also observed to enhance the formation of these gases, leading to the release of C_2H_6 in addition to the aforementioned gases.

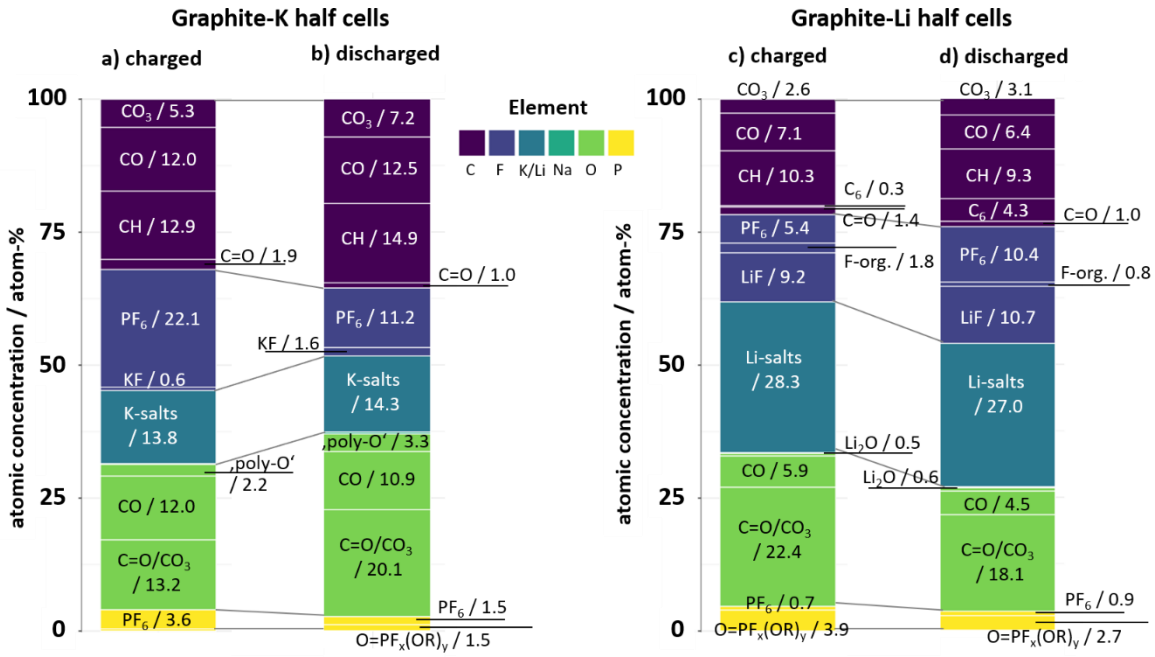

Figure 9. Bar plots of the atomic concentrations found of individual SEI components by XPS on (a) charged K−graphite, (b) discharged K− graphite, (c) charged Li−graphite, and (d) discharged Li−graphite electrodes. A small deviation from 100% contribution is associated with a minor fraction of unaccounted species. Adapted and modified from ref.[203]

Due to the high reactivity of potassium, the formation of the SEI in KIB in the full and half-cells differs considerably. Furthermore, the SEI differs from that observed in LIB. The Li^+-solvent complex is significantly more stable than the K^+-solvent complex for MPF_6 (M = Li or K) in carbonates[167,193]. A comparison of similar systems in LIB and KIB (electrode and electrolyte composition) reveals that SEI layers on graphite electrodes exhibit significant differences between K and Li EC:DEC systems[203]. In K-graphite systems, the SEI is more organic (**Figure 9**), less stable, and dissolves more easily in the electrolyte, resulting in rapid SEI growth and poor cycling stability. In contrast, Li-graphite systems have a stable SEI with a significant LiF content. Furthermore, electrolyte degradation products formed on the K surface may migrate to the working electrode, resulting in cross-talk even at open circuit voltage[202]. This presents a challenge in determining whether the SEI on the anode in K-ion half-cells forms exclusively on the anode or originates from the K metal. The most significant challenge currently facing the SEI of KIB full-cells is the instability of the surface layer. In contrast to LIB, where the surface layer remains stable after formation, the electrolyte in KIB is in a constant state of reaction with the anode surface, resulting in the loss of charge carriers and thus capacity. To enhance the applicability of KIB, it is necessary to develop more stable interphases with elevated proportions of inorganic, insoluble compounds.

2.7.2 Cathode electrolyte interphase (CEI)

The CEI forms on the surface of the cathode during battery cycling, as a result of electrolyte decomposition at high potentials (**Figure 7**). The distinction between SEI and CEI formation in an electrochemical environment and the reactions involved therein is due to the different operating voltage ranges of the cathode. The CEI can include a variety of decomposition products, including metal fluorides, organic carbonates, and other compounds, depending on the specific electrolyte chemistry[204]. Similar to the SEI, the CEI forms a passivation layer that protects the cathode material from continuous electrolyte decomposition. This layer allows the passage of metal ions while blocking electrons, thereby preventing further reactions. A stable CEI is crucial for preventing further electrolyte consumption and for maintaining the integrity of the cathode surface. The formation of a stable CEI is complicated by the instability of the electrolyte at higher operating voltages at the cathode, particularly in the case of KIB[173]. Even after the interphase has been formed, the electrolyte continues to decompose[180] , resulting in a continuous consumption of electrolytes and subsequent loss of ion carriers. It should be noted that the CEI is not static. Interphase evolves during the cycling process, and the breakdown or reforming of the interphase can lead to a reduction in battery performance. In order to address the challenges of electrolyte instability at the cathode-electrolyte interphase, especially during high-voltage applications, two main strategies can be employed. The first of these is the development of electrolytes with oxidation potential that is above the cathode's electrochemical potential. This ensures intrinsic thermodynamic stability[205,206]. Secondly, there are measures that can be taken to enhance the formation of the CEI, which involves the use of additives in the electrolyte that can form the CEI, electrode surface coatings, and modifications to the cathode surface that can be made prior to assembly[180]. The objective of these measures is to achieve rapid kinetic stability at the interphase from the beginning of operation.

Cathode materials are known by their strong nucleophilic and Lewis basic properties, which enable them to coordinate with oxygen atoms from electrolyte components (e.g., carbonates) and initiate redox reactions[207]. For LIB it is known that cathode materials are often covered by a native surface film of lithium carbonate (Li_2CO_3) and lithium hydroxide (LiOH), formed from reactions with CO_2 and moisture during storage and processing[208,209]. The formation of the Li_2CO_3 film on transition metal oxides (layered lithium cobalt oxide, spinel-type lithium manganese oxide and layered lithium nickel–cobalt–aluminum and lithium nickel–cobalt–oxides) can also result from incomplete conversion of carbonate precursors used in electrode synthesis[180]. The reaction of Li_2CO_3 with electrolyte salts ($LiPF_6$ and $LiBF_4$) has been observed[210]. Furthermore, the oxidation of organic carbonate-based electrolytes is influenced by the conductive additive in the cathode mix and the upper cut-off voltage[211]. It has been demonstrated that decomposition of $LiPF_6$/organic carbonate electrolytes commences above 4.5 V[212].

Similarly, in the case of the SEI, the composition and thickness of the KIB CEI exhibits notable differences between its half and full-cell configurations. At this time, CEI of KIB is not a major area of interest, although there are still some groups engaged in research in this area. For example, Larhrib *et. al.* studied the growth and ageing of SEI and CEI in KVPFO/graphite full-cells with using 0.8 M KPF_6 EC:DEC electrolyte[213]. The research team has made some findings on CEI. The application of higher open circuit voltage (OCV) at temperatures of 40 °C for 12 hours resulted in the formation of a thicker inorganic passivation layer. This may have enhanced electrode wetting and electrochemical performance. An upper cut-off voltage of 4.8 V was identified as the optimal value, as it facilitated the balanced formation of organic and inorganic passivation layers. This resulted in enhanced capacity retention and coulombic efficiency evolution, in comparison to the outcomes observed at upper cut-off voltage of 4.5 V and 5.0 V.

Zhao et al. employed the use of a highly solvating electrolyte, trimethyl phosphate (TMP), in combination with KTFSI salt, to achieve the formation of a stable inorganic CEI in $K_{0.5}MnO_2$/soft carbon full-cell[214]. The CEI formed in that electrolyte contained a greater quantity of KF, which permitted the formation of a more stable surface layer than that observed in the 0.8 M KPF_6 in EC:DEC. The assembled full-cell exhibits a prolonged cycle life (92.5 % after 500 cycles at 1 A g^{-1}) with ~100 % Coulombic efficiency. The discharge capacity of the cell under the specified cycling rate was approximately 55 mA h g^{-1}.

The reactions involved in the formation of CEI of PBA and their description for KIB form part of the presented work and will presented later in following chapters.

2.7 Additives

Electrolyte additives are defined as small quantities of specially formulated compounds that are introduced into the electrolyte with the objective of modifying the desired properties of the battery. In LIB and NIB, additives have been demonstrated to play pivotal roles in modifying the SEI, enhancing surface wettability, improving flame retardancy, reducing viscosity, increasing solvent solubility, and preventing overcharging. As was previously asserted, the most significant challenge associated with KIB electrolytes, including carbonate-based ones, is their instability when exposed to highly reducing negative electrodes and highly oxidising positive electrodes (**Figure 7**), as well as their high reactivity with potassium metal.

The replacement of the entire electrolyte mixture and the search for a more stable electrolyte represent a potential solution to the problem, although it is a lengthy and energy-intensive process[215]. In this context, electrolyte additives used in small quantities (typically ≤5 wt. % or vol. %) can effectively enhance the electrochemical properties of bulk electrolytes with minimal impact on their physical properties (e.g., viscosity, ionic conductivity, *etc*.)[174]. Additives serve to enhance the quality of SEI and CEI films, facilitate the passivation of metal surfaces, and provide other related features that are crucial for the optimal performance of high-performance batteries[216]. The use of additives is a common practice in the field of LIB, with the majority of commercially available electrolytes containing them[217]. The functional electrolyte additives are capable of exhibiting specific characteristics, including the ability to act as SEI formers, CEI builders, and overcharging protectors[218]. Additionally, they can be utilized to enhance the physical electrolyte properties, such as ionic conductivity and viscosity[216,218].

The additives employed as SEI formers are rapidly reduced before the electrochemical decomposition of the main solvents (e.g. carbonates) and conductive salts, which serve to protect them[184]. The products of these electrochemical reductions are forming stable SEI films with high electrical resistance, excellent ion selectivity and permeability, and robust tolerance to the expansion and contraction of electrode materials during cycling[219]. Consequently, there is a high demand for SEI-forming additives that generate minimal to no gaseous compounds upon electrochemical decomposition[187]. This is because these additives prevent cell swelling and electrode delamination, which are pivotal for the long-term cycling stability of batteries[187,217].

CEI builders are oxidized on the cathode surface prior to electrolyte, forming more uniform and stable CEI film[220]. It is generally required that the oxidative decomposition products effectively cover and/or coordinate with active sites (exposed transition metal ions, for example) on the positive electrode[221]. Furthermore, they must possess strong tolerance to further oxidation, resulting in minimal interphase impedance change and reduced gas evolution during operation[222,223].

Overcharging protectors demonstrate particular redox activities that guarantee the oxidation of these molecules occurs on the positive electrode when the battery's charge voltage surpasses the upper cut-off limit[224]. Furthermore, the oxidised products of these overcharging protectors should be soluble in the electrolytes and capable of diffusing back to the negative electrode, where they can be reversibly reduced to their original states[225].

Electrolyte additives are a crucial component in achieving the practical performance of LIB and NIB[217,226]. Nevertheless, the number of studies examining the use of additives in KIB is limited. For example, fluoroethylene carbonate (FEC), a well-known additive that is widely used in LIB[227,228] and NIB[48,229], has been evaluated in K cells[230,231]. High-voltage positive electrodes, such as PBA, frequently exhibit considerable irreversible capacity in K cells, particularly when employing KPF_6/carbonate ester electrolytes[7,89]. To mitigate these reactions, researchers have modified electrolytes comprising distinct solvents and additives, including FEC[3]. The addition of FEC to the electrolyte resulted in an improvement in Coulombic efficiency and a notable enhancement in the cycle performance of the PBA electrode, despite an increase in the polarization of the K cell[30]. Some studies suggest that FEC acts as a film-forming additive for K metal rather than PBA[232]. Additionally, it has been shown that FEC has a detrimental effect on graphite and hard carbon performance[233,234]. The impact of FEC on KIB differs significantly from that observed in NIB and LIB. This emphasises the importance of adapting electrolyte engineering principles derived from Li- and Na-ion batteries for application in K-ion systems. This is due to the differences in decomposition mechanisms and the physical properties of K-based SEI components. It is therefore essential to find an additive that will enhance the overall performance of KIB in order to optimise their functionality. Furthermore, the selection of an additive should not be based solely on the basis of its performance in other alkali metal systems.

2.6.1 Sulfur containing additives

Among functional electrolyte additives, sulfur-containing compounds are particularly attractive for KIB, due to a number of reasons. The replacement of a carbonyl carbon with a sulfur atom results in enhancing the electrochemical reduction susceptibility of sulfur-containing additives in comparison to organic carbonates[235]. Secondly, the electronegativity of sulfur is similar to that of carbon, allowing for organic sulfur chemistry to be nearly as diverse as traditional carbon chemistry. This versatility is advantageous for customising electrolyte additives to suit different application scenarios. easily accessible resource that provides fluorine-free alternatives to existing additives, thereby enabling the large-scale production of sulfur-containing compounds at an affordable cost[216]. This is an important consideration for the battery industry. From a chemical point of view, sulphur-containing additives can

be divided into sufonates (cyclic sulfonates and chain sulfonates), sulfates, sulfites, sufones and others (e.g. acid anhydrides, sulfides and sulfur-containing salts). Their structure and the most commonly used additive from each of these groups are shown in **Figure 10**.

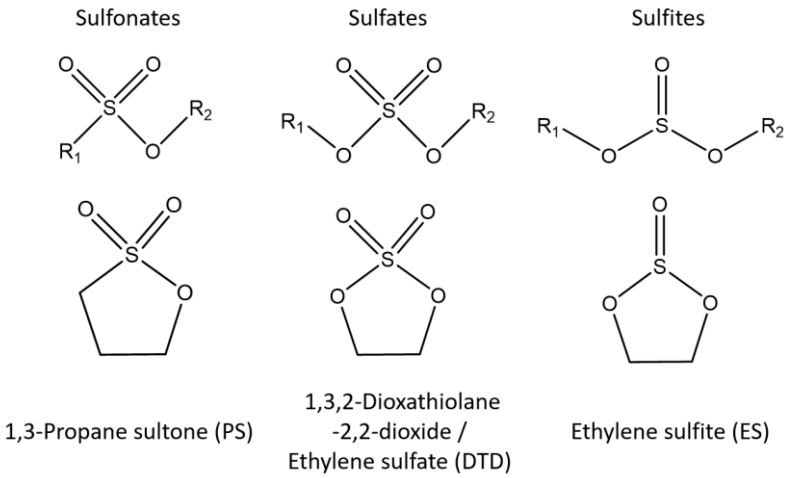

Figure 10. Structure and examples of the most commonly used group of sulfur additives: sulfonates, sulfates and sulfites

Sulfur additives are a well-established component of LIB[216,235]. Moreover, the majority of these additives can fulfil multiple roles. For instance, DTD, PS and ES can act as both SEI and CEI builders[236–238]. The aforementioned groups of additives were also employed in the post-lithium area. For instance, PS has been demonstrated to have excellent effects in inhibiting gas production and improving high-temperature performance, and thus it is introduced into the electrolyte and has been widely used. Zhang *et al.* demonstrated that the combination of FEC with PS as well as DTD to the electrolyte resulted in enhanced capacity retention in $Na(Ni_{0.4}Mn_{0.4}Cu_{0.1}Ti_{0.1})_{0.999}La_{0.001}O_2$ (NMCT-La)/hard carbon full-cell configurations[239]. The results demonstrated that the electrolyte comprising 1M $NaPF_6$ in EC:DMC (1:1), 2 % FEC + 2 % PS and 2 % FEC + 2 % DTD exhibited superior cycling stability compared to the electrolyte containing only 2 % FEC. The capacity retention was approximately 80 % with sulfur additives and 58.7 % with only FEC. The role of sulfur additives was to provide a dense and uniformly distributed SEI film on the hard carbon surface, which in turn allowed for the achievement of higher cycling stability[239]. At this time, sulfur-containing additives were not actively employed in KIB, with the exception of 1,3,2-Dioxathiolane-2,2-dioxide (DTD), which will be discussed in further detail below. Even this latter substance was not subjected to comprehensive investigation. Consequently, the application of this class of additive and their effects on battery performance in KIB represents an area of significant interest, which will be partially addressed in this thesis work.

1,3,2-Dioxathiolane-2,2 dioxide (DTD). With regard to the KIB, the most attractive sulfur-containing additive is DTD[179]. This additive has a higher reduction potential than most common electrolyte

additives[216]. It is used in both NIB[239] and LIB[240,241]. The employment of DTD as an electrolyte additive has been demonstrated to yield a number of beneficial outcomes with regard to battery performance. DTD has been shown to effectively inhibit the initial capacity decline, enhance initial discharge capacity, reduce volume expansion after exposure to elevated temperatures, and improve the charge-discharge performance and cycle life of batteries[242]. In LIB, the inclusion of DTD further enhances cycling performance, including initial coulombic efficiency, low-temperature performance, and the suppression of gas generation or explosion during high-temperature storage[216].

The reduction chemistry of DTD on the negative electrode was explored by Hall and colleagues using DFT calculations[186]. Their findings indicated that DTD undergoes a two-electron electrochemical reduction pathway, forming A_2DTD, where A represents an alkali metal (**Figure 11**). The initial product, A_2DTD, can be further reduced to A_2SO_4 and ethylene during the SEI-forming processes. Furthermore, A_2DTD can react with common organic solvents, such as EC and EMC, and even with DTD itself, leading to the formation of organic sulfite esters.

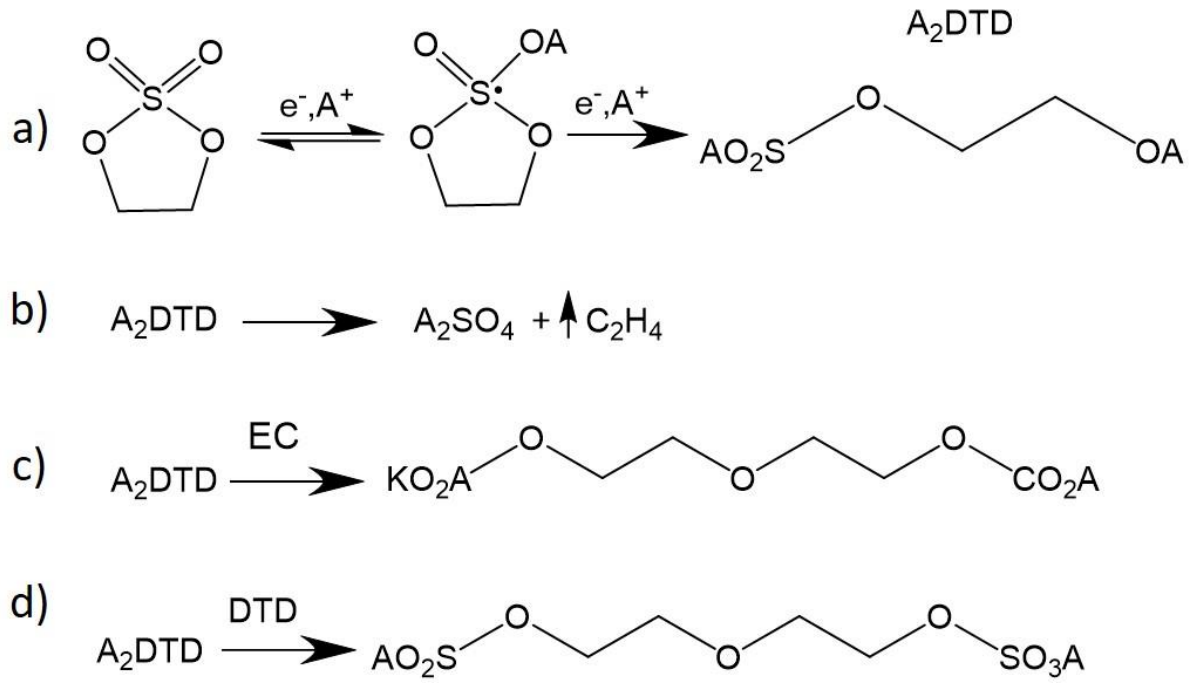

Figure 11. a) The two-electron electrochemical reduction of DTD; b) Decomposition of A_2DTD; A_2DTD reactions with c)EC d) DTD presented by Hall[186].

As previously stated, the utilisation of additives in KIBs is still in its nascent stages in general[17]. Nevertheless, DTD has emerged as one of the most promising additives for KIB, as evidenced by experimental results from the Komaba group[178,179]. These results indicate that the use of DTD can reduce the polarization of potassium and minimise the decomposition of the electrolyte by metal (**see Section 2.5.1**). The K/K cell filled with DTD-added electrolyte demonstrated an insignificant polarization of approximately 20 mV. The $K/K_2Mn[Fe(CN)_6]$ half-cell, with 1 wt. % DTD, demonstrated

greater coulombic efficiency and lower irreversible losses than the additive-free cells. The results of their gas chromatography mass spectrometry (GC–MS) analysis indicated that DTD suppressed the formation of electrolyte-soluble oligocarbonates (**Figure 6**), which would otherwise cause irreversible reactions at high potentials[179].

3 Methodology

3.1 Electrochemical methods

The following sections present the electrochemical characterisation techniques employed for the analysis of materials in this thesis.

OCV: Open Circuit Voltage

The OCV measurement is defined as a specific period of time during which the current is zero. During this period, the cell is disconnected from the power amplifier, allowing for the measurement of the evolution of the rest potential (equilibrium state). This phase is typically employed for the soaking of the separator and electrode in electrolyte, as well as for allowing the system to attain thermodynamic equilibrium prior to the cycling process. Furthermore, the OCV phase is utilised in the process of cell cycling between different phases of the cell cycle (i.e. when a cell has reached its maximum charge/discharge state). As an example, in this thesis, the OCV phase was utilised before cell cycling and between cycling sequences.

CV: Cyclic Voltammetry

Cyclic voltammetry (CV) is a widely utilised and potent electrochemical method, frequently employed to explore the oxidation and reduction processes. It serves as a valuable tool in investigating chemical reactions initiated by electron transfer, including catalytic processes. CV is reliable and straightforward method for determining redox potentials for electroactive species. The technique involves sweeping the potential of a fixed working electrode using a triangular waveform (**Figure 12a**). During the potential sweep, the potentiostat records the resulting current resulting from electrochemical reactions at the electrode interface, which is then correlated with the applied potential. The cyclic voltammogram depicts this current response plotted against the applied potential. **Figure 12b** presents a voltammogram of the reversible reduction of a 10 mM Fc^{+} solution to Fc, at a scan rate of 50 mV s^{-1}. This is presented to illustrate a typical reversible ox-red reaction.

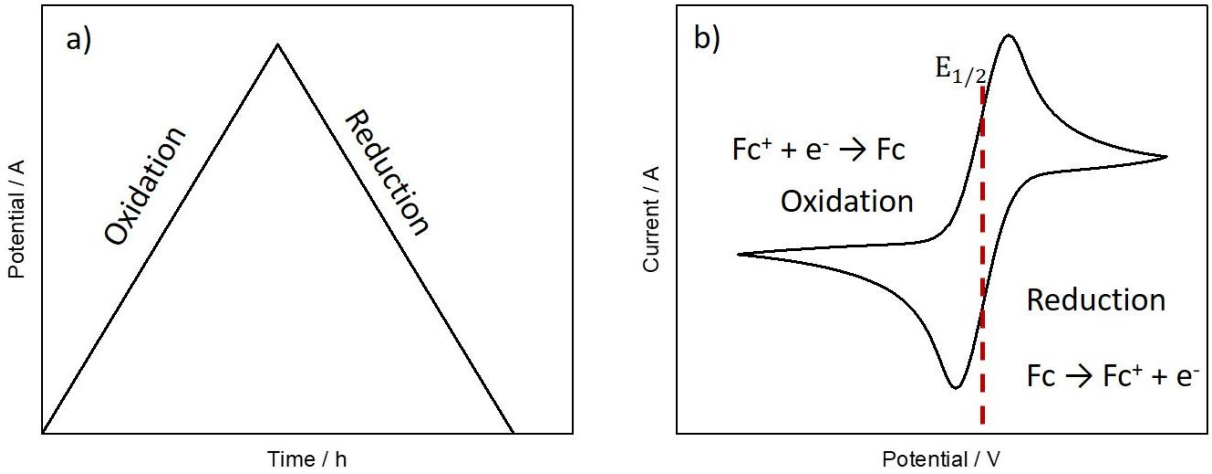

Figure 12. a) Change of potential over time during CV meauremets, b) voltammogram of the reversible reduction of a 10 mM Fc^+ solution to Fc, at a scan rate of 50 mV s^{-1}

The occurrence of peaks in a cyclic voltammogram is a phenomenon that requires explanation. To gain understand this phenomenon, it is necessary to consider the equilibrium between ferrocenium (Fc^+) and ferrocene (Fc). This equilibrium is described by the Nernst equation discussed before. The formal potential depends of experimental conditions and is often estimated using the experimentally determined $E_{1/2}$ value (**Figure 12b**). The Nernst equation allows to predict response to changes in species concentration or electrode potential. For example, if a potential of $E = E^{\circ\prime} \approx E_{1/2}$ is applied to an Fc^+ solution, then Fc^+ will be reduced to Fc until $[Fc^+] = [Fc]$, reaching equilibrium. During a CV experiment, as the potential is scanned, the concentration of species near the electrode changes over time according to the Nernst equation.

When scanning moved to negative potentials, Fc^+ is locally reduced to Fc at the electrode, generating a current and depleting Fc^+ at the electrode surface. It is crucial to emphasise the concentrations of Fc^+ and Fc relative to their distance from the electrode surface, which are influenced by the applied potential and the movement of species between the electrode surface and the bulk solution (see below). These factors collectively result in the characteristic "duck"-shaped voltammograms.

Galvanostatic Cycling with Potential Limitation (GCPL)

Galvanostatic cycling is a technique that employs a controlled current to cycle a cell between specified limits. These limits may be voltage or potential-related, defining the endpoints of the cell reaction. The voltage limits are selected in order to prevent or minimise any unwanted, irreversible reactions that may occur in highly oxidative or reductive potential regions. Alternatively, time limits can be used. The selection of these limits is dependent upon the specific objectives of the experiment and the configuration of the battery. In standard battery tests, which are two-electrode cell measurements,

the voltage limits are controlled by the working electrode voltage (E_{WE}). In the Biologic Potentiostat software, EC-Lab®, this technique is referred as GCPL. In a three-electrode setup where it is possible to record E_{WE} and counter electrode potential (E_{CE}) separately, so alternative techniques may be employed. For instance, in techniques referred to as GCPL2 and GCPL6, it is possible to set limits based on the cell voltage (E_{WE}-E_{CE}). In GCPL2, additional limits can be applied to both E_{WE} and E_{CE}, allowing control over both electrode potentials. In GCPL6, only the cell voltage is limited; however, E_{WE} and E_{CE} can still be monitored *vs*. RE. The numbers in these technique names refer to their sequence in the software.

The C-rate is a measure of the time required for a cell to reach a state of either full charge or discharge. It is typically calculated in relation to the theoretical capacity of the material. 'C' stands for the specific capacity of the electrode. As an illustration, the C-rate of 6C is the current density required to fully charge or discharge the cell with a given capacity within 10 minutes. For a C-rate of less than 1, C/20, for example, this corresponds to a complete charge or discharge in 20 hours.

The most crucial parameters that can be derived from galvanostatic cycling are Q_{ch} and Q_{dis} per cycle. These parameters permit the calculation of the dependence of capacity on current density (rate capability), as well as coulombic, energy, and charge efficiency (see **chapter 2.2.1**).

3.2 X-Ray Photoelectron Spectroscopy

One of the most effective techniques for analysing surfaces, particularly the composition of thin surface layers, is photoelectron spectroscopy (PES) or X-ray photoelectron spectroscopy (XPS). Surface analysis with XPS is conducted by irradiating a sample with monoenergetic soft x-rays (e.g., Al-Kα 1486.6 eV) and analysing the energy of the emitted electrons. Emission of these electrons is caused by the photoelectric effect, in which electrons of atoms in the surface region are released by absorbing a photon**.**

The probability of generating a photoelectron is described by Fermi's Golden Rule. This rule outlines the transition rate w_{fi} from an initial eigenstate |i⟩ (the electron wave function in the ground state) to a final state $|f\rangle$ (the electron wave function in the continuum) due to a perturbation (such as a photon or dipole operator: photon or dipole operator: $e\nabla$). Refer to:

$$w_{fi} = \frac{4\pi^2}{h}\left|\langle f\left|\vec{e}\vec{\nabla}\right|i\rangle\right|^2 \delta(E_f - E_i - h\nu) \qquad (16)$$

Where h is the Planck constant, $h\nu$ the photon energy, and $\delta(E_f - E_i - h\nu)$ the Dirac delta function. Is allowing a transition only when for $\delta(E_f - E_i - h\nu) = \delta(0) = 1$. The final energy state E_f corresponds to the kinetic energy E_k of the photoelectron and its interaction with surrounding electrons, $E_f(N-1)$,

resulting in $E_f = E_k + E_f(N-1)$. The initial energy state E_i is the interaction with surrounding electrons, $E_f(N-1)$, minus the binding energy E_{b}, ($E_i = E_f(N-1) - E_b$). Substituting these into the equation gives the kinetic energy of the emitted photoelectron: $E_k = h\nu - E_{\mathrm{b}}$.

When measuring XPS, the photoelectron is typically emitted from a solid rather than an isolated atom. Thus, the kinetic energy of the generated photoelectron must be adjusted by a work function ϕ_{samp}, which represents the minimum energy needed to remove the electron from the surface of the solid.

$$E_k = h\nu - E_b - \phi_{\mathrm{samp}} \tag{17}$$

If the sample is in electrical contact with the spectrometer, the Fermi levels of both are aligned. Consequently, the work function of the sample can be neglect; instead, the work function of the spectrometer can be utilised (ϕ_{spec}). This can be determined by measuring the Fermi level of a metallic sample with a binding energy set to zero, resulting in the kinetic energy being equal to:

$$E_k = h\nu - E_b - \phi_{\mathrm{samp}} + (\phi_{\mathrm{samp}} - \phi_{\mathrm{spec}}) = h\nu - E_b - \phi_{\mathrm{spec}} \tag{18}$$

With the exception of the nature of the atom and a particular core-level state, the binding energy is influenced by the chemical environment, specifically the charge (electron density). Consequently, photoelectron emission represents an analytical tool for the investigation of surface chemistry, offering information about the chemical environment and oxidation state of atoms.

The use of soft X-rays allows the observation of ejected photoelectrons at a depth of a few nanometres. The depth of the region that can be analysed is constrained by the inelastic mean free path (IMFP), which is the average distance an electron can travel in a solid without losing energy. The surface sensitivity is dependent upon the inelastic mean free path of the primary electrons in solids, which exhibits a relatively consistent behaviour, as illustrated in **Figure 13**. In order to provide an accurate analysis, it is essential that photoelectrons retain their kinetic energy to correlate it with the binding energy. Inelastic electron scattering gives rise to background signals in a spectrum. The intensity of the IMFP is determined by two factors: firstly, by the kinetic energy of the electron and, secondly, by the material properties to a lesser extent. The IMFP reaches a minimum value of approximately 50 eV and then increases considerably below 30 eV, as the excitation of plasmon waves becomes less probable (**Figure 13**). At high kinetic energies, the IMFP increases because electrons spend less time in the solid. The intensity of emitted photoelectrons with a given kinetic energy follows an exponential decay based on the distance d and angle α relative to the surface, as described by the Beer-Lambert law:

$$I_d = I_o \, exp\,(-\frac{\mathrm{d}}{\sin(\alpha \, IMPF)}) \tag{19}$$

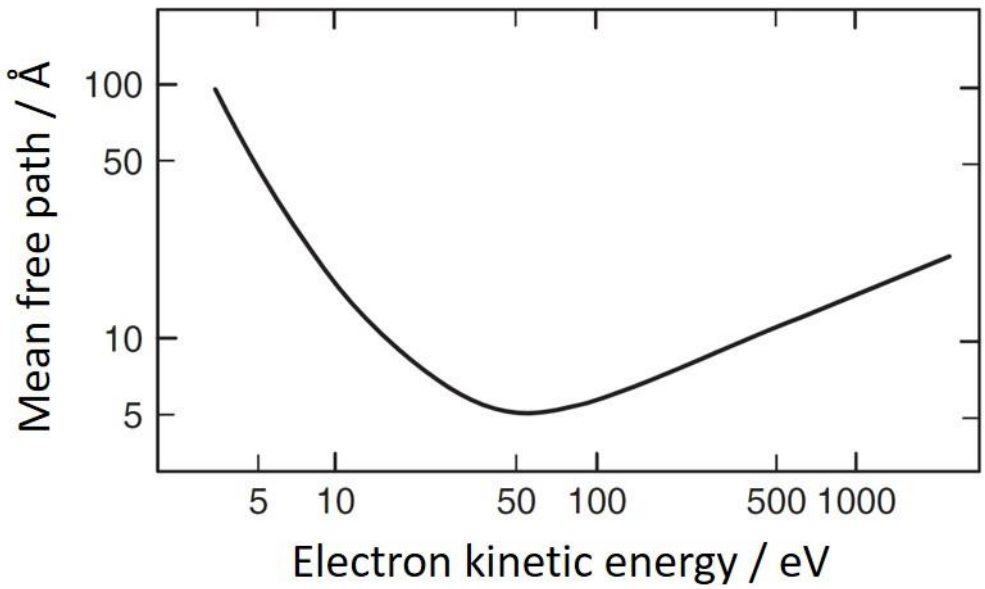

Figure 13. Inelastic mean free path of electrons in solids. Adapted and modified from ref.**[243]**

The thickness of the surface layer (SEI/CEI) is defined as d. I_0 is the intensity of the pristine electrode, which is directly exposed to the active material, while I_d is the remaining intensity when the active material is covered by the surface layer. The core level peak of the active material may disappear if the material is buried under a thick surface layer, depending on the photon energy used, which in turn depends on the depth of the analysis probe.

The core level peak intensities, which correspond to the area between the peak and the background, provide a metric for quantification and a means of determining the relative chemical composition of the surface layer of the sample. The photon flux is dependent on a number of factors, including the element itself, its concentration on the surface, the photoionisation cross-section and the instrumental parameters. As a result, it is necessary to correct the intensities with a setup-specific atomic sensitivity factor (ASF) for each emission line. The atomic concentration, in a multi-element can be calculated as the ratio between the ASF-corrected intensity of an element x, $I_{ASF,x}$ and the sum of all ASF-corrected intensities:

$$I_{ASF,x} = exp\left(-\frac{I_x/ASF_x}{\sum_x I_x/ASF_x}\right) \quad (20)$$

Flood gun

Surface charging, frequently associated with true insulators, can occur in a diverse range of materials beyond just insulating substances. This phenomenon is also observed in semiconductors, thin

insulating films on metals, native oxides, hybrid structures comprising conductors and insulators, and even conductive materials that are deliberately isolated from grounding. Consequently, over 70 % of materials analysed by XPS are subject to varying degrees of surface charging.

Upon activation of the X-ray source, an interaction with the sample results in the generation of positive charges in the form of core-holes within atoms. The presence of these charges results in a reduction in the kinetic energy of the emitted photoelectrons. The non-uniform distribution of this positive charge across the surface in three dimensions arises due to the electrical, physical, and chemical heterogeneity of the sample (thick CEI/SEI, for example), which can distort the chemical state spectra. Such distortions compromise the accuracy of the XPS measurements, necessitating the compensation for surface charge when analysing insulating materials or materials with an insulating layer on the surface.

To obtain reliable XPS spectra from insulating samples, it is crucial to control or neutralize the positive charge that accumulates on the surface. This is typically achieved through the utilisation of a **flood gun**, which emits a beam of low-energy electrons (ranging from 0.1 to 20 eV) to neutralize the surface charge. The electron gun is installed within the XPS analysis chamber and directs these electrons onto the sample surface, effectively compensating for the positive charge and stabilising the measurement process.

In contrast, for conductive materials that are properly grounded, the positive core holes generated by the X-ray interaction are instantaneously neutralised by electrons from the valence band (the Fermi sea), free electrons slightly above the Fermi level, and electrons supplied through the instrument's grounding system. In such cases, there is no net surface charge accumulation, and the use of a flood gun is unnecessary, as the kinetic energy of the photoelectrons remains unaffected, and no binding energy (BE) correction is required.

The flood gun plays a particularly crucial role in fields such as materials science, semiconductor research, and the analysis of non-conductive materials like oxides, polymers, and glasses. Without effective charge neutralization, the XPS results for these insulating samples would be unreliable, making the flood gun an indispensable tool in surface analysis.

4 Experimental

Materials. Graphite powder (C-NERGY Actilion GHDR 15-4) and carbon black (Super C65) were obtained from Imerys Graphite & Carbon, carboxymethyl cellulose (CMC−Na), and polyacrylic acid (PAA, M_v = 1.250 kg mol^{-1}) was acquired from Merck. Chemicals that used for PBA synthesis and referencing measurements: $FeSO_4 \cdot 7H_2O$ (99 %, VWR chemicals), polyvinylpyrrolidone (M_w = 40.000, Aldrich), $K_3Cit \cdot 5.5\ H_2O$ (99.5 %, Sigma-Aldrich), $K_4Fe(CN)_6 \cdot 3H_2O$ (99 %, Sigma), $K_3Fe(CN)_6 \cdot 3H_2O$ (99 %, VWR chemicals), $FeCl_3$ (98 %, Alpha Aesar), PVdF (HSV900, GelonLib), *N*-methyl-2-pyrrolidone (NMP, 99.5 %, Sigma-Aldrich). Electrolyte solvents and the additive, ethylene carbonate (EC, >99 %, anhydrous, BASF), diethyl carbonate (DEC, Merck, >99 %), propylene carbonate (PC, 99.7 %, Sigma-Aldrich), DTD (98 %, Sigma-Aldrich) and Ferrocene (99.5 %, Alpha Aesar) were used as received. Whatman GF/B separators were dried before use at 120 °C for 12 h under vacuum. Celgard 2325 separators were stored in the glovebox antechamber under vacuum overnight before use. Lithium discs (PI-KEM, purity: 99.9 %, 250 µm thick, 16 mm in diameter) were used as received. Potassium metal (chunks, 98 %, Thermo Scientific) was stored in mineral oil and cleaned in heptane prior to use.

Synthesis of $K_2Fe[Fe(CN)_6]$ and $KFe[Fe(CN)_6]$. $K_2Fe[Fe(CN)_6]$ and $KFe[Fe(CN)_6]$ were synthesized via a co-precipitation method [154]. Three solutions were prepared: (a) 0.782 g of $FeSO_4 \cdot 7H_2O$ and 0.100 g of polyvinylpyrrolidone in 20 mL of deionized water, (b) 0.244 g of $K_3Cit \cdot 5.5H_2O$ in 10 mL of deionized water, and (c) 1.268 g of $K_4Fe(CN)_6 \cdot 3H_2O$ in case of $K_2Fe[Fe(CN)_6]$ and $K_4Fe(CN)_6$ for $KFe[Fe(CN)_6]$ in 10 ml of deionized water. The solutions were added to the vessel in the order (a), (b), and (c). The resulting suspension was stirred for 36 h at ambient temperature. Subsequently, the resulting precipitate was centrifuged and washed with a mixture of ethanol and deionized water (1:1 ratio by volume) several times and dried at 150 °C for 12 h under vacuum (10^{-3} mbar).

Synthesis of $Fe[Fe(CN)_6]$. The synthesis of $Fe[Fe(CN)_6]$ was conducted by the addition of 0.03 mol FCl_3 into a stoichiometric amount of $K_3[Fe(CN)_6]$ at a slow rate. The resulting mixture was then stirred for 12 hours at room temperature. Upon completion, the precipitates were subjected to centrifugation and washed with deionized water on multiple iterations, before being finally dried at 80 °C for 8 hours. After drying, the obtained three powders was ground using a mortar.

Electrode Preparation. *Graphite electrodes*. The negative electrode consisted of a mixture of graphite, carbon black and a binder mixture of carboxymethyl cellulose and polyacrylic acid binders in a weight ratio 95:1:2:2. The total solid content of the electrode slurry was 1 g. A binder solution was prepared by dissolving CMC-Na (20 mg) in 1 ml of deionized water and mixing for 5 min at 2000 rpm in a Thinky mixer. PAA (20 mg) and 0.5 mL of water were added in the next step and the solution was mixed another 5 min. The resulting 1.5 mL binder solution was blended with 10 mg (of carbon black and mixed for 5 min at 2000 rpm. Then graphite was added after a 10 min mixing. An additional 2.8 mL of

deionized water was used for the slurry. The slurry was cast with a doctor blade on copper foil (Goodfellow, 0.01 mm, 99.9 %), dried under ambient conditions, and cut into discs of 16 mm in diameter (mass loadings: 2–3 mg_{AM} cm^{-1}). Before use electrodes were dried at 120 °C for 12 h under vacuum (10^{-3} mbar).

PBA electrodes. Electrode comprised 0.180 g $K_XFe[Fe(CN)_6]$ (x=0-2), 0.030 g of carbon black, and 0.030 g of PVdF (80:10:10 ratio by mass). The materials were weighed in a ball-mill container, and 0.8 mL of *N*-methyl-2-pyrrolidone was added. The container was transferred to a ball-mill mixer (3 balls, ZrO_2, 4 mm), and the slurry was mixed in two 10 min steps. At first carbon black and PVdF with 0.4 mL NMP, in the second step, PBA and 0.4 mL of NMP were added. Subsequently, the slurry was spread onto carbon-coated aluminum foil and dried under ambient conditions. $K_XFe[Fe(CN)_6]$ electrodes with a diameter of 16 mm were cut out and dried at 150 °C for $K_2Fe[Fe(CN)_6]$ and $KFe[Fe(CN)_6]$, and at 80 °C for $Fe[Fe(CN)_6]$ then dried for 12 h under vacuum (10^{-3} mbar).

Cells Configurations and Electrochemical Measurements - General. Experiments were performed in either stainless steel (SUS316L) 2032 round button type cells (coin cells) or Swagelok-type 3-el cells (**Scheme 1**). 3-el cells were built using the design with modification of the reference materials, specifically K-metal (K-RE), a KFF composite (KFF-RE), or an AgCl-RE, respectively. The design that was previously reported in ref[244] (Design B) is based on a concentric alignment of a WE-ring electrode and RE in the center. In the original design, the reference material is filled into a cavity in the reference electrode (**Scheme 1a**). The cavity was filled with reference electrode material until it reached the WE level. The setup can also be used for 2-el measurements, by using two disc electrodes and leaving the cavity empty. For measurements with AgCl-RE, the RE-component was replaced by the reference cell compartment in a glass tube with about the same diameter (as illustrated in **Scheme 1b**). All 3-el measurements with AgCl-RE were performed in an Ar-filled glovebox.

Electrolytes. The base electrolyte formulation comprised of 750 mM KPF_6 in EC:DEC (v/v = 1:1). A second electrolyte formulation was prepared from the base electrolyte by addition of 1 wt. % DTD. In addition, for a control experiment, an electrolyte comprising 500 mM KPF_6 in EC:PC (v/v = 1:1) and 5 vol. % FEC was prepared. Potassium metal electrodes were rolled to thin foils and cut into discs of 16 mm in diameter, prior to cell assembly.

Potentiostat and cell tests. All electrochemical tests were conducted on a Biologic VMP-3 potentiostat. Cycling tests in 3-el configurations were performed through control of the cell voltage ($E_{cell} = E_{WE}-E_{CE}$), labeled 'GCPL6 technique' (See **Section 3.1**) in the Biologic EC-Lab Software (V11.43).

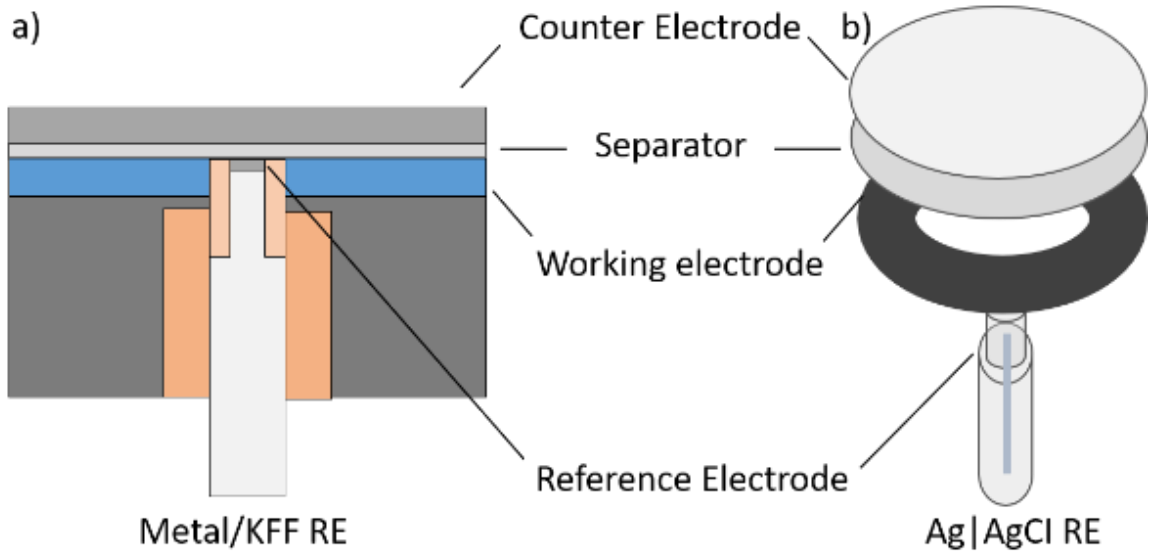

Scheme 1. 3-electrode cell scheme with metal or KFF (a) and AgCl-RE (b) as reference electrodes.

AgCl-Reference Electrodes. Ag/AgCl reference electrodes (AgCl-RE) were investigated as inert alternatives to K-metal and KFF composite reference materials in 3-el cell setups.

Preparation. Ag wire covered by AgCl was prepared electrochemically. All calibration measurements were performed in a 3-el glass cell (5 mL) with a 2 mL working volume. Silver wire (ChemPur Feinchemikalien, 0.25 mm diameter; 99.995 %) was used as a working electrode in an aqueous 100 mM HCl solution with 1 M KCl as supporting electrolyte and coil Cu-CE. After 1 cycle of CV in [0; 1 V] range at 20 mv s^{-1} the wire was ready to use. The reference electrode (glass tube with Ag|AgCl wire) was filled with a saturated solution of TBACl (99.5 %, Sigma-Aldrich) in the same solvent as that in the working electrode compartment (a mixture of carbonate solvents, such as EC:DEC, v/v = 1:1) to minimize discrepancies in the liquid junction potential between the two electrolyte solutions.

Calibration. The potentials of the respective AgCl-RE were calibrated against the ferrocenium/ferrocene (Fc^+/Fc) redox couple in the EC:DEC solution (10 mM Fc^+/Fc + 100 mM KPF_6 in EC:DEC) between Pt-WE disc electrode (6 mm diameter) and Cu-CE (coil).

Reference potential measurements. The AgCl-RE was employed to determine the electrode potentials of Li- and K-metal foils in the EC:DEC (v/v = 1:1) electrolyte mixtures comprising 1 M $LiPF_6$ and 0.75 M KPF_6. The standard potential of Li and K was determined by cyclic voltammetry in symmetrical Li/Li and K/K 3-electrode cells against the AgCl-RE at a scan rate of 0.5 mV s^{-1} in the potential range of -1.95 to -2.35 V (Li/Li) and -1.95 to -2.50 V (K/K), respectively. The redox potential was determined by identifying the zero-current intersection of the anodic and cathodic scans.

Symmetrical cell tests. K/K symmetric cells were assembled both as 2-el coin cells and 2-el Swagelok-type cells from two 16 mm potassium discs. A single layer of glass fiber separator was positioned

between the potassium discs and the separator was soaked with 150 µL of electrolyte. The tests comprised of an initial 6 h OCV step, and constant current cycling at ± 32 µA cm^{-1} in 8 hour steps.

2-electrode (2-el) half-cell tests*.* The half-cells were assembled in 2-el coin cells and comprised of either a graphite- or KFF-WE and a K-CE. The electrodes were placed between one layer of glass fiber separator, which had been soaked with 150 µL electrolyte, and the cells were then sealed with a coin cell crimper.

Galvanostatic cycling. 2-el *Coin*-Cell tests were conducted under constant-current constant-potential (CC-CP) conditions. Two initial cycles were conducted at C/20. On the following cycles the cycling rate was increased to C/10. (1C = 279 mA g^{-1} (graphite) & 120 mA g^{-1} (KFF)). The lower and upper cut-off voltages were chosen as 0.025-1.2 V vs. K^+/K for graphite and 2.5-4.3 vs. K^+/K for KFF half cells. In the CC step, a time limit of 35 h was set as additional safety measure. In the CV step, the time limit was 30 min and the current limit was equivalent to a current of C/40 in the first two cycles and C/20 in all following cycles.

Self-discharge Test of KFF/K half-cells. Several self-discharge tests were conducted in this study. In connection with the KFF-RE studies, a KFF/K-CE electrode with an 750 mM KPF_6 in EC:DEC (v/v=1:1) electrolyte) was cycled for 1 cycle under CC-CV conditions at a rate of C/20 (with time limitation of 35 h) and a CV phase of 30 min or until the equivalent of a C/40 current cut-off is reached. Then charged in the second sequence to 3.5 V vs. K^+/K, before the cell was put in a 70 h OCV interval. Similar tests were also recorded with KFF/K-CE half cells with the 750 mM KPF_6 in EC:DEC + 1 wt. % DTD and 500 mM KPF_6 in EC:PC (v/v=1:1) + 5 wt. % FEC electrolyte, respectively. In these tests the cells were first cycled for a full two cycles (cycled between 2.5-4.3 V vs. K^+/K and under CC-CV conditions with a constant current of C/20 and a 30 h time limit; in the CV phase the potential was held for a maximum of 30 min or until the current cut-off of C/40 was reached), and then fully charged to 4.3 V once more. Thereafter, the open-circuit voltage (OCV) was recorded over 100 hours. The C-Rate was C/20, with a time limit of 35 hours and a CV step of 30 minutes.

2-electrode (2-el) full-cell tests. The full-cell comprised the graphite electrode, one glass fiber separators and the KFF electrode were stacked on top of each other (N/P ratio ≈ 1.5). The separators were wetted with 150 µL electrolyte and then sealed with a coin cell crimper. Galvanostatic cycling of graphite/KFF full-cells was carried out similar to the half-cell tests with a CC-CP cycling protocol. In the initial two cycles, a rate of C/20 was applied, followed by eight cycles at C/10 (C=120 mAh g^{-1}) between the voltage limits of 2.0 V and 4.15 V. During the CP step, the limiting current was set at C/40 (half the current of the CC step) for the first two cycles, with the cycling rate increased to C/10 from the third cycle onwards. The limiting current in the CP step was increased in accordance with an equivalent of C/20.

3-electrode (3-el) Graphite Half-Cells with Li-RE and K-RE. For tests graphite/K-RE/K-CE and graphite/Li-RE/Li-CE 3-el cell configurations were conducted to evaluate drifts and overpotentials of the alkali metal quasi reference electrodes. For both experiments the same graphite electrodes can be used. The ring electrodes were obtained from cutting a 8 mm (in diameter) hole in the center of 16 mm electrode discs. The reference cavity was filled with the respective alkali metal and inserted into the cell setup. The graphite-WE and the reference electrode were covered by two layers of glass fiber separator that were soaked in 450 µL electrolyte (Li: 1M $LiPF_6$ in EC:DEC (v/v=1:1), K: 750 mM KPF_6 in EC:DEC (v/v=1:1). A 16 mm Li or K disc electrode was used as counter electrode (Li-CE and K-CE, respectively).

Galvanostatic cycling (Graphite/K-RE/K-CE). The graphite/K half-cell was cycled as previously reported with two initial cycles were conducted at C/20, followed by a rate increase to C/10. (1C = 279 mA g^{-1}) within the voltage limits of 0.025-1.2 V vs. K^+/K. In the CC step, a time limit of 35 h. In the CV step, the time limit was 10 min and the current limit was equivalent to a current of C/40 in the first two cycles and C/20 in all following cycles.

Galvanostatic cycling (Graphite/Li-RE/Li-CE). The graphite/Li half-cell were cycled for four cycles at C/20 (1C = 372 mA g^{-1}) within the voltage limits of 0.025-1.2 V vs. Li^+/Li. In the CV step, the time limit was 10 min and the current limit was equivalent to a current of C/40 in the first two cycles and C/20 in all following cycles.

3-electrode (3-el) Graphite Half-Cells with KFF-RE. In this experiment the reference cavity was filled with a KFF composite. The rest of the graphite/K half-cell configuration remained the same to the 3-el experiments with K-RE (see above).

KFF-RE preparation. The KFF-RE needed activation by oxidizing the material to the lower potential plateau at around 3.5 V vs. K^+/K. For the preparation step the KFF-RE was rewired and used as working electrode in a 2-el electrode setup against the K-CE in the 3-el cell setup, as reported previously in a similar experiment by Holtstiege *et al.*[245]. In the second cycle the cell was cycled to a potential of 3.7 V in two charging steps, taking into account a larger voltage drop during voltage relaxation of around 200 mV after reaching the targeted end point potential, due to setup-related overpotentials in this phase of the preparation. The stability of the KFF-RE against K-CE in this configuration was studied over 10 h at OCV.

Galvanostatic cycling (Graphite-WE/KFF-RE/K-CE). The graphite/K half-cell with KFF-RE was cycled for three cycles at C/20 (1C = 279 mA g^{-1}) within the voltage limits of -3.42 V to -2.2 V *vs*. KFF-RE. In the CV step, the time limit was 30 min and the current limit was equivalent to a current of C/40 in the first two cycles and C/20 in all following cycles.

3-electrode (3-el) cell setups with AgCl-RE. For this setup, the reference electrode pin in the Swagelok-type cell was replaced by the AgCl-RE capillary, which fit in diameter. In addition, the capillary was fixed in place and sealed around the reference electrode inset.

3-el-Graphite/K, 3-el-Graphite/Li and 3-el-KFF/K Half-cells. Ring electrodes were constructed from 16 mm diameter electrode discs by cutting a hole with an 8 mm diameter in the center of the disc. The electrodes were composed of either graphite-WE or KFF-WE. The ring-WEs were covered by two Whatman GF/B separators that had been soaked with 450 µL of electrolyte. Graphite half-cells were assembled with both Li-CE and K-CE. Furthermore, the CE was covered by a layer of Celgard separator in half-cell measurements.

Cyclic Voltammetry (CV) on KFF Electrodes. 3-el KFF/AgCl-RE/K-CE configurations were studied by CV in a voltage range from 0.4 V to 1.8 V *vs.* AgCl-RE. The scan rate was 1.5 mV min^{-1} (25 µV s^{-1}).

Galvanostatic cycling. The cut-off voltage in graphite/K-CE half-cells was 0.025 V and 1.3 V *vs.* K^+/K. The same limits were applied *vs.* Li-RE in the respective half-cell tests with a Li-based electrolyte. The voltage limits for KFF/K-CE half-cells were 2.5 V and 4.3 V *vs.* K^+/K. To reduce the impact of polarization effects, three-electrode half-cells containing AgCl-RE and Li-RE were evaluated at a constant current density of C/20. The CV step was limited to 10 minutes, with the current density equivalent to C/40.

Full-cells. KFF/graphite full-cell assemblies comprised of a graphite ring-electrodes against a KFF disc and two Whatman glass fiber separators soaked in 450 µL of electrolyte). The electrode masses were balanced around a N/P ratio of 0.62-0.72 to compensate for the significant losses of charge carriers on the first cycle. The active material masses for the 3-electrode measurements on the DTD-free and DTD-containing electrolyte (**Figure 22**) were 4.5 mg (graphite) and 16.4 mg (KFF) and 5.0 mg (graphite) and 15.8 mg (KFF), respectively. N/P ratios were based on the practical charge capacity of KFF (110 mAh g^{-1}) and discharge capacity of graphite (250 mAh g^{-1})[177] in half-cells, following the data presented in **Figure A3**.

Galvanostatic Cycling. The cycling parameters were identical to those employed in two-electrode cells, i.e. two initial cycles were conducted at C/20, before the rate was increased to C/10 within the voltage limits were 2 V and 4.25 V. In the CV step, the time limit was 10 min and the current limit was equivalent to a current of C/40 in the first two cycles and C/20 in all following cycles.

X-ray Photoelectron Spectroscopy. The measurements were conducted using a Thermo Scientific K-alpha XPS-spectrometer equipped with a glovebox compartment for inert gas transfers. The spectrometer used a monochromized Al Kα X-ray source with an excitation energy of 1486.6 eV. All samples, including OCV and cycled samples, were strictly handled under inert gas conditions in a glovebox and transferred between the glovebox and spectrometer without exposure to air or moisture. A set of spectra was acquired from each sample surface, comprising at least three different

spots. One spot was measured without the use of a flood gun, while two were measured with the flood gun (see **Chapter 3.2**). Data analysis was performed using Avantage software version 5.9931 from Thermo Scientific. The 'smart background' function, which is a Shirley background with an additional constraint that the background function is not greater than any data point in the measured region, was used for background subtraction. Voigt profiles with a Lorentzian contribution of 30 % were used for peak fitting. Graphite and carbon black signals were fitted with an asymmetric tail. The resulting data was exported to Origin (2021) for plotting.

5 Scope of the thesis

The field of potassium ion batteries is an emerging and rapidly evolving area of research, characterised by numerous challenges. These include the instability of the solid electrolyte interphase, electrolyte degradation and the lack of reliable reference electrodes. These factors make it difficult to achieve competitive capacity retention and cycling efficiencies in potassium ion batteries compared to corresponding Li-ion batteries. The majority of issues observed in K-ion batteries are associated with the high reactivity of potassium. For example, the findings obtained from half-cells cannot be extrapolated to those from full-cells, given the formation of soluble degradation products in the former, which then interact with the electrodes. One potential strategy to mitigate these degradation effects is the use of electrolyte additives, though the underlying reaction mechanisms remain barely understood.

To address these challenges, this thesis focuses on two critical aspects: the reliability of reference electrodes and the role of electrolyte additives in enhancing battery performance. The first objective of this thesis is to overcome these challenges through a comparative analysis of three reference electrodes: potassium metal, Prussian blue, and non-aqueous silver-silver chloride electrodes. The performance of these electrodes will be evaluated in different electrochemical setups, including half-cell and full-cell configurations. The implementation of a reliable reference electrode allows for the observation of electrolyte degradation processes and additive reactions, as well as the delivery of comprehensive electrochemical comparisons between half and full potassium ion cells. Moreover, the utilisation of a reliable reference electrode enables the simultaneous monitoring of processes occurring at both the counter and working electrodes, which is advantageous in terms of investigating the impact of electrolyte additives.

The reliable reference electrode will permit the attainment of the second objective of this thesis, namely a comprehensive analysis of the impact of the electrolyte additive DTD (1,3,2-dioxathiolane 2,2-dioxide) on the performance of potassium-ion batteries. The objective of the presented work is twofold: firstly, to examine reference electrodes and, secondly, to investigate the impact of DTD on cathode and anode behaviour in half-cell and full-cell configurations. The additive DTD (1,3,2-dioxathiolane 2,2-dioxide) has been selected for its potential to enhance cathode performance in half-cell setups. A combination of advanced electrochemical techniques and surface-sensitive methods, such as X-ray photoelectron spectroscopy (XPS), will be employed to conduct a thorough analysis of impact of DTD on electrode behaviour. This comprehensive approach aims to provide valuable insights into the role of DTD in the overall performance and stability of potassium ion batteries.

6 Study of Reference electrodes for KIBs

As outlined in the Theoretical Background, KIB face the challenges in the reliability of reference electrodes. A detailed examination of reference electrodes is a crucial step in resolving this issue. The present chapter focuses on three selected systems: a) K-metal as quasi-reference ('K-RE') electrode). b) a partly charged $K_2Fe[Fe(CN)_6]$ (KFF-RE) and c) an AgCI-RE in a separate reference cell compartment. The objective of this chapter is to provide a detailed comparison of the three reference electrode systems, highlighting the advantages and disadvantages of each. Furthermore, the most suitable and versatile choice for half and full-cell setups will be identified. The most reliable setup will be used to study K-metal electrode degradation and polarization effects, investigate graphite/KFF cells without the detrimental influence of degradation products from RE side, and examine the effect of DTD on electrochemistry in half and full-cells.

The standard electrolyte formulation in this section was a mixture comprising 0.75 mM KPF_6 in EC:DEC (v/v = 1:1). Unless stated differently, experiments were performed in the cell design provided by Bünzli *et al.* [244] (**Scheme 1**).

6.1 Potassium metal reference or quasi-reference (K-RE/K-QRE)

6.1.1 Polarization tests

As previously stated, the optimal reference electrode should be non-polarizable. Consequently, the initial phase of the K-RE examination comprised stripping/plating experiments conducted in a symmetric 2-el configuration. This approach was employed to determine the electrode polarization and potential drift over time, which serve as indicators of the reactivity and stability of the K-metal electrode in the respective electrolyte[175,246].

Figure 14 shows the potential profile of stripping/plating over the initial 160 hours. During the OCV phase (the initial five hours), the cell voltages demonstrated a slight offset from 0 V (approximately −2 mV). At a constant current of 32 µA cm^{-2}, the overpotential remained relatively stable and symmetric around a potential of ± 41 mV in Swagelok-type cell (**Figure 14a**), exhibiting a time-dependent potential drift of 5 mV over a period of 155 hours. It is observed that the coin cell (**Figure 14b**) has a higher degree of polarisation in comparison to Bünzli cell configuration, reaching ±66 mV during the initial 60 hours and subsequently increasing to ±105 mV at 150 hours. Given the high reactivity of potassium metal, the potential drift in Swagelok-type cell is within an acceptable range for the duration of short-term experiments (<200 h).

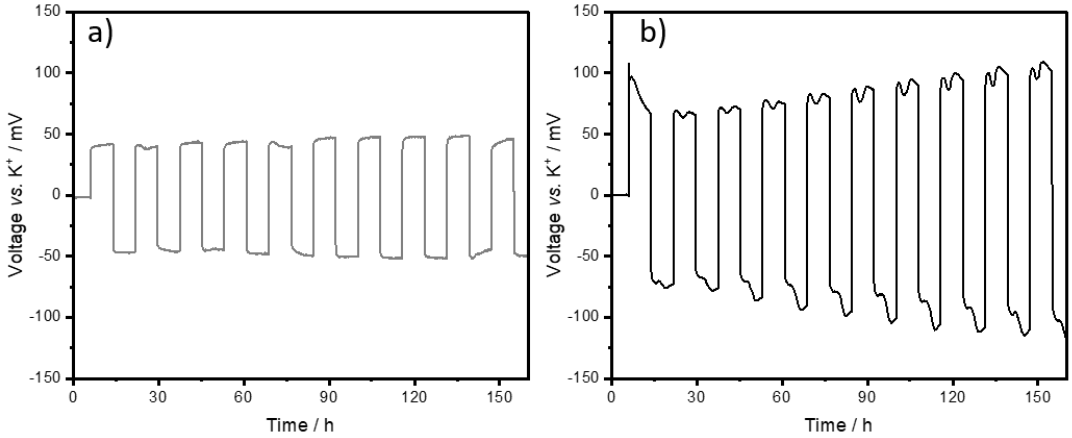

Figure 14. Voltage profile of K vs. K 2-electrode symmetric cell a) Bünzli cell b) Coin cell in an electrolyte comprising 0.75 mM KPF_6 in EC:DEC.

However, a review of the literature highlighted that the potassium acting as a QRE (see **section 2.3.1**) in 2-el configurations is significantly affected by both the electrolyte composition and the applied current density[179,246,247]. In the aforementioned studies a notable offset was observed in the initial OCV, accompanied by elevated overpotential values exceeding 1V[179,247].The problems encountered were attributed to the presence of impurities in the K-metal, especially at the electrode surface. This emphasizes the significant influence of the grade of potassium purchased and the method of preparation into electrodes on the performance of K-RE[178,248,249]. The following section will demonstrate the challenges and complexities that emerge from the employment of the K-metal reference electrode.

6.1.2 K-RE in 3-el setup

Tests were conducted with a K-metal reference (K-RE) in three-electrode setups, in a configuration identical to that reported by Bünzli *et. al.*[244]. The graphite was selected as the working electrode (Gr-WE) due to the extensive knowledge base surrounding this material. The K-metal was employed as the counter electrode (K-CE). The voltage profiles for Gr-WE *vs.* K-RE are shown in the top panel of **Figure 15a**. As in 2-el coin-cell setup (**Figure 15b**) the profiles show the (de)intercalation process of K-ions at the graphite electrode. The theoretical section offered a comprehensive overview of the electrochemical intercalation of potassium, which can be referenced for a detailed discussion.

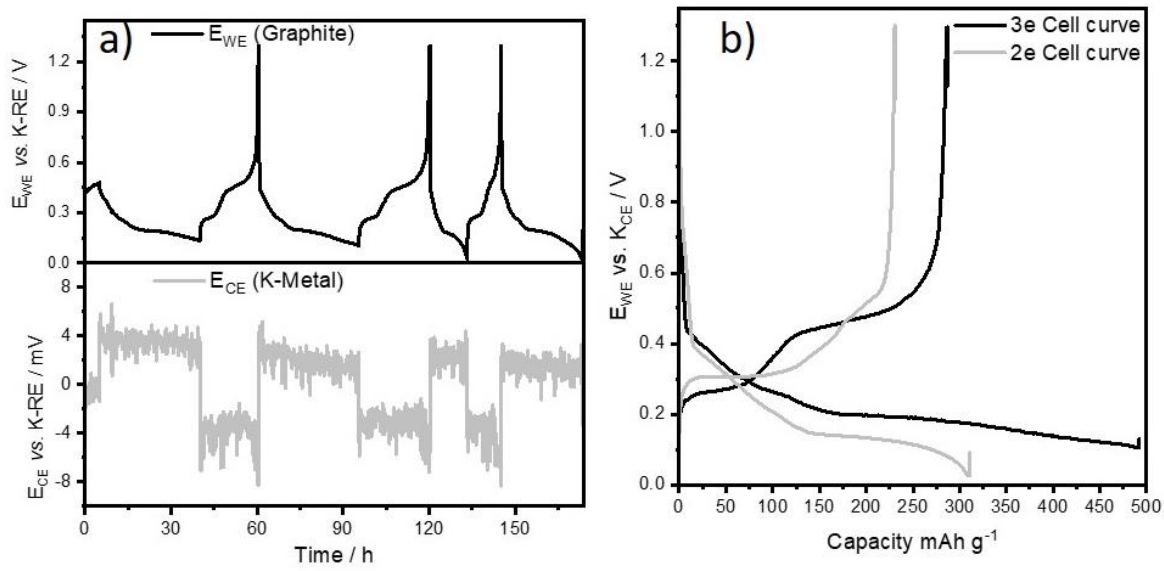

Figure 15. a) 3-electrode measurements with K-RE. The top panel shows the potential profile of graphite vs. K-RE, the bottom panel that of K-CE vs. K-RE. b) Graphite/K half-cell voltage curve in 2-el and 3-el K-RE cells. The experiments were conducted in an electrolyte comprising 0.75 mM KPF_6 in EC:DEC.

The first two SEI formation cycles[230] are conducted within a time limit of 35 hours per cycling sequence. During the specified time interval, the electrode did not reach the lower cut-off limit of 25 mV *vs.* K-RE (3-el) and *vs.* K-QRE (2-el) during intercalation, as evidenced by the potential profiles depicted in **Fig. 15a** (top). The deintercalation reaction is characterised by a two-step profile, exhibiting a pronounced increase in potential towards the end of the discharge process, until the upper cut-off limit of 1.3 V is reached.

As documented in the existing literature, the concentration of electrolyte degradation products in the presence of K metal is considerable[159,202]. The thick surface layers identified in previous XPS studies[250] demonstrate a considerable degree of irreversible reactions, which prolong the intercalation process during the initial cycles[177]. The third cycle, which was conducted after the C-rate was increased from C/20 to C/10, demonstrated a shorter overall cycling sequence that reached the lower end point potential. In the 3-el configuration, it is additionally feasible to monitor the K-CE potential profile, as represented in the lower panel of **Figure 15a**. The polarization of K-CE *vs*. K-RE is lower than in the K/K symmetric cell experiment in **Figure 15** and lies between ±4 mV with a noise level of the K-CE potential of less than ±1.5 mV.

6.2 Partly charged KFF as reference electrode (KFF-RE)

As previously stated in the theoretical background chapter (**Chapter 2.3.2**), partially charged cathodes have been successfully employed as RE in LIB and NIB. This approach is further examined herein by utilising partly charged KFF as a reference in a 3-el setup with a Gr-WE and K-CE.

In this experimental procedure, the reference electrode cavity of the cell, illustrated in **Scheme 1**, was loaded with the KFF electrode formulation. Prior to conducting the three-electrode experiment, it was necessary to prepare the KFF-RE. This was done by conditioning the KFF-RE in this setup by cycling the cell in a 2-el configuration against the K-CE, in a manner similar to that employed in a previous study by Holtstiege et al.[245]. In order to achieve the requisite state of charge and activate the material, the KFF-RE was first cycled for one full cycle. Thereafter, it was oxidised in the subsequent sequence to a target potential of 3.70 V vs. K^+/K. (**Figure 16a**).The voltage profile of the KFF-RE/K-CE setup exhibits the characteristic 2-step process with a sloping section in the high potential region until the cut-off is reached at 4.3 V, in accordance with previous results[12,154]. In comparison to the coated electrodes, the overpotential in this configuration was about 200-300 mV higher. This is also indicated by the notable IR drop that occurred when the cell entered the OCV phase at the conclusion of the experiment. Following a period of relaxation, the potential reached the first voltage plateau at approximately 3.40 V vs. K^+/K. The OCV remained constant for a duration of 10 hours (**Fig. 16a**, green area), after the cell was reconnected to the 3-el configuration.

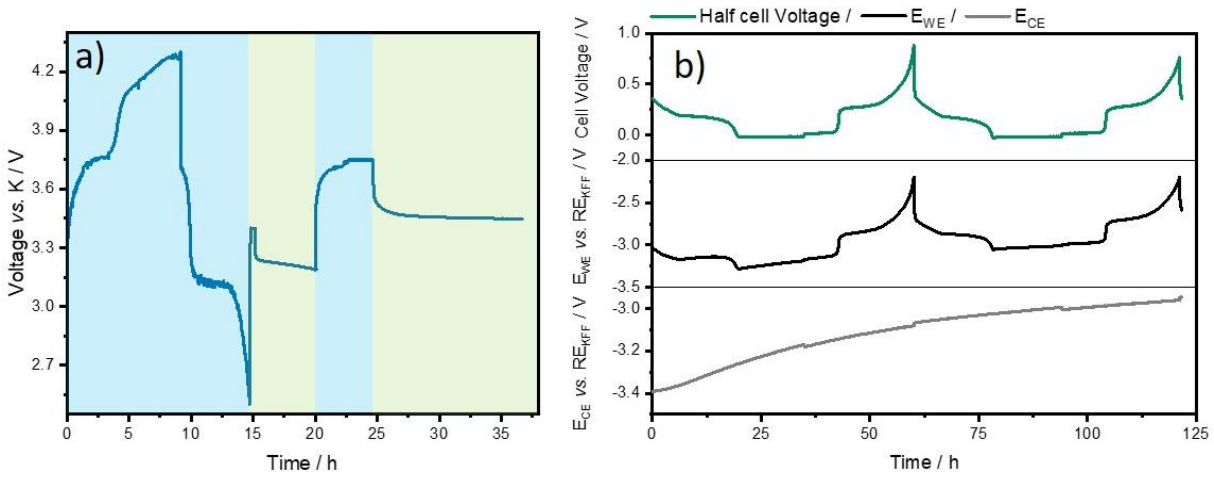

Figure 16. a) KFF-RE preparation in a 3-el Gr-WE/K-CE/KFF-RE setup. The KFF-RE electrode was cycled in a (rewired) 2-el configuration (KFF vs. K-CE) for 1 cycle and then stopped on the next sequence at a target voltage of 3.70 V. b) 3-electrode measurements with KFF-RE. The top panel shows the cell voltage of graphite *vs.* K-CE, the middle panel displays the potential transient of graphite vs. KFF-RE and in the bottom panel shows the potential profile of K-CE *vs.* KFF-RE. Electrolyte: 0.75 M KPF_6 in EC:DEC

The Gr-WE was cycled with similar settings as in **Fig. 16b (top)** but to a lower cut-off limit of −3.375 V *vs.* KFF-RE (the OCV potential in the 2-el configuration). **Figure 16a** shows the cell voltage (Gr-WE *vs.* K-CE) in the top, E (Gr-WE) *vs.* KFF-RE in the middle and E (K-CE) *vs.* KFF-RE in the bottom panel, respectively. In the initial stages, the voltage profile is comparable to those displayed in **Fig. 16a (top),** however, it also displays a several-hour-long plateau at 0 V, which is suggestive of K-metal plating. During the cycling process, it was observed that both profiles exhibited a significant potential drift of 400 mV *vs.* KFF-RE after 150 h. This

effect can be attributed to a drift in the KFF-RE potential, which will be discussed in more details in the following sections. The initial cycling sequence, namely K-intercalation into graphite, resulted in a decrease in the Gr-WE potential, while the KFF-RE potential exhibited drifted in the same direction, ultimately rendering the set cut-off limit unattainable. A constant K-plating potential is reached for the remaining duration of the sequence until the time limitation stopped the process (i.e., Gr-WE and K-CE potentials drift with similar slope, to the drift of KFF-RE).

6.2.1 Self-discharge of KFF electrodes

To explain the potential drift of KFF in the preceding section, the effects of electrolytes on the self-discharge process were investigated. Experiments were conducted on 2-el KFF/K-CE cells with varying electrolytes (**Figure 17**).

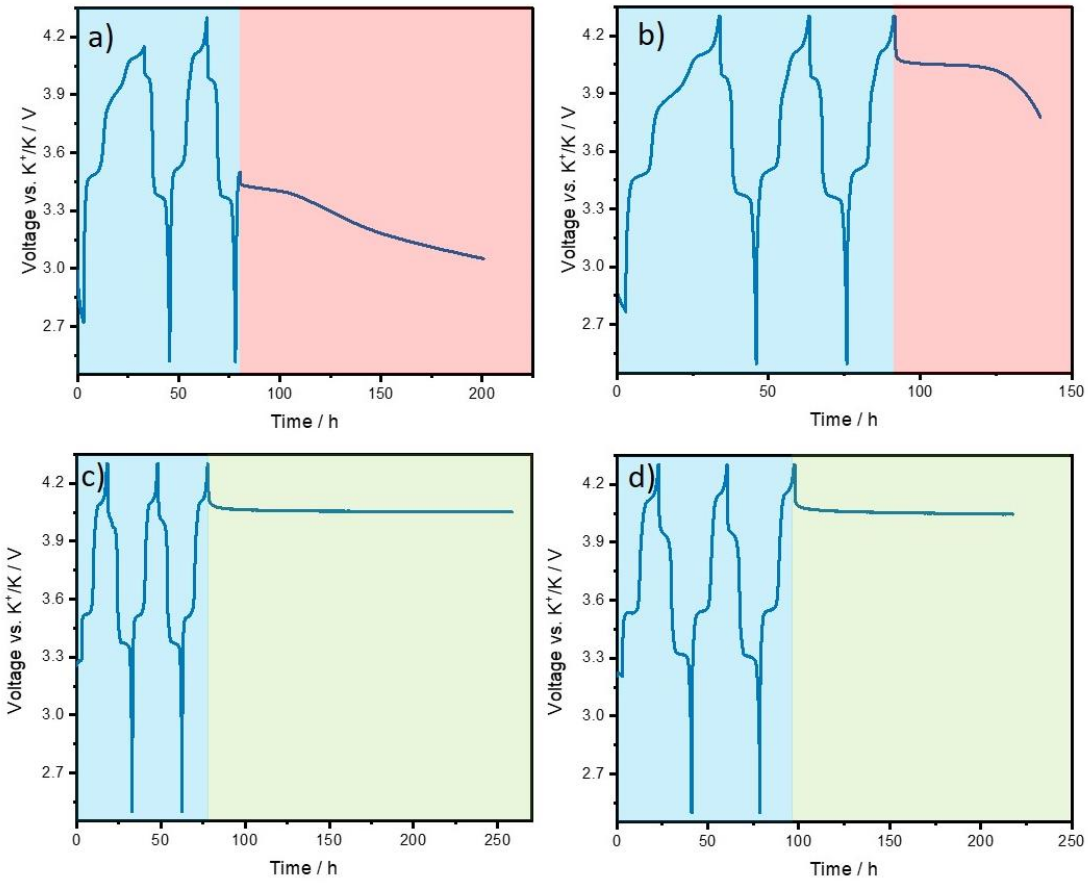

Figure 17. Self-discharge of KFF in a 2-electrode setup against K-CE Electrolyte: 0.75 M KPF_6 in EC:DEC a) at the first plateau b) at the second plateau c) EC:DEC 0.75 KPF_6 1 wt. % DTD d) EC:PC 0.5 KPF_6

Following two complete charging cycles, the cell was left at a prolonged OCV period to observe the drift in the voltage profile, as illustrated in **Figure 17a, b** (red area; OCV phase). The current was stopped after the cell reached 3.50 V (**Fig. 17a**) on the third cycle and at cut-off limit of 4.3 V after two

and half cycles (**Fig. 17b**). It can be observed that in EC:DEC electrolyte without additive (**Fig. 17a, b**), following the initial IR drop, there was a slight drift in the voltages, which increased by approximately 40 mV over time until a marked voltage drop was observed after approximately 40 hours of OCV. This behaviour was noted at both the lower and upper voltage plateaus, namely 3.40 V and 4.15 V, respectively. At the former, the voltage reached 3.20 V after another period of 30 hours at open circuit voltage (OCV). Similarly, at the latter, the voltage reached 3.70 V after a further 20 hours. The use of the electrolyte additive DTD (**Fig. 17c**) or FEC (**Fig. 17d)** prevents this behaviour, whereby a voltage is stable following the initial IR drop.

Due to the negligible self-discharge observed in the majority of LIBs, it is only evident over extended periods of time[251]. Accordingly, there is no obligation to test this effect at the laboratory scale in coin cells for lithium-based systems. Such tests are typically conducted on a larger scale later, for example, with pouch cells[252]. In contrast, in the post-lithium area, self-discharge and cross-talk reactions are observed with greater frequency. It is therefore necessary to consider these effects and to provide the relevant tests[253]. It can be assumed that the SEI components in the surface layer of K-CE dissolve over time, making the K-metal surface more accessible to electrolyte components and resulting in the formation of soluble degradation products. Similarly, severe crosstalk was reported in K-ion setups by several groups [175,179,250] as early as the first OCV phase after cell assembly. It has been demonstrated that the formation of soluble degradation products from EC and DEC is significantly accelerated in the presence of K-metal, resulting in the formation of diethyl 2,5-dioxahexanedioate (DEDD, **Figure 6**)[159,175]. In 2-el half-cell setups, this leads to high degrees of irreversible reactions at the positive electrode due to crosstalk[179]. The observed absence of self-discharge in the presence of additives could be attributed to the passivation of the K-metal surface and the suppression of DEDD formation.

6.3 Self-discharge induced by K-RE in full-cell configurations

To highlight the impact of K-metal when employed within the parameters of a RE experiment, a full-cell configuration utilising K-RE was conducted and compared to a 2-el KFF/K half and a full cell. Previous results would suggest that any introduction of metallic potassium inevitably leads to formation of DEDD that induces the observed self-discharge at the KFF electrode. Consequently, the application of K-RE in a full-cell should result in the emergence of certain effects, which are absent in a 2-el cell. A comparison of voltage profiles obtained from a Gr/K-RE/KFF 3-el cell (dark blue) and KFF/K-CE 2-el cell (light blue) is provided in **Figure 18a**. Additionally, the cell voltages of both a 2-el KFF/graphite (i.e. a K-metal-free cell) and the 3-el KFF/K-RE/graphite full-cells are also illustrated for comparison purposes in **Figure 18b** and **18c**, respectively.

As illustrated in **Figure 18a**, the potential profiles between the 2-el and 3-el cells exhibit a slight shift against each other on the voltage axis. This is an effect of the polarised K-QRE in the 2-el half-cell setup. The most significant feature is that both cells display a two-step voltage profile in the voltage region above 3.75 V, where a single plateau would be expected (see also **Figure 17**). A comparison of the potential profile of the KFF electrode (versus K-RE) with that of the K-metal-free 2-el full-cell (**Figure 18b,** blue) demonstrates the absence of a second voltage step above 3.7 V. It should be noted that the profile of the 2-el cell displays only the voltage between graphite and KFF. The 2-el cell reaches the upper voltage cut-off limit of 4.25 V after approximately 20 hours. The 3-el cell with K-RE (**Fig. 18c, violet**) has a notable slower increase in potential, reaching a maximum of 4.10 V on the first cycle. Although the 3-el cell also reaches the upper cut-off on the second cycle, the high-potential component of irreversible reactions can still be observed clearly.

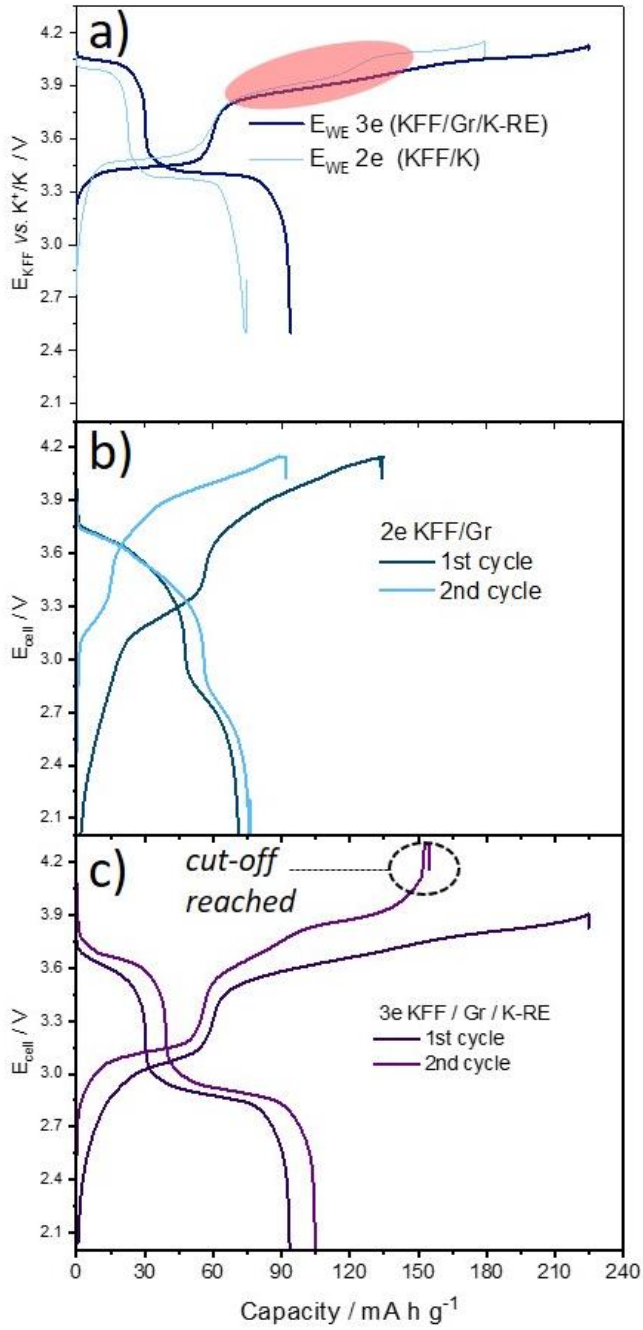

Figure 18. Comparisons of a) KFF potential on the first cycle in a KFF/K-RE/graphite 3-el full-cell and 2-el KFF/K half-cell. To demonstrate further the influence of K-metal, even in small quantities the cell potentials of full-cells on the 1st and 2nd cycle are presented in b) for a 2-el KFF/Gr full-cell (i.e. without K-metal in the cell) and in c) a corresponding 3-el KFF/graphite full-cell with a K-RE. The electrolyte for all experiments was 750 mM KPF_6 in EC:DEC (v/v = 1:1). The cells were cycled at a C-rate of C/20.

As is evident from **Fig. 18a** and **Fig. 18b**, the 3-el K-RE cell, in a similar manner to the 2-el KFF/K-CE half cell, are subject to a considerably greater degree of parasitic processes than the 2-el KFF/Gr full-cell, which contains no K-metal. A low C.E. of 43 % on the first and 68 % on the second cycle in 3-el cell is also indicative. Despite the considerable irreversible losses exhibited by the 2-el KFF/Gr full-cell,

resulting in the rapid disappearance of the lower voltage step, its first cycle CE was observed to be 12 % higher. It is remarkable that the initial discharge capacity of the 3-el cell (95 mA h g^{-1}) was higher than that of the 2-el cell (76 mA h g^{-1}), although the latter exhibited a higher C.E. and cell have similar balancing.

Although, the 2-el KFF/Gr full-cell displays considerable irreversible losses, leading to a rapid disappearance of the lower voltage step, its first cycle C.E. was 12 % higher. Interestingly, the first cycle discharge capacities were higher for the 3-el cell (95 mA h g^{-1} *vs.* 76 mA h g^{-1}), despite lower C.E. and similar balancing. The reason for this phenomenon is unclear; however, it may be attributed to the additional K-source provided by K-RE.

In sum, even minor quantities of K-metal, for instance in the form of a K-RE, can be enough to prompt unwanted electrolyte degradation processes in full-cell configurations. Consequently, K-RE electrodes represent a significant issue in such setups.

6.4 Summary: Limitations of K-metal and KFF reference electrodes in Potassium-Ion Batteries

The fundamental issue with K-RE and KFF-RE is that even minimal quantities of potassium metal, such as those present in a K-RE or K-CE, have the potential to initiate electrolyte degradation processes. While the use of passivation additives can mitigate crosstalk reactions in half-cell configurations, allowing for the potential implementation of K-RE (as shown in **Figures 15, A1a, b**), in full-cell setups, K-RE electrodes further contribute to electrolyte degradation even with passivation additives (**Figure A1c**), making them unsuitable for these configurations.

The implementation of KFF-RE presents a significant challenge due to the potential of potassium to induce crosstalk with cathode material. This can ultimately lead to shifts in the absolute reference electrode potential and, consequently, distortion of the cycling outcomes, as well as the absence of conclusive insights. While practical electrolyte formulations can suffice for material testing, as long as they offer a common basis for comparison, robust REs must be compatible with a wide range of electrolyte formulations. Relying exclusively on specific formulations, such as PC-containing solvents or the DTD additive, can create compatibility issues with electrodes. Consequently, the use of KFF-RE and K-RE is restricted to a limited number of electrolyte formulations and cell configurations, which makes it impractical for broader applications.

6.5 Ag/AgCl reference electrodes (3-electrode setup)

Given the limitations of RE systems discussed in the previous chapter, it is clear that there is a need for alternative RE that can be effectively used in KIB. As discussed in the theory chapter, the most widely used RE in non-aqueous electrochemistry are $Ag^+|Ag$ systems[50,178,254]. Other alternatives, like $Ag|Ag_2S$[255] and Ag|AgCl[51], have also been reported to offer high reliability[256]. Furthermore, some of these silver-based REs have been employed in battery research; for instance, the $Ag^+|Ag$ reference electrode, placed in a separate compartment, has been successfully used to study electrolyte degradation processes in NIB, allowing investigations without the interference and side reactions associated with Na-RE[257]. The utilisation of a RE with low reactivity towards the electrolyte, in contrast to potassium metal, is a particularly advantageous. This is especially the case if the RE can be located in a separate electrode compartment. Consequently, the RE can be modified and adapted to a wide range of electrolytes. However, a key challenge with silver-based systems is that most cell setups place these RE within thin layer setup [258]. It would be beneficial to have a connection between the RE and a soaked separator, as this would allow a test to be conducted under conditions that more closely resemble actual battery cycling. The modified cell design proposed by Bünzli et al.[244] addresses this issue by allowing experiments to be conducted under the aforementioned conditions, thereby ensuring a relatively stable contact between silver-based RE and the separator. This approach is rarely documented in the literature, particularly with regard to KIB.

This subchapter presents the results of a reliability test of AgCI-RE. It examines the potential drift over time and validates the RE against the Fc^+/Fc redox couple. Furthermore, a comparison between REs in the revised cell setup will be provided. The potential to evaluate transients in Li/graphite cells (3-el-setups) will be conducted by comparing them against either a Li-RE or AgCI-RE.

6.5.1 Calibration (AgCl-RE in a 3-el battery cell setup)

The original cell developed by Bünzli et al. [244] was designed for use with metallic RE. However, the construction enables the RE inset to be replaced with a standard AgCI-RE electrode in a glass capillary with a membrane, which can be used in any electrochemical measurement. This allows AgCI-RE to be used in coin cell-like geometry. Furthermore, as with any RE it is possible to validate the potential of the electrode *vs.* the Fc^+/Fc redox couple in the chosen electrolyte. Aging of the AgCl-RE over 100 days was first studied in a 3-el setup with a Cu-coil CE, a Pt-disc WE and 2 mL electrolyte solution (100 mM KPF_6 and 10 mM Fc^+/Fc in EC:DEC, v/v=1:1). As demonstrated by the CV curves in **Figure 19a**, the cathodic half-wave potentials exhibited no notable fluctuations during the cathodic sweep. The anodic half-wave potential decreased by 22 mV. The observed drift of the AgCl-RE can be attributed to minor differences in the concentration of ferrocene in the two solutions, as well as potential changes at the

Ag-wire surface. For instance, the formation of the soluble $[AgCl_2]^-$ complex can occur in organic solvents [259]. It is important to note that a change in calibration potential may be more significant when comparing two RE prepared at different times. This can be attributed to variations in the concentration of the saturated solution TBACI and the thickness of the AgCI layer. Nevertheless, the potential remains relatively steady in terms of the time drift of a single RE over time (**Appendix A2**).

6.5.2 Li-graphite cycling

To demonstrate the applicability of AgCI-RE, it was provided a comparison between curves observed in lithium/graphite cells (3-electrode setups) using either a Li-RE or an AgCl-RE. It was concluded that the Li-based systems were the optimal choice for the validation of the two REs due to their stability and well-described electrochemical behaviour in the literature.

The potential profiles of the graphite working electrode (Gr-WE, top) and lithium counter electrode (Li-CE, middle) half-cell reactions are plotted for 3-electrode setups employing either Li-RE or AgCl-RE (**Fig. 19b**). Both cells exhibited the characteristic intercalation plateau of graphite and similar capacities (353 and 362 mAh g^{-1}, respectively). Notably, no differences were observed in the potential profiles of the Gr-WE.

It is noteworthy that the Li-CE exhibited varying polarisation behaviors depending on the specific type of reference electrode employed. With the Li-RE, the Li-CE potential declined from 3 mV to 0 mV during the 5-hour OCV phase. During the cycling process, the Li-CE polarization initially reached 11 mV and subsequently stabilized around 8 ± 2 mV in following cycles. In contrast, with the AgCl-RE, the initial OCV drift was more significant, reaching 17 mV (from -2.281 to -2.298 V) for the Li-CE at the end of the OCV phase. With the AgCl-RE, the initial OCV drift was more pronounced, reaching 17 mV (from -2.281 to -2.298 V) for the Li-CE at the end of the OCV phase. The application of current at the initial stage of the cycling sequence resulted in a positive potential jump at the Li-CE, reaching approximately 30 mV. Thereafter, the potential moved to around 15 mV during the first charge sequence. The electrode potentials recorded during the charging sequences were similar in both the Li-RE and AgCl-RE cells. However, a higher polarisation of the Li-CE *vs*. AgCl-RE was observed during the discharge sequences, with values reaching up to 30 mV.

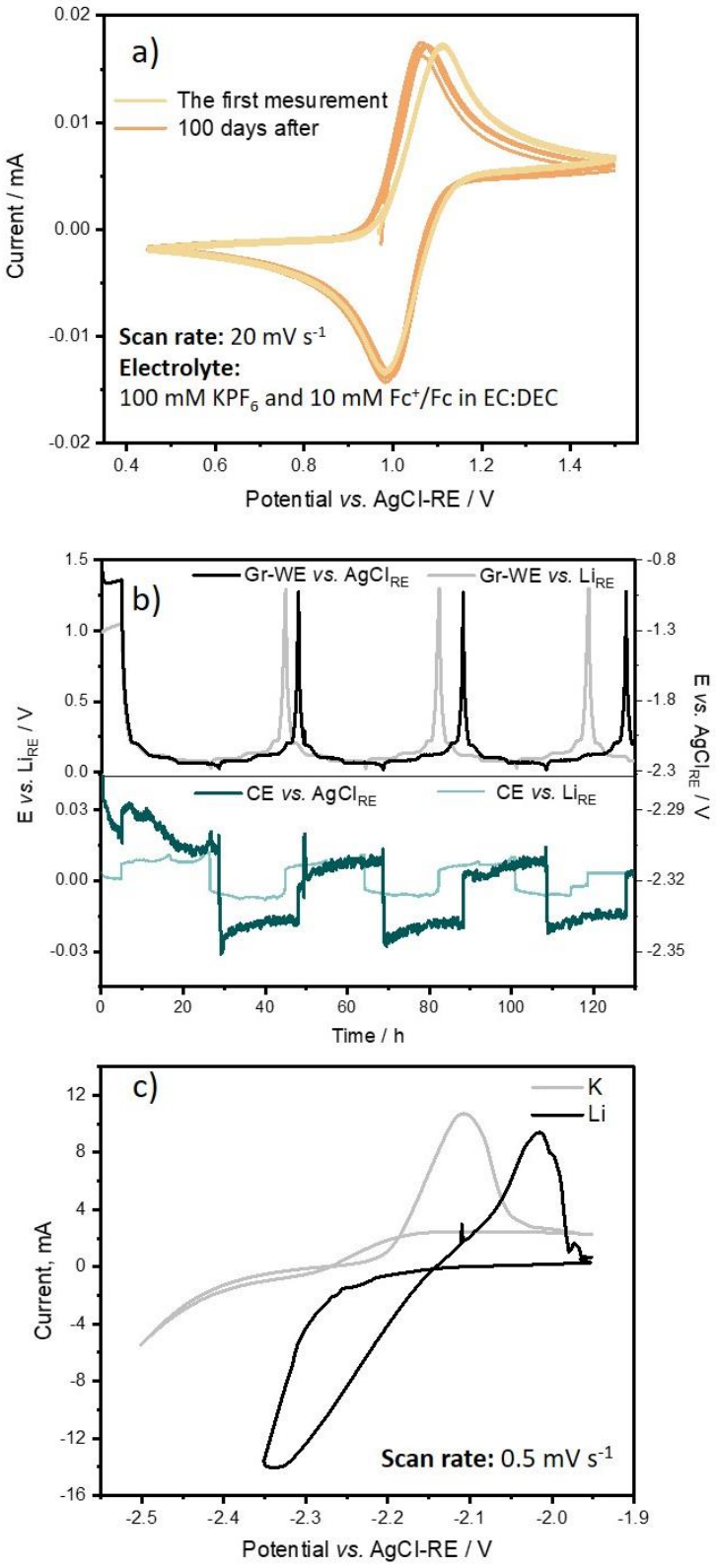

Figure 19. a) aging and potential drift of AgCl-RE after assembly and after 100 days by comparison of cyclic voltammograms (scan rate 20 mV s^{-1}) in 100 mM KPF_6 and 10 mM Fc^+/Fc in EC:DEC, v/v=1:1 electrolyte (against Pt and Cu electrodes); b) Potential profiles from Graphite/Li 3-el-cells vs. Li or AgCl-RE in 1 M $LiPF_6$ in EC:DEC (v/v = 1:1) that were cycled at a rate of C/20.c) Striping plating CV measurements in EC:DEC electrolyte Salt concentration for Li: 1 M, for K 0.75 M. Scan rate: 0.5 mV s^{-1}

6.5.3 AgCl-RE Reference Potentials. AgCl-RE Reference Potentials

The reliable RE enables the estimation of the electrode's redox potential in any electrolyte that is compatible with RE. In the present case, this is the K^+/K potential in EC:DEC-based battery electrolytes. There is a lack of experimental data on the electrode potential of alkali metals in battery electrolyte solvents or solvent mixtures. Hence, these potentials can be experimentally evaluated with AgCI-RE.
The alkali metal potentials of lithium and potassium were determined by conducting cyclic voltammetry stripping/plating experiments. The standard electrode potentials (E_0) were subsequently calculated using the Nernst equation, based on the crossover potential of the anodic and cathodic sweeps in the zero-current region (**Table 2, Figure 18c**)**.** The K^+/K standard electrode potential was measured to have a value of −0.12 V *vs.* Li^+/Li in the EC:DEC electrolyte, which is in agreement with the data previously published[6]. The Komaba group recorded the process of potassium plating and stripping at an electrode potential of −0.15 V vs. Li^+/Li in 0.5 M KPF_6 EC:DEC, the value of E_0 (K^+/K)=−0.12 V vs. Li^+/Li.

Table 2. The standard electrode potentials determined from the zero-potential intercept of the anodic and cathodic scan of cyclic voltammetry measurements for both K- and Li-metal electrodes in EC:DEC-based electrolytes against a AgCI-RE with EC:DEC-based reference solution.

Electrode potential	Reference electrode	solvent in *reference* compartment	E_0 / V EC:DEC
Li^+/Li	AgCl-RE	EC:DEC (v/v = 1:1)	−2.26
K^+/K	AgCl-RE	EC:DEC (v/v = 1:1)	−2.38

The conducted experiments demonstrate that AgCl-RE provides greater versatility and reliability compared to the previously discussed K-RE and KFF-RE. This makes it a suitable candidate for achieving the objectives of this chapter: to study the degradation and polarisation effects of K-metal electrodes, to study graphite/KFF cells without the negative influence of K-RE, and to explore the effect of DTD on the electrochemistry of both half and full-cells.

6.6 The DTD Additive Studied in an AgCl-RE based 3-el Setup

The previous chapter demonstrated that the AgCl-RE was the optimal and versatile choice for both half and full-cell setups. This section examines the utilisation of the AgCl-RE in investigating the influence of the electrolyte additive DTD on electrode reactions at both the positive and negative electrodes across diverse cell configurations. The utilisation of 3-electrode setups with AgCl-RE permits the examination of electrode processes at the WE and CE, avoiding the risk of interference from degradation products. The effectiveness of the AgCl-RE setup is validated through a comparison of the EC:DEC-based standard electrolyte, with and without the DTD additive, in different cell setups. The recent research conducted by Hosaka *et al.*[179] has identified DTD as one of the most effective additives for mitigating electrolyte decomposition at K-metal electrodes, thereby suppressing DEDD [234]. However, their study also indicates that DTD is not fully compatible with graphite electrodes. Furthermore, the effects of DTD on full-cell KIB performance are not fully explored in that publication or in other previous literature.

6.6.1 Cyclic voltammetry on KFF/AgCl-RE/K cell

In the previous chapter, the process of EC:DEC decomposition in the KFF/K half-cell was observed. This section will investigate the decomposition processes in greater detail, employing the cycling voltammetry technique. This technique allows for the detection of the potentials of redox transitions of KFF and potential electrolyte decomposition. This will facilitate insight into the degradation process, which will in turn allow for a more accurate interpretation of the subsequent cycling results. The cycling curves of the KFF electrodes in both electrolytes are presented in **Figure 20.**

Two peaks of conversion are observed in the KFF system. The first occurs around 0.95 V *vs.* AgCl-RE (0.93 V for 0 wt. % and 0.96 V for 1 wt. % DTD) and is associated with the conversion of $K_2Fe[Fe(CN)_6]$ to $KFe[Fe(CN)_6]$. The second conversion peak is observed at approximately 1.58 V *vs.* AgCl-RE and is associated with the conversion of $KFe[Fe(CN)_6]$ to $Fe[Fe(CN)_6]$. Nevertheless, in the DTD-free electrolyte (purple curve), a third process is identified. From approximately 1.2 V, two peaks with similar peak current appear in the voltammogram at 1.48 V and 1.58 V *vs.* AgCl-RE. This finding is consistent with the two-step voltage profile observed at potentials exceeding 3.8 V vs. K^+/K in the experiments discussed in the chapter on KFF self-discharge behavior (**Figure 17a, b**).

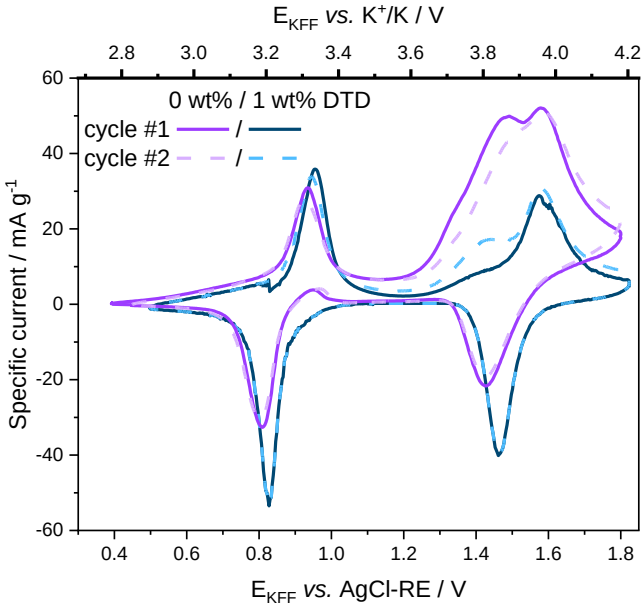

Figure 20. Cyclic voltammogram (v = 25 µV s^{-1}) of a KFF/K 3-el cell in EC:DEC 750 mM KPF_6 with (blue) and without (purple) DTD.

The backward scan showed that the peak at 1.48 V *vs.* AgCl-RE exhibited no corresponding redox species, indicating that it originates from irreversible reactions and exhibits significant overlap with the second oxidation step of KFF. Given that this peak is below the second redox potential of KFF, it can be concluded that the cathode material cannot be fully charged in the half-cell (i.e. in the presence of K-metal). In comparison, the cell with a DTD-containing electrolyte (blue) exhibits considerably less intense peak currents within the potential range above 1.2 V during the initial scan for this irreversible reaction (located at 1.42 V). A notable decrease in peak current was observed on the second scan.
In the presence of DTD, the redox processes at 0.80 V in the additive-free electrolyte (anodic sweep) exhibit a positive shift of 40 mV. Above the electrolyte degradation potential, both the peak position and the potential difference of the redox peaks in the electrolyte without DTD are observed to increase in comparison to the electrolyte with 1 wt. % DTD. A comparison of the peak area ratios between the anodic and cathodic sweeps in the voltage region above 1.2 V reveals that the additive-free electrolyte exhibits a ratio of approximately 8, which highlights the significant extent of irreversible processes at the electrode in the absence of the DTD additive. In contrast, the electrolyte with DTD displays a peak area ratio of only 1.6.

6.6.2 Galvanostatic experiments

In the 3-el cell galvano-static experiments are presented at **Figure 21**, the voltage cell measurement and control are done between WE and CE (i.e. cycled like a 2-el setup, see methodology section GCPL6 technique). In this cycling technique, AgCl-RE serves a mere observational role, tracking the potential at each electrode individually.

Half-cell experiments with AgCl-RE. Both KFF and graphite were then studied in 3-electrode galvanostatic cycling experiments. The potential profiles of WE and CE vs. AgCl-RE for the four cells are shown in **Figure 21**.

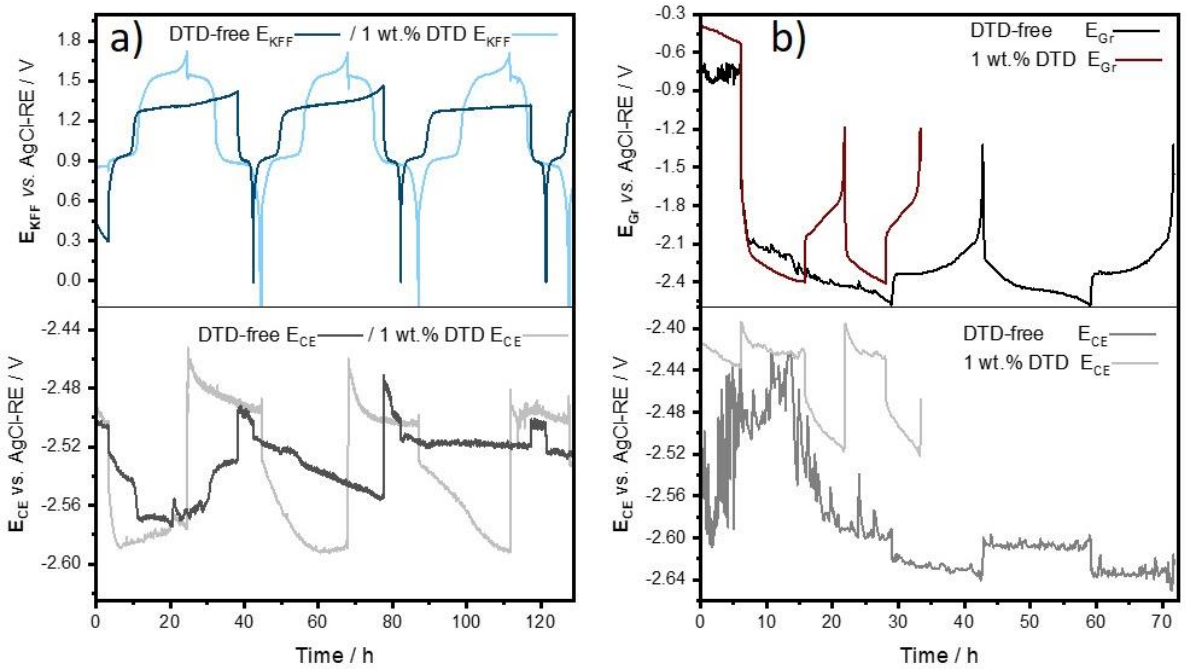

Figure 21. 3-el measurements with AgCl-RE: a) KFF/K half-cell with and without 1 wt. % DTD. The top and middle panel correspond to KFF vs. AgCl-RE (dark blue 0 wt. %, light blue 1 wt. % DTD) and K-CE vs. AgCl-RE (black 0 wt. %, grey 1 wt. % DTD); b) Gr/K half-cell with and without 1 wt. % DTD. The potential transients in the top and middle panel correspond to graphite vs. AgCl-RE (black 0 wt. %, red 1 wt. % DTD) and K-CE vs. AgCl-RE (dark grey 0 wt. %, light grey 1 wt. % DTD), respectively.

Working electrode potentials The K^+/AgCl-RE/K half-cell cycle curves in 3-el cell, presented in **Figure 21a (top panel)**, are largely in accordance with the experiments conducted by Hosaka et al. [179] and the results presented in the previous chapter (**Figure 17a, b**). In particular, a long electrolyte decomposition plateau of the KFF-WE potential is observed (as indicated by the CV experiments above), and the upper cut-off limit is not approached before the time limit of the experiment is reached. In the contrast, the distinctive two-step reaction of KFF is observed, with the upper cut-off limit reached at the end of the oxidation process in the electrolyte containing the DTD additive. In the graphite/AgCl-RE/K configuration at **Figure 21b (top panel),** the WE in the DTD-containing electrolyte demonstrates a larger polarization, a rapid potential drop at the outset of the intercalation process, and a sloping profile devoid of the conventional intercalation characteristics described in theoretical background section (**Fig. 5).** This finding is also consistent with the prior research of Hosaka et al.*al.* [179]. The electrode is unable to reach a fully charged state before reaching the lower cut-off limit due to the high degree of polarisation and rapid potential drop. The removal of voltage noise from the

potential profile of the electrode in the additive-free electrolyte is not feasible with the current cell construction. This may be attributed to the lack of a constant RE pressure at the separator. However, it disappeared after the initial cycling sequence, thus excluding loose contacts as a potential cause. Furthermore, it was observed in other tests (e.g. **Appendix Figure A3a-d**) with additive-free EC:DEC-based electrolytes and K-metal electrodes.

The K-CE potentials. 3-el setup with reliable RE as AgCl-RE is key to analysing the CE potentials. The K-CE potentials for the four samples are presented in the middle panels of **Figures 21a** and **21b**. To date, there has been no analysis of KIB CE in the literature, with the exception of symmetric cell tests [246,247,260]. The potential profiles of K-metal electrodes exhibit notable distinctions from those observed in symmetric cells. This phenomenon requires further investigation to understand the underlying causes of this deviation. In both the KFF/K and Gr/K configurations, the overpotential of K-CE in the DTD-containing electrolyte is higher than that observed in the corresponding additive-free case. The symmetric cell data presented in previous studies [179,261] demonstrated a lower overpotential for electrolytes containing DTD. In the present system, the opposite appears to be the case, as evidenced by the 3-el cells under examination and the symmetric cell that have been previously presented. This may be attributed to the history and surface conditions of the potassium electrode. In contrast to the symmetric cell data illustrated in **Fig. 14**, significant potential fluctuations are observed in the potential transient, and in the case of additive-free electrolytes, there are also sudden jumps and fluctuations exceeding tens of mV. The K-CE potentials demonstrated considerable fluctuations during the initial cycling sequence, particularly in the Gr/K half-cell (**Fig. 21b**) cycled without the DTD additive showed potential fluctuations of up to 160 mV during the first 20h of the experiment. The profile of the WE in **Fig. 21b** also illustrates the potential spikes, which typically disappear after the initial cycling sequence. In regard to the stability of AgCl-RE, as evidenced in both the Gr/Li configuration and the aging test over the initial 100 days (**Fig. 19**), it can be reasonably assumed that significant fluctuations originating from the RE are unlikely. However, in addition to the aforementioned reactivity of EC and DEC at the K-metal surface, the pressure of the RE capillary on the cell separators in our 3-el setup is susceptible to changes. These include, for example, fluctuations in pressure due to vibrations in the glovebox and changes in atmospheric pressure inside the box.

One notable aspect of the potential profiles of the Gr/K half-cells is the relative reaction potential of K-CE, which depends on the electrolyte formulation. In the presence of the electrolyte additive DTD, the average reaction potential exhibits a shift of approximately +200 mV with respect to the K-CE potential in the additive-free electrolyte. The potential shift causes WE to reach the lower cut-off limit before reaching the fully potassiated state, resulting in termination of the cycle sequence. This can be clearly seen by comparison of the Gr-WE potentials in the top panel. As a result, the graphite electrode cannot reach its fully charged state. The aforementioned effect is not observable in a 2-el cell due to

the control of potential by E_{WE}-E_{CE}. Consequently, a 2-el cycling curve cell will always reach the cut-off limit, as evidenced by the comparison of the cell voltage curve in Appendix (**Figure A3a, b)**. A similar process was observed in LIB to that previously reported by Ko *et al.*[262,263]*,* who found that the CE potentials of Li metal shifted in electrolytes with high salt concentrations. The authors acknowledged that in electrolytes with high concentrations, the degradation of salt is more pronounced. Furthermore, they noted that the formation of an 'anion-derived' SEI results in the development of a surface layer that affects the effective electrode potential of the Li-CE. An analogous effect could be responsible for the observed upshift, although it is DTD that is decomposing during oxidation at the K-CE. In addition, the current direction appears to impact this process, as evidenced by the observation that both K-CE potentials in the KFF/K cells exhibit a comparable OCV potential during the brief resting interval between cycles, with a value of approximately -2.51 V. This indicates that under an initial anodic current (as in the case of KFF/K), where K-ions are plated onto K-CE, the surface chemistry of K-metal remains similar. In contrast, under cathodic current, where K-ions are removed from K-CE, the redox potential of K-CE shifts to a higher potential, resulting in a significant change in surface chemistry. Furthermore, it is noteworthy that neither the potential profiles obtained with nor without the DTD additive align with those observed in symmetric cell configurations. A comparison of the two cases is provided in the appendix (**A3c & A3d**).

***DTD in 3-el full-cell setups*.** In half-cell experiments, DTD demonstrated notable interaction with the negative electrode, whether it was the K-CE in the KFF half-cell or the graphite-WE in the anode half-cell. This raises the question of whether DTD is suitable for use in systems that do not include a reactive metallic CE. To investigate this, a three-electrode full-cell configuration was employed, comprising a graphite negative electrode, a KFF positive electrode, and an AgCl-RE to avoid the use of potassium metal, for the reasons mentioned earlier.

Figure 22 presents the potential profiles of the first cycles for the KFF-WE, Gr-CE, and the cell potential (E_{cell}). In this experiment, an excess cathode areal capacity with an N/P ratio of around 0.55 was employed to offset initial losses. Furthermore, this ratio enables the systematic observation of the additive's effect on graphite behaviour. Additionally, it was observed that the AgCl reference electrode does not significantly impact the electrodes' cycling curve. It is important to note that the chosen N/P ratio may not be optimal, and the additive's impact may vary with different N/P ratios.

The KFF-WE potential curves in cells with and without DTD (**Figure 22**, top) exhibit a two-step profile that is consistent with the profiles presented above in **Figures 17c** and **22a**. This result aligns with previous findings that the excessive formation of DEDD at the potassium counter electrode plays a pivotal role in the high level of irreversible reactions that occur during cycling and self-discharge under OCV. The lower potential plateaus of the two cells differ by 80 mV, with the 0.92 V (0 wt. % DTD) and 1.00 V (1 wt. % DTD) *vs.* AgCl-RE values aligning with the results of the CV experiments (**Fig. 20**). The

second cycling sequence demonstrates a notable absence of the lower discharge potential, indicating the presence of considerable irreversible losses during the charging process at the negative electrode. These losses are attributed to the formation of the SEI, which is a primary source of charge carrier inventory loss. Consequently, the reduction reaction is constrained by the remaining active charge carrier inventory.

Upon analysis of the Gr-CE potential profiles (**Fig. 22, middle**), it becomes clear that the primary cause of the fast capacity decay can be attributed to the poor electrochemical behaviour of the graphite electrode in the presence of DTD (grey line), as previously demonstrated in the discussion above (**Fig. 21b**). The potential in the DTD-containing cell is observed to lack the characteristic intercalation plateau seen in the DTD-free standard electrolyte. Instead, it rapidly drops to low potentials until the cell's cut-off limit is reached. It is noteworthy that in subsequent cycles, indications of potassium plating emerge, exhibiting a constant potential section at −2.56 V *vs.* AgCl-RE. Meanwhile, the end-point potentials during discharge are observed to slipping, due to the KFF electrode being unable to retain the upper potential step. As the potential end-point of KFF shifts to higher potentials, the graphite end-point potentials must also shift until the cut-off voltage is reached. In contrast, the Gr-CE in the DTD-free cell (black line) displays the characteristic intercalation features and demonstrates higher retention of the charge carrier inventory in comparison to the cell with the DTD additive. As the potential end point of KFF is shifting to higher potentials, the graphite end point potentials must shift as well until the cut-off (cell) voltage is reached. In contrast, the Gr-CE in the DTD-free cell (black line) shows the characteristic intercalation features and retains the charge carrier inventory better than the cell with DTD additive.

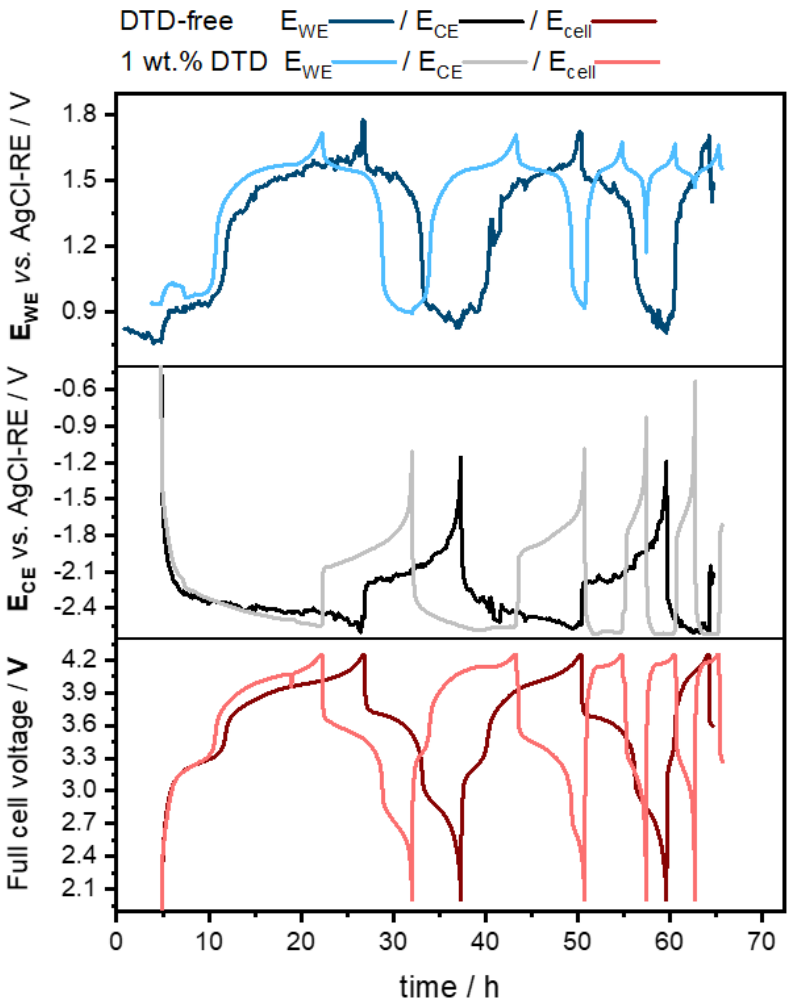

Figure 22. 3-el full-cell measurements with AgCl-RE with and without DTD: The top panel is KFF vs. AgCl-RE (dark blue 0 wt. %, light blue 1 wt. % DTD), the middle panel is graphite vs. AgCl-RE (black 0 wt. %, grey 1 wt. % DTD); in the bottom panel the cell voltage is shown (dark red 0 wt. %, light red 1 wt. % DTD).

6.7 Summary of the chapter

The thin layer set-ups typically employed in battery research often render the implementation of a suitable RE a challenging task. This chapter has demonstrated the reasons why the selection of an appropriate RE is particularly challenging for KIB systems. It has highlighted the challenges faced by positive electrodes due to crosstalk with electrolyte degradation products such as DEDD[159,202,264]. The positive electrode material KFF, which is widely used in KIB, exhibited significant irreversible reactions, as evidenced by its extended two-step potential profile above 3.75 V *vs.* K^+/K in 2-el (**Fig. 18**) and 3-el cell (**Fig. 22**) tests. The CV experiments (**Fig. 20**) clearly showed an additional feature on the anodic scan. Furthermore, under OCV conditions, KFF/K-CE half-cells undergo a self-discharge process triggered by DEDD and similar compounds (ethylene bis(alkyl dicarbonates)), as shown in **Scheme 2**. The formation of these compounds can be

initiated by even small amounts of K-metal, which consequently limits the applicability of K-metal-based REs in 3-el full-cell tests. This essentially invalidates two common approaches for 3-el measurements[50,257] in half and full-cells: the use of metallic electrodes (K-RE) and partially charged electrode materials with a flat potential region, as explored with a KFF electrode. Avoiding K-RE is crucial as the measured potential of the electrode is highly dependent on its preparation history and purity[247,248]. Similar problems have been reported for the Na-ion system[50,257], supporting conclusions. The rapid degradation of K-metal, coupled with its sensitivity to preparation history and material grade, presents numerous challenges, thereby underscoring the necessity for alternative RE for KIB.

Therefore, an alternative reference electrode (AgCl-RE) utilising Ag wire in a saturated TBACl solution was proposed. The electrode is located within a separate glass capillary compartment, as illustrated in **Scheme 2**. The electrolyte solvent mixture can be adjusted as needed and referenced to the ferrocene redox couple (Fc^+/Fc), thereby ensuring compatibility with a range of electrolyte compositions. This approach effectively eliminates the issues associated with the formation of DEDD in electrolytes in contact with K-metal. The proposed configuration of the cell allows to introduce a silver-based reference electrode while maintaining the geometry of the coin cell battery and utilising a separator of a few hundred microns in thickness, thereby reducing the volume of the electrolyte. This setup can be employed independently of the cell chemistry and adapted to different electrolyte formulations. Nevertheless, some minor issues related to the setup persist in this first generation. For example, the cell does not have a tight seal around the RE compartment, so it can only be used in a glove box. Consequently, there is a slight degree of solvent evaporation from the cell compartment, which may potentially affect long-term measurements. Additionally, maintaining constant contact pressure between the soaked separator in the cell compartment and the RE-capillary membrane is challenging, which may explain the voltage fluctuations observed in some experiments.

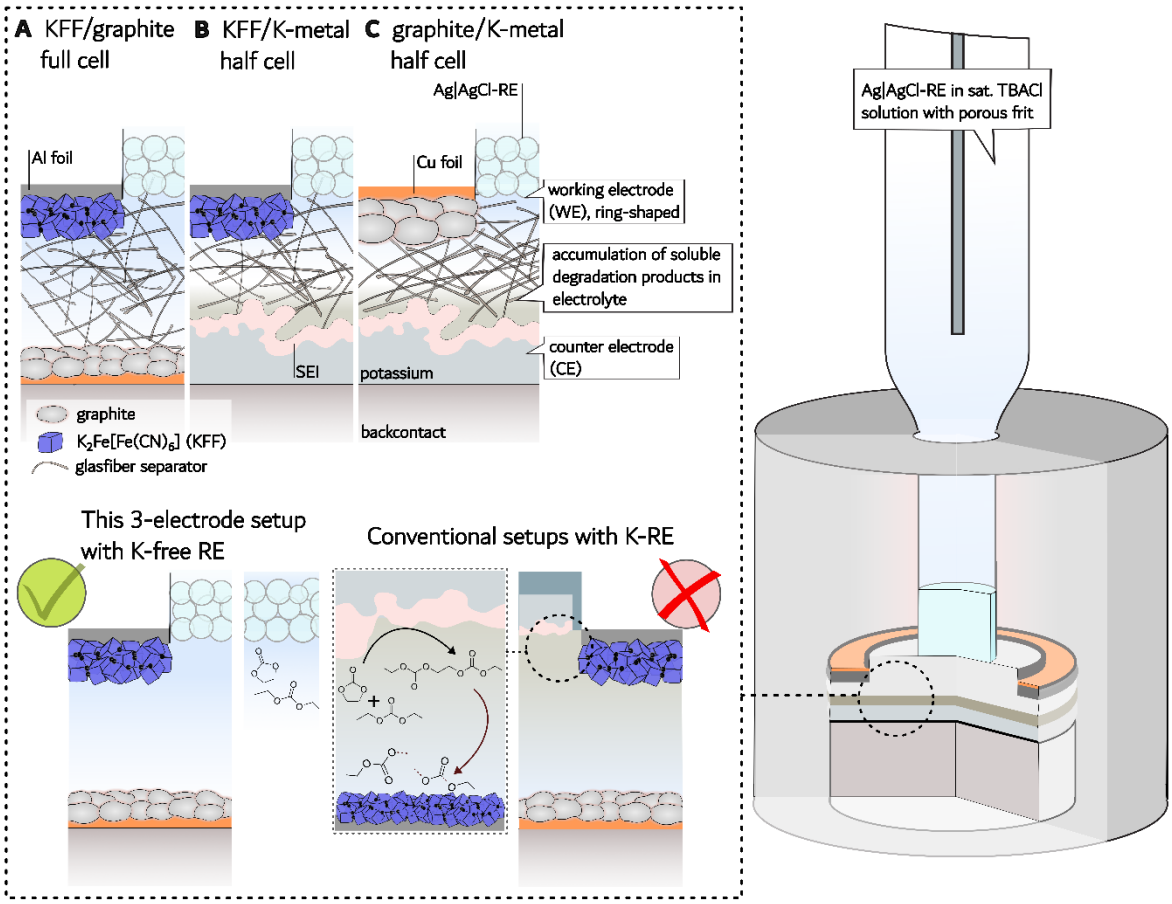

Scheme 2. Illustration of the cell setup and the cross-talk induced reactions at the negative and positive electrodes in K-ion batteries due to the formation of ethylene bis(alkyl dicarbonates) at the reactive potassium counter or reference electrode.

The aforementioned advantages demonstrate that the AgCl-RE based 3-el configuration facilitates the unbiased measurements of reactive KIB system species. This setup is free from the influence of degraded electrolyte components, thus ensuring the reliability of the measurements. The presented cell configuration with AgCl-RE was employed to conduct experiments with the following objectives: 1) understand the deterioration of the K-metal electrode and polarization effects, 2) study graphite/KFF cells without the detrimental influence of K-RE and 3) investigate the impact of DTD on the electrochemistry in half and full-cells.

The self-discharge processes at the KFF electrode, caused by electrolyte degradation products formed at the K-metal electrode, have been outlined by comparing the electrochemical responses of galvanostatic and cyclic voltammetric measurements in different 2 and 3-electrode configurations using either K-RE, KFF-RE or AgCl-RE. The AgCl-RE was the only reference that allowed both sides of the electrode to be monitored individually, independent of the electrode and electrolyte chosen.

This approach has the advantage of preventing interference in the electrode potential profiles resulting from the presence of degradation products. The results of the experiments demonstrate that the

actual redox potential and polarization of K-metal have a significant impact on the accelerated degradation of half-cell configurations. Furthermore, it might induce misleading effects and detrimental electrode processes. In accordance with previous findings by Hosaka *et al.*[178] and Ko *et al.* [262,263], the 3-el measurements demonstrated that the impact of DTD on the graphite electrode is characterised by two distinct effects: In K/graphite half-cells, the redox potential of the K-metal electrode shifts towards more positive values, which is likely due to the formation of a resistive passivation layer on K-CE. consequently, the cell voltage between Gr-WE and K-CE narrows, resulting in the Gr-WE reaching the lower cut-off limit prematurely. In graphite/KFF full-cells, DTD contributes to the degradation of graphite, as the characteristic intercalation signatures were not observed. Additionally, indications of K-plating were evident from the second cycle onwards.

In conclusion, although further improvements to the setup are necessary in the future, the general approach of transferring the RE into a separate cell compartment appears to be a promising and viable strategy for minimising interferences between the RE and other cell components. This approach represents a viable method for investigating the behaviour of KIB electrodes.

7 Surface analysis of KIB electrodes

The preceding chapter examined the electrochemical effects of DTD cell performance, including how it supresses DEDD formation and how it degrades graphite cycling performance. The objective of this chapter is to complete the electrochemical examination by presenting an analysis of electrode surfaces in both half and full-cells, with a particular investigation of the effects of DTD. To achieve this, XPS will be employed as the primary method of investigation. In a previous study, potassium salts were analysed in order to ascertain whether they constituted the expected SEI components[203]. Moreover, a series of works can be employed for the purpose of validating the components of the SEI of graphite[213,240,265,266]. In order to gain a greater understanding of the interphases of electrodes, an investigation was conducted on both the anode and cathode surfaces

A significant aspect of this chapter is the surface analysis of KFF. Despite its prevalence as cathode material in KIB, there is a noticeable lack of publications addressing the surface characteristics of this additive. Furthermore, none of the current literature addresses the chemical processes involved in the KIB cell directly[267–270].A review of the literature reveals a lack of sufficient insight into the CEI of KFF, particularly in relation to the influence of DTD. Given that the CEI plays a crucial role in determining the stability of the cathode, understanding its interaction with DTD could offer valuable information about the formation of protective films and electrolyte degradation, both on the cathode and anode sides.

The primary objectives of this chapter are as follows:

1. To provide a comprehensive set of XPS reference data for KFF electrodes, including peak positions and assignments for precursor materials, powders, and coated electrodes, aiding in the precise characterization of cycled samples.
2. To investigate the influence of DTD on both cathode and anode surfaces, and compare its impact in half-cell and full-cell configurations, building on the electrochemical data discussed in the previous chapter.

To address these objectives, a comparative study was conducted between cells containing 1 wt. % DTD and additive-free cells.

7.1 KFF Reference Measurement.

This chapter presents X-ray PES data for KFF electrodes, providing information on peak positions and assignments for precursors, powder, and coated electrodes in different charge states (fully (de)potassinated). The fitting model and underlying principles are presented below. The wealth of existing data on graphite allows a reliable fit to be used with sufficient confidence. However, there is a gap in the data and models available for PBA cathode XPS fitting, and this section is intended to fill this gap.

The conductivity of cathode material and precursor materials is relatively low, which may require the application of charge compensation by FG. The different charge states of potassium (iron) ferricyanides with varying iron oxidation states were employed, including powders and coated electrodes of Prussian White (KFF, $K_2Fe[Fe(CN)_6]$), Prussian Blue (PB, $KFe[Fe(CN)_6]$), Prussian Green (PG, $Fe[Fe(CN)_6]$), as well as potassium ferricyanides $K_3Fe(CN)_6$ (KFe3) and $K_4Fe(CN)_6$ (KFe2). The corresponding XPS spectra, which have been fitted and analysed, are presented in the Appendix (**Figure A4-A9**). The C1s-K2p, N1s and F1s regions have been selected for discussion as they are the most characteristic of PBA and will be used as a reference in the following chapter when analysing cycled electrodes. The powder spectra were referenced to the CN sp^3-C signal at 285 eV, which is minimally affected by the iron oxidation state and is consistent with the positions observed for KFe2 and KFe3 materials[271]. In the case of coated electrodes, the spectra were referenced to the PVDF F1s signal at 688.15 eV, which was chosen as the optimal reference point due to significant signal overlap in the 284-287 eV binding energy (BE) range for all electrodes, including those subjected to cycling. After the calibration, the CN sp^3-C signal for the electrodes was observed at 285 ± 0.1 eV, which is within the measurement error margin. The binding energies of fitted peaks for these key regions in the reference materials are presented in **Table 3.**

Table 3. Summary of XPS fitting results for binding energies (BE) for carbon, nitrogen and fluorine.

Sample		$K_3Fe(CN)_6$	$K_4Fe(CN)_6$	$Fe[Fe(CN)_6]$ Electrode	$KFe[Fe(CN)_6]$ Powder	$K_2Fe[Fe(CN)_6]$ Powder	$K_2Fe[Fe(CN)_6]$ Electrode
Element	Bond						
C1s	sp^2-C / C-C			284.9			284.3
	sp^3-C / -CH-			286.4			286.1
	-C≡N	285	285	285.1	285	285	284.9
	-CO-/-C-N-/CH_2(PVDF)	286.4	286.6	286.73	286.65	286.5	286.9
	-(C=O)OR					287.5	
	-CO_3-	289.0	289.0	288.6	288.6	288.8	288.5
	CF_2			291.2			291.1
	$K2p_{3/2}$	292.9	293.1		293.5	293.7	293.6
	$K2p_{1/2}$	295.7	295.9		296.3	296.5	296.4
	$2K2p_{3/2}$				294.2		
	$2K2p_{1/2}$				297.0		
F1s	PVDF			688.15			688.15
N1s	C≡N	398.2	397.9	398.0	398.1	397.9	397.9
	C-N		399.4	399.3	400.0	399.9	400.3
	NO			400.8			
	NO_3			402.9	402.3	402.1	402.2

C1s/K2p signals. The C1s-K2p region of the cyanates, which is divided into 3-6 components depending on the sample composition (powder or coated electrode), is shown in the left column of **Figure 23**. The basic component, the C≡N group (light blue), is present in all samples and has a binding energy (BE) of 285 ± 0.1 eV. The materials used for electrode coating and synthesis are related to the remaining peaks. For the preparation of the PG and KFF electrodes, for example, carbon black and polyvinylidene fluoride (PVdF) have been added. The C-C sp^2 peak (light grey) is the main signal from the carbon black. For the KFF and PG electrodes it is located at 284.3 and 284.9 eV respectively. PVdF has two main peaks in C1s-K2p region, the -$\underline{C}F_2$ (red) peak at 291.2 ± 0.1 eV and the polarised -$\underline{C}H_2$- group (pink) at 286.7 ± 0.1 eV. Their BE position, peak area ratio and BE distance have been set according to the literature, i.e. 4.6 eV distance and 1:1 peak area ratio[272]. To minimise the complexity of the fitted spectra resulting from the overlapping of several peaks [273], the -CH_2- (PVdF) signal and the carbon-oxygen signal (C-

O) from alkoxide/ether species are combined into a single peak (dark yellow, labelled CH_{PVdF}/CO) at 286.5 ± 0.1 eV. Furthermore, a minor contribution of carbon-nitrogen species (single bond) is identified, exhibiting a binding energy (BE) range similar to that of the other two peaks(according to literature[274,275]). These contributions are clearly visible in the N1s spectra (right column, **Figure 23**) Due to the high sensitivity of XPS, the precursor substances employed in the synthesis can also be identified. For example, within the BE region, ranging from 287 to 289 eV, the presence of carbonyl (C=O) species can be observed. This is due to the presence of trace amounts citrate and poly(vinylpyrrolidone) employed for the synthesis. Moreover, the presence of surface groups of carbon black may also be observed in this region. Additionally, analysis of the N1s spectra indicates the presence of N-C=O species derived from oxidised cyanide functional groups at the KFF surface. Furthermore, the N1s spectra indicate the presence of N-C=O species from oxidised cyanide groups at the KFF surface.

The C1s measurement region has been expanded to include the K2p signals (blue) within the 292–300 eV range, located just above the C1s region. The characteristic BE difference between the $K2p_{3/2}$ and the $K2p_{1/2}$ peak is 2.8 eV with an intensity ratio of 2:1. A clear difference is evident between the BE of K2p peaks in cyanates and those observed in PBA spectra the binding energy of $K2p_{3/2}$ in KFe2 and KFe3 spectra is 293 ± 0.1 eV, with no dependence on the oxidation state of iron. The $K2p_{3/2}$ peak in the spectrum of the KFF powder and pristine electrode sample was observed at slightly higher BE of 293.7 eV. In contrast, in the half-oxidized PB samples (pristine electrode) the $K2p_{3/2}$ signal is split into two components. One is located at the identical position as in the KFF samples and a second one located at 294.2 eV (violet), which is attributed to a separation of the local K^+ environments depending on the surrounding Fe oxidation states. The K-ions in the environment of Fe^{3+} exhibit a higher BE. A significant aspect of the following analysis of KFF electrode spectra is the distance between the $K2p_{3/2}$ and C≡N signals, which is 8.7 eV. In a composite electrode comprising a mixture of carbon black and PBA, the C≡N signal displays a distinct overlap with the carbon signal (-C-C-) of carbon black. As a result, the distance can be utilized as a valuable tool in the following fitting process. As confirmed by the absence of K2p signals, the fully oxidized species exhibits no significant amounts of potassium. Furthermore, the presence of a substantial proportion of Fe^{3+} iron charge states in the Fe2p and Fe3p spectra (**Figure A9a, b**) is also in accordance with this conclusion.

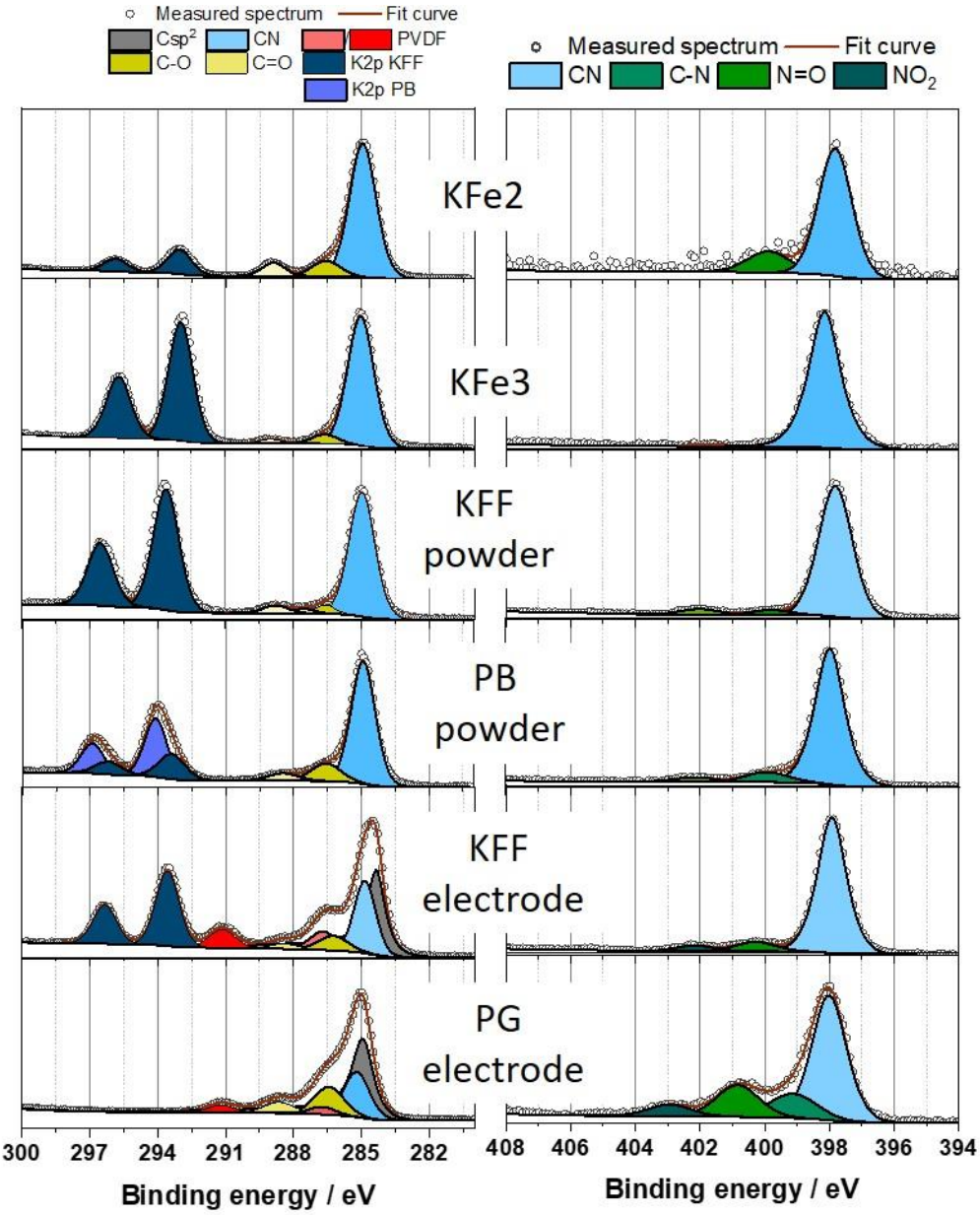

Figure 23. Comparison of the C1s(left), N1s(right) spectre of Potassium (iron)ferricyanides: a) $K_4Fe(CN)_6$](KFe2); b) $K_3Fe(CN)_6$ (KFe3); c) KFF ($K_2Fe[Fe(CN)_6]$)powder; d) Prussian blue (PB) $K_2Fe[Fe(CN)_6]$ powder; e) KFF electrode; f)Prussian Green (PG) $Fe[Fe(CN)_6]$ electrode

N1s signals. N1s region for all cathode reference samples (right column) is presented at **Figure 23.** It can be observed that the cyanide group (C≡N, light blue) signal is the most dominant among the signals present in this region (**Figure 23)**. The peak is located at 398 ± 0.1 eV. The position is observed to be minimally dependent on the charge state of iron. NIST database indicates that the BE is shifted to 398.1 eV by Fe^{3+}[276] in KFe3 and to 397.9 eV by Fe^{2+}[277]. In PBA, the BE of the C≡N peak is also independent of the oxidation state. The main N1s peak for PBA samples consistently appears at 398 ± 0.1 eV, which is also in accordance with the literature[271,273,278]. It is evident that the oxidation states of iron have no impact on the -CN peak, which allows for the calibration of PBA cathode materials to be

conducted using this signal. The C-N single bond is observed in the 399-400 eV range. In the KFe3 spectrum, it appears at 399.4 eV, while in the PBA samples, it is present at 400.1 ± 0.2 eV. The presence of the intense C≡N signal makes it challenging to distinguish the C-N peak. The occurrence of additional peaks at higher energies is attributed to N-C=O, while low-intensity signals above 402 eV are related to nitrate contamination.

7.1.1 PBA calibration/fitting model

In general, the saturated -CH- peak at 285 eV is employed as a standard for the calibration of carbon materials. However, this approach is not viable for KFF electrodes. In the cycled C1s-K2p spectra, in addition to the carbon black and PVDF peaks, the CEI-related components overlap with the -CH- bond signal, making it difficult to accurately identify the peak. The most complex C1s-K2p region can be fitted more effectively with the assistance of markers that help to distinguish between the numerous overlapping peaks. As demonstrated, K2p from KFF and C=N exhibit a discernible distance of 8.7 eV, which can assist in differentiating CEI salt peaks or peaks associated with the discharge state of the cathode. Another peak that may be useful for this purpose is the -$\underline{C}F_2$- peak of PVdF, with a distance of 6.1 eV from $\underline{C}$≡N. It can be reasonably assumed that precise alignment of the peak distance at the time of adjusting the peak position will result in uniform fitting and reliable data, which in turn will facilitate a reasonable analysis.

It is important that the calibration process includes the use of a peak in the region where CEI products are not typically present or have a minimal presence. Alternatively, the calibration peak should have an intensity that can be easily identified. In the case of PBA, the utilisation of signals from CN in the C1s and N1s regions is a viable approach. These peaks have characteristic positions that are not affected by the charge state of the iron, as was demonstrated. The N1s peak is the most optimal choice due to its significantly higher intensity compared to other peaks in the region, with a contribution that is more than three times greater than that of any other peak (**Figure 24**), making it easy to detect. In the C1s region, the CN peak is observed to overlap with the carbon black C-sp^2 signal. Additionally, it is not the most intense peak in the region (**Figure 24**).

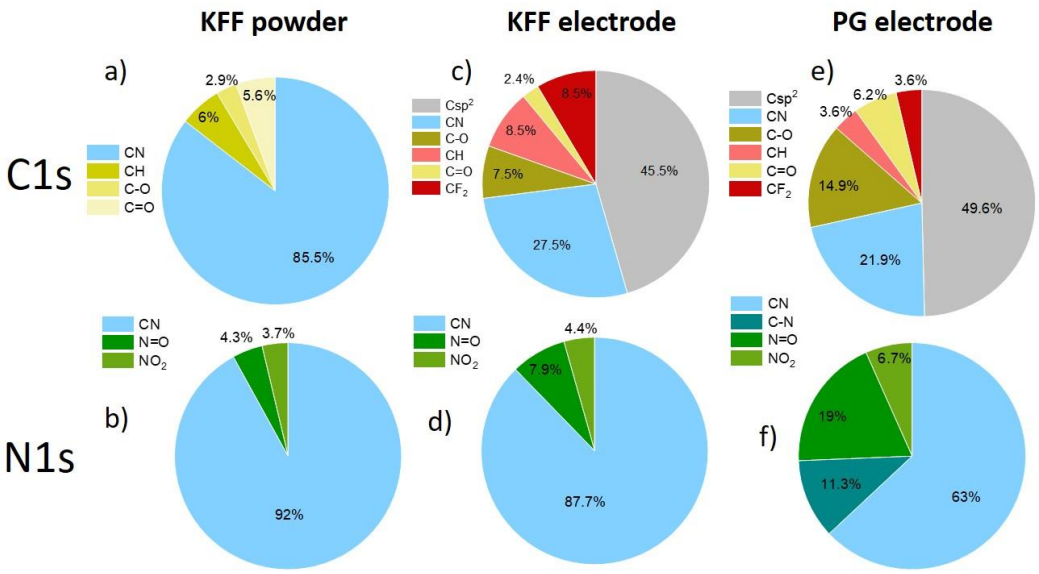

Figure 24. C1s and N1s forms contribution of KFF powder(a)C1s1, b)N1s), electrode(c)C1s, d) N1s) and PG electrode (e)C1s, f)N1s)

The utilisation of subsequent peaks as markers for calibration represents a strategy that allows precise fitting to be achieved. It has been demonstrated from the N1s spectra (**Figure 23**) that the cyano group (C≡N) signal is unaffected by the charge state of the electrode and does not overlap with the expected product of the electrolyte or any decomposition products. The second peak that can be employed for calibration is the F1s signal of PVdF is present in all electrodes and exhibits minimal overlap with the salt (KPF_6) that will be used in cycling tests, thereby offering a suitable second peak for calibration purposes.

7.2 Effects of DTD at the half and full-cells electrode surface

In order to complete the 3-el cell test and identify the discrepancy between electrode surfaces with 1 wt. % DTD and 0 wt. % DTD in both half and full-cell configurations, it was examined a range of electrodes, including those that had been cycled, KFF electrodes, and electrodes that had been stored in the electrolyte (referred to as 'OCV samples'). The cells were stopped in a fully discharged state, that is to say, in a depotassinated state for the cathode (KFF) or in a fully potassinated state for the anode (graphite). Subsequently, the electrodes were rinsed immediately to remove any residual electrolyte salt. The electrodes were then analysed by non-destructive XPS utilising 1487 eV Al Kα photon energies. The results for the cathode and anode as well as half and full-cells will be discussed in separate chapters in order to facilitate a more consistent discussion.

7.2.1 PES of half-cell electrodes

Effects of DTD at the KFF surface in the half-cell

As discussed in the electrochemical test chapter, the incorporation of 1 wt. % DTD has proven effective in mitigating K-metal/KFF crosstalk reactions in half-cell configurations, as demonstrated by the self-discharge tests (**Figure 17**). These effects will be discussed further in the following sections, where surface analysis will be presented. Given the observations in the half-cell tests, which included crosstalk reactions and significant decomposition in the case of the KFF/K cell without additive and passivation of the graphite surface by additive during the first cycle, samples stored in the electrolyte and cycled once, with and without the additive, were selected for further investigation. Rest of the regions are presented in Appendix section (**Figures A10-A13**)

PES of half-cell KFF electrodes

C1s-K2p spectra. **Figure 25** presents the C1s-K2p spectra of both cycled and OCV KFF electrodes, with and without the addition of 1 wt. % DTD in the electrolyte. Most of the peaks observed in the spectra correspond to those previously discussed in the reference chapter. These include the bulk carbon black sp^2-C signal (grey) at 284.7 ± 0.1 eV, the C≡N signal (light blue) at 285 eV, the -CO-/-CN-/-CH-PVDF peak (yellow) at 286.6 ± 0.1 eV, and the PVDF -CF_2- peak (red) at 290.7 ± 0.2 eV. In addition to the bulk signal, CEI-related peaks are present, including saturated hydrocarbon species (-CH-; dark grey) at 285.5±0.1 eV, carboxylates (-(C=O)OR-; light yellow) at 288.5 ± 0.1 eV, and carbonates (either K_2CO_3 if inorganic, or R_1O-(C=O)-OR_2 if organic; BE = 289.7 ± 0.2 eV; orange). The K2p signals are found at 293.7 ± 0.1 eV and 292.9 ± 0.2 eV ($K2p_{3/2}$).

OCV. The absence of the C≡N and C-sp^2 KFF signals in the OCV sample spectrum indicates that the CEI thickness is greater than the XPS penetration depth of 7-9 nm. Moreover, the spectrum demonstrates the presence of intense carbonyl and carboxyl peaks, as well as a distinguishable carbonate peak. The K2p signal was found to correlate with the electrolyte salt signal. This correlation will be confirmed by the absence of any signals in the N1s (**Figure 26**) region (therefore K2p is not related to KFF) and the presence of an intense KPF_6 signal in the F1s (**Figure 27**) spectrum. By contrast, the passivation of the K-metal surface, which serves to prevent the degradation of the electrolyte, is evidenced by the characteristic KFF peaks observed in the OCV DTD spectra. This suggests that the CEI layer, in the presence of the additive, has a significantly thinner composition than that observed in the 0 wt. % DTD sample. Also, CEI of this sample does not contain carbonate peak, which is presented in additive-free case. In the C1s region C-O, C-sp^2 and C≡N exhibit the highest intensity.

Cycled electrodes. The most notable difference between the OCV 1 cycled spectra is the splitting of the K2p signal into two signals, which is a characteristic feature of cycled KFF[279], as discussed above (**Figure 23**, **Section 7.1**). Furthermore, this phenomenon will be observed when the KFF is cycled in its full-cell configuration. It is noteworthy that following a single cycle, it was observed that the signals associated with the decomposition products were less intense than those observed in OCV sample. The spectrum of the sample after one cycle without additive demonstrates presence of bulk signal in contrast to OCV one. The cycling process results in the formation of the SEI at the K-CE surface, which mitigates the level of electrolyte degradation. This does not entirely prevent it, but rather reduces its intensity, as evidenced by the higher intensity of the peaks assigned to the degradation products (C-O, C=O, CO_3, CH) is higher for the half-cell cycled without the additive. The CH and C-O signals exhibit a greater intensity than the CN peak. The carbonate peak is still only visible in the additive-free half-cell spectrum. This indicates the formation of electrolyte degradation products at the electrode surface in the absence of a passivation agent, which is DTD, for potassium metal.

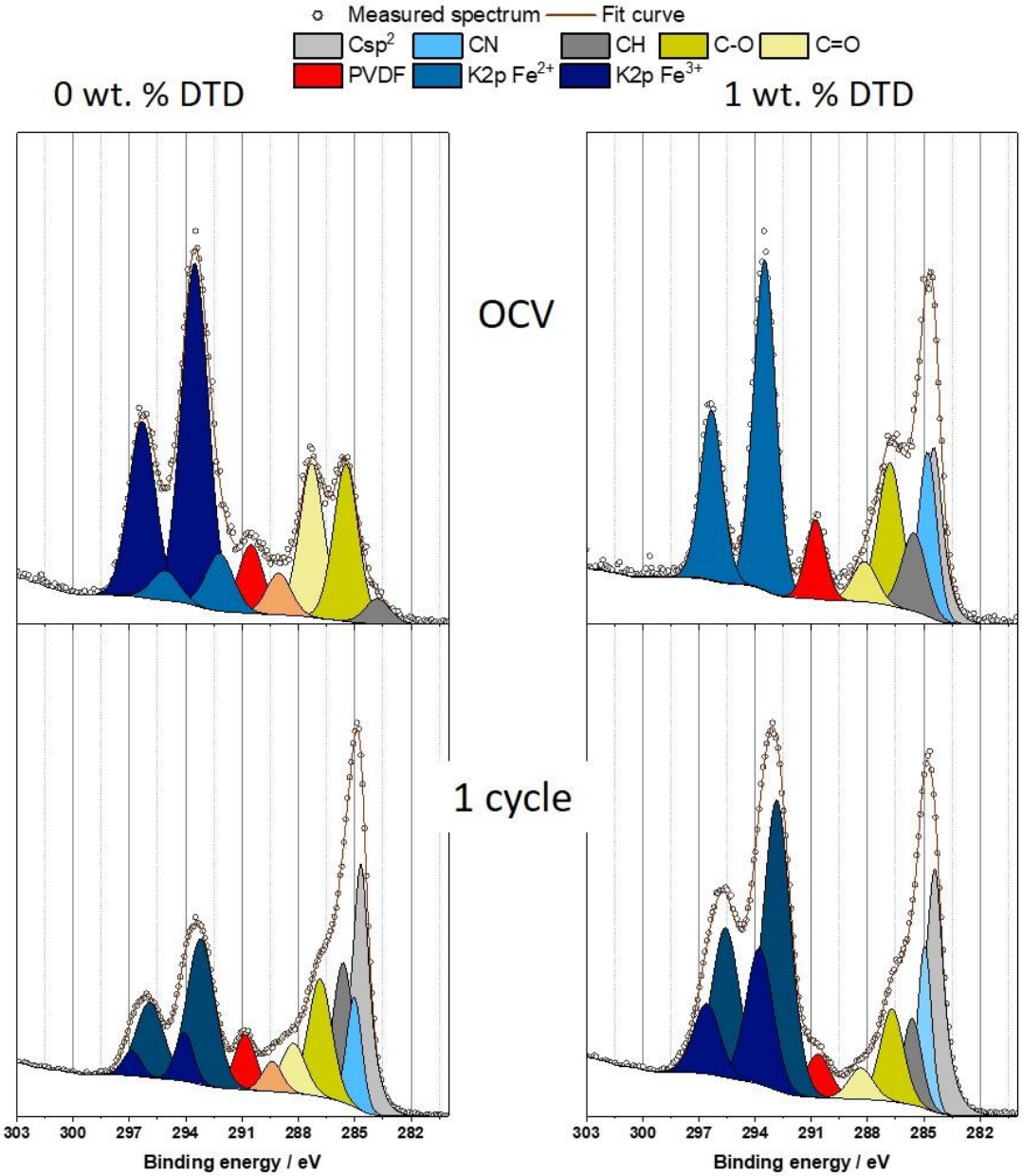

Figure 25. C1s−K 2p spectra of half-cell KFF electrodes stored in electrolyte and after one charge and discharge in 750 mM KPF_6 EC:DEC without additive (left column) and 1 wt. % (right column)

The 1 cycle DTD sample displays a relatively lower intensity of carbon-oxygen signals in comparison to the additive-free sample. However, in general, the spectrum of the sample cycled with DTD is found to be similar to that of the OCV sample, with the exception of the K2p splitting.

N1s spectra. **Figure 26** presents the N1s spectra of the half-cells KFF. As previously stated, the C≡N bond (light blue, 398.0 ± 0.1 eV) is absent in the OCV 0 wt. % DTD sample due to the formation of a thick CEI layer. In the remaining samples, this peak remains constant. As a pristine electrode, all samples display a signal attributed to a carbon-nitrogen single bond, with a BE of 400 eV (green) and nitrate trace signals at 402 eV (dark blue).

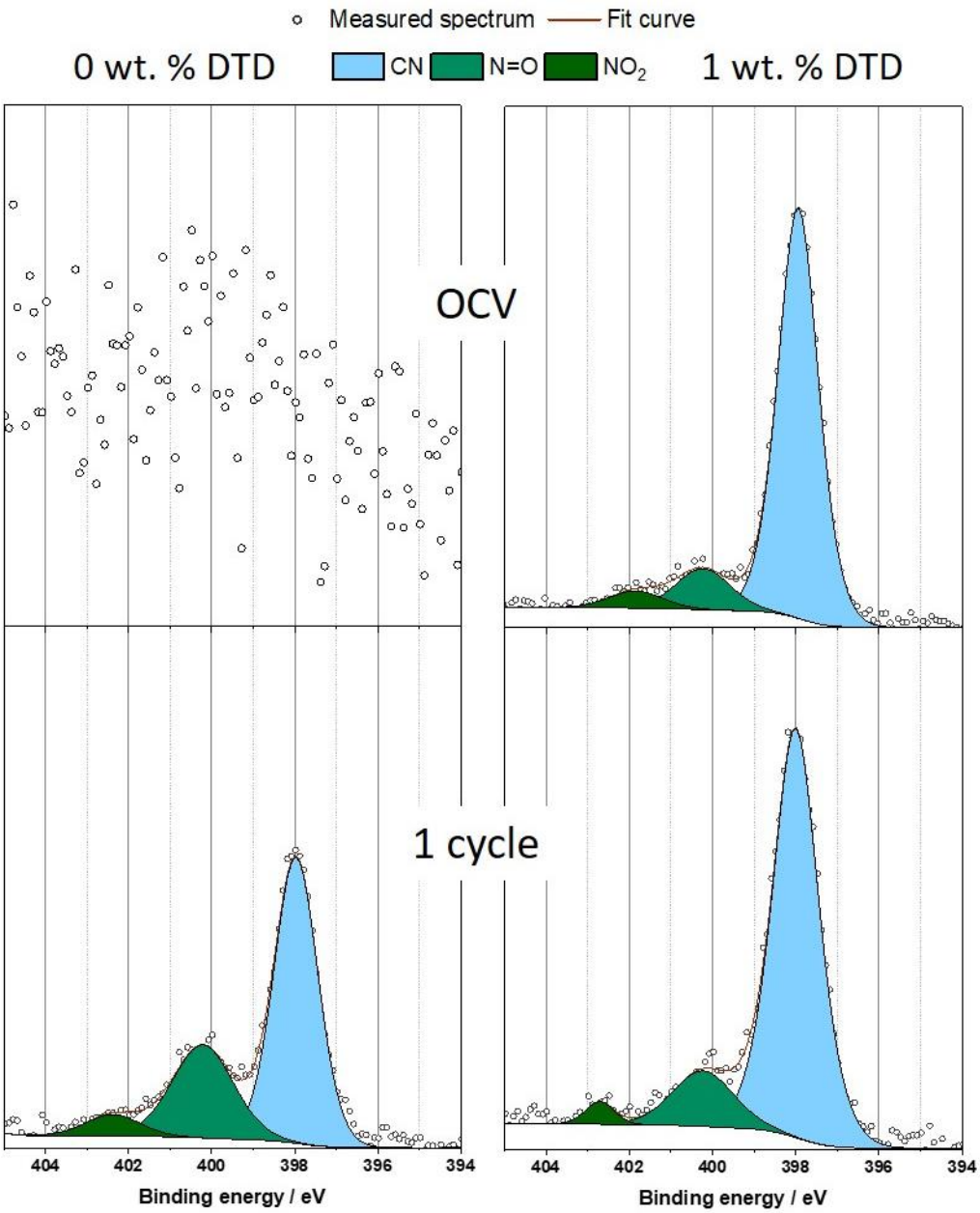

Figure 26. N1s spectra of half-cell KFF electrodes stored in electrolyte and after one charge and discharge in 750 mM KPF_6 EC:DEC without additive (left column) and 1 wt. % (right column)

A comparison of cycled spectra indicates that the additive also prevents oxidation of the KFF surface. The ratio of C≡N and C-N=O peaks in the N1s spectrum of the cathode cycled without the additive is 1:4. In the presence of DTD, the ratio increases to 1:5. The data suggest that KFF cycled in electrolyte without the additive undergoing oxidation during cycling, potentially due to a reaction with decarbonates or other products of electrolyte decomposition.

F1s spectra. As can be seen from all spectra of the half-cells, the electrolyte salt signal overlaps the PVdF signal. In the F1s spectra (**Figure 27**), the KPF_6 signal at 687.7 ± 0.1 eV (purple) is the most intense in the region across all spectra. The light blue belongs to the organic fluorinated compounds and

appears at 689.4 ± 0.2 eV. The KF (pink) signal is observed at 684.3 ± 0.1 eV in all samples, with the exception of the cycled DTD sample, where the peak is located at 682.9 eV.

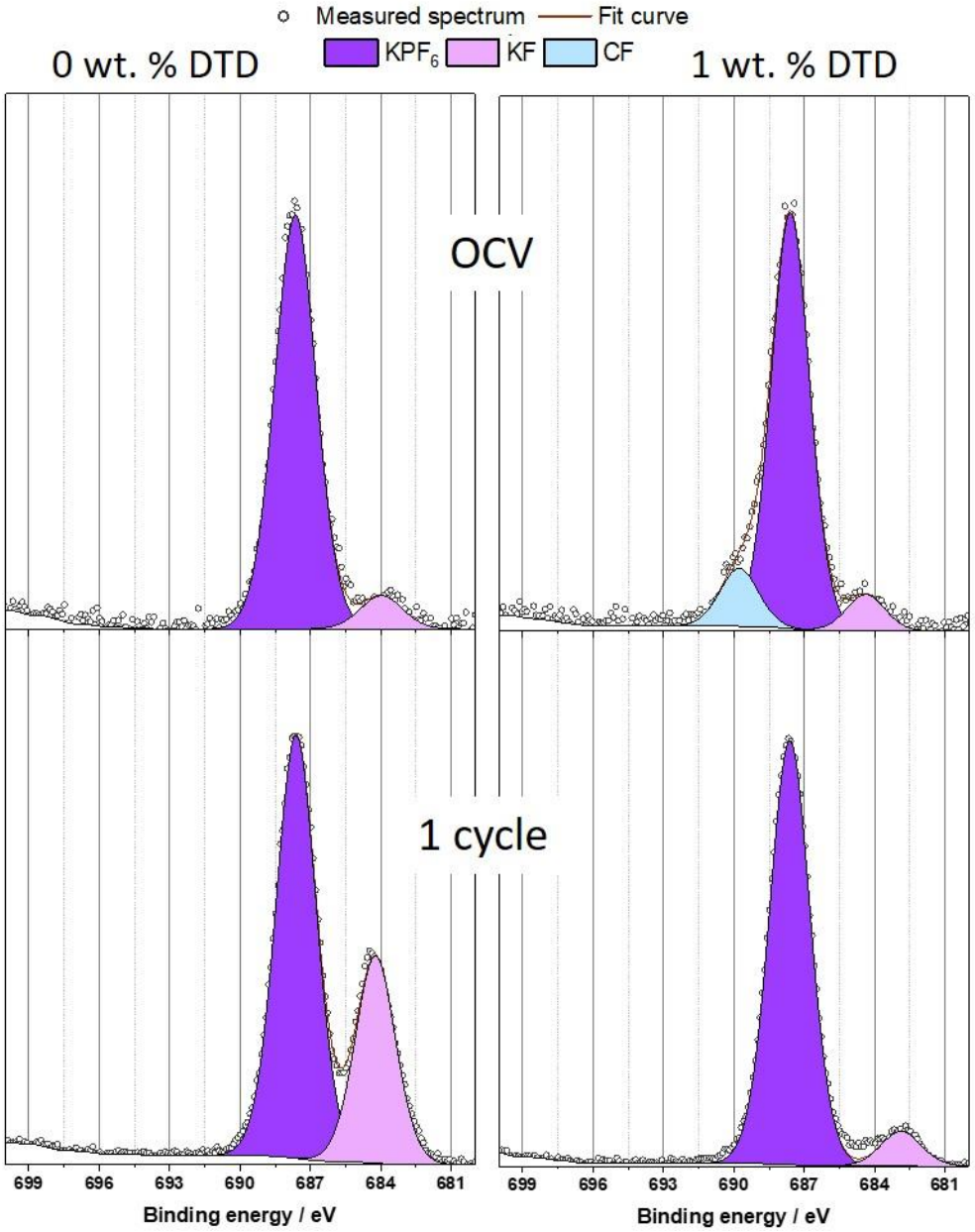

Figure 27. F1s spectra of half-cell KFF electrodes stored in electrolyte and after one charge and discharge in 750 mM KPF_6 EC:DEC without additive (left column) and 1 wt. % (right column)

The OCV F1s spectra indicate no significant distinction between the sample stored without the additive and with DTD. Both exhibit an intense salt peak and minor KF peak resulting from storage in the electrolyte. However, a significant distinction became evident afterward. When the sample was cycled in an electrolyte without the additive intensity of KF peak was increased, which was not evident in the case of cycling with 1 wt. % DTD. This also demonstrates how DTD prevents the formation of oxidising

products of salt decomposition on the KFF surface. The BE of KF at 684.3 ± 0.1 eV, which is 1 eV higher than the typical BE value, may be attributed to the influence of surface charging effects.

Effects of DTD at graphite surface

In light of the extensive existing literature on the half-cell SEI of graphite, this discussion will focus on the effects of DTD graphite surfaces. The impact of the additive on the anode surface is most evident in the C1s-K2p and F1s spectra. Consequently, the discussion will be limited to this regions for graphite half-cells. The spectra of the remaining regions and pristine powder and electrodes are presented in the appendix (**Figures A14-A19**).

C1s-K2p region. The C1s-K2p spectra of the graphite half-cell electrodes that were stored and cycled in electrolytes without and with 1 wt. % DTD are displayed in **Figure 28** below. The spectra show the bulk active material signal (sp^2-C, graphite; BE=283.3 ± 0.1 eV; light grey), saturated hydrocarbon species (sp^3-C, -CH-; BE=285.0 eV; dark grey), alkoxides (-CO-; BE=286.6 ± 0.1 eV; yellow), carboxylates -(C=O)OR; BE=288.2 ± 0.2 eV light yellow) and carbonates (K_2CO_3 if inorganic, or R_1O-(C=O)-OR_2; if organic in nature; BE=289.7 ± 0.2 eV; orange). The K2p signal is the prominent doublet peak at around 293.3 ± 0.2 eV ($2p_{3/2}$) also DTD samples exhibit additional potassium peak at 292.8 eV associated with charging effect caused by formation of passivation film.

OCV spectra. As can be observed in the spectra of the electrode stored in electrolyte (**Figure 28, top panels**), the passivation effect of DTD at the potassium surface resulted in a reduction in the intensity of the cross-talk reaction. This is evidenced by a comparison of the 1 wt. % DTD and 0 wt. % DTD spectra. The migration process of decomposition products from the CE to the WE (cross-talk reaction) is so intense that the bulk C-sp^2 signal exhibits the lowest peak intensity within the region. The presence of an intensive K2p peak, in addition to ethers, carboxylates and carbonates, also indicates that dense film was formed, as was previously reported in a related study[203]. As evidenced by the results of the self-discharge tests (**Figure 17**), DTD can assist in the mitigation of cross-talk reactions through the passivation of the potassium surface. This is demonstrated by the presence of a relatively intense C-sp^2 peak in the OCV DTD sample. It is important to note that the chemical passivation of K-CE by the additive does not entirely prevent cross-talk reactions. This is evidenced by the presence of the K2p signal. Furthermore, the film formed with DTD exhibits low conductivity, as indicated by the second K2p signal, caused by the charging effect. The presence of intensive -CH- and -CO- can be attributed to the products of DTD dimerisation and the reaction of the additive with the electrolyte solvent (**Figure 9**)**.** The rest of the carbon-oxygen signals (carboxylate and carbonates) can be related to the residuals of DTD and EC:DEC electrolyte. Nevertheless, the film formed in the 1 wt. % DTD OCV sample is thinner in comparison to that formed in the 0 wt. % DTD OCV sample. This is inferred from

the weaker K2p and the pronounced Csp^2 bulk signal observed in the former, in comparison to the latter.

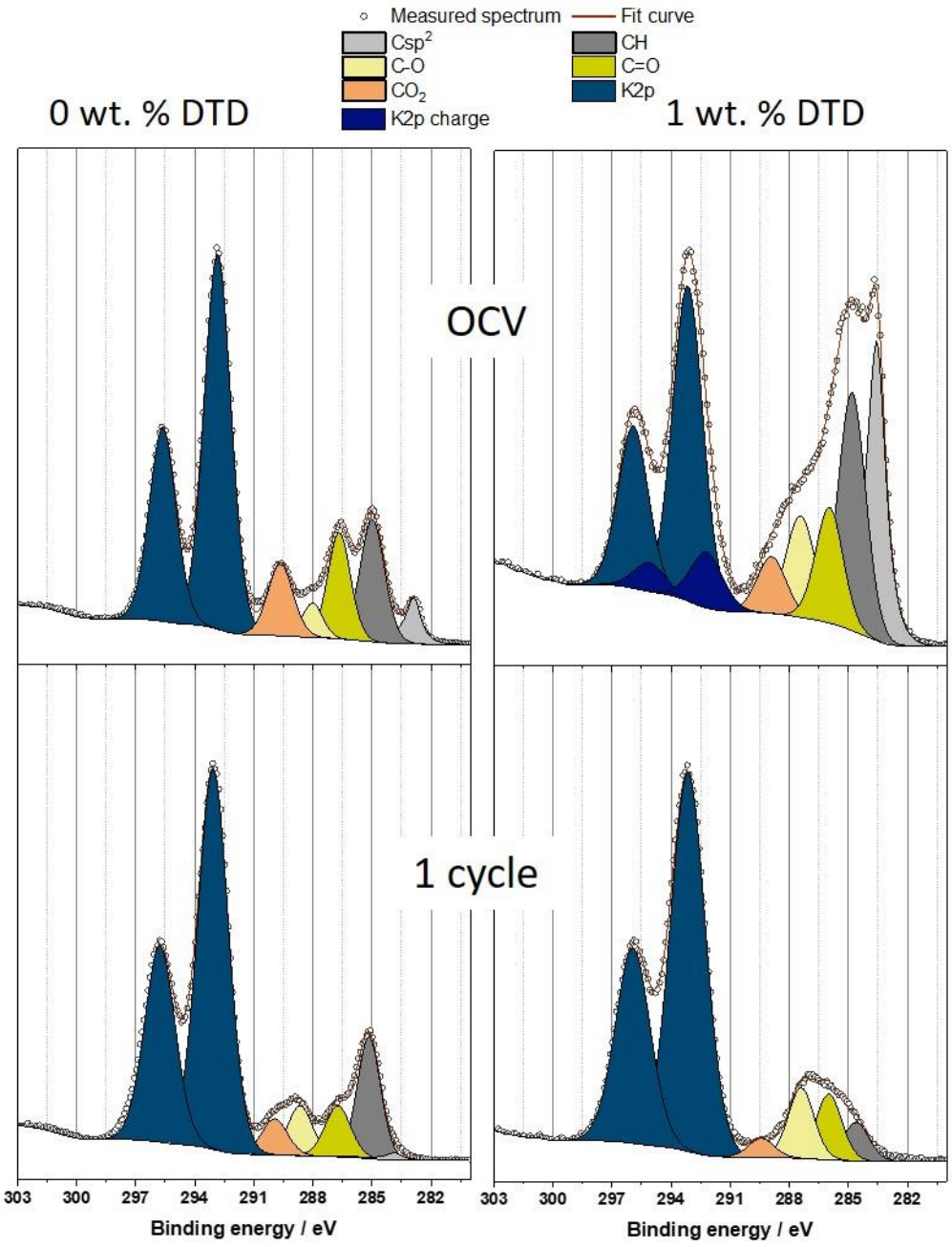

Figure 28. C1s−K 2p spectra of half-cell graphite electrodes stored in electrolyte and after one charge and discharge in 750 mM KPF_6 EC:DEC without additive (left column) and 1 wt. % (right column)

*Cycled samples***.** Negative effects of DTD at graphite observed in electrochemical test become visible with cycling. The spectra of samples that have been cycled without the additive demonstrate the typical SEI signal. In the C1s region, only the -CH-, C-O, C=O, and CO_2 signals are presented for cycled samples. At the first cycle of a sample cycled without an additive, the CH signal exhibits the greatest

intensity, while the carbon-oxygen peaks display a similar intensity, approximately half that of the CH signal.

F1s spectra. In the F1s spectra (**Figure 29**) the impact of DTD is most evident. The most intense peak in all spectra is the signal of KPF_6 (violet) at 687 ± 0.2 eV. KF (pink) is found at 683.3 ± 0.2 eV. In the case of cycled DTD, an additional peak associated with the charge effect is observed at 686.3 eV (dark pink). DTD prevents salt decomposition during storage in the electrolyte, as evidenced by the OCV spectra. The OCV 1 wt. % DTD spectrum does not exhibit a signal of KF. In contrast, after cycling, the passivation film at the graphite surface displays a markedly higher amount of KF than the spectrum of graphite cycled without an additive. Moreover, the film is more insulating in nature, which resulted in the emergence of a second peak of KPF_6, due to charging, a phenomenon previously observed in the literature[250,279].

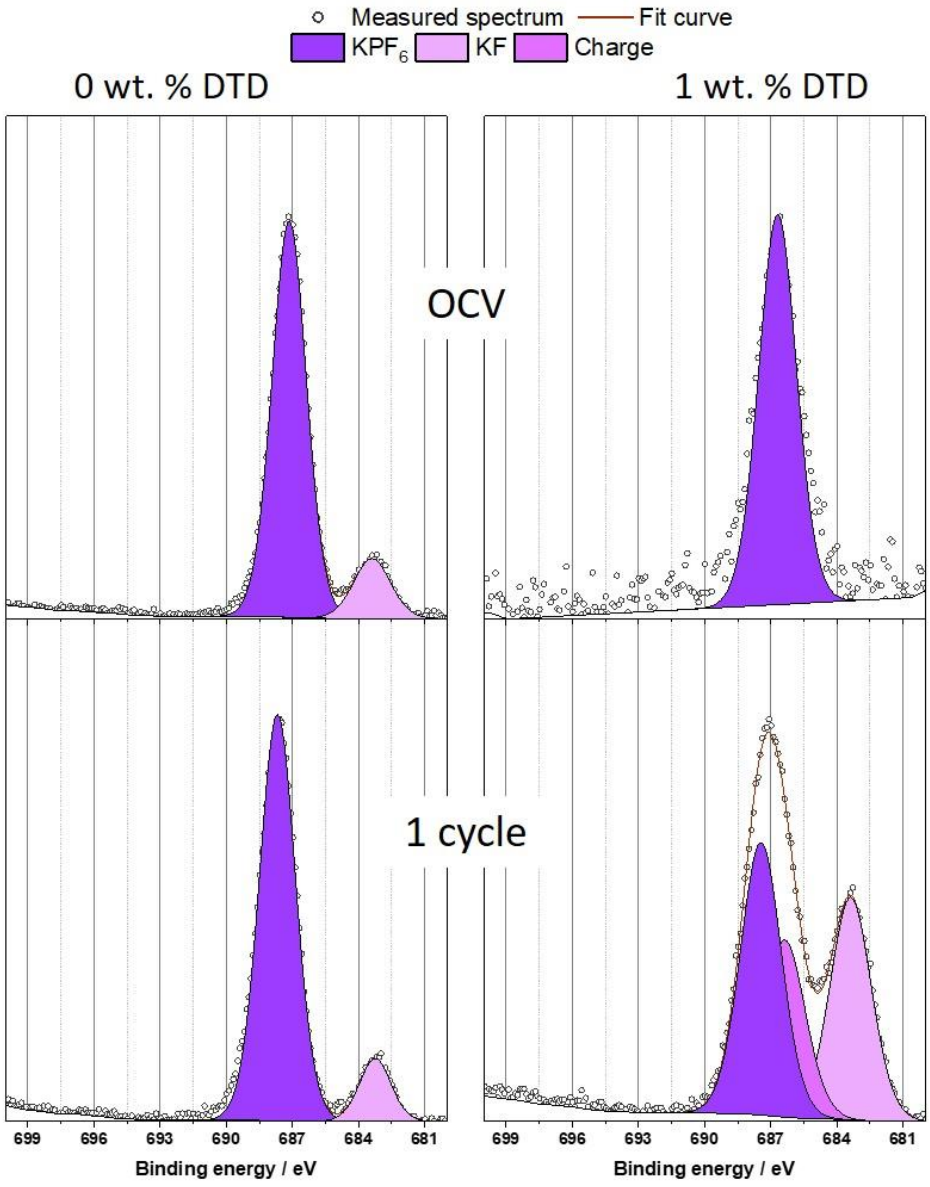

Figure 29 F1s spectra of half-cell graphite electrodes stored in electrolyte and after one charge and discharge in 750 mM KPF_6 EC:DEC without additive (left column) and 1 wt. % (right column)

Summary of subchapter: Effects of DTD at electrodes surfaces in half-cell configuration

The surface analysis of KFF and graphite electrodes supports the findings obtained from electrochemical analysis. The ability to passivate the anode surface is indicated by the presence of a thin CEI layer of KFF and a dense SEI of graphite electrodes stored in an electrolyte solution containing 1 wt. % DTD, as evidenced by the XPS spectra.

The XPS spectra of KFF and graphite stored in electrolyte suggest that the additive forms a passivation film on the K-metal surface, effectively preventing the precipitation of K-CE/electrolyte reaction products that are typically observed in samples stored in additive-free electrolyte. The positive impact of DTD on the cycling performance of KFF was further highlighted by XPS analysis. Cycling KFF in a half-cell with 1 wt. % DTD electrolyte successfully protects the cathode surface from oxidation. For additive free samples it was shown that the formation of decomposition products at the KFF surface during cycling was lower, in comparison to the results observed when the electrode was stored in electrolyte without the additive. The observed stabilisation can be attributed to the formation of a more stable SEI at the K-CE side during the cycling process, which effectively inhibits further decomposition.

However, the addition of DTD to the anode half-cell has resulted in the formation of a dense passivation film during cycling, which has led to the observed reduction in graphite capacity by two time, as evidenced by electrochemical testing. The passivation film formed by DTD is presumed to be more insulating, as evidenced by the emergence of charge-associated peaks. In conclusion, DTD interacts primarily with the potassium surface in the absence of current. However, under current, as demonstrated by electrochemical tests, DTD reacts with the anode side of the cell. To gain a more comprehensive understanding of the interaction between the DTD and the electrode surface, further investigations in a full cell will be presented in the subsequent chapter.

7.2.2 Effects of DTD at the full-cell electrode surface

This chapter presents a comparative analysis of electrode materials within full-cell configurations, with a particular focus on the impact of DTD on electrode surfaces. This investigation encompasses both cycled KFF and graphite electrodes, as well as electrodes stored in electrolyte, with the objective of elucidating the surface evolution of these materials under different conditions. Given the comparatively less intensive formation of the SEI and the CEI in full-cells in comparison to half-cells, XPS analysis was additionally conducted on full-cells after 10 cycles. The cells were stopped in their fully discharged state (deintercalated for graphite and fully potassinated (reduced) for the KFF cathode) prior to immediate electrode rinsing to remove any residual electrolyte salt. As in previous chapter, the results for the cathode and anode will be discussed in separate chapters in order to facilitate a more consistent discussion. Other regions are presented in Appendix (**Figures A20-A32**)

PES of full-cell KFF electrodes

C1s-K2p spectra. **Figure 30** presents the C1s/K2p spectra for both KFF electrodes stored under OCV conditions or cycled for 1 or 10 cycles in either a DTD-free or 1 wt. % DTD-containing electrolyte. The majority of the peaks identified in the spectra were also observed in the reference chapter. These included the bulk carbon black sp^2-C signal (grey) at 284.4 ± 0.1 eV, C≡N signal (light blue) at 285 eV, -CO-/-CN-/-CH-$_{PVdF}$; peak (yellow) at 286.6 ± 0.1 eV and PVDF -CF_2- peak (red) at 290.7 ± 0.2 eV. It can be observed that the bulk signal is accompanied by the presence of CEI signals, which comprise saturated hydrocarbon species (-CH-;dark grey) at 285.5 ± 0.1 eV, carboxylates (-(C=O)OR-; light yellow) at 288.5 ± 0.1 eV.

The K2p spectrum exhibits a splitting into two distinct signals. The lower-energy peak, located at 293.8 ±0.1 eV (blue), is attributed to KFF. As previously discussed, the BE distance between the C≡N and KFF K2p peaks was employed as an additional constraint during the fitting process. The peak distance between the K2$p_{3/2}$ and C≡N signals was fixed at 8.7 eV, resulting in the emergence of a second, higher-energy peak at 294.4 ± 0.2 eV (dark blue). This higher-energy peak correlates with a region that is consistent with the second peak observed in the PB spectrum, indicating an association with K^+ ions in the vicinity of Fe^{3+}. It is important to note that the K2p signal from KPF_6 was previously reported to in the same region[250]. Therefore, this signal is likely a combination of contributions from the salt as well as the partially discharged surface of the cathode.

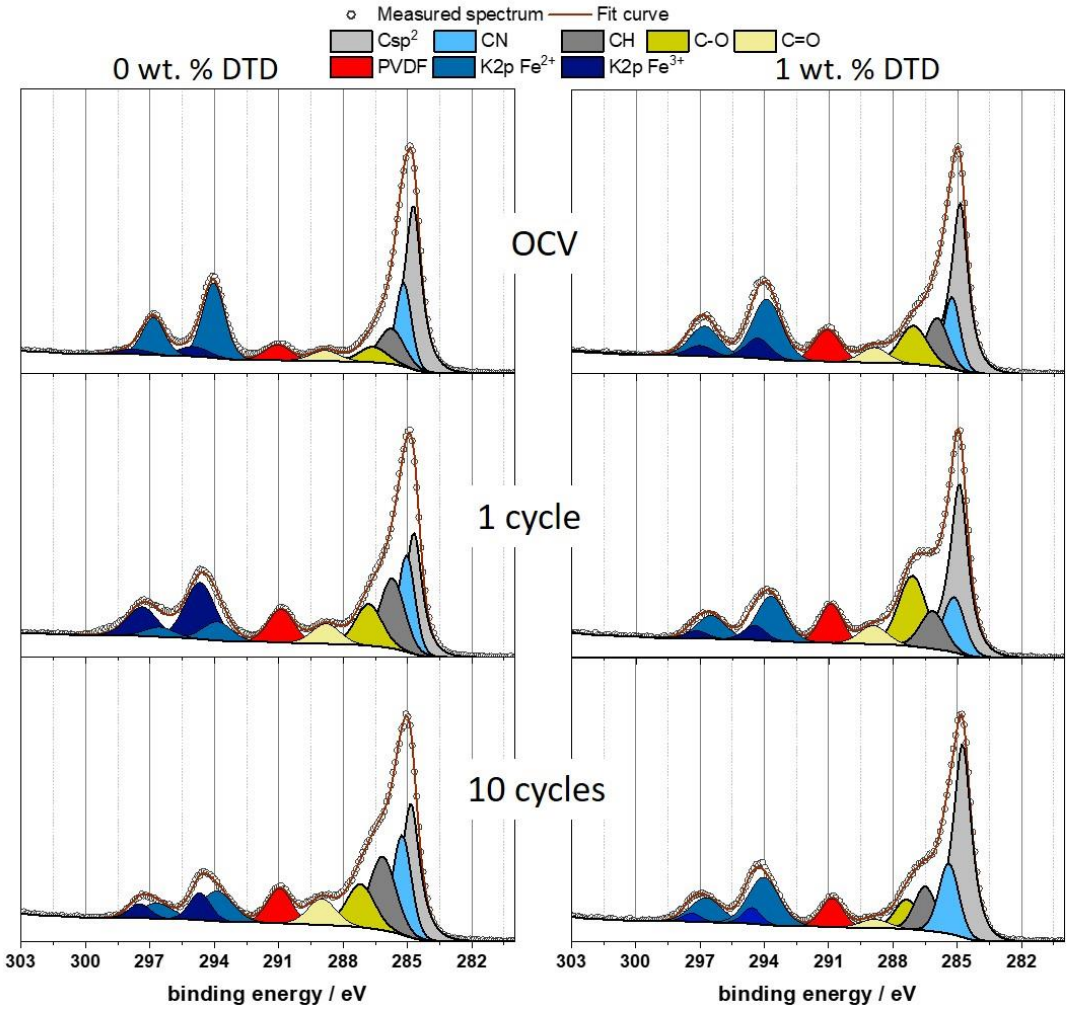

Figure 30. C1s−K 2p spectra of full-cell KFF electrodes stored in electrolyte, cycled 1 and 10 cycles in 750 mM KPF_6 EC:DEC without additive (left column) and 1 wt. % (right column)

OCV sample. The C1s spectra of KFF electrodes stored in the two electrolytes show only minor variations compared to the pristine electrode. The most notable change is the appearance of a more pronounced saturated -CH- peak. In the DTD-containing OCV sample, the -C-O-/-C-N- and -C=O peaks exhibit higher atomic percentages (**Appendix Table A1**). Another difference from the pristine electrode is the presence of a faint salt/PB signal alongside the main KFF K2p peak. Furthermore, a salt/PB signal is present in addition to the main KFF peak, indicating the presence of residual electrolyte traces on the electrode surface or partial self-discharge (depotassiation) during storage in the electrolyte.

Cycled samples. The spectra of the samples that were cycled without the additive exhibited a high degree of similarity between the first and 10th cycles. The intensity of the peaks associated with the electrolyte decomposition products, including carboxylates and -C-O/-C-N groups, has been increased in comparison to the OCV spectrum. The intensity of these peaks increases after the initial cycle and remains at a comparable level after the tenth cycle. The main distinction between the first and tenth cycles is observed in the K2p region. During the initial cycle, the intensity of the high BE K2p doublet

(dark blue) is significantly higher than that of the lower BE K2p doublet (blue), which is likely attributed to extensive CEI/SEI formation, resulting in increased electrolyte decomposition on the surface. By the tenth cycle, the ratio of the area of two signals approaches 1:1.2 (**Appendix Table A1**), indicating the dissolution of the initially formed products. A comparison of surface layers formed in a DTD-free and DTD-containing electrolyte mixture reveals a number of compositional differences. As in 0 wt. % DTD samples, the electrolyte decomposition products signals increased at the first cycle in 1 wt. % DTD spectrum. However, in contrast to the additive-free samples, the increase was more intense, particularly at the peak at 286.6 ± 0.2 eV. Furthermore, a notable difference was observed after 10 cycles. The relative intensity of the carbon-oxide peaks (yellow and dark yellow) exhibited a decrease in intensity after 10 cycles, in comparison to the first cycle. In contrast, no significant changes were identified in the K2p signal when compared to the OCV spectrum, as well as in the Csp^2 and C≡N signals.

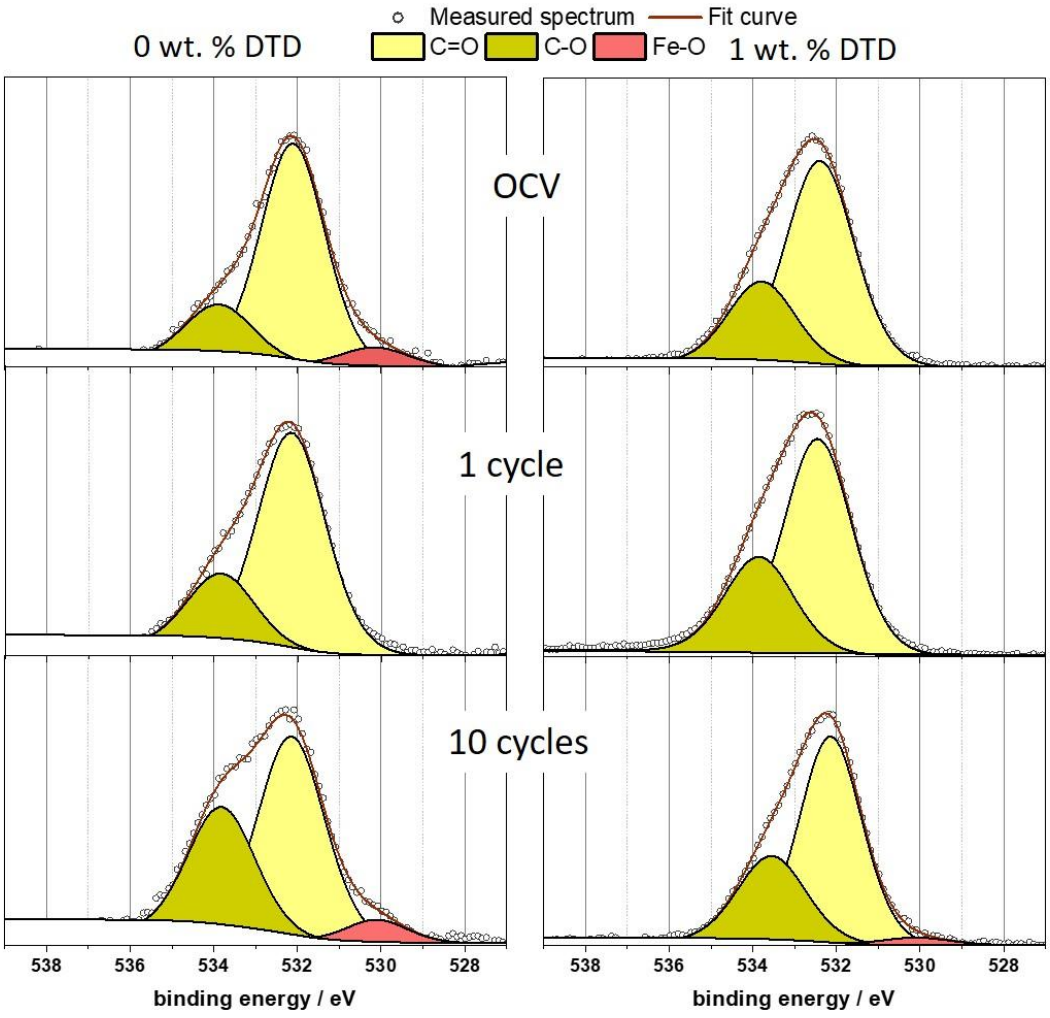

Figure 31. O1s spectra of full-cell KFF electrodes stored in electrolyte, cycled 1 and 10 cycles in 750 mM KPF_6 EC:DEC without additive (left column) and 1 wt. % (right column)

O1s spectra. **Figure 31** shows a comparison of O1s CEI spectra. All the spectra demonstrate two main intensive peaks at 532.3 ± 0.2 eV (C=O, light yellow) and 533.9 ± 0.2 eV (C-O, dark yellow). Some of samples have minor contribution of Fe-O at 530 ± 0.2 eV (red) The presence of the Fe-O peak is not associated with the cycling process and is observed in both powder and pristine electrodes (**Figure A4, A5**).

It was observed that in the 0 wt. % DTD O1s spectra, the relative intensity of the -C-O- is increasing with the number of cycles. A similar trend was also present in the carbon spectra (**Figure 30**). However, this pattern was not evident in the spectra of 1 wt. % DTD. Furthermore, the C-O/C=O ratio remained relatively consistent, despite the presence of a notable discrepancy in the C1s spectrum. The phenomenon can be attributed to a number of factors, including: 1) the overlap of the C=O and SO_4 signals[240,280] and 2) the peak observed in the C1s region (C-O) is also associated with the -CN- bond signal and CH signals of PVdF. Consequently, these signals contribute to the peak intensity, and thus there is no correlation between the C-O C1s and C-O O1s signals.

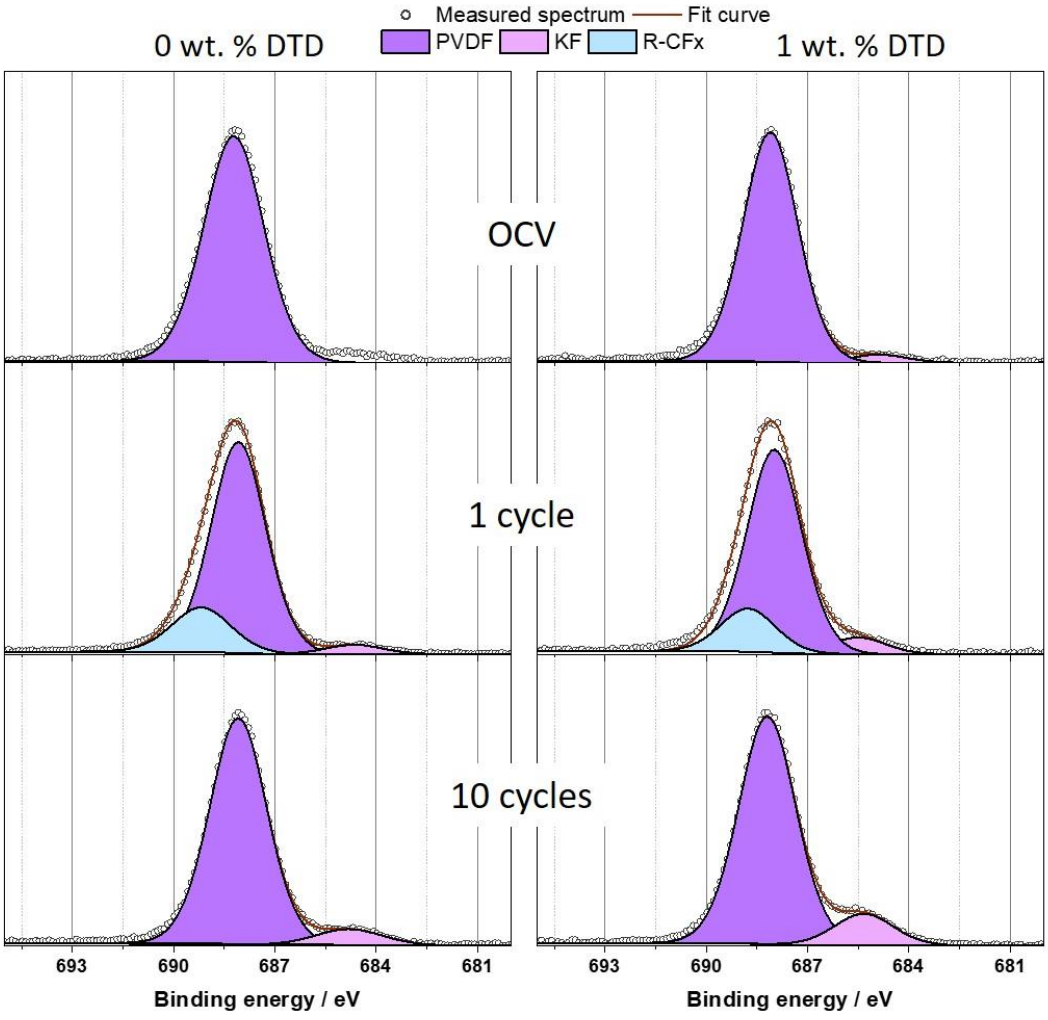

Figure 32. F1s spectra of full-cell KFF electrodes stored in electrolyte, cycled 1 and 10 cycles in 750 mM KPF_6 EC:DEC without additive (left column) and 1 wt. % (right column)

F1s spectra. In the F1s spectra (**Figure 32**) the most intense peak in all spectra is the signal of PVDF(-CF_2-) at 688.2 eV (purple). The light blue peak belongs to organic fluorinated compounds and appears at 689.4 ± 0.2 eV. Despite the expectation that the chemical shift energy of KF, a common SEI component, would be approximately 683.5 eV[203], KF (pink) was observed exhibited a value of 685.3 ± 0.1 eV.

It should be noted that the KPF_6 peak has a binding energy of approximately 687 eV[203], which results in an overlay with the intensive PVDF peak. Based on a few key parameters, including the absence or low intensity of the salt signal in the K2p region, and the low atomic percentage of the P2p signal (**Table A1**), it can be concluded that the KPF_6 salt peak is present in low quantities at the surface of the samples.

The BE of 685.3 ± 0.1 eV is typical for FeF_3 [281,282]. However, it is unlikely to be the case since Fe spectra do not contain signals of high-polarised iron. Therefore, it can be hypothesised that the nature of this peak is probably related to KF shifted due to charge effects or be another product of KPF_6 degradation. In a pristine electrode, the peak is absent (**Figure A5c**); however, it emerges following the electrode's immersion in electrolyte, so it has electrolyte salt related nature. Furthermore, the intensity of the peak increases with cycling, and the presence of the additive enhances this effect. After 10 cycles, the atomic percentage of this peak in the DTD spectrum is twice that observed in the 0 wt. % DTD spectrum. The observed phenomenon is notable for its contrast with the findings presented in the half-cell spectra (**Figure 27**), where the intensity of the KF signal was found to be significantly higher in the spectrum of electrode that was cycled without the additive.

Other core level spectra. The following section presents a concise overview of select additional features observed in other core-level spectra.

***N1s spectra*.** The C≡N bond (light blue, 398.0 eV) remains unaffected by storing in the electrolyte for all investigated cells, as demonstrated by the N1s spectra (**Figure 33a, b**). Following the normalisation to the maximum intensity and calibration, the spectra are almost identical, particularly in the case of the in 0 wt. % DTD samples. As a pristine electrode, all the samples exhibit a signal attributed to a nitrogen-oxygen bond, with a BE 400 eV (green) and nitrate trace signals at 402 eV (dark blue). The most striking difference in all the spectra the signal of -CN- in the samples that cycled in 1 wt. % DTD electrolyte. This phenomenon was also observed in the C1s spectrum (**Figure 30**), which highlight the connection of these peaks. However, in the tenth cycle, the intensity of the C-N=O peak decreased to a ratio that was even slightly lower than that of the C≡N peak in the other spectra. In general, it can be concluded that the intensity of this peak is not related to the cycling process.

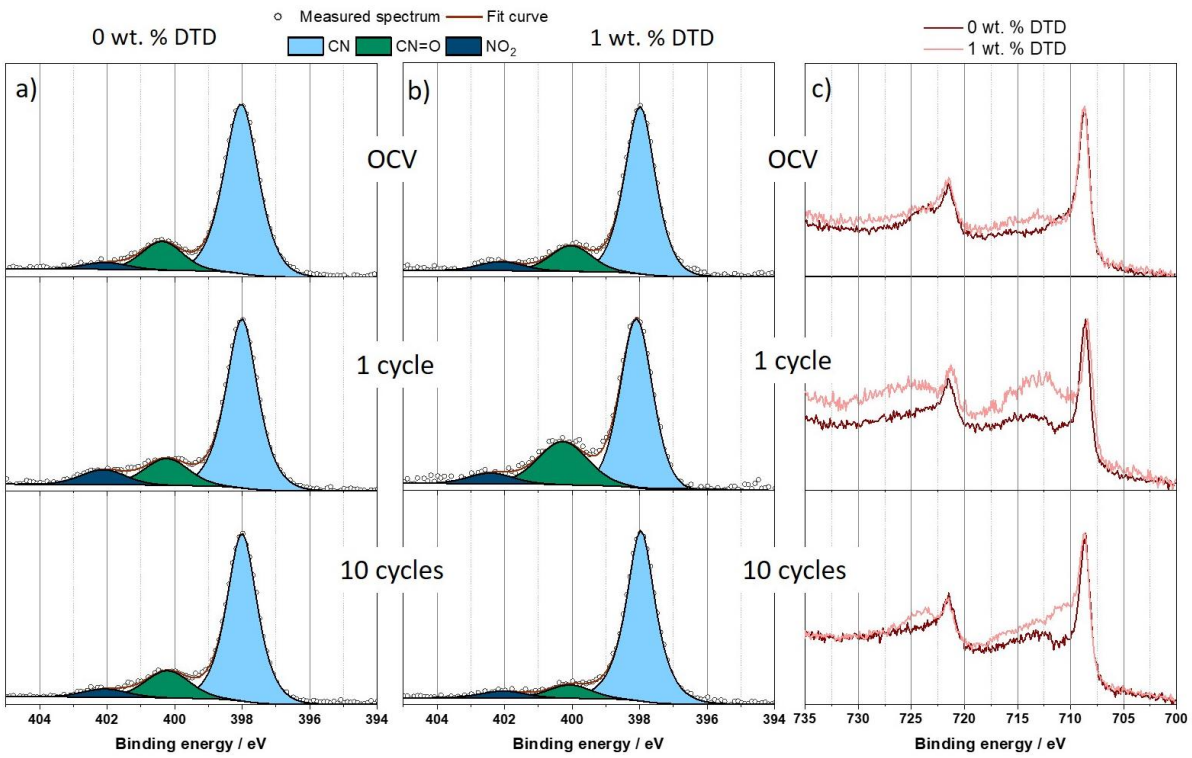

Figure 33 N1s (a and b) and c) Fe2p spectra of KFF full-cell electrodes stored in electrolyte, cycled 1 and 10 cycles in 750 mM KPF_6 EC:DEC with (for N1s b), dark red for iron) and without 1 wt. % DTD (for N1s a), light red for iron)

Fe2p A comparative analysis of Fe2p spectra (**Figure 33c**) reveals significant distinctions between WA and DTD samples. All of the spectra demonstrate $Fe2p_{3/2}$ main peak at 708.6 ± 0.2 eV associated with the Fe^{2+}-$(CN)_6$ bond. Region at 710 eV is typical for Fe^{3+}-$(CN)_6$ bond. The corresponding $Fe2p_{1/2}$ peaks are located 12.8 eV above of $Fe2p_{3/2}$ peaks. The aforementioned signal at 710 eV is only presented in the cycled samples and that its intensity increases with the number of cycles, with a more intensity observed in the DTD samples. In cycled DTD samples in the region 712-717 eV samples cycled with the additive have numerous of signals. In consideration of the reviewed spectra, it can be proposed that the observed peaks may be ascribed to Fe-O. It should be noted that signals of satellites may also be presented in the region.

A comparison of surface layers formed in electrolyte mixtures with and without DTD has revealed a number of compositional differences. In samples cycled in the absent of 1 wt. % DTD, the signals resulting from electrolyte decomposition products exhibited an increase during the initial cycle. However, in samples containing the additive, this increase was more pronounced, particularly at the peak at 286.6 ± 0.2 eV. Additionally, there was a significant change in the surface during cycling, with the relative intensity of the carbon-oxide peaks being less intense than in the first cycle. Conversely, no significant changes were observed in the K2p spectra when compared to the OCV spectrum.

Graphite full-cells PES

The C1s-K2p spectra. The C1s-K2p spectra of the graphite electrodes that were stored and cycled in electrolytes without and with 1 wt. % DTD are shown in **Figure 34** below. The spectra demonstrate the presence of a bulk active material signal (sp^2-C, graphite; BE=283.3 ± 0.1 eV; light grey) saturated hydrocarbon species (sp^3-C, -CH-; BE=285.0 eV; dark grey), ethers (-CO-; BE=286.6 ± 0.1 eV; yellow), carboxylates -(C=O)OR; BE=288.2 ± 0.2 eV light yellow) and carbonates (K_2CO_3 if inorganic, or R_1O-(C=O)-OR_2; if organic in nature; BE=289.7 ± 0.2 eV; orange). The K2p signal is observed to be a prominent doublet peak, occurring at approximately 293.3 ± 0 .2 eV ($2p_{3/2}$).

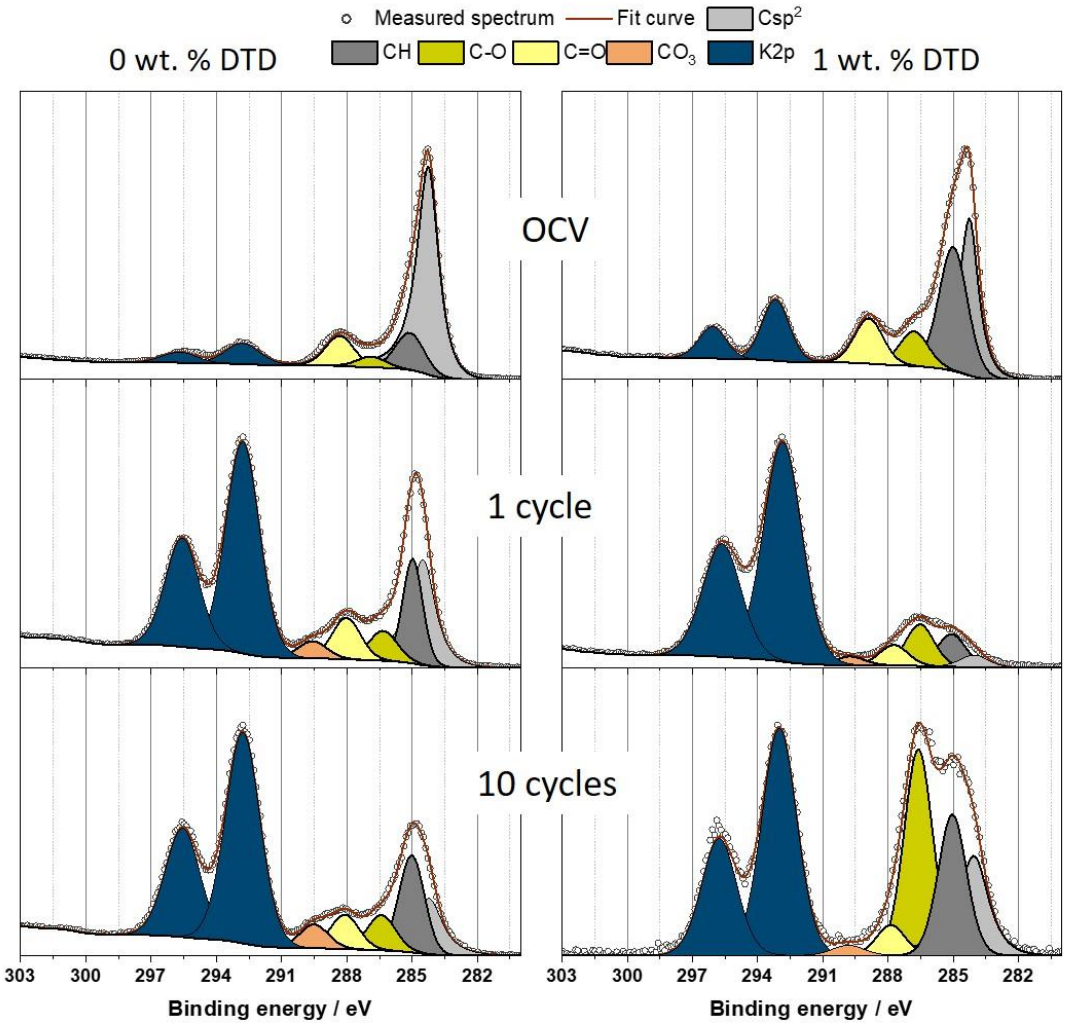

Figure 34 C1s−K 2p spectra of full-cell graphite electrodes stored in electrolyte, cycled 1 and 10 cycles in 750 mM KPF_6 EC:DEC without additive (left column) and 1 wt. % (right column)

Notable differences can be observed between the 0 and 1 wt. % DTD OCV samples. The OCV 0 wt. % DTD sample closely resemble the pristine electrode (**Figure A15a**), with the exception of the presence of a weak potassium signal ($Csp^2/K2p_{3/2}$ Atomic % ratio ~20, **Appendix Table A2**). In contrast, the K2p peak intensity in the OCV DTD sample is about three times higher than in the additive-free sample (C-

$sp^2/K2p_{3/2}$ Atomic % ratio ~7 in 1 wt. % DTD and ratio ~22 in 0 wt. % DTD, **Appendix Table A2**). Additionally, the Atomic concentration of CH, C-O, C=O peaks higher in C1s OCV 1 wt. % DTD spectrum. This is a particularly intriguing finding, as it indicates the formation of surface deposits even in the absence of cycling, without the involvement of electrochemically induced reactions. Given the low sulfur concentration (~0.3 atomic %). on the OCV 1 wt. % DTD sample surface, this is an unexpected result. In general, the C1s OCV DTD spectrum is found to be highly similar to that observed in the C1s OCV DTD half-cell spectrum (**Figure 28**).

The distinction between the SEI layers of graphite in electrolytes with and without DTD is more evident in the spectra obtained after the first cycle. In the additive-free 1 cycle C1s spectrum, the intensity of the -CH- peak was observed to be double that of the OCV spectrum. The remaining typical SEI signals are also observed. Within the carbon-oxygen related signals, the carboxylates and (poly)ester have the highest intensity (approximately half that of the -CH- signal). The addition of DTD results in a SEI that is thicker than the XPS probing depth of the spectrometer. This is evident from the low intensity of the carbon signals in comparison to the intense K2p signals (total atomic percentage of all carbon signal is comparable to K2p contribution) in the 1 cycle DTD spectrum, which is similar to that observed in half-cell spectra. Furthermore, the presence of the additive results in the appearance of an intense C-O peak, which suggests the presence of a significant amount of alcohols or (poly)ether-type compounds. Carboxylates and carbonates are presented, although in contrast to the 1 cycle 0 wt. % DTD spectrum, they exhibit a considerably lower relative intensity than the C-O signal with respect to the K2p signal. The 1-cycle DTD spectrum displays a greater degree of similarity to the 1 wt. % DTD half-cell spectrum (**Figure 28**) than to the signal produced by the 0 wt. % DTD full-cell.

Notable differences between the 0 wt. % and 1 wt. % DTD are also evident in the 10-cycle spectra. In the context of additive-free cell analysis, the C1s region demonstrates the highest atomic percentage for the -CH- signal. At the the percentage of the graphite bulk is decreased in comparison with the 1 cycle spectrum (19 % at the first cycle and 11 % at the tenth). This indicates an increase in the thickness of the SEI. In comparison to the initial cycle, the concentration of the -CO- and carbonate signals is also increased. The C-sp^2 signal is increased with increasing cycle number in 1 wt. % DTD spectra, which would suggest a decrease in the SEI layer thickness. Concurrently, the intensities of the -CH- and C-O peaks increased in parallel with the reduction in K2p atomic concentration, which lends further evidence to the dissolution of K-salt species in the SEI layer. It is noteworthy that the atomic concentration of the -(C=O)OR signal is observed to decrease in the OCV-1 cycle-10 cycles line in both electrolytes (**Appendix Table A2**).

O1s spectra graphite. The O1s spectra of graphite from full-cell (**Figure 35**) consist of three main peaks an ether peak (-CO-, dark yellow) at 533.6 ± 0.2 eV., an oxygen from (poly)ester or alkyl carbonates (dark yellow) at approximately 532.5 eV and carbonate/carboxylate/DTD peak at 531 ± 0.2 eV. In the

case of the WA spectra, the Na KLL Auger line was observed at around 535 eV (pink). The introduction of Na-ions into the system is attributed to the CMC-Na binder of the graphite electrodes. Additionally, the samples cycled with DTD exhibited a peak with an unusually low BE for graphite spectra. The peak observed at 529.3 eV (red) can be attributed to the KOH.

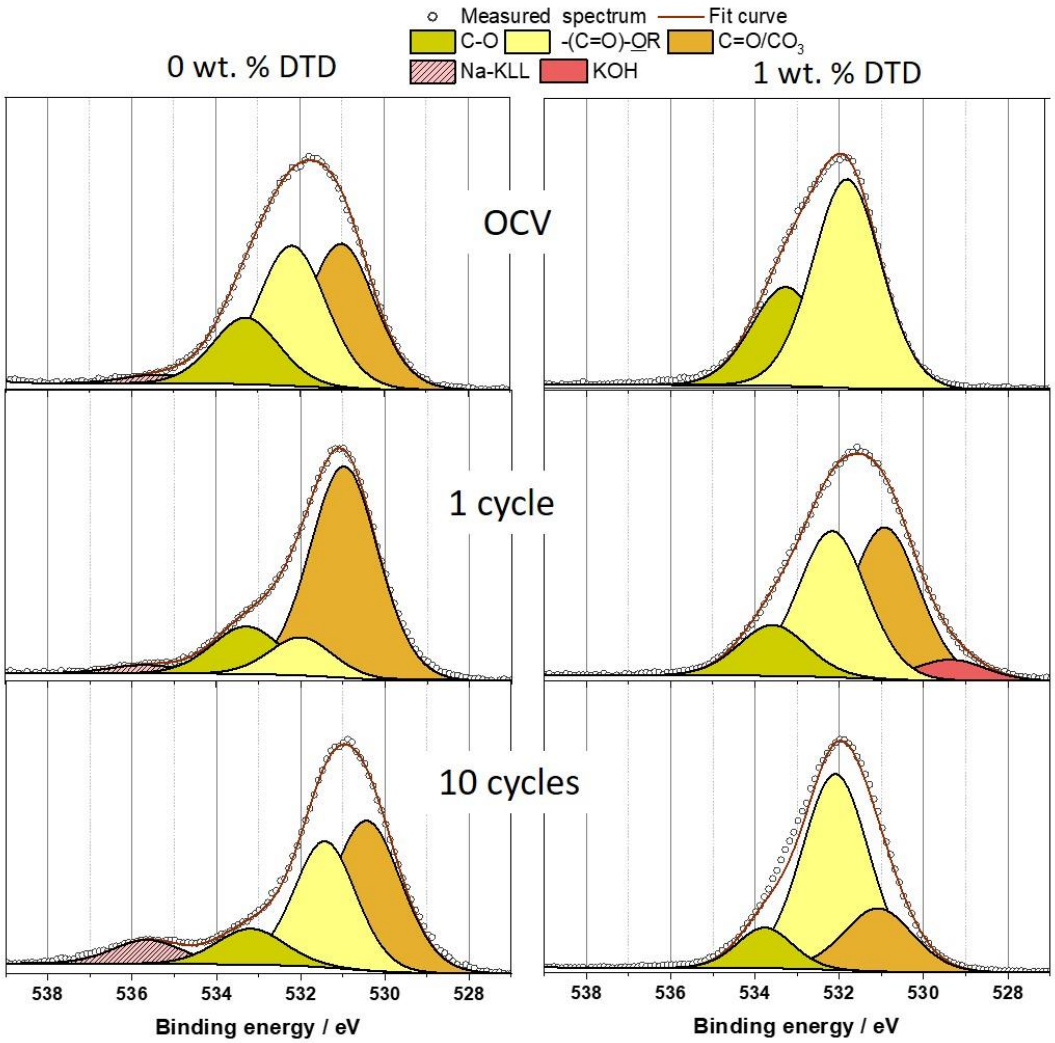

Figure 35. O1s spectra of full-cell graphite electrodes stored in electrolyte, cycled 1 and 10 cycles in 750 mM KPF_6 EC:DEC without additive (left column) and 1 wt. % (right column)

With the exception of the OCV DTD spectrum, all the remaining spectra exhibit all three base signals: ether, alkyl carbonates, and carboxyl/carbonates. In the case of OCV, the signals originating from the ester and alkyl carbonates are attributed to oxygen groups on the surface of graphite. These signals are also present in the pristine electrode spectrum (**Figure A15c**), exhibiting an identical intensity ratio (C-O/O(C=O) intensity ratio ~1/3). The carbonate signal is associated with the residual electrolyte at the surface of the electrode.

The impact of DTD becomes evident in the spectra of electrodes that were cycled. In the 1-cycle 0 wt. % DTD spectrum, the carbonate/carboxyl peak is the most intense, exceeding the carbonyl and C-O

signals by a factor of five. In contrast, the O1 spectrum of the 1-cycle DTD samples features two dominant signals, with the alkyl carbonate peak having an almost equal concentration (**Table A2**) to the carbonate peak. The peak at 531 eV remains the most prominent in the 0 wt. % DTD spectrum after 10 cycles, but the signal for (poly)ester or alkyl carbonate groups increases significantly, with an approximate 1:4 ratio compared to the first cycle. In the 10-cycle DTD sample, the alkyl carbonate group signal is the most intense. Its contribution is three times that of the C-O and CO_3/C=O groups. It is important to note that the DTD signal is also present in the same region, and therefore contributes to the high intensity of this peak in the spectra of samples that have been cycled with the additive.

F1s spectra graphite. In the F1s spectra (**Figure 36**) the most intense peak in all spectra is the signal of KPF_6 (violet) at 687.0 ± 0.2 eV. KF (pink) is found at 683.3 ± 0.2 eV for most of the samples, except for the 10 cycles DTD sample, where the peak is observed at 684.3 eV.

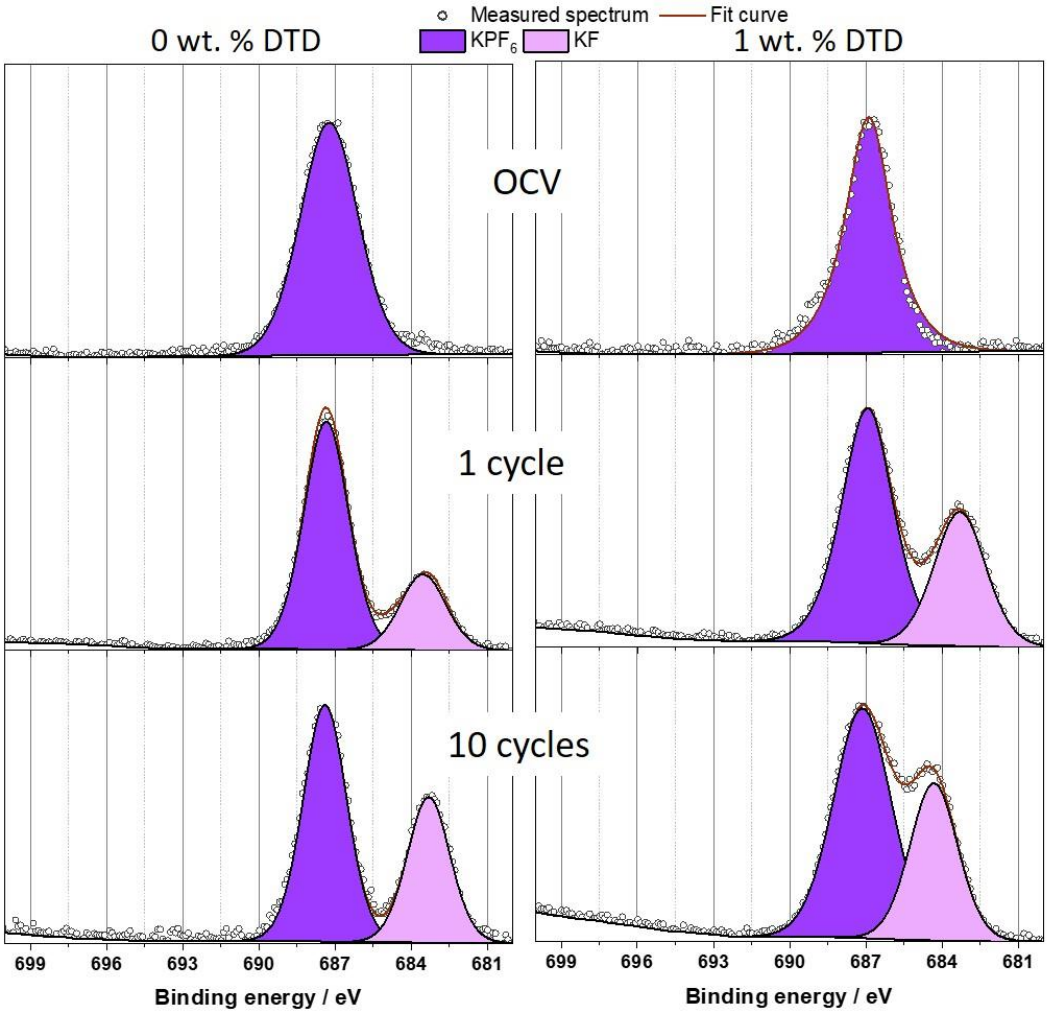

Figure 36. O1s spectra of full-cell graphite electrodes stored in electrolyte, cycled 1 and 10 cycles in 750 mM KPF_6 EC:DEC without additive (left column) and 1 wt. % (right column)

The sole peak observed in electrolyte-stored samples was that of the salt. The presence of an additive during cycling results in a higher concentration of the electrolyte salt decomposition products in the SEI. In the spectrum of one-cycled graphite without DTD, the ratio between KPF_6 and KF peaks is 1:3. The addition of the additive results in a ratio of 1:2. The ratio in the additive-free sample increased to 2:1.2 after 10 cycles, whereas in the sample cycled in 1 wt. % DTD electrolyte, it increased to 2:1.6. However, it is important to note that KF was more prominent in SEI of cycled samples with DTD. It is also a matter of interest to note that the KF signal has been shifted in a 10-cycle cycled DTD spectrum. The BE is 1 eV higher than in other spectra. Although the precise cause of this phenomenon can be identified with a high degree of certainty, the observed increase in relative shifts can be attributed to an increase in differential charging. This can be attributed to the insulating nature of DTD, KPF_6 and KF deposits in the SEI, which contributes to differential charging effects[279].

7.2.3 Conclusion of the subchapter: impact of DTD at full-cell electrode surfaces

The degradation products formed at the surface graphite in the presence of DTD look similar in both half and full-cell samples. However, in the presence of potassium metal, DTD reacts more intensively, forming a thick passivation film at the K-CE or graphite anode. The film remains present in a full-cell, but after 10 cycles, its thickness decreased (the Csp^2 signal atomic percentage grew from 2 % at the first cycle to 6 % at the 10th). The bulk carbon signal is observed both in the DTD-containing and the additive-free samples in cycle-aged cells (10 cycles). Additionally, the SEI formed with DTD shows a lower concentration of inorganic salt decomposition products after 10 cycles. The surface of the DTD samples displayed a higher intensity of signals from C-O in the C1s and O1s spectra, which could be interpreted as evidence of the formation of oligomeric degradation products of DTD with the electrolyte solvents EC and DEC.

The differences in SEI of cycled graphite in electrolyte with and without DTD suggest that in the latter case, despite the formation of SEI at the first cycle, the electrolyte is still decomposing. This is evidenced by the thicker SEI at the 10th cycle compared to the first. This results in notable amount of trapped inorganic products in the surface layer. Evidently, the intensity of signals associated with carbonate has a major contribution in the O1s spectra after 1 and 10 cycles. After 10 cycles, samples cycled with the additive showed a significantly smaller carbonate signal compared to samples without the additive. The high intensity of C-O peaks indicates that the interphase still consists mainly of DTD polymerization products rather than electrolyte decomposition products as in the additive-free sample. Simultaneously, DTD has a positive effect on the KFF surface. In full-cells, the level of electrolyte decomposition is lower, resulting in less distinctness compared to the half-cell. After 10 cycles, the cathode cycled in electrolyte containing the additive showed a lower level of oxidation

products on the surface. The Fe2p spectra of DTD exhibit fewer signals of iron oxidation products associated with the oxidation of iron cyanate groups. In the C1 spectrum, the DTD samples show weaker signals related to C=O or oxidized cyanides (C-N=O).

In summary, during the first cycle, DTD forms a dense film on the anode which dissolves to a significant extent by the 10th cycle. It results in denser SEI at 1st cycle compared to 0 wt. % DTD, but due to the dissolution of DTD SEI and the continued formation of 0 wt. % DTD SEI, at 10th cycle. DTD-derived SEI have less thickness than those formed without the additive. The SEI formed in the electrolyte containing DTD is of a more organic nature, most likely formed from the products of oligomeric degradation of DTD and reaction between the additive and electrolyte solvents. Due to the continuous consumption of charge carriers during the formation SEI in the 0 wt. % DTD cell resulted in a constant reduction in discharge capacity (**Figure A33a, c**). In contrast, the 1 wt. % DTD cell exhibited a lower initial capacity, followed by an increase in discharge capacity after four cycles, due to the dissolution of the SEI (**Figure A33b, d**). Neither behaviour is preferable, but the results show how actively interphaces in KIB are changing. Although the expected improvements were not fully achieved, this work provided valuable insights into the KFF CEI that can benefit future research efforts. In addition, the study demonstrated how DTD forms a dense film on the anode and highlighted the effects of sulphur-containing additives. These findings are particularly useful in understanding the behaviour of sulphur additives and can guide further investigations when using similar additives in future studies.

8 Conclusion and Outlook

A variety of analytical techniques are required to provide a comprehensive analysis of the reactions occurring at the electrode-electrolyte interphases in potassium-ion batteries. In this thesis two complementary approaches are employed: electrochemical analysis to study the dominant electrode processes and X-ray photoelectron spectroscopy (XPS) for detailed surface information. The primary objectives were firstly to develop a reliable reference electrode for 3-electrode measurements for investigating the impact of K-metal as counter or reference electrode on parasitic electrolyte degradation processes, and to provide a detailed analysis of the effect of the electrolyte additive DTD on the electrochemistry in both half and full-cells. Secondly, the resulting surface layers at the negative and positive electrodes were characterised in dependence of the electrolyte composition. In this context, a new XPS fitting model was developed for the Prussian Blue Analogue $K_2Fe[Fe(CN)_6]$ (KFF) on the basis of KFF at its different charging states and its precursor compounds.

The use of potassium metal as a reference electrode in research is unreliable due to its high reactivity, which presents significant challenges for accurately studying electrochemical processes, such as electrolyte degradation and electrode performance. Although a metal potential can be stable, the reactions between the reactive surface and the electrolyte result in the formation of dicarbonates, which impede the cathode from reaching the fully charged stage. These products react with the cathode, causing additional side reactions and self-discharge, particularly at open circuit voltage conditions. The use of passivation agents, such as the electrolyte additive DTD, has been shown to prevent the formation of dicarbonates, thereby preventing crosstalk and self-discharge. This ability has prompted a more detailed investigation of the behaviour of DTD. The electrochemical impact of the electrolyte additive DTD was investigated using AgCl-RE at both half and full-cells. The examination of reference electrodes revealed that a three-electrode configuration with an AgCl-RE offers the RE that is not influenced by the cell chemistry. This enables its utilisation in any electrolyte or configuration (half or full-cell). Despite the limitations of cell design, including the lack of constant pressure between the RE and separator, it offers enhanced reliability compared to REs employed in previous studies. In the context of KIB, this was one of the first analyses in a three-electrode cell that did not employ a potassium metal reference electrode. The utilisation of AgCl-RE enables the observation of effects and reactions that are not observable in a two-electrode configuration. These include an increase in the polarisation of the counter electrode in a half-cell and the possibility of observing intercalation processes on the graphite side in a full-cell.

Electrochemical characterisation was complimented by XPS analysis of KFF and graphite electrodes in full and half-cell setups with electrolyte with and without DTD. The XPS spectrum of KFF electrodes was validated and described in detail. This included the compilation of a reference database for KFF,

including reference peak positions and assignments for different electrode states (e.g., precursors, powders, and coated electrodes). In this thesis, it is for the first time demonstrated that the oxidation state of iron has a direct impact on the binding energy of the potassium K2p signal. In contrast, it was shown that cyanide-related peaks in the N1s and C1s regions remain unaffected by charge state and can thus be employed for calibration. The observations presented herewith can be utilised as a valuable supplementary technique in the analysis of PBA surfaces, given that the majority of existing research has concentrated on the complex iron spectra.

The combination of surface and electrochemical analysis demonstrated that the decomposition of the electrolyte at high voltages in KIB is significantly influenced by the presence of K-metal. In the absence of this latter component, the instability and low cycling performance observed can be attributed to the instability of the SEI. Unfortunately, DTD that is capable of mitigating electrolyte decomposition in KFF/half-cell and enhancing the cycling performance of the LIB full-cell, has a negative impact on KFF/graphite cells. This can be explained by the formation of a dense and unstable SEI resulting from oligomerisation/reaction with carbonates. This interphase hinders K^+ intercalation and can even cause plating of potassium at the graphite surface. Furthermore, the unstable interphase is a principal cause of the reduced columbic efficiency of full cells cycled with 1 wt.% DTD, which is even lower than that of additive-free cells.

Nevertheless, this thesis offers valuable insights into the electrochemical decomposition of carbonate electrolytes, thereby establishing a foundation for future research to develop methods, approaches and a database exclusively for KIB-specific issues and features. The results presented herein represent an improvement over previous studies in that they offer a versatile three-electrode setup, which allows for detailed investigation of the battery system and observation of electrolyte decomposition reactions or additive impact at both electrodes without interference of potassium metal. Furthermore, future XPS analyses of PBA would be enhanced by the incorporation of observations presented in the thesis, allowing for a more complete understanding of the processes occurring at the cathode surface.

In the future, the utilisation of a dependable reference electrode and an understanding of KIB interphaces and processes will enable the development of an electrolyte formulation or/and an additive combination that achieves robust interphase. That interphase must be stable over the cycling process and provide efficient K^+ ion permeability. One of the main ways to achieve this is through the investigation of additives. This is a key challenge of KIB for the moment. Achieving this will permit the overcoming of the principal issues associated with the low coulombic efficiency of KIB, enabling the realisation of LIB-level performance at least in this pivotal parameter for the battery. This will pave the way for industrial production and the establishment of a presence in the battery market.

Bibliography

[1] N. Yabuuchi, K. Kubota, M. Dahbi, S. Komaba, Research Development on Sodium-Ion Batteries, Chem. Rev. 114 (2014) 11636–11682. https://doi.org/10.1021/cr500192f.

[2] D. Aurbach, Z. Lu, A. Schechter, Y. Gofer, H. Gizbar, R. Turgeman, Y. Cohen, M. Moshkovich, E. Levi, Prototype systems for rechargeable magnesium batteries, Nature 407 (2000) 724–727. https://doi.org/10.1038/35037553.

[3] T. Hosaka, K. Kubota, A.S. Hameed, S. Komaba, Research Development on K-Ion Batteries, Chem. Rev. 120 (2020) 6358–6466. https://doi.org/10.1021/acs.chemrev.9b00463.

[4] W. Zhang, J. Yin, W. Wang, Z. Bayhan, H.N. Alshareef, Status of rechargeable potassium batteries, Nano Energy 83 (2021) 105792. https://doi.org/10.1016/j.nanoen.2021.105792.

[5] H. Haynes, W.M. W.M., CRC Handbook of Chemistry and Physics, 97th ed., CRC Press, 2016. https://doi.org/10.1201/9781315380476.

[6] S. Komaba, T. Hasegawa, M. Dahbi, K. Kubota, Potassium intercalation into graphite to realize high-voltage/high-power potassium-ion batteries and potassium-ion capacitors, Electrochem. Commun. 60 (2015) 172–175. https://doi.org/10.1016/j.elecom.2015.09.002.

[7] K. Kubota, M. Dahbi, T. Hosaka, S. Kumakura, S. Komaba, Towards K-Ion and Na-Ion Batteries as “Beyond Li-Ion,” Chem. Rec. 18 (2018) 459–479. https://doi.org/10.1002/tcr.201700057.

[8] Z. Wu, J. Zou, S. Chen, X. Niu, J. Liu, L. Wang, Potassium-ion battery cathodes: Past, present, and prospects, J. Power Sources 484 (2021) 229307. https://doi.org/10.1016/j.jpowsour.2020.229307.

[9] Y. Matsuda, H. Nakashima, M. Morita, Y. Takasu, Behavior of Some Ions in Mixed Organic Electrolytes of High Energy Density Batteries, J. Electrochem. Soc. 128 (1981) 2552. https://doi.org/10.1149/1.2127289.

[10] Y. Li, Y. Lu, P. Adelhelm, M.-M. Titirici, Y.-S. Hu, Intercalation chemistry of graphite: alkali metal ions and beyond, Chem. Soc. Rev. 48 (2019) 4655–4687. https://doi.org/10.1039/C9CS00162J.

[11] C. Vaalma, G.A. Giffin, D. Buchholz, S. Passerini, Non-Aqueous K-Ion Battery Based on Layered $K_{0.3}MnO_2$ and Hard Carbon/Carbon Black, J. Electrochem. Soc. 163 (2016) A1295–A1299. https://doi.org/10.1149/2.0921607jes.

[12] X. Bie, K. Kubota, T. Hosaka, K. Chihara, S. Komaba, A novel K-ion battery: hexacyanoferrate(II)/graphite cell, J. Mater. Chem. A 5 (2017) 4325–4330. https://doi.org/10.1039/C7TA00220C.

[13] K. Hurlbutt, S. Wheeler, I. Capone, M. Pasta, Prussian Blue Analogs as Battery Materials, Joule 2 (2018) 1950–1960. https://doi.org/10.1016/j.joule.2018.07.017.

[14] Z. Yang, J. Zhang, M.C.W. Kintner-Meyer, X. Lu, D. Choi, J.P. Lemmon, J. Liu, Electrochemical Energy Storage for Green Grid, Chem. Rev. 111 (2011) 3577–3613. https://doi.org/10.1021/cr100290v.

[15] M. Baumann, M. Häringer, M. Schmidt, L. Schneider, J.F. Peters, W. Bauer, J.R. Binder, M. Weil, Prospective Sustainability Screening of Sodium-Ion Battery Cathode Materials, Adv. Energy Mater. 12 (2022) 2202636. https://doi.org/10.1002/aenm.202202636.

[16] Z. Wang, X. Feng, Y. Bai, H. Yang, R. Dong, X. Wang, H. Xu, Q. Wang, H. Li, H. Gao, C. Wu, Probing the Energy Storage Mechanism of Quasi-Metallic Na in Hard Carbon for Sodium-Ion Batteries, Adv. Energy Mater. 11 (2021) 2003854. https://doi.org/10.1002/aenm.202003854.

[17] X. Zhang, J. Meng, X. Wang, Z. Xiao, P. Wu, L. Mai, Comprehensive Insights into Electrolytes and Solid Electrolyte Interfaces in Potassium-Ion Batteries, Energy Storage Mater. 38 (2021) 30–49. https://doi.org/10.1016/j.ensm.2021.02.036.

[18] W. Li, H. Yao, K. Yan, G. Zheng, Z. Liang, Y.-M. Chiang, Y. Cui, The synergetic effect of lithium polysulfide and lithium nitrate to prevent lithium dendrite growth, Nat. Commun. 6 (2015) 7436. https://doi.org/10.1038/ncomms8436.

[19] J. Xie, Y.-C. Lu, A retrospective on lithium-ion batteries, Nat. Commun. 11 (2020) 2499. https://doi.org/10.1038/s41467-020-16259-9.

[20] D. Guyomard, J.M. Tarascon, Rechargeable $Li1+xMn2O4$/Carbon Cells with a New Electrolyte Composition: Potentiostatic Studies and Application to Practical Cells, J. Electrochem. Soc. 140 (1993) 3071. https://doi.org/10.1149/1.2220987.

[21] A. AJ Torriero, Understanding the Differences between a Quasi-Reference Electrode and a Reference Electrode, Med. Anal. Chem. Int. J. 3 (2019). https://doi.org/10.23880/MACIJ-16000144.

[22] J.R. Belt, D.M. Bernardi, V. Utgikar, Development and Use of a Lithium-Metal Reference Electrode in Aging Studies of Lithium-Ion Batteries, J. Electrochem. Soc. 161 (2014) A1116. https://doi.org/10.1149/2.062406jes.

[23] S.S. Zhang, K. Xu, T.R. Jow, Study of the charging process of a LiCoO2-based Li-ion battery, Spec. Issue Sel. Pap. Present. Int. Workshop Molten Carbonate Fuel Cells Relat. Sci. Technol. 2005 Together Regul. Pap. 160 (2006) 1349–1354. https://doi.org/10.1016/j.jpowsour.2006.02.087.

[24] R. Raccichini, M. Amores, G. Hinds, Critical Review of the Use of Reference Electrodes in Li-Ion Batteries: A Diagnostic Perspective, Batteries 5 (2019) 12. https://doi.org/10.3390/batteries5010012.

[25] J. Conder, C. Villevieille, How reliable is the Na metal as a counter electrode in Na-ion half cells?, Chem. Commun. 55 (2019) 1275–1278. https://doi.org/10.1039/C8CC07852A.

[26] C. Bommier, D. Leonard, Z. Jian, W.F. Stickle, P.A. Greaney, X. Ji, New Paradigms on the Nature of Solid Electrolyte Interphase Formation and Capacity Fading of Hard Carbon Anodes in Na-Ion Batteries, Adv. Mater. Interfaces 3 (2016) 1600449. https://doi.org/10.1002/admi.201600449.

[27] D.I. Iermakova, R. Dugas, M.R. Palacín, A. Ponrouch, On the Comparative Stability of Li and Na Metal Anode Interfaces in Conventional Alkyl Carbonate Electrolytes, J. Electrochem. Soc. 162 (2015) A7060. https://doi.org/10.1149/2.0091513jes.

[28] C. Müller, Z. Wang, A. Hofmann, P. Stüble, X. Liu-Théato, J. Klemens, A. Smith, Influences on Reliable Capacity Measurements of Hard Carbon in Highly Loaded Electrodes, Batter. Supercaps 6 (2023) e202300322. https://doi.org/10.1002/batt.202300322.

[29] P. Stüble, C. Müller, J. Klemens, P. Scharfer, W. Schabel, M. Häringer, J.R. Binder, A. Hofmann, A. Smith, Enabling Long-term Cycling Stability of Na3V2(PO4)3/C vs. Hard Carbon Full-cells, Batter. Supercaps 7 (2024) e202300375. https://doi.org/10.1002/batt.202300375.

[30] T. Hosaka, S. Muratsubaki, K. Kubota, H. Onuma, S. Komaba, Potassium Metal as Reliable Reference Electrodes of Nonaqueous Potassium Cells, J. Phys. Chem. Lett. 10 (2019) 3296–3300. https://doi.org/10.1021/acs.jpclett.9b00711.

[31] T. Hosaka, K. Kubota, H. Kojima, S. Komaba, Highly concentrated electrolyte solutions for 4 V class potassium-ion batteries, Chem. Commun. 54 (2018) 8387–8390. https://doi.org/10.1039/C8CC04433C.

[32] D.P. Abraham, S.D. Poppen, A.N. Jansen, J. Liu, D.W. Dees, Application of a lithium–tin reference electrode to determine electrode contributions to impedance rise in high-power lithium-ion cells, Electrochimica Acta 49 (2004) 4763–4775. https://doi.org/10.1016/j.electacta.2004.05.040.

[33] A.N. Jansen, D.W. Dees, D.P. Abraham, K. Amine, G.L. Henriksen, Low-temperature study of lithium-ion cells using a LiySn micro-reference electrode, 13th Int. Meet. Lithium Batter. 174 (2007) 373–379. https://doi.org/10.1016/j.jpowsour.2007.06.235.

[34] S. Solchenbach, D. Pritzl, E.J.Y. Kong, J. Landesfeind, H.A. Gasteiger, A Gold Micro-Reference Electrode for Impedance and Potential Measurements in Lithium Ion Batteries, J. Electrochem. Soc. 163 (2016) A2265. https://doi.org/10.1149/2.0581610jes.

[35] D. Pritzl, J. Landesfeind, S. Solchenbach, H.A. Gasteiger, An Analysis Protocol for Three-Electrode Li-Ion Battery Impedance Spectra: Part II. Analysis of a Graphite Anode Cycled vs. LNMO, J. Electrochem. Soc. 165 (2018) A2145. https://doi.org/10.1149/2.0461810jes.

[36] F.J. Simon, L. Blume, M. Hanauer, U. Sauter, J. Janek, Development of a Wire Reference Electrode for Lithium All-Solid-State Batteries with Polymer Electrolyte: FEM Simulation and Experiment, J. Electrochem. Soc. 165 (2018) A1363. https://doi.org/10.1149/2.0671807jes.

[37] J.L. Gómez-Cámer, P. Novák, Electrochemical impedance spectroscopy: Understanding the role of the reference electrode, Electrochem. Commun. 34 (2013) 208–210. https://doi.org/10.1016/j.elecom.2013.06.016.

[38] E.C. Cengiz, J. Rizell, M. Sadd, A. Matic, N. Mozhzhukhina, Review—Reference Electrodes in Li-Ion and Next Generation Batteries: Correct Potential Assessment, Applications and Practices, J. Electrochem. Soc. 168 (2021) 120539. https://doi.org/10.1149/1945-7111/ac429b.

[39] F. Linsenmann, D. Pritzl, H.A. Gasteiger, A Reference Electrode for In Situ Impedance Measurements in Sodium-Ion Batteries, J. Electrochem. Soc. 166 (2019) A3668–A3674. https://doi.org/10.1149/2.0741915jes.

[40] J. Hou, R. Girod, N. Nianias, T.-H. Shen, J. Fan, V. Tileli, Lithium-Gold Reference Electrode for Potential Stability During In Situ Electron Microscopy Studies of Lithium-Ion Batteries, J. Electrochem. Soc. 167 (2020) 110515. https://doi.org/10.1149/1945-7111/ab9eea.

[41] I. Sultana, T. Ramireddy, M.M. Rahman, Y. Chen, A.M. Glushenkov, Tin-based composite anodes for potassium-ion batteries, Chem. Commun. 52 (2016) 9279–9282. https://doi.org/10.1039/C6CC03649J.

[42] W.D. McCulloch, X. Ren, M. Yu, Z. Huang, Y. Wu, Potassium-Ion Oxygen Battery Based on a High Capacity Antimony Anode, ACS Appl. Mater. Interfaces 7 (2015) 26158–26166. https://doi.org/10.1021/acsami.5b08037.

[43] H. Okamoto, In-K (indium-potassium), J. Phase Equilibria 13 (1992) 217–218. https://doi.org/10.1007/BF02667497.

[44] K. Lei, C. Wang, L. Liu, Y. Luo, C. Mu, F. Li, J. Chen, A Porous Network of Bismuth Used as the Anode Material for High-Energy-Density Potassium-Ion Batteries, Angew. Chem. Int. Ed. 57 (2018) 4687–4691. https://doi.org/10.1002/anie.201801389.

[45] B. Jagger, J. Aspinall, S. Kotakadi, J. Cattermull, S. Dhir, M. Pasta, Potassium Alloy Reference Electrodes for Potassium-Ion Batteries: The K-In and K-Bi Systems, ACS Mater. Lett. (2024) 4498–4506. https://doi.org/10.1021/acsmaterialslett.4c01219.

[46] F. La Mantia, C.D. Wessells, H.D. Deshazer, Y. Cui, Reliable reference electrodes for lithium-ion batteries, Electrochem. Commun. 31 (2013) 141–144. https://doi.org/10.1016/j.elecom.2013.03.015.

[47] J. Costard, M. Ender, M. Weiss, E. Ivers-Tiffée, Three-Electrode Setups for Lithium-Ion Batteries: II. Experimental Study of Different Reference Electrode Designs and Their Implications for Half-Cell Impedance Spectra, J. Electrochem. Soc. 164 (2017) A80–A87. https://doi.org/10.1149/2.0241702jes.

[48] T. Akçay, M. Häringer, K. Pfeifer, J. Anhalt, J.R. Binder, S. Dsoke, D. Kramer, R. Mönig, Na3V2(PO4)3–A Highly Promising Anode and Cathode Material for Sodium-Ion Batteries, ACS Appl. Energy Mater. 4 (2021) 12688–12695. https://doi.org/10.1021/acsaem.1c02413.

[49] J. Cattermull, K. Sada, K. Hurlbutt, S.J. Cassidy, M. Pasta, A.L. Goodwin, Uncovering the Interplay of Competing Distortions in the Prussian Blue Analogue $K_2Cu[Fe(CN)_6]$, Chem. Mater. 34 (2022) 5000–5008. https://doi.org/10.1021/acs.chemmater.2c00288.

[50] S.E. Lee, M.H. Tang, Reliable Reference Electrodes for Nonaqueous Sodium-Ion Batteries, J. Electrochem. Soc. 166 (2019) A3260. https://doi.org/10.1149/2.0401914jes.

[51] Y. Lyu, P. Mollik, A.L. Oláh, D.P. Halter, Construction and Evaluation of Cheap and Robust Miniature Ag/AgCl Reference Electrodes for Aqueous and Organic Electrolytes, ChemElectroChem 11 (2024) e202300792. https://doi.org/10.1002/celc.202300792.

[52] D. Pletcher, A First Course in Electrode Processes, The Royal Society of Chemistry, 2009. https://doi.org/10.1039/9781839169083.

[53] R.S. Kingsbury, S. Flotron, S. Zhu, D.F. Call, O. Coronell, Junction Potentials Bias Measurements of Ion Exchange Membrane Permselectivity, Environ. Sci. Technol. 52 (2018) 4929–4936. https://doi.org/10.1021/acs.est.7b05317.

[54] P.H. Barry, J.M. Diamond, Junction potentials, electrode standard potentials, and other problems in interpreting electrical properties of membranes, J. Membr. Biol. 3 (1970) 93–122. https://doi.org/10.1007/BF01868010.

[55] A. Eftekhari, Potassium secondary cell based on Prussian blue cathode, J. Power Sources 126 (2004) 221–228. https://doi.org/10.1016/j.jpowsour.2003.08.007.

[56] H. Wang, M. Yoshio, KPF6 dissolved in propylene carbonate as an electrolyte for activated carbon/graphite capacitors, J. Power Sources 195 (2010) 1263–1265. https://doi.org/10.1016/j.jpowsour.2009.08.073.

[57] K.-Y. Zhang, Z.-Y. Gu, E.H. Ang, J.-Z. Guo, X.-T. Wang, Y. Wang, X.-L. Wu, Advanced polyanionic electrode materials for potassium-ion batteries: Progresses, challenges and application prospects, Mater. Today 54 (2022) 189–201. https://doi.org/10.1016/j.mattod.2022.02.013.

[58] Y. Chen, W. Luo, M. Carter, L. Zhou, J. Dai, K. Fu, S. Lacey, T. Li, J. Wan, X. Han, Y. Bao, L. Hu, Organic electrode for non-aqueous potassium-ion batteries, Nano Energy 18 (2015) 205–211. https://doi.org/10.1016/j.nanoen.2015.10.015.

[59] J. Ma, E. Zhou, C. Fan, B. Wu, C. Li, Z.-H. Lu, J. Li, Endowing CuTCNQ with a new role: a high-capacity cathode for K-ion batteries, Chem. Commun. 54 (2018) 5578–5581. https://doi.org/10.1039/C8CC00802G.

[60] B. Tian, J. Zheng, C. Zhao, C. Liu, C. Su, W. Tang, X. Li, G.-H. Ning, Carbonyl-based polyimide and polyquinoneimide for potassium-ion batteries, J. Mater. Chem. A 7 (2019) 9997–10003. https://doi.org/10.1039/C9TA00647H.

[61] Z. Jian, Y. Liang, I.A. Rodríguez-Pérez, Y. Yao, X. Ji, Poly(anthraquinonyl sulfide) cathode for potassium-ion batteries, Electrochem. Commun. 71 (2016) 5–8. https://doi.org/10.1016/j.elecom.2016.07.011.

[62] S.-Y. Yang, Y.-J. Chen, G. Zhou, Z.-W. Fu, Multi-Electron Fused Redox Centers in Conjugated Aromatic Organic Compound as a Cathode for Rechargeable Batteries, J. Electrochem. Soc. 165 (2018) A1422. https://doi.org/10.1149/2.0831807jes.

[63] B. Esser, F. Dolhem, M. Becuwe, P. Poizot, A. Vlad, D. Brandell, A perspective on organic electrode materials and technologies for next generation batteries, J. Power Sources 482 (2021) 228814. https://doi.org/10.1016/j.jpowsour.2020.228814.

[64] K. Mizushima, P.C. Jones, P.J. Wiseman, J.B. Goodenough, LixCoO2 (0, Mater. Res. Bull. 15 (1980) 783–789. https://doi.org/10.1016/0025-5408(80)90012-4.

[65] C. Delmas, J.-J. Braconnier, C. Fouassier, P. Hagenmuller, Electrochemical intercalation of sodium in NaxCoO2 bronzes, Solid State Ion. 3–4 (1981) 165–169. https://doi.org/10.1016/0167-2738(81)90076-X.

[66] P. Strobel, C. Mouget, Electrochemical lithium insertion into layered manganates, Mater. Res. Bull. 28 (1993) 93–100. https://doi.org/10.1016/0025-5408(93)90076-P.

[67] S. Guo, H. Yu, Z. Jian, P. Liu, Y. Zhu, X. Guo, M. Chen, M. Ishida, H. Zhou, A High-Capacity, Low-Cost Layered Sodium Manganese Oxide Material as Cathode for Sodium-Ion Batteries, ChemSusChem 7 (2014) 2115–2119. https://doi.org/10.1002/cssc.201402138.

[68] H. Kim, J.C. Kim, S.-H. Bo, T. Shi, D.-H. Kwon, G. Ceder, K-Ion Batteries Based on a P2-Type K0.6CoO2 Cathode, Adv. Energy Mater. 7 (2017) 1700098. https://doi.org/10.1002/aenm.201700098.

[69] H. Kim, D.-H. Seo, J.C. Kim, S.-H. Bo, L. Liu, T. Shi, G. Ceder, Investigation of Potassium Storage in Layered P3-Type K0.5MnO2 Cathode, Adv. Mater. 29 (2017) 1702480. https://doi.org/10.1002/adma.201702480.

[70] C. Liu, S. Luo, H. Huang, Y. Zhai, Z. Wang, Layered potassium-deficient P2- and P3-type cathode materials KxMnO2 for K-ion batteries, Chem. Eng. J. 356 (2019) 53–59. https://doi.org/10.1016/j.cej.2018.09.012.

[71] Y.-S. Xu, S.-J. Guo, X.-S. Tao, Y.-G. Sun, J. Ma, C. Liu, A.-M. Cao, High-Performance Cathode Materials for Potassium-Ion Batteries: Structural Design and Electrochemical Properties, Adv. Mater. 33 (2021) 2100409. https://doi.org/10.1002/adma.202100409.

[72] X. Liu, Y. Guo, Q. Zhang, X. Zhou, Y. Yuan, Y. Zhang, J. Han, A. Nie, J. Lu, Y. You, K-Rich Spinel Interface of Air-Stable Layered Oxide Cathodes for Potassium-Ion Batteries, Adv. Mater. n/a (2024) 2407980. https://doi.org/10.1002/adma.202407980.

[73] J.U. Choi, J. Kim, J.-Y. Hwang, J.H. Jo, Y.-K. Sun, S.-T. Myung, K0.54[Co0.5Mn0.5]O2: New cathode with high power capability for potassium-ion batteries, Nano Energy 61 (2019) 284–294. https://doi.org/10.1016/j.nanoen.2019.04.062.

[74] C. Masquelier, L. Croguennec, Polyanionic (Phosphates, Silicates, Sulfates) Frameworks as Electrode Materials for Rechargeable Li (or Na) Batteries, Chem. Rev. 113 (2013) 6552–6591. https://doi.org/10.1021/cr3001862.

[75] J.B. Goodenough, H.Y.-P. Hong, J.A. Kafalas, Fast Na+-ion transport in skeleton structures, Mater. Res. Bull. 11 (1976) 203–220. https://doi.org/10.1016/0025-5408(76)90077-5.

[76] X. Lin, J. Huang, H. Tan, J. Huang, B. Zhang, K3V2(PO4)2F3 as a robust cathode for potassium-ion batteries, Energy Storage Mater. 16 (2019) 97–101. https://doi.org/10.1016/j.ensm.2018.04.026.

[77] T. Hosaka, T. Shimamura, K. Kubota, S. Komaba, Polyanionic Compounds for Potassium-Ion Batteries, Chem. Rec. 19 (2019) 735–745. https://doi.org/10.1002/tcr.201800143.

[78] J. Hyoung, J.W. Heo, M.S. Chae, S.-T. Hong, Electrochemical Exchange Reaction Mechanism and the Role of Additive Water to Stabilize the Structure of VOPO4·2 H2O as a Cathode Material for Potassium-Ion Batteries, ChemSusChem 12 (2019) 1069–1075. https://doi.org/10.1002/cssc.201802527.

[79] R. Lian, D. Wang, X. Ming, R. Zhang, Y. Wei, J. Feng, X. Meng, G. Chen, Phase transformation, ionic diffusion, and charge transfer mechanisms of KVOPO4 in potassium ion batteries: first-principles calculations, J. Mater. Chem. A 6 (2018) 16228–16234. https://doi.org/10.1039/C8TA06708B.

[80] J. Liao, Q. Hu, B. Che, X. Ding, F. Chen, C. Chen, Competing with other polyanionic cathode materials for potassium-ion batteries via fine structure design: new layered KVOPO4 with a tailored particle morphology, J. Mater. Chem. A 7 (2019) 15244–15251. https://doi.org/10.1039/C9TA03192H.

[81] J. Liao, Q. Hu, X. He, J. Mu, J. Wang, C. Chen, A long lifespan potassium-ion full battery based on KVPO4F cathode and VPO4 anode, J. Power Sources 451 (2020) 227739. https://doi.org/10.1016/j.jpowsour.2020.227739.

[82] H. Kim, D.-H. Seo, M. Bianchini, R.J. Clément, H. Kim, J.C. Kim, Y. Tian, T. Shi, W.-S. Yoon, G. Ceder, A New Strategy for High-Voltage Cathodes for K-Ion Batteries: Stoichiometric KVPO4F, Adv. Energy Mater. 8 (2018) 1801591. https://doi.org/10.1002/aenm.201801591.

[83] K. Chihara, A. Katogi, K. Kubota, S. Komaba, KVPO4F and KVOPO4 toward 4 volt-class potassium-ion batteries, Chem. Commun. 53 (2017) 5208–5211. https://doi.org/10.1039/C6CC10280H.

[84] S.S. Fedotov, A.S. Samarin, E.V. Antipov, KTiOPO4-structured electrode materials for metal-ion batteries: A review, J. Power Sources 480 (2020) 228840. https://doi.org/10.1016/j.jpowsour.2020.228840.

[85] X. Wu, Z. Jian, Z. Li, X. Ji, Prussian white analogues as promising cathode for non-aqueous potassium-ion batteries, Electrochem. Commun. 77 (2017) 54–57. https://doi.org/10.1016/j.elecom.2017.02.012.

[86] Y. Xiao, J. Xiao, H. Zhao, J. Li, G. Zhang, D. Zhang, X. Guo, H. Gao, Y. Wang, J. Chen, G. Wang, H. Liu, Prussian Blue Analogues for Sodium-Ion Battery Cathodes: A Review of Mechanistic Insights, Current Challenges, and Future Pathways, Small n/a (2024) 2401957. https://doi.org/10.1002/smll.202401957.

[87] C. Zhang, Y. Xu, M. Zhou, L. Liang, H. Dong, M. Wu, Y. Yang, Y. Lei, Potassium Prussian Blue Nanoparticles: A Low-Cost Cathode Material for Potassium-Ion Batteries, Adv. Funct. Mater. 27 (2017) 1604307. https://doi.org/10.1002/adfm.201604307.

[88] J. Dai, S. Tan, L. Wang, F. Ling, F. Duan, M. Ma, Y. Shao, X. Rui, Y. Yao, E. Hu, X. Wu, C. Li, Y. Yu, High-Voltage Potassium Hexacyanoferrate Cathode via High-Entropy and Potassium Incorporation for Stable Sodium-Ion Batteries, ACS Nano 17 (2023) 20949–20961. https://doi.org/10.1021/acsnano.3c02323.

[89] X. Jiang, T. Zhang, L. Yang, G. Li, J.Y. Lee, A Fe/Mn-Based Prussian Blue Analogue as a K-Rich Cathode Material for Potassium-Ion Batteries, ChemElectroChem 4 (2017) 2237–2242. https://doi.org/10.1002/celc.201700410.

[90] M. Fiore, S. Wheeler, K. Hurlbutt, I. Capone, J. Fawdon, R. Ruffo, M. Pasta, Paving the Way toward Highly Efficient, High-Energy Potassium-Ion Batteries with Ionic Liquid Electrolytes, Chem. Mater. 32 (2020) 7653–7661. https://doi.org/10.1021/acs.chemmater.0c01347.

[91] M. Xie, M. Xu, Y. Huang, R. Chen, X. Zhang, L. Li, F. Wu, Na2NixCo1−xFe(CN)6: A class of Prussian blue analogs with transition metal elements as cathode materials for sodium ion batteries, Electrochem. Commun. 59 (2015) 91–94. https://doi.org/10.1016/j.elecom.2015.07.014.

[92] X. Bie, K. Kubota, T. Hosaka, K. Chihara, S. Komaba, Synthesis and electrochemical properties of Na-rich Prussian blue analogues containing Mn, Fe, Co, and Fe for Na-ion batteries, J. Power Sources 378 (2018) 322–330. https://doi.org/10.1016/j.jpowsour.2017.12.052.

[93] B. Huang, Y. Liu, Z. Lu, M. Shen, J. Zhou, J. Ren, X. Li, S. Liao, Prussian Blue [$K_2FeFe(CN)_6$] Doped with Nickel as a Superior Cathode: An Efficient Strategy To Enhance Potassium Storage Performance, ACS Sustain. Chem. Eng. 7 (2019) 16659–16667. https://doi.org/10.1021/acssuschemeng.9b04012.

[94] C.-J. Du, F.-X. Bu, D.-M. Jiang, Q.-H. Zhang, J.-S. Jiang, Prussian blue analogue K2Zn3[Fe(CN)6]2 quasi square microplates: large-scale synthesis and their thermal conversion into a magnetic nanoporous ZnFe2−xO4–ZnO composite, CrystEngComm 15 (2013) 10597–10603. https://doi.org/10.1039/C3CE41753K.

[95] L. Xue, Y. Li, H. Gao, W. Zhou, X. Lü, W. Kaveevivitchai, A. Manthiram, J.B. Goodenough, Low-Cost High-Energy Potassium Cathode, J. Am. Chem. Soc. 139 (2017) 2164–2167. https://doi.org/10.1021/jacs.6b12598.

[96] A. Dostal, G. Kauschka, S.J. Reddy, F. Scholz, Lattice contractions and expansions accompanying the electrochemical conversions of Prussian blue and the reversible and irreversible insertion of rubidium and thallium ions, J. Electroanal. Chem. 406 (1996) 155–163. https://doi.org/10.1016/0022-0728(95)04427-2.

[97] L. Wang, J. Song, R. Qiao, L.A. Wray, M.A. Hossain, Y.-D. Chuang, W. Yang, Y. Lu, D. Evans, J.-J. Lee, S. Vail, X. Zhao, M. Nishijima, S. Kakimoto, J.B. Goodenough, Rhombohedral Prussian White as Cathode for Rechargeable Sodium-Ion Batteries, J. Am. Chem. Soc. 137 (2015) 2548–2554. https://doi.org/10.1021/ja510347s.

[98] J. Liao, Z. Yuan, Q. Hu, X. Sheng, L. Song, Y. Xu, Y. Du, X. Zhou, Heat-Resistant Carbon-Coated Potassium Magnesium Hexacyanoferrate Nanoplates for High-Performance Potassium-Ion Batteries, Angew. Chem. Int. Ed. n/a (2024) e202409145. https://doi.org/10.1002/anie.202409145.

[99] P. Xiao, J. Song, L. Wang, J.B. Goodenough, G. Henkelman, Theoretical Study of the Structural Evolution of a Na2FeMn(CN)6 Cathode upon Na Intercalation, Chem. Mater. 27 (2015) 3763–3768. https://doi.org/10.1021/acs.chemmater.5b01132.

[100] J. Song, L. Wang, Y. Lu, J. Liu, B. Guo, P. Xiao, J.-J. Lee, X.-Q. Yang, G. Henkelman, J.B. Goodenough, Removal of Interstitial H2O in Hexacyanometallates for a Superior Cathode of a Sodium-Ion Battery, J. Am. Chem. Soc. 137 (2015) 2658–2664. https://doi.org/10.1021/ja512383b.

[101] J. Liao, Q. Hu, Y. Yu, H. Wang, Z. Tang, Z. Wen, C. Chen, A potassium-rich iron hexacyanoferrate/dipotassium terephthalate@carbon nanotube composite used for K-ion full-cells with an optimized electrolyte, J. Mater. Chem. A 5 (2017) 19017–19024. https://doi.org/10.1039/C7TA05460B.

[102] W.R. Brant, R. Mogensen, S. Colbin, D.O. Ojwang, S. Schmid, L. Häggström, T. Ericsson, A. Jaworski, A.J. Pell, R. Younesi, Selective Control of Composition in Prussian White for Enhanced Material Properties, Chem. Mater. 31 (2019) 7203–7211. https://doi.org/10.1021/acs.chemmater.9b01494.

[103] M. Sha, L. Liu, H. Zhao, Y. Lei, Anode materials for potassium-ion batteries: Current status and prospects, Carbon Energy 2 (2020) 350–369. https://doi.org/10.1002/cey2.57.

[104] M. Naguib, R.A. Adams, Y. Zhao, D. Zemlyanov, A. Varma, J. Nanda, V.G. Pol, Electrochemical performance of MXenes as K-ion battery anodes, Chem. Commun. 53 (2017) 6883–6886. https://doi.org/10.1039/C7CC02026K.

[105] R.A. Adams, J.-M. Syu, Y. Zhao, C.-T. Lo, A. Varma, V.G. Pol, Binder-Free N- and O-Rich Carbon Nanofiber Anodes for Long Cycle Life K-Ion Batteries, ACS Appl. Mater. Interfaces 9 (2017) 17872–17881. https://doi.org/10.1021/acsami.7b02476.

[106] B. Kishore, V. G, N. Munichandraiah, K2Ti4O9: A Promising Anode Material for Potassium Ion Batteries, J. Electrochem. Soc. 163 (2016) A2551. https://doi.org/10.1149/2.0421613jes.

[107] P. Li, X. Zheng, H. Yu, G. Zhao, J. Shu, X. Xu, W. Sun, S.X. Dou, Electrochemical potassium/lithium-ion intercalation into TiSe2: Kinetics and mechanism, Energy Storage Mater. 16 (2019) 512–518. https://doi.org/10.1016/j.ensm.2018.09.014.

[108] V. Ramezankhani, N.D. Luchinin, S.N. Marshenya, M.V. Zakharkin, A.A. Golubnichiy, A.V. Morozov, O. Emilianova, K.J. Stevenson, E.V. Antipov, A.M. Abakumov, S.S. Fedotov, Exploring KTiPO4F as a robust polyanion anode material for potassium-ion batteries, J. Mater. Chem. A 12 (2024) 18404–18411. https://doi.org/10.1039/D3TA08103F.

[109] J. Han, Y. Niu, S. Bao, Y.-N. Yu, S.-Y. Lu, M. Xu, Nanocubic KTi2(PO4)3 electrodes for potassium-ion batteries, Chem. Commun. 52 (2016) 11661–11664. https://doi.org/10.1039/C6CC06177J.

[110] M. Shimizu, R. Yatsuzuka, T. Koya, T. Yamakami, S. Arai, Tin Oxides as a Negative Electrode Material for Potassium-Ion Batteries, ACS Appl. Energy Mater. 1 (2018) 6865–6870. https://doi.org/10.1021/acsaem.8b01209.

[111] C. Li, K. Pfeifer, X. Luo, G. Melinte, J. Wang, Z. Zhang, Y. Zhang, P. Dong, A. Sarapulova, H. Ehrenberg, S. Dsoke, Investigation of SnS2-rGO Sandwich Structures as Negative Electrode for Sodium-Ion and Potassium-Ion Batteries, ChemSusChem 16 (2023) e202202281. https://doi.org/10.1002/cssc.202202281.

[112] L.C. Loaiza, L. Monconduit, V. Seznec, Si and Ge-Based Anode Materials for Li-, Na-, and K-Ion Batteries: A Perspective from Structure to Electrochemical Mechanism, Small 16 (2020) 1905260. https://doi.org/10.1002/smll.201905260.

[113] S. Imtiaz, I.S. Amiinu, Y. Xu, T. Kennedy, C. Blackman, K.M. Ryan, Progress and perspectives on alloying-type anode materials for advanced potassium-ion batteries, Mater. Today 48 (2021) 241–269. https://doi.org/10.1016/j.mattod.2021.02.008.

[114] C. Li, Q. Deng, H. Tan, C. Wang, C. Fan, J. Pei, B. Cao, Z. Wang, J. Li, Para-Conjugated Dicarboxylates with Extended Aromatic Skeletons as the Highly Advanced Organic Anodes for K-Ion Battery, ACS Appl. Mater. Interfaces 9 (2017) 27414–27420. https://doi.org/10.1021/acsami.7b08974.

[115] Q. Deng, J. Pei, C. Fan, J. Ma, B. Cao, C. Li, Y. Jin, L. Wang, J. Li, Potassium salts of para-aromatic dicarboxylates as the highly efficient organic anodes for low-cost K-ion batteries, Nano Energy 33 (2017) 350–355. https://doi.org/10.1016/j.nanoen.2017.01.016.

[116] C. Wang, W. Tang, Z. Yao, Y. Chen, J. Pei, C. Fan, Using an organic acid as a universal anode for highly efficient Li-ion, Na-ion and K-ion batteries, Org. Electron. 62 (2018) 536–541. https://doi.org/10.1016/j.orgel.2018.06.027.

[117] G. Zhang, X. Liu, L. Wang, H. Fu, Recent advances of biomass derived carbon-based materials for efficient electrochemical energy devices, J. Mater. Chem. A 10 (2022) 9277–9307. https://doi.org/10.1039/D2TA01442D.

[118] C. Vaalma, G.A. Giffin, D. Buchholz, S. Passerini, Non-Aqueous K-Ion Battery Based on Layered K0.3MnO2 and Hard Carbon/Carbon Black, J. Electrochem. Soc. 163 (2016) A1295. https://doi.org/10.1149/2.0921607jes.

[119] Z. Jian, S. Hwang, Z. Li, A.S. Hernandez, X. Wang, Z. Xing, D. Su, X. Ji, Hard–Soft Composite Carbon as a Long-Cycling and High-Rate Anode for Potassium-Ion Batteries, Adv. Funct. Mater. 27 (2017) 1700324. https://doi.org/10.1002/adfm.201700324.

[120] S.K. Saju, S. Chattopadhyay, J. Xu, S. Alhashim, A. Pramanik, P.M. Ajayan, Hard carbon anode for lithium-, sodium-, and potassium-ion batteries: Advancement and future perspective, Cell Rep. Phys. Sci. 5 (2024) 101851. https://doi.org/10.1016/j.xcrp.2024.101851.

[121] J. Zhao, X. Zou, Y. Zhu, Y. Xu, C. Wang, Electrochemical Intercalation of Potassium into Graphite, Adv. Funct. Mater. 26 (2016) 8103–8110. https://doi.org/10.1002/adfm.201602248.

[122] A.V. Desai, R.E. Morris, A.R. Armstrong, Advances in Organic Anode Materials for Na-/K-Ion Rechargeable Batteries, ChemSusChem 13 (2020) 4866–4884. https://doi.org/10.1002/cssc.202001334.

[123] J. Asenbauer, T. Eisenmann, M. Kuenzel, A. Kazzazi, Z. Chen, D. Bresser, The success story of graphite as a lithium-ion anode material – fundamentals, remaining challenges, and recent developments including silicon (oxide) composites, Sustain. Energy Fuels 4 (2020) 5387–5416. https://doi.org/10.1039/D0SE00175A.

[124] L. Fan, R. Ma, Q. Zhang, X. Jia, B. Lu, Graphite Anode for a Potassium-Ion Battery with Unprecedented Performance, Angew. Chem. Int. Ed. 58 (2019) 10500–10505. https://doi.org/10.1002/anie.201904258.

[125] J.-M. Tarascon, M. Armand, Issues and challenges facing rechargeable lithium batteries, Nature 414 (2001) 359–367. https://doi.org/10.1038/35104644.

[126] H. Zhang, Y. Yang, D. Ren, L. Wang, X. He, Graphite as anode materials: Fundamental mechanism, recent progress and advances, Energy Storage Mater. 36 (2021) 147–170. https://doi.org/10.1016/j.ensm.2020.12.027.

[127] K. Nobuhara, H. Nakayama, M. Nose, S. Nakanishi, H. Iba, First-principles study of alkali metal-graphite intercalation compounds, J. Power Sources 243 (2013) 585–587. https://doi.org/10.1016/j.jpowsour.2013.06.057.

[128] D. Guerard, A. Herold, Intercalation of lithium into graphite and other carbons, Carbon 13 (1975) 337–345. https://doi.org/10.1016/0008-6223(75)90040-8.

[129] H. Moriwake, A. Kuwabara, C.A.J. Fisher, Y. Ikuhara, Why is sodium-intercalated graphite unstable?, RSC Adv. 7 (2017) 36550–36554. https://doi.org/10.1039/C7RA06777A.

[130] Y. Okamoto, Density Functional Theory Calculations of Alkali Metal (Li, Na, and K) Graphite Intercalation Compounds, J. Phys. Chem. C 118 (2014) 16–19. https://doi.org/10.1021/jp4063753.

[131] J.C. Pramudita, V.K. Peterson, J.A. Kimpton, N. Sharma, Potassium-ion intercalation in graphite within a potassium-ion battery examined using in situ X-ray diffraction, Powder Diffr. 32 (2017) S43–S48. https://doi.org/10.1017/S0885715617000902.

[132] C. Hartwigsen, W. Witschel, E. Spohr, Charge density and charge transfer in stage-1 alkali-graphite intercalation compounds, Phys. Rev. B 55 (1997) 4953–4959. https://doi.org/10.1103/PhysRevB.55.4953.

[133] H. Kim, J. Hong, G. Yoon, H. Kim, K.-Y. Park, M.-S. Park, W.-S. Yoon, K. Kang, Sodium intercalation chemistry in graphite, Energy Environ. Sci. 8 (2015) 2963–2969. https://doi.org/10.1039/C5EE02051D.

[134] K. Fredenhagen, G. Cadenbach, Die Bindung von Kalium durch Kohlenstoff, Z. Für Anorg. Allg. Chem. 158 (1926) 249–263. https://doi.org/10.1002/zaac.19261580122.

[135] W. Rüdorff, E. Schulze, Über Alkaligraphitverbindungen, Z. Für Anorg. Allg. Chem. 277 (1954) 156–171. https://doi.org/10.1002/zaac.19542770307.

[136] Y. Wang, P. Puech, I. Gerber, A. Pénicaud, Resonant Raman scattering of graphite intercalation compounds KC8, KC24, and KC36, J. Raman Spectrosc. 45 (2014) 219–223. https://doi.org/10.1002/jrs.4445.

[137] S. Schweidler, L. de Biasi, A. Schiele, P. Hartmann, T. Brezesinski, J. Janek, Volume Changes of Graphite Anodes Revisited: A Combined Operando X-ray Diffraction and In Situ Pressure Analysis Study, J. Phys. Chem. C 122 (2018) 8829–8835. https://doi.org/10.1021/acs.jpcc.8b01873.

[138] D.D.L. Chung, Review Graphite, J. Mater. Sci. 37 (2002) 1475–1489. https://doi.org/10.1023/A:1014915307738.

[139] H. Shi, J. Barker, M.Y. Saïdi, R. Koksbang, Structure and Lithium Intercalation Properties of Synthetic and Natural Graphite, J. Electrochem. Soc. 143 (1996) 3466. https://doi.org/10.1149/1.1837238.

[140] L. Samuelson, I.P. Batra, C. Roetti, A comparison of electronic properties of various modifications of graphite, Solid State Commun. 33 (1980) 817–820. https://doi.org/10.1016/0038-1098(80)90839-X.

[141] D E Nixon, G S Parry, Formation and structure of the potassium graphites, J. Phys. Appl. Phys. 1 (1968) 303. https://doi.org/10.1088/0022-3727/1/3/303.

[142] M.S. Dresselhaus, G. Dresselhaus, Intercalation compounds of graphite, Adv. Phys. 51 (2002) 1–186. https://doi.org/10.1080/00018730110113644.

[143] K. Share, A.P. Cohn, R.E. Carter, C.L. Pint, Mechanism of potassium ion intercalation staging in few layered graphene from in situ Raman spectroscopy, Nanoscale 8 (2016) 16435–16439. https://doi.org/10.1039/C6NR04084E.

[144] H. Onuma, K. Kubota, S. Muratsubaki, W. Ota, M. Shishkin, H. Sato, K. Yamashita, S. Yasuno, S. Komaba, Phase evolution of electrochemically potassium intercalated graphite, J. Mater. Chem. A 9 (2021) 11187–11200. https://doi.org/10.1039/D0TA12607A.

[145] L. Ni, G. Xu, C. Li, G. Cui, Electrolyte formulation strategies for potassium-based batteries, Exploration 2 (2022) 20210239. https://doi.org/10.1002/EXP.20210239.

[146] K. Xu, Nonaqueous Liquid Electrolytes for Lithium-Based Rechargeable Batteries, Chem. Rev. 104 (2004) 4303–4418. https://doi.org/10.1021/cr030203g.

[147] A.N. Dey, B.P. Sullivan, The Electrochemical Decomposition of Propylene Carbonate on Graphite, J. Electrochem. Soc. 117 (1970) 222. https://doi.org/10.1149/1.2407470.

[148] M. Li, C. Wang, Z. Chen, K. Xu, J. Lu, New Concepts in Electrolytes, Chem. Rev. 120 (2020) 6783–6819. https://doi.org/10.1021/acs.chemrev.9b00531.

[149] H. Adenusi, G.A. Chass, S. Passerini, K.V. Tian, G. Chen, Lithium Batteries and the Solid Electrolyte Interphase (SEI)—Progress and Outlook, Adv. Energy Mater. 13 (2023) 2203307. https://doi.org/10.1002/aenm.202203307.

[150] S.C. Kim, J. Wang, R. Xu, P. Zhang, Y. Chen, Z. Huang, Y. Yang, Z. Yu, S.T. Oyakhire, W. Zhang, L.C. Greenburg, M.S. Kim, D.T. Boyle, P. Sayavong, Y. Ye, J. Qin, Z. Bao, Y. Cui, High-entropy electrolytes for practical lithium metal batteries, Nat. Energy 8 (2023) 814–826. https://doi.org/10.1038/s41560-023-01280-1.

[151] X. Chen, Q. Zhang, Atomic Insights into the Fundamental Interactions in Lithium Battery Electrolytes, Acc. Chem. Res. 53 (2020) 1992–2002. https://doi.org/10.1021/acs.accounts.0c00412.

[152] H. Zhang, L. Qiao, M. Armand, Organic Electrolyte Design for Rechargeable Batteries: From Lithium to Magnesium, Angew. Chem. Int. Ed. 61 (2022) e202214054. https://doi.org/10.1002/anie.202214054.

[153] K. Liu, Y. Liu, D. Lin, A. Pei, Y. Cui, Materials for lithium-ion battery safety, Sci. Adv. 4 (n.d.) eaas9820. https://doi.org/10.1126/sciadv.aas9820.

[154] A.D. Khudyshkina, P.A. Morozova, A.J. Butzelaar, M. Hoffmann, M. Wilhelm, P. Theato, S.S. Fedotov, F. Jeschull, Poly(ethylene oxide)-Based Electrolytes for Solid-State Potassium Metal Batteries with a Prussian Blue Positive Electrode, ACS Appl. Polym. Mater. 4 (2022) 2734–2746. https://doi.org/10.1021/acsapm.2c00014.

[155] A.D. Khudyshkina, U.-C. Rauska, A.J. Butzelaar, M. Hoffmann, M. Wilhelm, P. Theato, F. Jeschull, Impact of Nano-sized Inorganic Fillers on PEO-based Electrolytes for Potassium Batteries, Batter. Supercaps 7 (2024) e202300404. https://doi.org/10.1002/batt.202300404.

[156] H. Fei, Y. Liu, Y. An, X. Xu, J. Zhang, B. Xi, S. Xiong, J. Feng, Safe all-solid-state potassium batteries with three dimentional, flexible and binder-free metal sulfide array electrode, J. Power Sources 433 (2019) 226697. https://doi.org/10.1016/j.jpowsour.2019.226697.

[157] H. Gao, L. Xue, S. Xin, J.B. Goodenough, A High-Energy-Density Potassium Battery with a Polymer-Gel Electrolyte and a Polyaniline Cathode, Angew. Chem. Int. Ed. 57 (2018) 5449–5453. https://doi.org/10.1002/anie.201802248.

[158] J. Kalhoff, G.G. Eshetu, D. Bresser, S. Passerini, Safer Electrolytes for Lithium-Ion Batteries: State of the Art and Perspectives, ChemSusChem 8 (2015) 2154–2175. https://doi.org/10.1002/cssc.201500284.

[159] A. Hofmann, F. Müller, S. Schöner, F. Jeschull, Revealing the Formation of Dialkyl Dioxahexane Dioate Products from Ethylene Carbonate based Electrolytes on Lithium and Potassium Surfaces, Batter. Supercaps (2023) e202300325. https://doi.org/10.1002/batt.202300325.

[160] L. Deng, T. Wang, Y. Hong, M. Feng, R. Wang, J. Zhang, Q. Zhang, J. Wang, L. Zeng, Y. Zhu, L. Guo, A Nonflammable Electrolyte Enabled High Performance K0.5MnO2 Cathode for Low-Cost Potassium-Ion Batteries, ACS Energy Lett. 5 (2020) 1916–1922. https://doi.org/10.1021/acsenergylett.0c00912.

[161] Q.-K. Zhang, X.-Q. Zhang, H. Yuan, J.-Q. Huang, Thermally Stable and Nonflammable Electrolytes for Lithium Metal Batteries: Progress and Perspectives, Small Sci. 1 (2021) 2100058. https://doi.org/10.1002/smsc.202100058.

[162] B. Li, J. Zhao, Z. Zhang, C. Zhao, P. Sun, P. Bai, J. Yang, Z. Zhou, Y. Xu, Electrolyte-Regulated Solid-Electrolyte Interphase Enables Long Cycle Life Performance in Organic Cathodes for Potassium-Ion Batteries, Adv. Funct. Mater. 29 (2019) 1807137. https://doi.org/10.1002/adfm.201807137.

[163] L. Zhou, Z. Cao, W. Wahyudi, J. Zhang, J.-Y. Hwang, Y. Cheng, L. Wang, L. Cavallo, T. Anthopoulos, Y.-K. Sun, H.N. Alshareef, J. Ming, Electrolyte Engineering Enables High Stability and Capacity Alloying Anodes for Sodium and Potassium Ion Batteries, ACS Energy Lett. 5 (2020) 766–776. https://doi.org/10.1021/acsenergylett.0c00148.

[164] Z. Wang, K. Dong, D. Wang, S. Luo, Y. Liu, Q. Wang, Y. Zhang, A. Hao, C. Shi, N. Zhao, A nanosized SnSb alloy confined in N-doped 3D porous carbon coupled with ether-based electrolytes toward high-performance potassium-ion batteries, J. Mater. Chem. A 7 (2019) 14309–14318. https://doi.org/10.1039/C9TA03851E.

[165] L. Wang, J. Zou, S. Chen, G. Zhou, J. Bai, P. Gao, Y. Wang, X. Yu, J. Li, Y.-S. Hu, H. Li, TiS2 as a high performance potassium ion battery cathode in ether-based electrolyte, Energy Storage Mater. 12 (2018) 216–222. https://doi.org/10.1016/j.ensm.2017.12.018.

[166] M. Okoshi, Y. Yamada, S. Komaba, A. Yamada, H. Nakai, Theoretical Analysis of Interactions between Potassium Ions and Organic Electrolyte Solvents: A Comparison with Lithium, Sodium, and Magnesium Ions, J. Electrochem. Soc. 164 (2016) A54. https://doi.org/10.1149/2.0211702jes.

[167] T.A. Pham, K.E. Kweon, A. Samanta, V. Lordi, J.E. Pask, Solvation and Dynamics of Sodium and Potassium in Ethylene Carbonate from ab Initio Molecular Dynamics Simulations, J. Phys. Chem. C 121 (2017) 21913–21920. https://doi.org/10.1021/acs.jpcc.7b06457.

[168] S. Amara, J. Toulc'Hoat, L. Timperman, A. Biller, H. Galiano, C. Marcel, M. Ledigabel, M. Anouti, Comparative Study of Alkali-Cation-Based (Li+, Na+, K+) Electrolytes in Acetonitrile and Alkylcarbonates, ChemPhysChem 20 (2019) 581–594. https://doi.org/10.1002/cphc.201801064.

[169] L.B. Silva, L.C.G. Freitas, Structural and thermodynamic properties of liquid ethylene carbonate and propylene carbonate by Monte Carlo Simulations, J. Mol. Struct. THEOCHEM 806 (2007) 23–34. https://doi.org/10.1016/j.theochem.2006.10.014.

[170] Q. Li, Z. Cao, W. Wahyudi, G. Liu, G.-T. Park, L. Cavallo, T.D. Anthopoulos, L. Wang, Y.-K. Sun, H.N. Alshareef, J. Ming, Unraveling the New Role of an Ethylene Carbonate Solvation Shell in Rechargeable Metal Ion Batteries, ACS Energy Lett. 6 (2021) 69–78. https://doi.org/10.1021/acsenergylett.0c02140.

[171] H. Yin, C. Han, Q. Liu, F. Wu, F. Zhang, Y. Tang, Recent Advances and Perspectives on the Polymer Electrolytes for Sodium/Potassium-Ion Batteries, Small 17 (2021) 2006627. https://doi.org/10.1002/smll.202006627.

[172] K. Xu, Electrolytes and Interphases in Li-Ion Batteries and Beyond, Chem. Rev. 114 (2014) 11503–11618. https://doi.org/10.1021/cr500003w.

[173] B. Larhrib, L. Larbi, L. Madec, Nonaqueous potassium-ion full-cells: Mapping the progress and identifying missing puzzle pieces, J. Energy Chem. 93 (2024) 384–399. https://doi.org/10.1016/j.jechem.2024.01.033.

[174] H. Zhao, X. Yu, J. Li, B. Li, H. Shao, L. Li, Y. Deng, Film-forming electrolyte additives for rechargeable lithium-ion batteries: progress and outlook, J. Mater. Chem. A 7 (2019) 8700–8722. https://doi.org/10.1039/C9TA00126C.

[175] L. Madec, V. Gabaudan, G. Gachot, L. Stievano, L. Monconduit, H. Martinez, Paving the Way for K-Ion Batteries: Role of Electrolyte Reactivity through the Example of Sb-Based Electrodes, ACS Appl. Mater. Interfaces 10 (2018) 34116–34122. https://doi.org/10.1021/acsami.8b08902.

[176] S. Xing, A. Khudyshkina, U.-C. Rauska, A.J. Butzelaar, D. Voll, P. Theato, J. Tübke, F. Jeschull, Degradation of Styrene-Poly(ethylene oxide)-Based Block Copolymer Electrolytes at the Na and K Negative Electrode Studied by Microcalorimetry and Impedance Spectroscopy, J. Electrochem. Soc. 171 (2024) 040516. https://doi.org/10.1149/1945-7111/ad3b72.

[177] F. Jeschull, J. Maibach, Inactive materials matter: How binder amounts affect the cycle life of graphite electrodes in potassium-ion batteries, Electrochem. Commun. 121 (2020) 106874. https://doi.org/10.1016/j.elecom.2020.106874.

[178] T. Hosaka, T. Matsuyama, R. Tatara, Z.T. Gossage, S. Komaba, Impact of electrolyte decomposition products on the electrochemical performance of 4 V class K-ion batteries, Chem. Sci. 14 (2023) 8860–8868. https://doi.org/10.1039/D3SC02111D.

[179] T. Hosaka, T. Fukabori, T. Matsuyama, R. Tatara, K. Kubota, S. Komaba, 1,3,2-Dioxathiolane 2,2-Dioxide as an Electrolyte Additive for K-Metal Cells, ACS Energy Lett. 6 (2021) 3643–3649. https://doi.org/10.1021/acsenergylett.1c01238.

[180] S.P. Kühn, K. Edström, M. Winter, I. Cekic-Laskovic, Face to Face at the Cathode Electrolyte Interphase: From Interface Features to Interphase Formation and Dynamics, Adv. Mater. Interfaces 9 (2022) 2102078. https://doi.org/10.1002/admi.202102078.

[181] E. Peled, H. Yamin, Solid Electrolyte Interphase (SEI) Electrodes. Part 1. The Kinetics of Lithium in LiAlCl4-SOCl2, Isr. J. Chem. 18 (1979) 131–135. https://doi.org/10.1002/ijch.197900016.

[182] B. Horstmann, J. Shi, R. Amine, M. Werres, X. He, H. Jia, F. Hausen, I. Cekic-Laskovic, S. Wiemers-Meyer, J. Lopez, D. Galvez-Aranda, F. Baakes, D. Bresser, C.-C. Su, Y. Xu, W. Xu, P. Jakes, R.-A. Eichel, E. Figgemeier, U. Krewer, J.M. Seminario, P.B. Balbuena, C. Wang, S. Passerini, Y. Shao-Horn, M. Winter, K. Amine, R. Kostecki, A. Latz, Strategies towards enabling lithium metal in batteries: interphases and electrodes, Energy Environ. Sci. 14 (2021) 5289–5314. https://doi.org/10.1039/D1EE00767J.

[183] S. Visco, E. Nimon, L. De Jonghe, Encyclopedia of electrochemical power sources, Elsevier 4 (2009) 376–383.

[184] A. Wang, S. Kadam, H. Li, S. Shi, Y. Qi, Review on modeling of the anode solid electrolyte interphase (SEI) for lithium-ion batteries, Npj Comput. Mater. 4 (2018) 15. https://doi.org/10.1038/s41524-018-0064-0.

[185] N.D. Rodrigo, C. Jayawardana, L. Rynearson, E. Hu, X.-Q. Yang, B.L. Lucht, Use of Ethylene Carbonate Free Ester Solvent Systems with Alternative Lithium Salts for Improved Low-Temperature Performance in NCM622|| Graphite Li-ion Batteries, J. Electrochem. Soc. 169 (2022) 110504. https://doi.org/10.1149/1945-7111/ac9d0a.

[186] D.S. Hall, J.P. Allen, S.L. Glazier, L.D. Ellis, L. Ma, J.M. Peters, I.G. Hill, J.R. Dahn, The Solid-Electrolyte Interphase Formation Reactions of Ethylene Sulfate and Its Synergistic Chemistry with Prop-1-ene-1,3-Sultone in Lithium-Ion Cells, J. Electrochem. Soc. 164 (2017) A3445. https://doi.org/10.1149/2.0181714jes.

[187] S.J. An, J. Li, C. Daniel, D. Mohanty, S. Nagpure, D.L. Wood, The state of understanding of the lithium-ion-battery graphite solid electrolyte interphase (SEI) and its relationship to formation cycling, Carbon 105 (2016) 52–76. https://doi.org/10.1016/j.carbon.2016.04.008.

[188] K. Rah, B. Choi, C. Kim, Effective Measures of Thickness Evolution of the Solid Electrolyte Interphase of Graphite Anodes for Li-Ion Batteries, Langmuir 40 (2024) 7550–7559. https://doi.org/10.1021/acs.langmuir.4c00113.

[189] H. Jin, S. Pyo, H. Seo, J. Cho, J. Han, J. Han, H. Yun, H. Kim, J. Lee, B. Min, J. Yoo, Y.S. Kim, LiF-Rich Solid Electrolyte Interphase Formation by Establishing Sacrificial Layer on the Separator, Small n/a (2024) 2401928. https://doi.org/10.1002/smll.202401928.

[190] P. Jankowski, W. Wieczorek, P. Johansson, SEI-forming electrolyte additives for lithium-ion batteries: development and benchmarking of computational approaches, J. Mol. Model. 23 (2016) 6. https://doi.org/10.1007/s00894-016-3180-0.

[191] Q. Wu, M.T. McDowell, Y. Qi, Effect of the Electric Double Layer (EDL) in Multicomponent Electrolyte Reduction and Solid Electrolyte Interphase (SEI) Formation in Lithium Batteries, J. Am. Chem. Soc. 145 (2023) 2473–2484. https://doi.org/10.1021/jacs.2c11807.

[192] S. Tsubouchi, Y. Domi, T. Doi, M. Ochida, H. Nakagawa, T. Yamanaka, T. Abe, Z. Ogumi, Spectroscopic Characterization of Surface Films Formed on Edge Plane Graphite in Ethylene Carbonate-Based Electrolytes Containing Film-Forming Additives, J. Electrochem. Soc. 159 (2012) A1786. https://doi.org/10.1149/2.028211jes.

[193] S. Han, Structure and dynamics in the lithium solvation shell of nonaqueous electrolytes, Sci. Rep. 9 (2019) 5555. https://doi.org/10.1038/s41598-019-42050-y.

[194] K. Xu, Y. Lam, S.S. Zhang, T.R. Jow, T.B. Curtis, Solvation Sheath of Li+ in Nonaqueous Electrolytes and Its Implication of Graphite/Electrolyte Interface Chemistry, J. Phys. Chem. C 111 (2007) 7411–7421. https://doi.org/10.1021/jp068691u.

[195] V.A. Agubra, J.W. Fergus, The formation and stability of the solid electrolyte interface on the graphite anode, J. Power Sources 268 (2014) 153–162. https://doi.org/10.1016/j.jpowsour.2014.06.024.

[196] D.M. Seo, D. Chalasani, B.S. Parimalam, R. Kadam, M. Nie, B.L. Lucht, Reduction Reactions of Carbonate Solvents for Lithium Ion Batteries, ECS Electrochem. Lett. 3 (2014) A91. https://doi.org/10.1149/2.0021409eel.

[197] G.V. Zhuang, H. Yang, B. Blizanac, P.N. Ross, A Study of Electrochemical Reduction of Ethylene and Propylene Carbonate Electrolytes on Graphite Using ATR-FTIR Spectroscopy, Electrochem. Solid-State Lett. 8 (2005) A441. https://doi.org/10.1149/1.1979327.

[198] J.O. Besenhard, M. Winter, J. Yang, W. Biberacher, Filming mechanism of lithium-carbon anodes in organic and inorganic electrolytes, Proc. Seventh Int. Meet. Lithium Batter. 54 (1995) 228–231. https://doi.org/10.1016/0378-7753(94)02073-C.

[199] S. Leroy, H. Martinez, R. Dedryvère, D. Lemordant, D. Gonbeau, Influence of the lithium salt nature over the surface film formation on a graphite electrode in Li-ion batteries: An XPS study, Appl. Surf. Sci. 253 (2007) 4895–4905. https://doi.org/10.1016/j.apsusc.2006.10.071.

[200] C.L. Campion, W. Li, W.B. Euler, B.L. Lucht, B. Ravdel, J.F. DiCarlo, R. Gitzendanner, K.M. Abraham, Suppression of Toxic Compounds Produced in the Decomposition of Lithium-Ion Battery Electrolytes, Electrochem. Solid-State Lett. 7 (2004) A194. https://doi.org/10.1149/1.1738551.

[201] M. Broussely, Ph. Biensan, F. Bonhomme, Ph. Blanchard, S. Herreyre, K. Nechev, R.J. Staniewicz, Main aging mechanisms in Li ion batteries, Sel. Pap. Press. 12th Int. Meet. Lithium Batter. 146 (2005) 90–96. https://doi.org/10.1016/j.jpowsour.2005.03.172.

[202] L. Caracciolo, L. Madec, G. Gachot, H. Martinez, Impact of the Salt Anion on K Metal Reactivity in EC/DEC Studied Using GC and XPS Analysis, ACS Appl. Mater. Interfaces 13 (2021) 57505–57513. https://doi.org/10.1021/acsami.1c19537.

[203] F. Allgayer, J. Maibach, F. Jeschull, Comparing the Solid Electrolyte Interphases on Graphite Electrodes in K and Li Half Cells, ACS Appl. Energy Mater. 5 (2022) 1136–1148. https://doi.org/10.1021/acsaem.1c03491.

[204] J. Xu, CEI and SEI Formation in Li-Ion Batteries, in: V.S. Saji (Ed.), Corros. Degrad. Fuel Cells Supercapacitors Batter., Springer Nature Switzerland, Cham, 2024: pp. 307–324. https://doi.org/10.1007/978-3-031-57012-4_13.

[205] J.B. Goodenough, Y. Kim, Challenges for Rechargeable Li Batteries, Chem. Mater. 22 (2010) 587–603. https://doi.org/10.1021/cm901452z.

[206] N.-S. Choi, J.-G. Han, S.-Y. Ha, I. Park, C.-K. Back, Recent advances in the electrolytes for interfacial stability of high-voltage cathodes in lithium-ion batteries, RSC Adv. 5 (2015) 2732–2748. https://doi.org/10.1039/C4RA11575A.

[207] Y. Xie, H. Gao, J. Gim, A.T. Ngo, Z.-F. Ma, Z. Chen, Identifying Active Sites for Parasitic Reactions at the Cathode–Electrolyte Interface, J. Phys. Chem. Lett. 10 (2019) 589–594. https://doi.org/10.1021/acs.jpclett.8b03592.

[208] G.V. Zhuang, G. Chen, J. Shim, X. Song, P.N. Ross, T.J. Richardson, Li2CO3 in LiNi0.8Co0.15Al0.05O2 cathodes and its effects on capacity and power, J. Power Sources 134 (2004) 293–297. https://doi.org/10.1016/j.jpowsour.2004.02.030.

[209] K. Matsumoto, R. Kuzuo, K. Takeya, A. Yamanaka, Effects of CO2 in air on Li deintercalation from LiNi1−x−yCoxAlyO2, J. Power Sources 81–82 (1999) 558–561. https://doi.org/10.1016/S0378-7753(99)00216-5.

[210] Y. Bi, T. Wang, M. Liu, R. Du, W. Yang, Z. Liu, Z. Peng, Y. Liu, D. Wang, X. Sun, Stability of Li2CO3 in cathode of lithium ion battery and its influence on electrochemical performance, RSC Adv. 6 (2016) 19233–19237. https://doi.org/10.1039/C6RA00648E.

[211] G. Zampardi, F. La Mantia, Solid–Electrolyte Interphase at Positive Electrodes in High-Energy Li-Ion Batteries: Current Understanding and Analytical Tools, Batter. Supercaps 3 (2020) 672–697. https://doi.org/10.1002/batt.201900177.

[212] M. Egashira, H. Takahashi, S. Okada, J. Yamaki, Measurement of the electrochemical oxidation of organic electrolytes used in lithium batteries by microelectrode, J. Power Sources 92 (2001) 267–271. https://doi.org/10.1016/S0378-7753(00)00553-X.

[213] B. Larhrib, L. Madec, L. Monconduit, H. Martinez, A novel K-ion KVPO4F0.5O0.5/graphite full cell: Correlation between XPS SEI studies and electrochemical testing results, J. Power Sources 588 (2023) 233743. https://doi.org/10.1016/j.jpowsour.2023.233743.

[214] S. Zhao, G. Li, B. Zhang, S. Zhang, Y. Liu, J. Zhou, M. Luo, S. Guo, Highly-Solvating Electrolyte Enables Mechanically Stable and Inorganic-Rich Cathode Electrolyte Interphase for High-Performing Potassium-Ion Batteries, Adv. Mater. 36 (2024) 2405184. https://doi.org/10.1002/adma.202405184.

[215] J. Xing, S. Bliznakov, L. Bonville, M. Oljaca, R. Maric, A Review of Nonaqueous Electrolytes, Binders, and Separators for Lithium-Ion Batteries, Electrochem. Energy Rev. 5 (2022) 14. https://doi.org/10.1007/s41918-022-00131-z.

[216] B. Tong, Z. Song, H. Wan, W. Feng, M. Armand, J. Liu, H. Zhang, Z. Zhou, Sulfur-containing compounds as electrolyte additives for lithium-ion batteries, InfoMat 3 (2021) 1364–1392. https://doi.org/10.1002/inf2.12235.

[217] A.M. Haregewoin, A.S. Wotango, B.-J. Hwang, Electrolyte additives for lithium ion battery electrodes: progress and perspectives, Energy Environ. Sci. 9 (2016) 1955–1988. https://doi.org/10.1039/C6EE00123H.

[218] H. Zhang, G.G. Eshetu, X. Judez, C. Li, L.M. Rodriguez-Martínez, M. Armand, Electrolyte Additives for Lithium Metal Anodes and Rechargeable Lithium Metal Batteries: Progress and Perspectives, Angew. Chem. Int. Ed. 57 (2018) 15002–15027. https://doi.org/10.1002/anie.201712702.

[219] E. Peled, S. Menkin, Review—SEI: Past, Present and Future, J. Electrochem. Soc. 164 (2017) A1703. https://doi.org/10.1149/2.1441707jes.

[220] H. Wang, X. Li, F. Li, X. Liu, S. Yang, J. Ma, Formation and modification of cathode electrolyte interphase: A mini review, Electrochem. Commun. 122 (2021) 106870. https://doi.org/10.1016/j.elecom.2020.106870.

[221] J. Xu, Critical Review on cathode–electrolyte Interphase Toward High-Voltage Cathodes for Li-Ion Batteries, Nano-Micro Lett. 14 (2022) 166. https://doi.org/10.1007/s40820-022-00917-2.

[222] J. Li, H. Liu, J. Xia, A.R. Cameron, M. Nie, G.A. Botton, J.R. Dahn, The Impact of Electrolyte Additives and Upper Cut-off Voltage on the Formation of a Rocksalt Surface Layer in LiNi0.8Mn0.1Co0.1O2 Electrodes, J. Electrochem. Soc. 164 (2017) A655. https://doi.org/10.1149/2.0651704jes.

[223] I. Takahashi, H. Kiuchi, A. Ohma, T. Fukunaga, E. Matsubara, Cathode Electrolyte Interphase Formation and Electrolyte Oxidation Mechanism for Ni-Rich Cathode Materials, J. Phys. Chem. C 124 (2020) 9243–9248. https://doi.org/10.1021/acs.jpcc.0c02198.

[224] S. Tobishima, Y. Ogino, Y. Watanabe, Influence of electrolyte additives on safety and cycle life of rechargeable lithium cells, J. Appl. Electrochem. 33 (2003) 143–150. https://doi.org/10.1023/A:1024039302020.

[225] Q. Gu, M. Wang, Y. Liu, Y. Deng, L. Wang, J. Gao, Electrolyte Additives for Improving the High-Temperature Storage Performance of Li-Ion Battery NCM523‖Graphite with Overcharge Protection, ACS Appl. Mater. Interfaces 14 (2022) 4759–4766. https://doi.org/10.1021/acsami.1c22304.

[226] B. Song, X. Xiong, Y. Peng, X. Liu, W. Gao, T. Wang, F. Wang, Y. Ma, Y. Zhong, X.-B. Cheng, Z. Zhu, J. He, Y. Wu, Review of Electrolyte Additives for Secondary Sodium Batteries, Adv. Energy Mater. 14 (2024) 2401407. https://doi.org/10.1002/aenm.202401407.

[227] V. Etacheri, O. Haik, Y. Goffer, G.A. Roberts, I.C. Stefan, R. Fasching, D. Aurbach, Effect of Fluoroethylene Carbonate (FEC) on the Performance and Surface Chemistry of Si-Nanowire Li-Ion Battery Anodes, Langmuir 28 (2012) 965–976. https://doi.org/10.1021/la203712s.

[228] N.-S. Choi, K.H. Yew, K.Y. Lee, M. Sung, H. Kim, S.-S. Kim, Effect of fluoroethylene carbonate additive on interfacial properties of silicon thin-film electrode, J. Power Sources 161 (2006) 1254–1259. https://doi.org/10.1016/j.jpowsour.2006.05.049.

[229] A. Bouibes, N. Takenaka, T. Fujie, K. Kubota, S. Komaba, M. Nagaoka, Concentration Effect of Fluoroethylene Carbonate on the Formation of Solid Electrolyte Interphase Layer in Sodium-Ion Batteries, ACS Appl. Mater. Interfaces 10 (2018) 28525–28532. https://doi.org/10.1021/acsami.8b07530.

[230] V.A. Nikitina, S.M. Kuzovchikov, S.S. Fedotov, N.R. Khasanova, A.M. Abakumov, E.V. Antipov, Effect of the electrode/electrolyte interface structure on the potassium-ion diffusional and charge transfer rates: towards a high voltage potassium-ion battery, Electrochimica Acta 258 (2017) 814–824. https://doi.org/10.1016/j.electacta.2017.11.131.

[231] J. Liang, L. Liu, X. Liu, X. Meng, L. Zeng, J. Liu, J. Li, Z. Shi, Y. Yang, O3-Type $NaCrO_2$ as a Superior Cathode Material for Sodium/Potassium-Ion Batteries Ensured by High Structural Reversibility, ACS Appl. Mater. Interfaces 13 (2021) 22635–22645. https://doi.org/10.1021/acsami.1c04997.

[232] S. Baek, S. Jie, B. Lee, Effects of fluoroethylene carbonate additive on potassium metal anode, J. Mech. Sci. Technol. 37 (2023) 3657–3665. https://doi.org/10.1007/s12206-023-0630-3.

[233] S.U. Yoon, H. Kim, H.-J. Jin, Y.S. Yun, Effects of fluoroethylene carbonate-induced solid-electrolyte-interface layers on carbon-based anode materials for potassium ion batteries, Appl. Surf. Sci. 547 (2021) 149193. https://doi.org/10.1016/j.apsusc.2021.149193.

[234] A.W. Ells, R. May, L.E. Marbella, Potassium Fluoride and Carbonate Lead to Cell Failure in Potassium-Ion Batteries, ACS Appl. Mater. Interfaces 13 (2021) 53841–53849. https://doi.org/10.1021/acsami.1c15174.

[235] P. Jankowski, N. Lindahl, J. Weidow, W. Wieczorek, P. Johansson, Impact of Sulfur-Containing Additives on Lithium-Ion Battery Performance: From Computational Predictions to Full-Cell Assessments, ACS Appl. Energy Mater. 1 (2018) 2582–2591. https://doi.org/10.1021/acsaem.8b00295.

[236] H. Lee, S. Choi, S. Choi, H.-J. Kim, Y. Choi, S. Yoon, J.-J. Cho, SEI layer-forming additives for LiNi0.5Mn1.5O4/graphite 5V Li-ion batteries, Electrochem. Commun. 9 (2007) 801–806. https://doi.org/10.1016/j.elecom.2006.11.008.

[237] T. Yang, W. Wang, S. Li, J. Lu, W. Fan, X. Zuo, J. Nan, Sulfur-containing C2H2O8S2 molecules as an overall-functional electrolyte additive for high-voltage LiNi0.5Co0.2Mn0.3O2/graphite batteries with enhanced performance, J. Power Sources 470 (2020) 228462. https://doi.org/10.1016/j.jpowsour.2020.228462.

[238] B.T. Yu, W.H. Qiu, F.S. Li, L. Cheng, A study on sulfites for lithium-ion battery electrolytes, Spec. Issue Sel. Pap. 6th Int. Conf. Lead-Acid Batter. LABAT 2005 Varna Bulg. 11th Asian Battery Conf. 11 ABC Ho Chi Minh City Vietnam Together Regul. Pap. 158 (2006) 1373–1378. https://doi.org/10.1016/j.jpowsour.2005.10.033.

[239] Q. Zhang, Z. Wang, X. Li, H. Guo, W. Peng, J. Wang, G. Yan, Comparative study of 1,3-propane sultone, prop-1-ene-1,3-sultone and ethylene sulfate as film-forming additives for sodium ion batteries, J. Power Sources 541 (2022) 231726. https://doi.org/10.1016/j.jpowsour.2022.231726.

[240] L. Madec, J. Xia, R. Petibon, K.J. Nelson, J.-P. Sun, I.G. Hill, J.R. Dahn, Effect of Sulfate Electrolyte Additives on $LiNi_{1/3}Mn_{1/3}Co_{1/3}O_2$ /Graphite Pouch Cell Lifetime: Correlation between XPS Surface Studies and Electrochemical Test Results, J. Phys. Chem. C 118 (2014) 29608–29622. https://doi.org/10.1021/jp509731y.

[241] X. Li, Z. Yin, X. Li, C. Wang, Ethylene sulfate as film formation additive to improve the compatibility of graphite electrode for lithium-ion battery, Ionics 20 (2014) 795–801. https://doi.org/10.1007/s11581-013-1036-5.

[242] T. Taskovic, L.M. Thompson, A. Eldesoky, M.D. Lumsden, J.R. Dahn, Optimizing Electrolyte Additive Loadings in NMC532/Graphite Cells: Vinylene Carbonate and Ethylene Sulfate, J. Electrochem. Soc. 168 (2021) 010514. https://doi.org/10.1149/1945-7111/abd833.

[243] A. Klein, T. Mayer, A. Thissen, W. Jaegermann, Photoelectron Spectroscopy in Materials Science and Physical Chemistry: Analysis of Composition, Chemical Bonding, and Electronic Structure of Surfaces and Interfaces, in: Methods Phys. Chem., 2012: pp. 477–512. https://doi.org/10.1002/9783527636839.ch15.

[244] C. Bünzli, H. Kaiser, P. Novák, Important Aspects for Reliable Electrochemical Impedance Spectroscopy Measurements of Li-Ion Battery Electrodes, J. Electrochem. Soc. 162 (2015) A218–A222. https://doi.org/10.1149/2.1061501jes.

[245] F. Holtstiege, A. Wilken, M. Winter, T. Placke, Running out of lithium? A route to differentiate between capacity losses and active lithium losses in lithium-ion batteries, Phys. Chem. Chem. Phys. 19 (2017) 25905–25918. https://doi.org/10.1039/C7CP05405J.

[246] B. Larhrib, L. Madec, Toward Highly Reliable Potassium-Ion Half and Full Coin Cells, Batter. Supercaps 6 (2023) e202300061. https://doi.org/10.1002/batt.202300061.

[247] T. Hosaka, S. Muratsubaki, K. Kubota, H. Onuma, S. Komaba, Potassium Metal as Reliable Reference Electrodes of Nonaqueous Potassium Cells, J. Phys. Chem. Lett. 10 (2019) 3296–3300. https://doi.org/10.1021/acs.jpclett.9b00711.

[248] S. Dhir, B. Jagger, A. Maguire, M. Pasta, Fundamental investigations on the ionic transport and thermodynamic properties of non-aqueous potassium-ion electrolytes, Nat. Commun. 14 (2023) 3833. https://doi.org/10.1038/s41467-023-39523-0.

[249] J. Rizell, W. Chrobak, N. Mozhzhukhina, S. Xiong, A. Matic, Electrochemical Signatures of Potassium Plating and Stripping, J. Electrochem. Soc. 171 (2024) 020517. https://doi.org/10.1149/1945-7111/ad2593.

[250] F. Allgayer, J. Maibach, F. Jeschull, Comparing the Solid Electrolyte Interphases on Graphite Electrodes in K and Li Half Cells, ACS Appl. Energy Mater. 5 (2022) 1136–1148. https://doi.org/10.1021/acsaem.1c03491.

[251] T. Roth, L. Streck, N. Mujanovic, M. Winter, P. Niehoff, A. Jossen, Transient Self-Discharge after Formation in Lithium-Ion Cells: Impact of State-of-Charge and Anode Overhang, J. Electrochem. Soc. 170 (2023) 080524. https://doi.org/10.1149/1945-7111/acf164.

[252] G. Bridgewater, M.J. Capener, J. Brandon, M.J. Lain, M. Copley, E. Kendrick, A Comparison of Lithium-Ion Cell Performance across Three Different Cell Formats, Batteries 7 (2021) 38. https://doi.org/10.3390/batteries7020038.

[253] Y. Mo, W. Zhou, K. Wang, K. Xiao, Y. Chen, Z. Wang, P. Tang, P. Xiao, Y. Gong, S. Chen, P. Gao, J. Liu, Engineering Electrode/Electrolyte Interphase Chemistry toward High-Rate and Long-Life Potassium Ion Full-Cell, ACS Energy Lett. 8 (2023) 995–1002. https://doi.org/10.1021/acsenergylett.2c02659.

[254] M.J. Trahan, S. Mukerjee, E.J. Plichta, M.A. Hendrickson, K.M. Abraham, Studies of Li-Air Cells Utilizing Dimethyl Sulfoxide-Based Electrolyte, J. Electrochem. Soc. 160 (2012) A259. https://doi.org/10.1149/2.048302jes.

[255] B.E. Murdock, C.G. Armstrong, D.E. Smith, N. Tapia-Ruiz, K.E. Toghill, Misreported non-aqueous reference potentials: The battery research endemic, Joule 6 (2022) 928–934. https://doi.org/10.1016/j.joule.2022.04.009.

[256] E.C. Cengiz, J. Rizell, M. Sadd, A. Matic, N. Mozhzhukhina, Review—Reference Electrodes in Li-Ion and Next Generation Batteries: Correct Potential Assessment, Applications and Practices, J. Electrochem. Soc. 168 (2021) 120539. https://doi.org/10.1149/1945-7111/ac429b.

[257] S.E. Lee, M.H. Tang, Electroactive decomposition products cause erroneous intercalation signals in sodium-ion batteries, Electrochem. Commun. 100 (2019) 70–73. https://doi.org/10.1016/j.elecom.2019.01.024.

[258] Y. Yamada, Y. Iriyama, T. Abe, Z. Ogumi, Kinetics of Lithium Ion Transfer at the Interface between Graphite and Liquid Electrolytes: Effects of Solvent and Surface Film, Langmuir 25 (2009) 12766–12770. https://doi.org/10.1021/la901829v.

[259] K.R. Cho, M. Kim, B. Kim, G. Shin, S. Lee, W. Kim, Investigation of the AgCl Formation Mechanism on the Ag Wire Surface for the Fabrication of a Marine Low-Frequency-Electric-Field-Detection Ag/AgCl Sensor Electrode, ACS Omega 7 (2022) 25110–25121. https://doi.org/10.1021/acsomega.2c01481.

[260] Y. Feng, A.M. Rao, J. Zhou, B. Lu, Selective Potassium Deposition Enables Dendrite-Resistant Anodes for Ultrastable Potassium-Metal Batteries, Adv. Mater. 35 (2023) 2300886. https://doi.org/10.1002/adma.202300886.

[261] M. Hamada, R. Tatara, K. Kubota, S. Kumakura, S. Komaba, All-Solid-State Potassium Polymer Batteries Enabled by the Effective Pretreatment of Potassium Metal, ACS Energy Lett. 7 (2022) 2244–2246. https://doi.org/10.1021/acsenergylett.2c01096.

[262] S. Ko, X. Han, T. Shimada, N. Takenaka, Y. Yamada, A. Yamada, Electrolyte design for lithium-ion batteries with a cobalt-free cathode and silicon oxide anode, Nat. Sustain. (2023). https://doi.org/10.1038/s41893-023-01237-y.

[263] S. Ko, T. Obukata, T. Shimada, N. Takenaka, M. Nakayama, A. Yamada, Y. Yamada, Electrode potential influences the reversibility of lithium-metal anodes, Nat. Energy 7 (2022) 1217–1224. https://doi.org/10.1038/s41560-022-01144-0.

[264] G.G. Eshetu, S. Grugeon, H. Kim, S. Jeong, L. Wu, G. Gachot, S. Laruelle, M. Armand, S. Passerini, Comprehensive Insights into the Reactivity of Electrolytes Based on Sodium Ions, ChemSusChem 9 (2016) 462–471. https://doi.org/10.1002/cssc.201501605.

[265] L. Caracciolo, L. Madec, H. Martinez, XPS Analysis of K-based Reference Compounds to Allow Reliable Studies of Solid Electrolyte Interphase in K-ion Batteries, ACS Appl. Energy Mater. 4 (2021) 11693–11699. https://doi.org/10.1021/acsaem.1c02400.

[266] H. Wang, D. Zhai, F. Kang, Solid electrolyte interphase (SEI) in potassium ion batteries, Energy Environ. Sci. 13 (2020) 4583–4608. https://doi.org/10.1039/D0EE01638A.

[267] M.J. Piernas-Muñoz, E. Castillo-Martínez, O. Bondarchuk, M. Armand, T. Rojo, Higher voltage plateau cubic Prussian White for Na-ion batteries, J. Power Sources 324 (2016) 766–773. https://doi.org/10.1016/j.jpowsour.2016.05.050.

[268] C. Gervais, M.-A. Languille, G. Moretti, S. Réguer, X-ray Photochemistry of Prussian Blue Cellulosic Materials: Evidence for a Substrate-Mediated Redox Process, Langmuir 31 (2015) 8168–8175. https://doi.org/10.1021/acs.langmuir.5b00770.

[269] D.A. El Mously, A.M. Mahmoud, A.M. Abdel-Raoof, E. Elgazzar, Synthesis of Prussian Blue Analogue and Its Catalytic Activity toward Reduction of Environmentally Toxic Nitroaromatic Pollutants, ACS Omega 7 (2022) 43139–43146. https://doi.org/10.1021/acsomega.2c05694.

[270] Y. Xu, Z. Yuan, L. Song, T. Ding, D. Sun, L. Wang, X. Zhou, Ultrathin Cobalt-Based Prussian Blue Analogue Nanosheet-Assembled Nanoboxes Interpenetrated with Carbon Nanotubes as a Fast Electron/Potassium-Ion Conductor for Superior Potassium Storage, Nano Lett. 23 (2023) 9594–9601. https://doi.org/10.1021/acs.nanolett.3c03281.

[271] A. Cano, J. Rodríguez-Hernández, L. Reguera, E. Rodríguez-Castellón, E. Reguera, On the Scope of XPS as Sensor in Coordination Chemistry of Transition Metal Hexacyanometallates, Eur. J. Inorg. Chem. 2019 (2019) 1724–1732. https://doi.org/10.1002/ejic.201801556.

[272] H. Hantsche, High resolution XPS of organic polymers, the scienta ESCA300 database. By G. Beamson and D. Briggs, Wiley, Chichester 1992, 295 pp., hardcover, £ 65.00, ISBN 0-471-93592-1, Adv. Mater. 5 (1993) 778–778. https://doi.org/10.1002/adma.19930051035.

[273] A.N. Mansour, J.K. Ko, G.H. Waller, C.A. Martin, C. Zhang, X. Qiao, Y. Wang, X. Zhou, M. Balasubramanian, Structural Analysis of $K_4Fe(CN)_6 \cdot 3H_2O$, $K_3Fe(CN)_6$ and Prussian Blue, ECS J. Solid State Sci. Technol. 10 (2021) 103002. https://doi.org/10.1149/2162-8777/ac2591.

[274] A P Monkman, G C Stevens, D Bloor, X-ray photoelectron spectroscopic investigations of the chain structure anddoping mechanisms in polyaniline, J. Phys. Appl. Phys. 24 (1991) 738. https://doi.org/10.1088/0022-3727/24/5/017.

[275] N. Hellgren, R.T. Haasch, S. Schmidt, L. Hultman, I. Petrov, Interpretation of X-ray photoelectron spectra of carbon-nitride thin films: New insights from in situ XPS, Carbon 108 (2016) 242–252. https://doi.org/10.1016/j.carbon.2016.07.017.

[276] N. Vannerberg, V. Ng, THE ESCA-SPECTRA OF SODIUM AND POTASSIUM CYANIDE AND OF THE SODIUM AND POTASSIUM SALTS OF THE HEXACYANO-METALLATES OF THE FIRST TRANSITION METAL SERIES., in: 1976. https://api.semanticscholar.org/CorpusID:230171479.

[277] H. Konno, K. Sasaki, M. Tsunekawa, T. Takamori, R. Furuich, X-Ray photoelectron spectroscopic analysis of surface products on pyrite formed by bacterial leaching, Bunseki Kagaku 40 (1991) 609–616. https://doi.org/10.2116/bunsekikagaku.40.11_609.

[278] A. Cano, Y. Avila, M. Avila, E. Reguera, Structural information contained in the XPS spectra of nd10 metal cyanides, J. Solid State Chem. 276 (2019) 339–344. https://doi.org/10.1016/j.jssc.2019.05.021.

[279] F. Jeschull, E. Kataev, I. Panasenko, C. Njel, R. Félix, J. Maibach, Why Half-Cell Samples Provide Limited Insight Into the Aging Mechanisms of Potassium Batteries, Adv. Energy Mater. n/a (2024) 2403811. https://doi.org/10.1002/aenm.202403811.

[280] C.D. Wagner, D.A. Zatko, R.H. Raymond, Use of the oxygen KLL Auger lines in identification of surface chemical states by electron spectroscopy for chemical analysis, Anal. Chem. 52 (1980) 1445–1451. https://doi.org/10.1021/ac50059a017.

[281] D. He, Y. Zhang, D. Cao, M. Sun, J. Xia, Y. Yang, Y. Ding, H. Chen, A flexible free-standing FeF3/reduced graphene oxide film as cathode for advanced lithium-ion battery, J. Alloys Compd. 909 (2022) 164702. https://doi.org/10.1016/j.jallcom.2022.164702.

[282] Y. Shi, P. Yin, J. Li, X. Xu, Q. Jiang, J. Li, H.M.K. Sari, J. Wang, W. Li, J. Hu, Q. Lin, J. Liu, J. Yang, X. Li, Ultra-high rate capability of in-situ anchoring FeF3 cathode onto double-enhanced conductive Fe/graphitic carbon for high energy density lithium-ion batteries, Nano Energy 108 (2023) 108181. https://doi.org/10.1016/j.nanoen.2023.108181.

Appendix

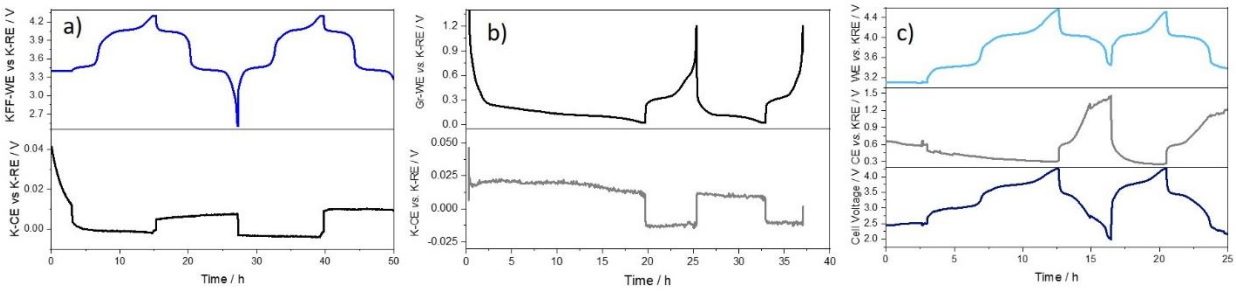

Figure A 1. Application of K-RE in 3-el setup in 0.75 M KPF_6 EC:DEC electrolyte with 1 wt. % DTD a) KFF/K half-cell b) Graphite/K half-cell c) KFF/graphite full cell. Scan rate: C/20

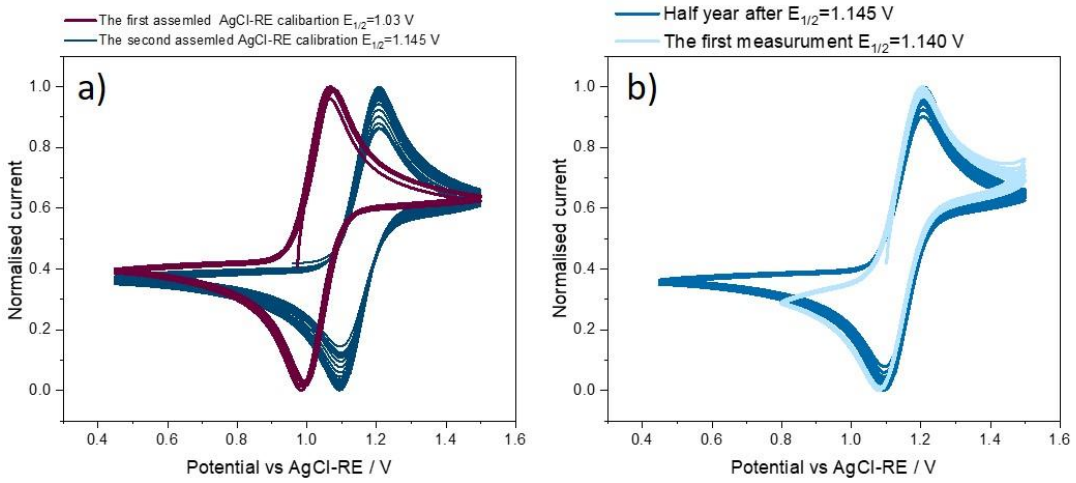

Figure A 2. a) potential difference of two AgCl-RE b) aging and potential drift of AgCl-RE after assembly and after half year by comparison of cyclic voltammograms (scan rate 20 mV s^{-1}) in 100 mM KPF_6 and 10 mM Fc^+/Fc in EC:DEC, v/v=1:1 electrolyte (against Pt and Cu electrodes);

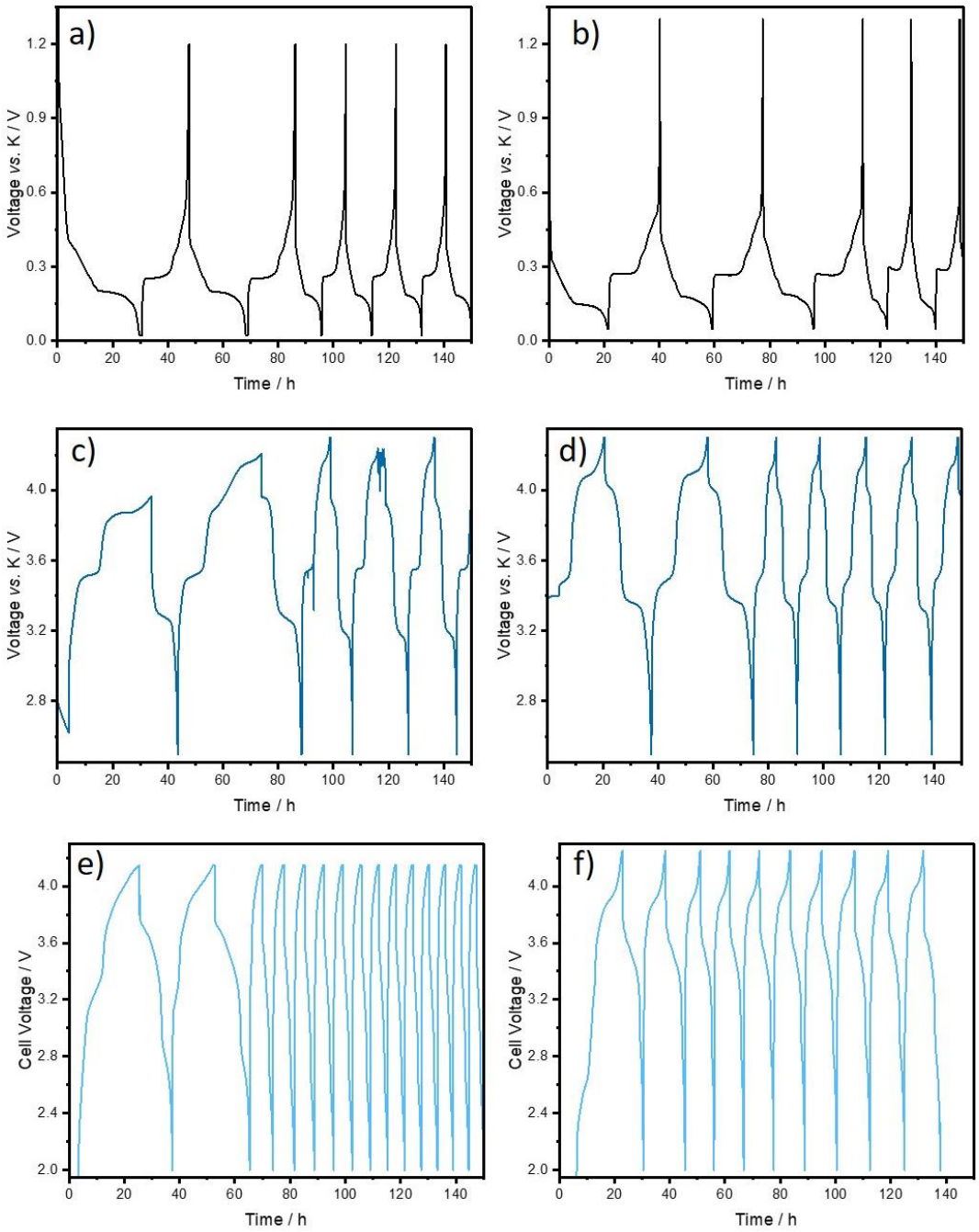

Figure A 3. Two electrode cell cycling curves in graphite half-cells (750 mM KPF_6 in EC:DEC): a) without DTD b) with 1 wt. % DTD; KFF half cells c) without DTD d) with 1 wt. % DTD; KFF vs. graphite full cell e) without DTD f) with 1 wt. % DTD;

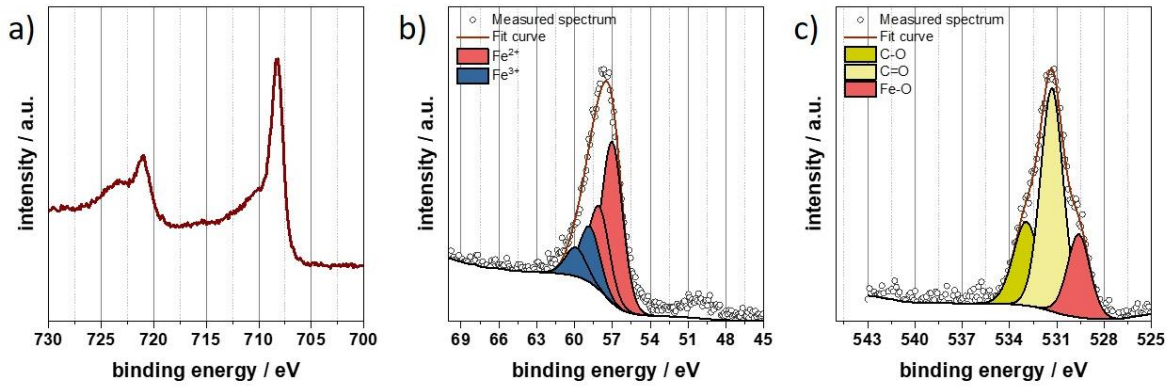

Figure A 4. XPS spectra of KFF powder: a) Fe2p spectrum; b) Fe3p spectrum; c) O1s spectrum

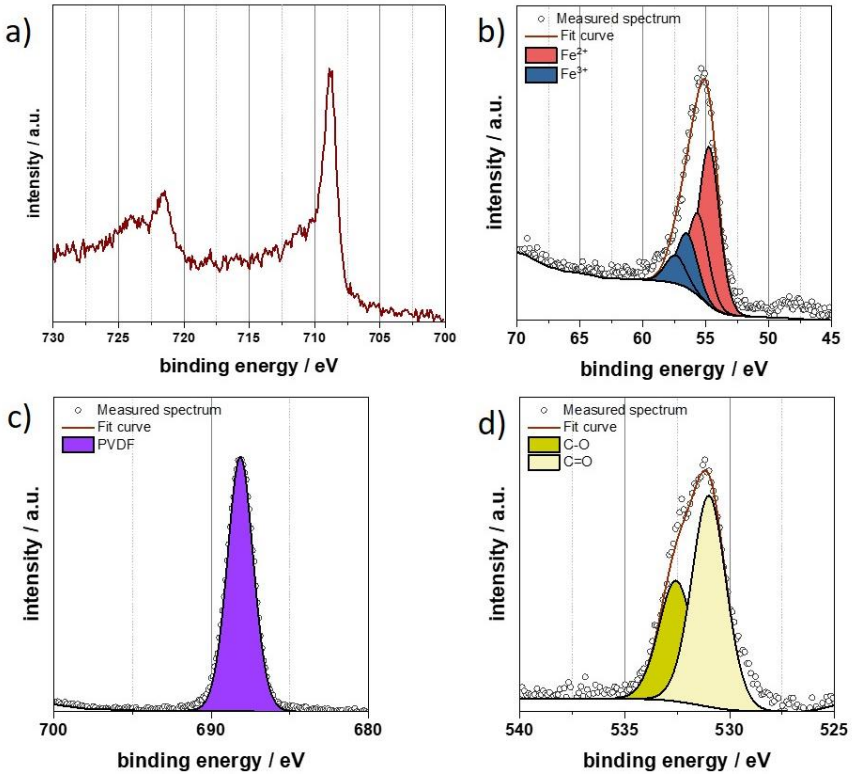

Figure A 5. XPS spectra of KFF electrode: a) Fe2p spectrum; b) Fe3p spectrum; c) F1s spectrum; d) O1s spectrum

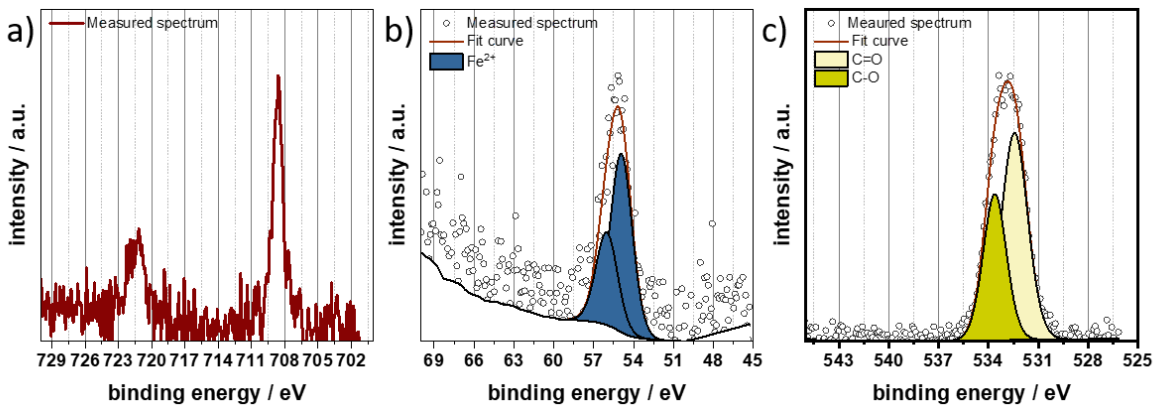

Figure A 6. XPS spectra of KFe2 powder a) Fe2p spectrum; b) Fe3p spectrum; c) O1s spectrum

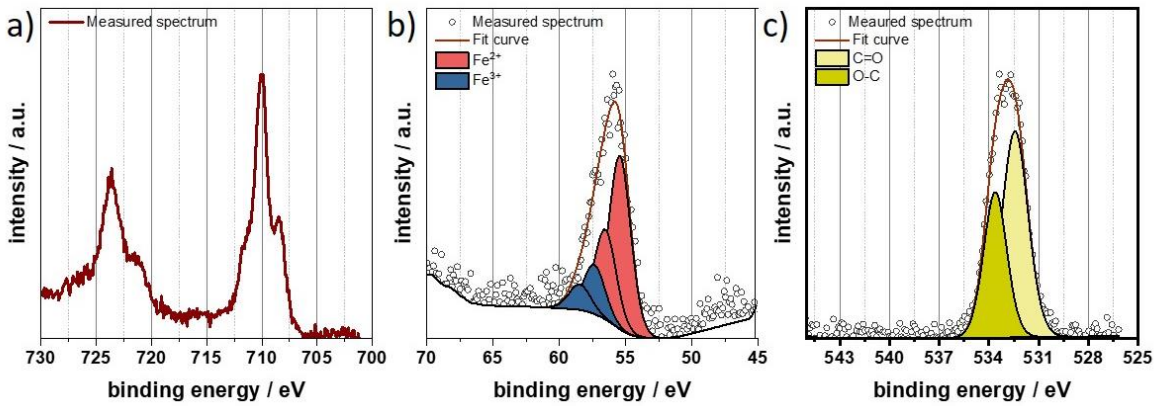

Figure A 7. XPS spectra of KFe3 powder a) Fe2p spectrum; b) Fe3p spectrum; c) O1s spectrum

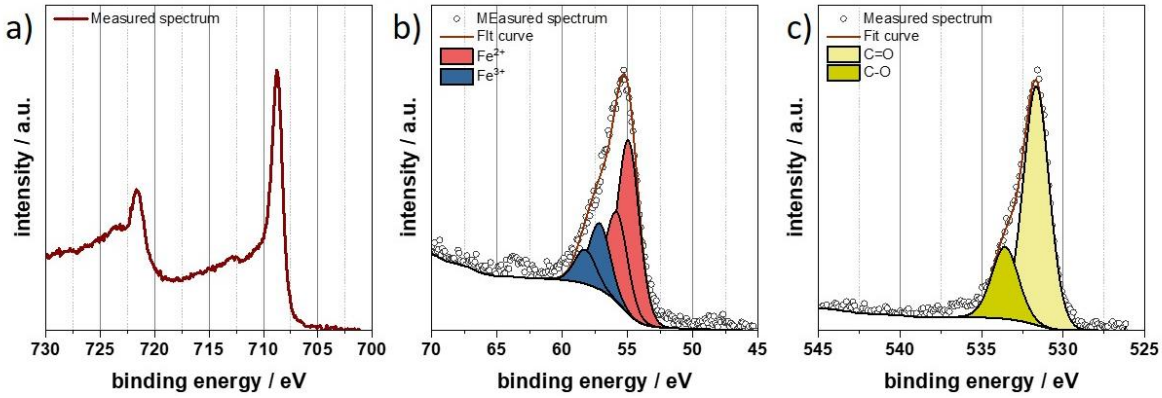

Figure A 8. XPS spectra of Prussian Blue powder a) Fe2p spectrum; b) Fe3p spectrum; c) O1s spectrum

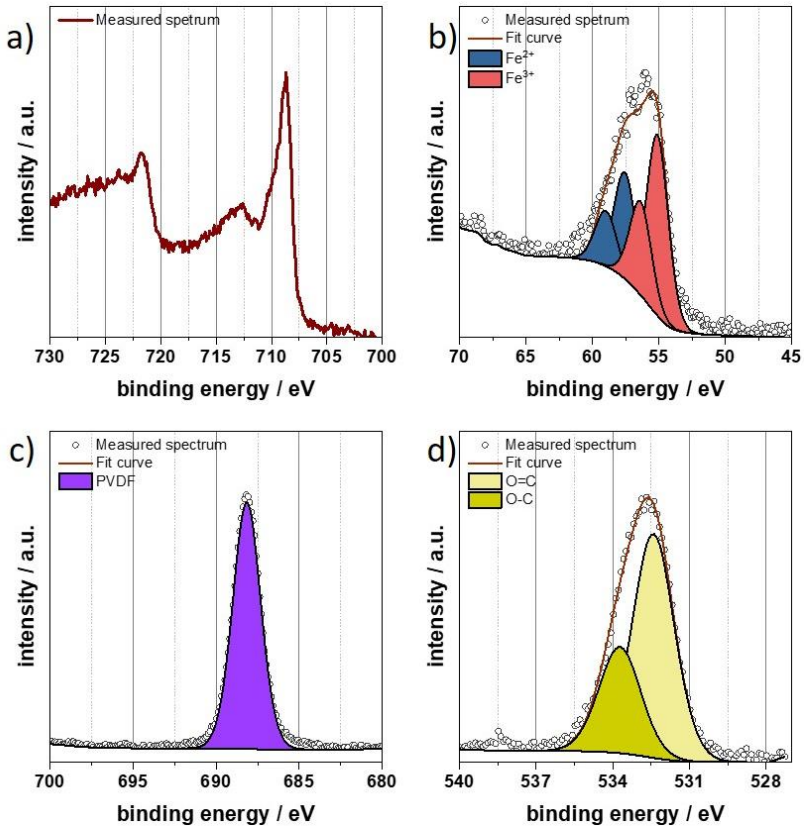

Figure A 9. XPS spectra of Prussian Green electrode: a) Fe2p spectrum; b) Fe3p spectrum; c) F1s spectrum; d) O1s spectrum

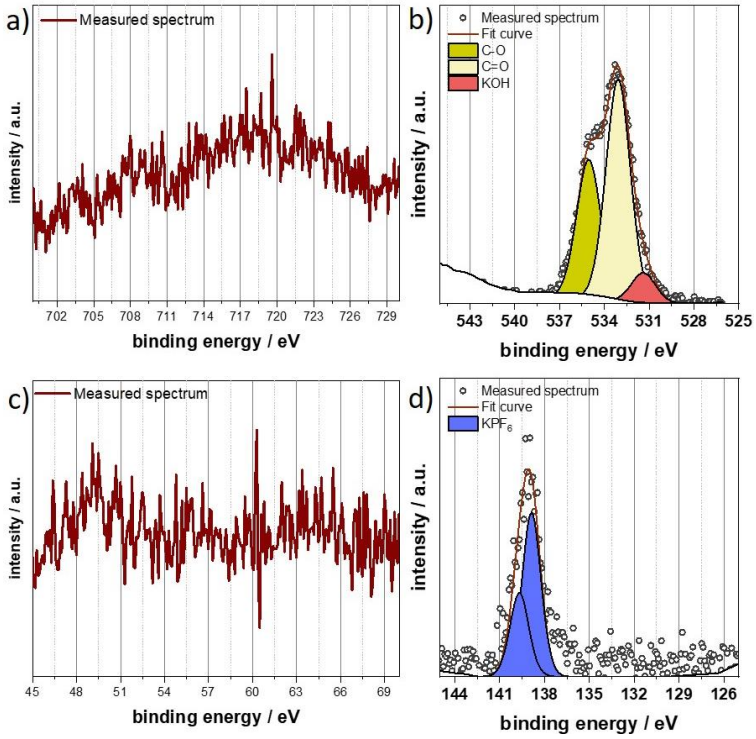

Figure A 10. a)Fe2p; b)O1s; c)Fe3p; d)P2p spectra of half cell KFF electrode stored in 750 mM KPF_6 EC:DEC electrolyte

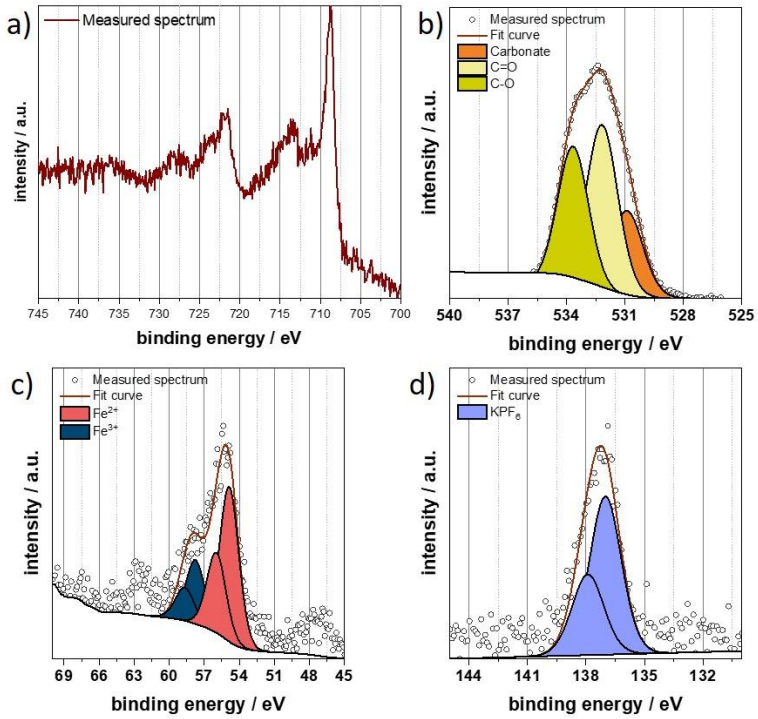

Figure A 11. a)Fe2p; b)O1s; c)Fe3p; d)P2p spectra of half cell KFF electrode cycled 1 cycle in 750 mM KPF_6 EC:DEC electrolyte

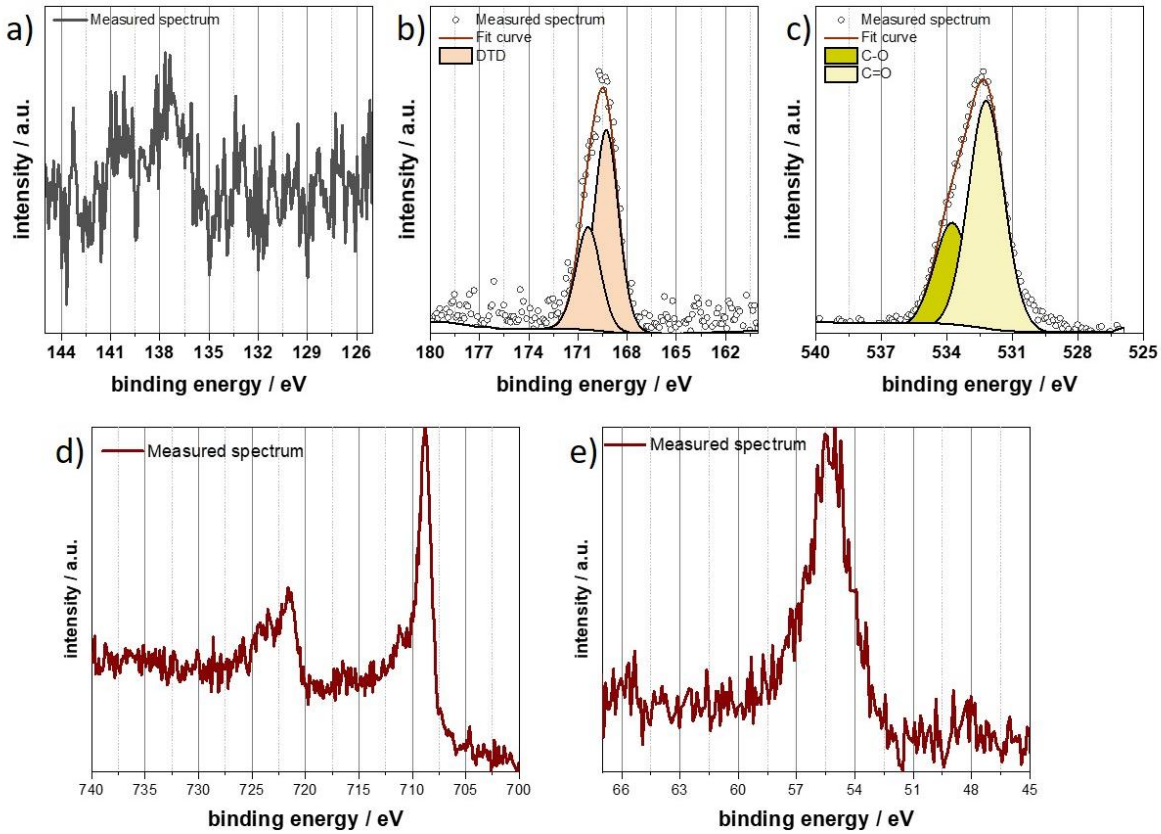

Figure A 12. a)P2p; b)S2p; c)O1s; d)F2p; e) Fe3p spectra of half cell KFF electrode stored in 750 mM KPF_6 EC:DEC 1 wt. % DTD electrolyte

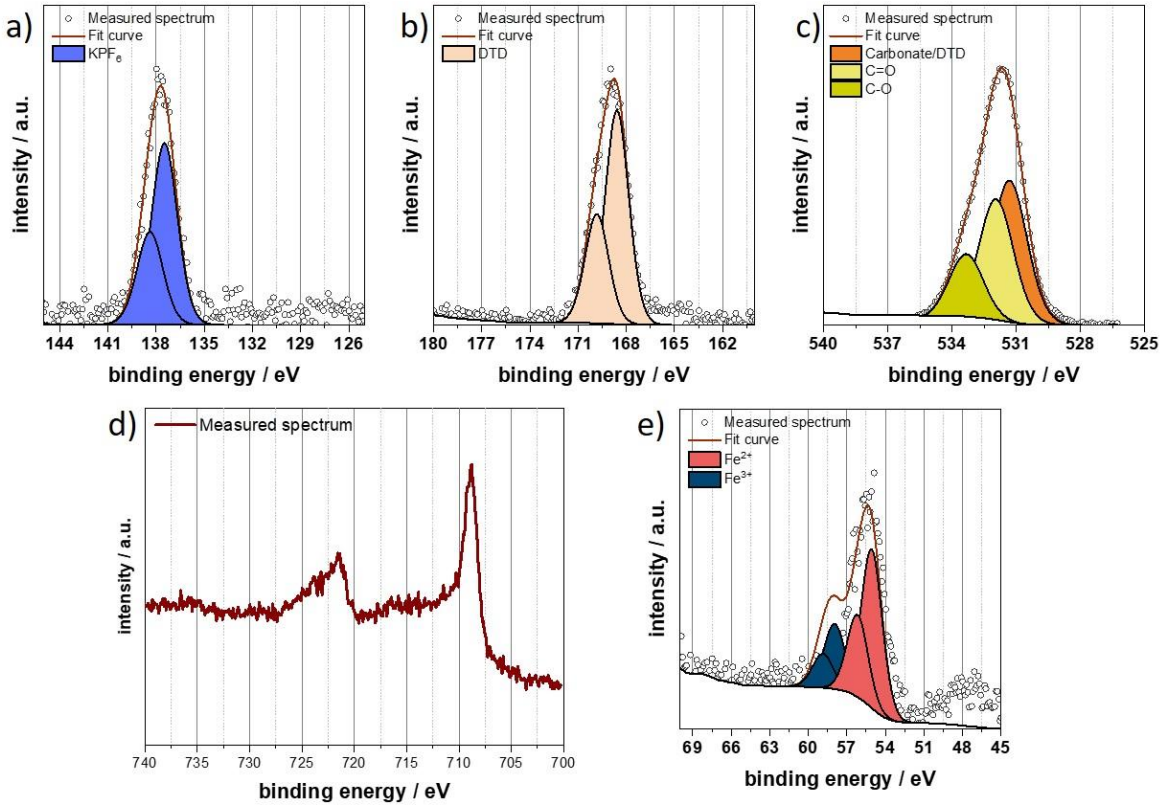

Figure A 13. a)P2p; b)S2p; c)O1s; d)F2p; e) Fe3p spectra of half cell KFF electrode cycled 1 cycle in 750 mM KPF_6 EC:DEC 1 wt. % DTD electrolyte

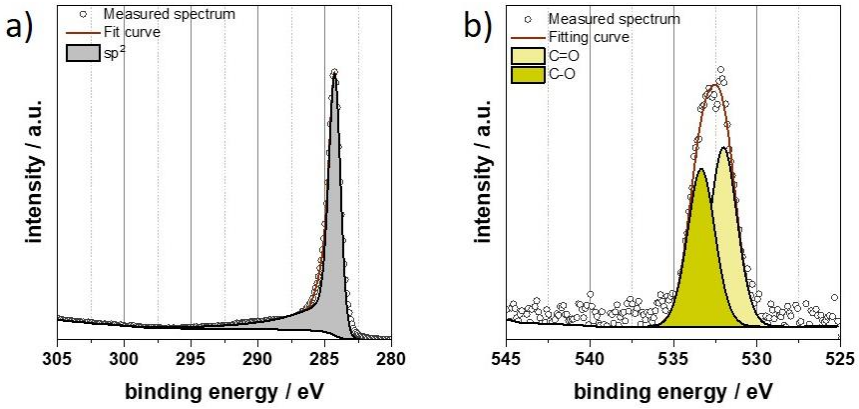

Figure A 14. XPS spectra of graphite powder: a) C1s spectrum; b) O1s spectrum

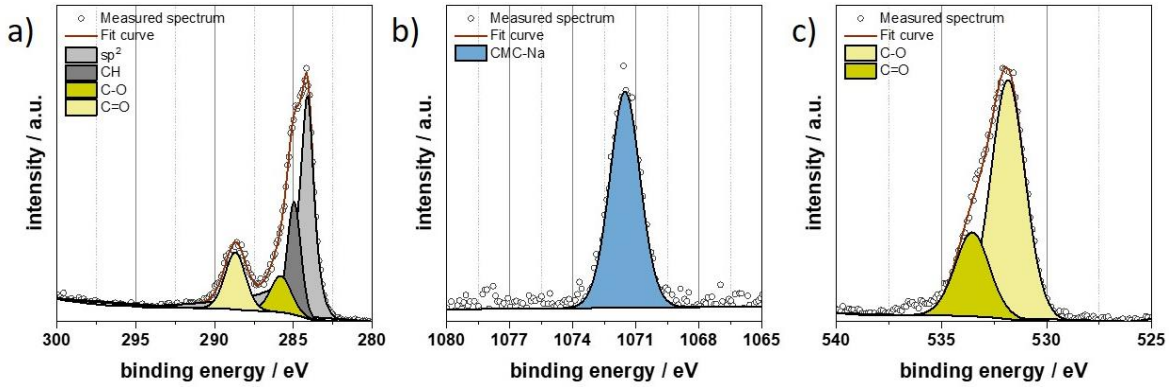

Figure A 15 XPS spectra of coated graphite electrode: a) C1s spectrum; b) Na1s spectrum; c) O1s spectrum

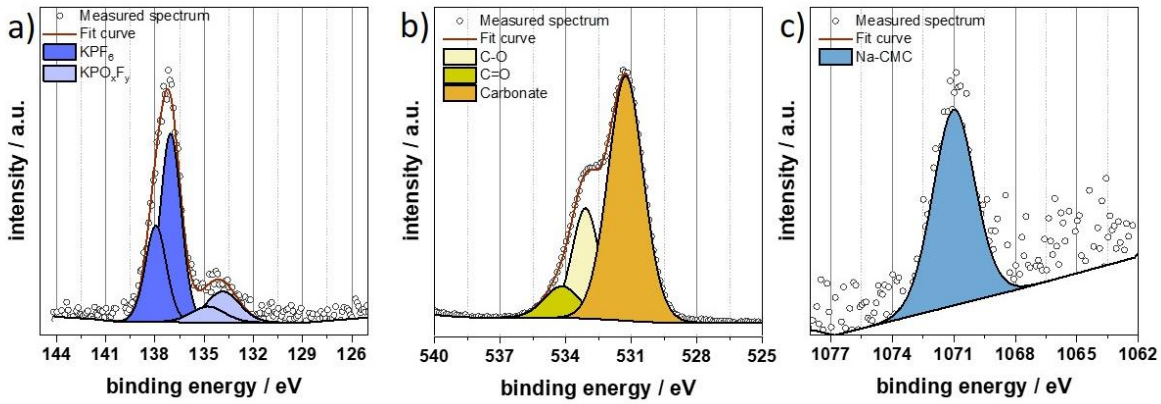

Figure A 16. a)P2p; b) O1s; c)Na1s spectra of half cell graphite electrode stored in 750 mM KPF_6 EC:DEC electrolyte

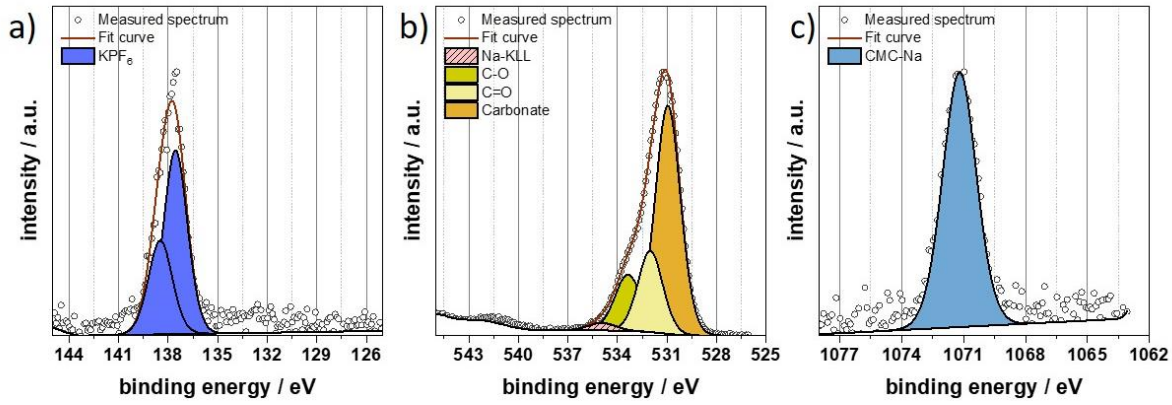

Figure A 17. a)P2p; b) O1s; c)Na1s spectra of half cell graphite electrode cycled 1 cycle in 750 mM KPF_6 EC:DEC electrolyte

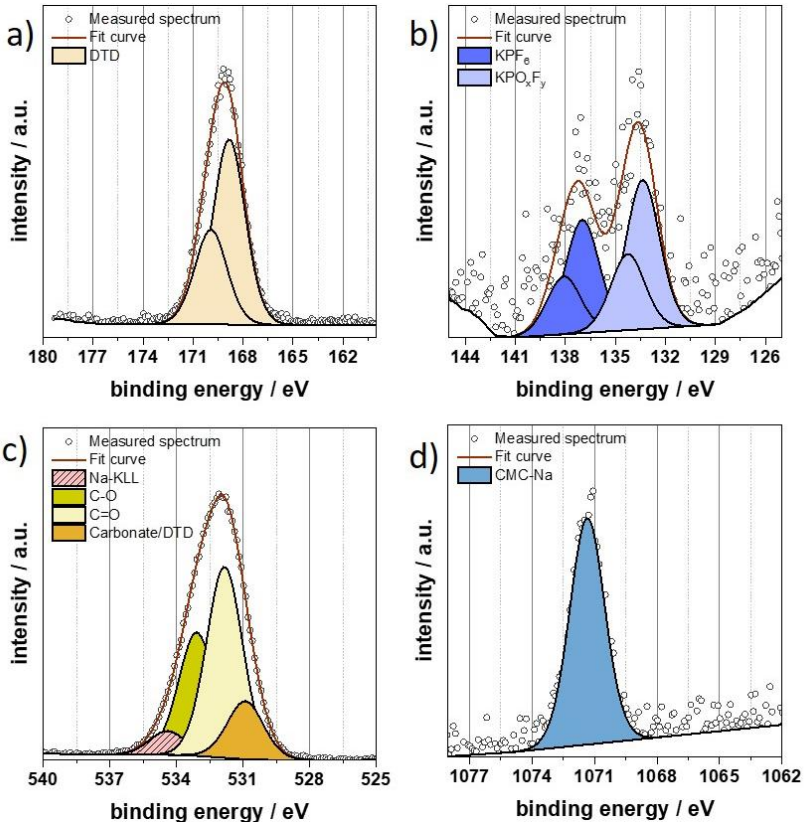

Figure A 18 a)S2p; b)P2p; c) O1s; d)Na1s spectra of half cell graphite electrode stored in 750 mM KPF_6 EC:DEC 1 wt. % DTD electrolyte

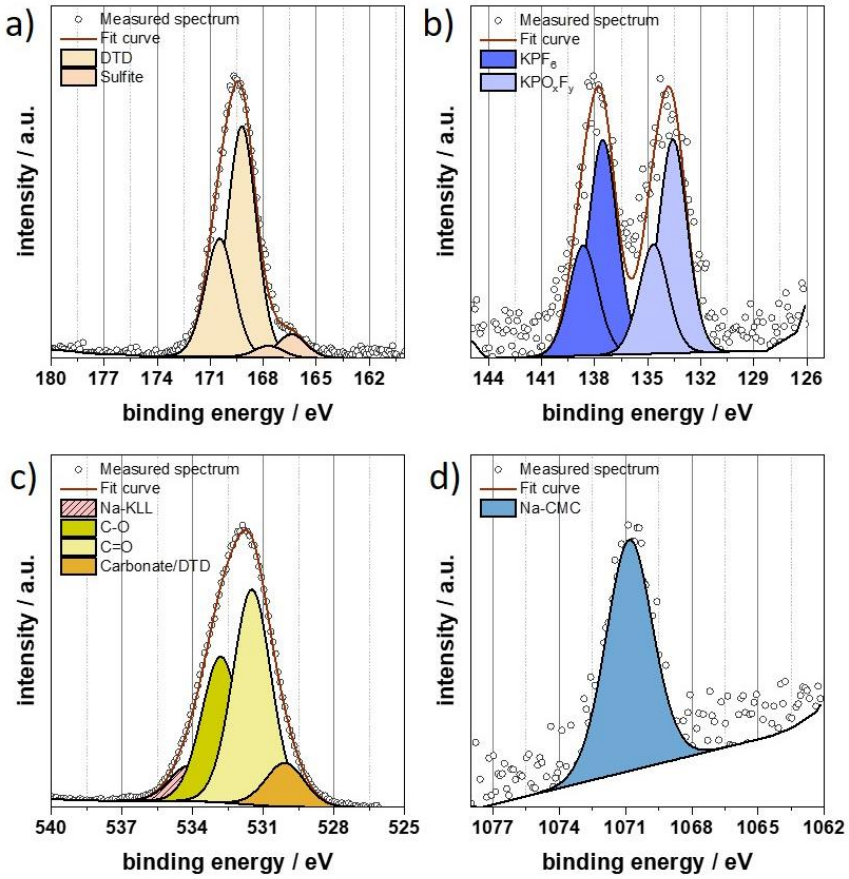

Figure A 19. a)S2p; b)P2p; c) O1s; d)Na1s spectra of half cell graphite electrode cycled 1 cycle in 750 mM KPF_6 EC:DEC 1 wt. % DTD electrolyte

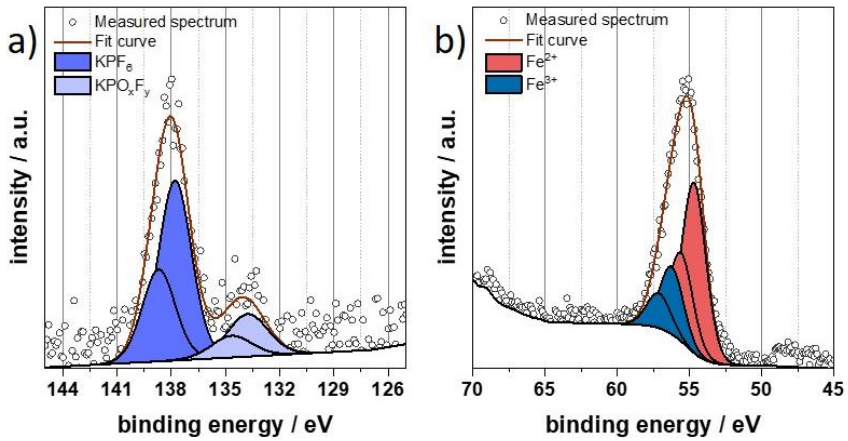

Figure A 20. a)P2p; b) Fe3p spectra of Full cell KFF electrode stored in 750 mM KPF_6 EC:DEC electrolyte

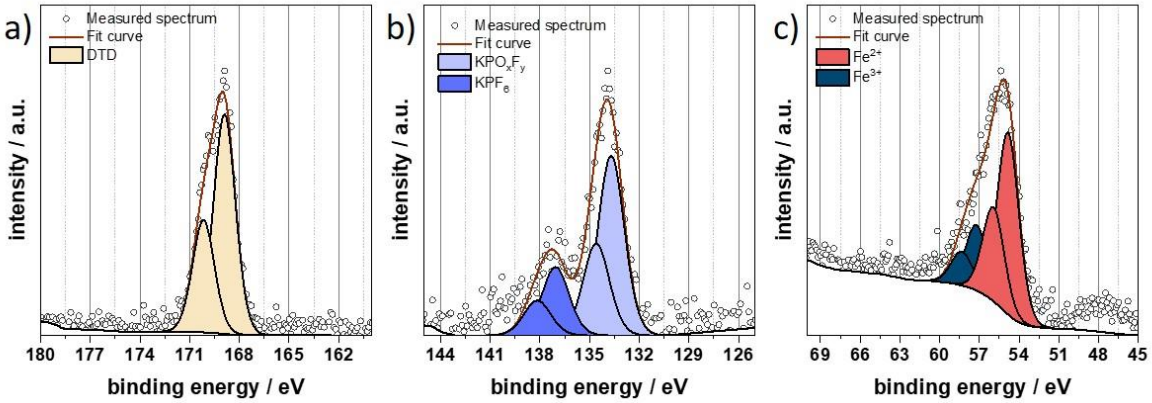

Figure A 21. a)S2p: b)P2p; bc Fe3p spectra of Full cell KFF electrode stored in 750 mM KPF_6 EC:DEC electrolyte 1 wt. DTD

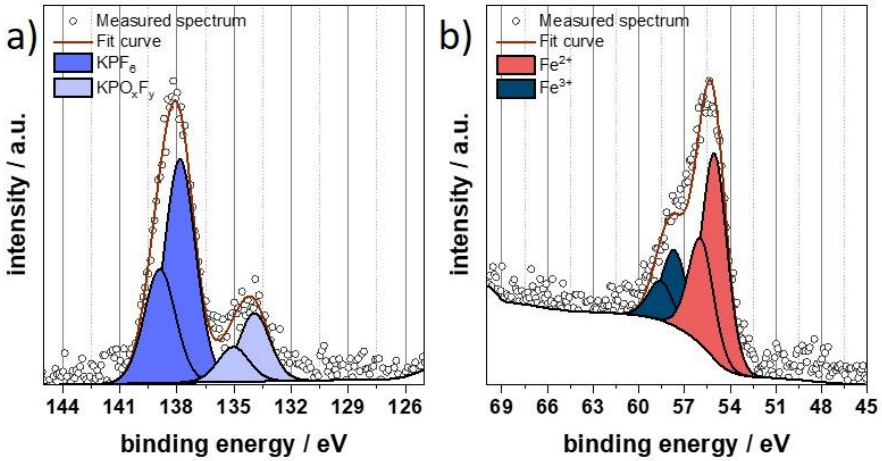

Figure A 22. a)P2p; b) Fe3p spectra of Full cell KFF electrode cycled 1 cycle in 750 mM KPF_6 EC:DEC electrolyte

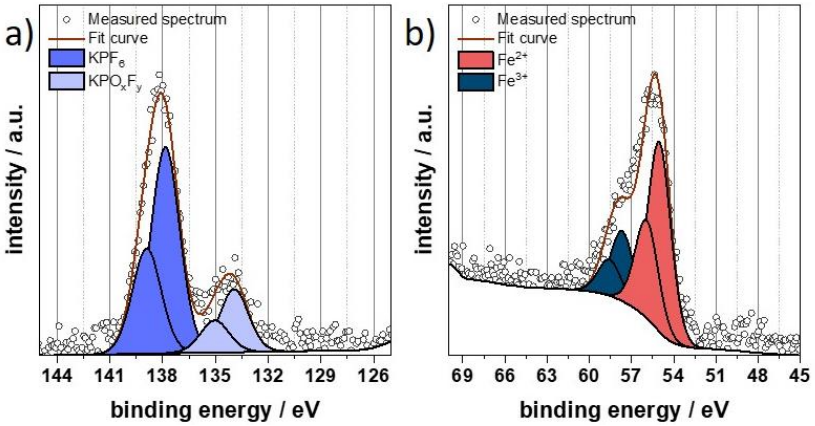

Figure A 23. a)P2p; b) Fe3p spectra of Full cell KFF electrode cycled 1 cycle in 750 mM KPF_6 EC:DEC electrolyte

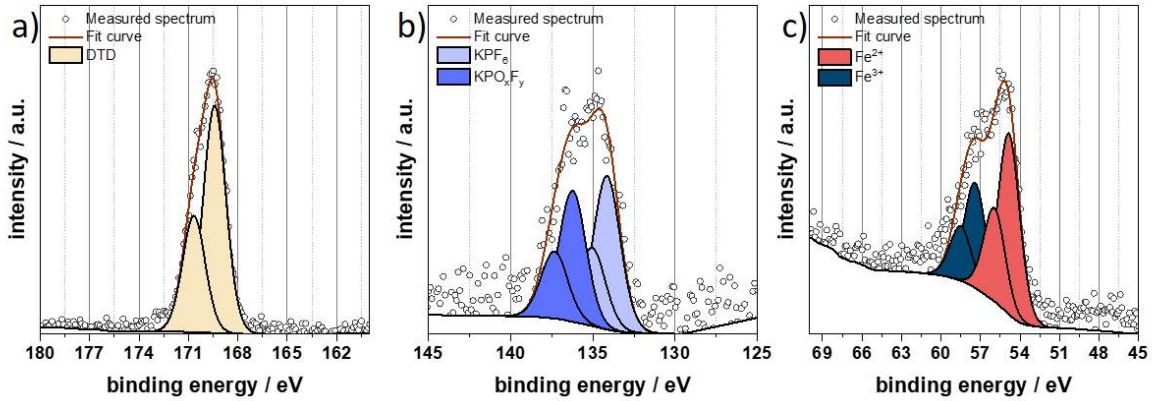

Figure A 24. a)S2p; b)P2p; c)Fe3p spectra of Full cell KFF electrode cycled 1 cycle in 750 mM KPF_6 EC:DEC 1 wt. % DTD electrolyte

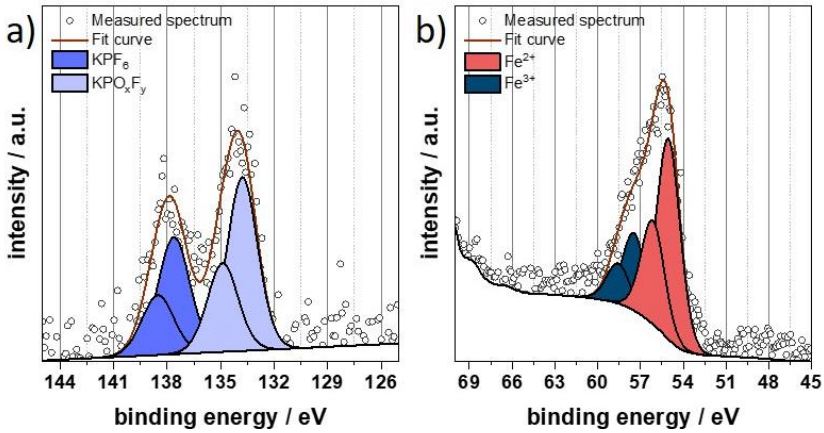

Figure A 25. a)P2p; b) Fe3p spectra of Full cell KFF electrode cycled 10 cycles in 750 mM KPF_6 EC:DEC electrolyte

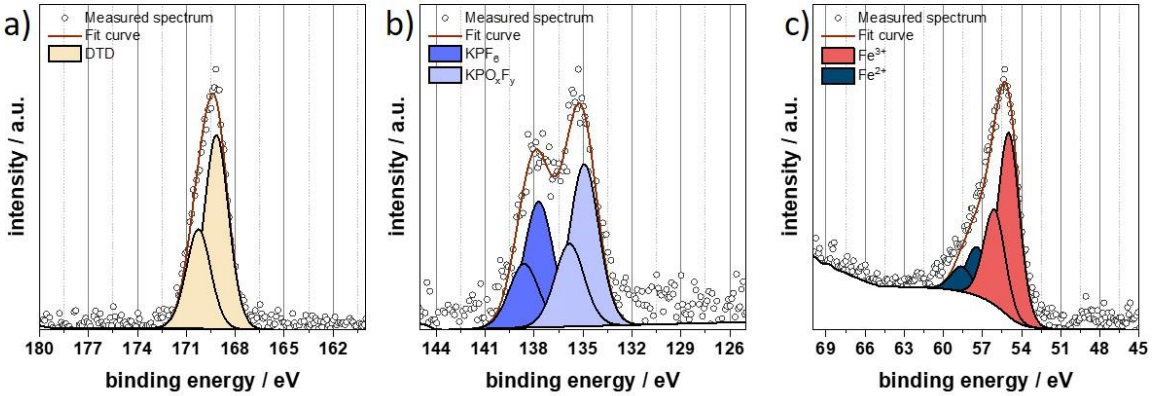

Figure A 26. a)S2p; b)P2p; c)Fe3p spectra of Full cell KFF electrode cycled 10 cycles in 750 mM KPF_6 EC:DEC 1 wt. % DTD electrolyte

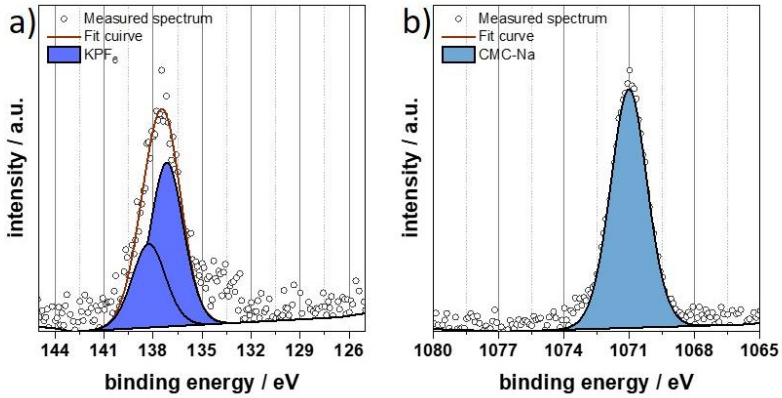

Figure A 27. a)P2p; b) Na1s spectra of Full cell graphite electrode stored in 750 mM KPF_6 EC:DEC electrolyte

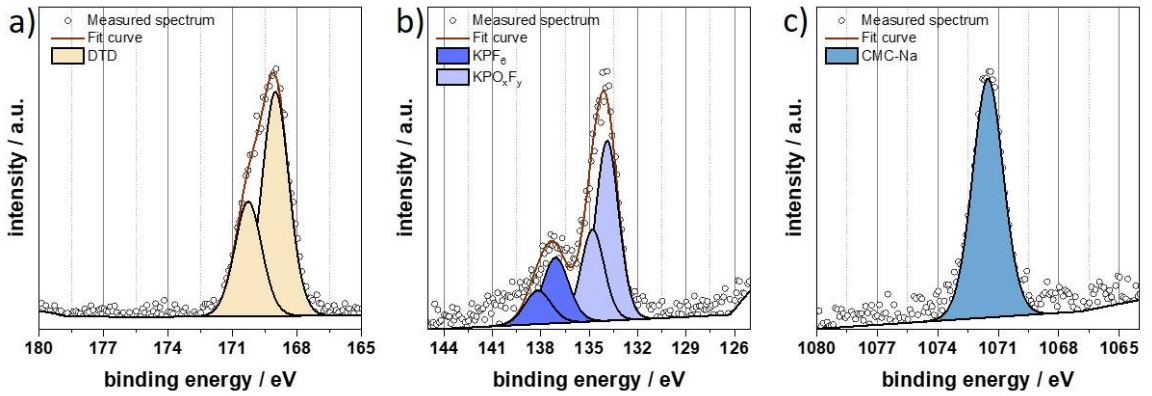

Figure A 28. a)S2p; b)P2p; c)Na1s spectra of Full cell graphite electrode stored in 750 mM KPF_6 EC:DEC 1 wt. % DTD electrolyte

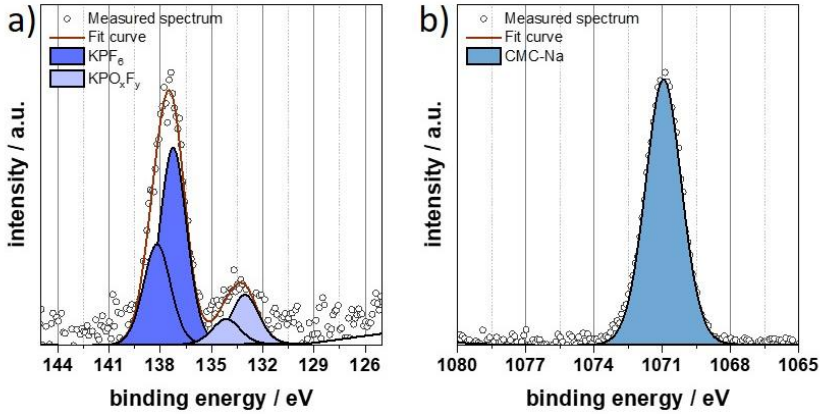

Figure A 29. a)P2p; b) Na1s spectra of Full cell graphite electrode cycled 1 cycle in 750 mM KPF_6 EC:DEC electrolyte

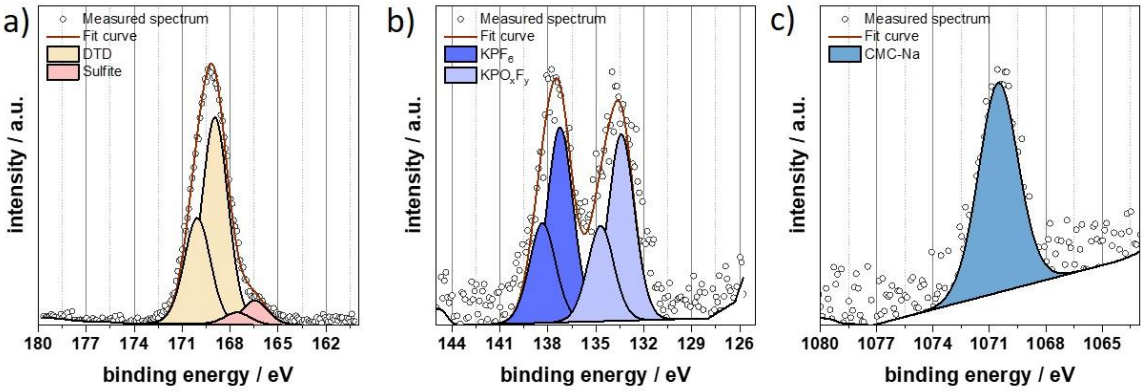

Figure A 30. a)S2p; b)P2p; c)Na1s spectra of Full cell graphite electrode cycled 1 cycle in 750 mM KPF_6 EC:DEC 1 wt. % DTD electrolyte

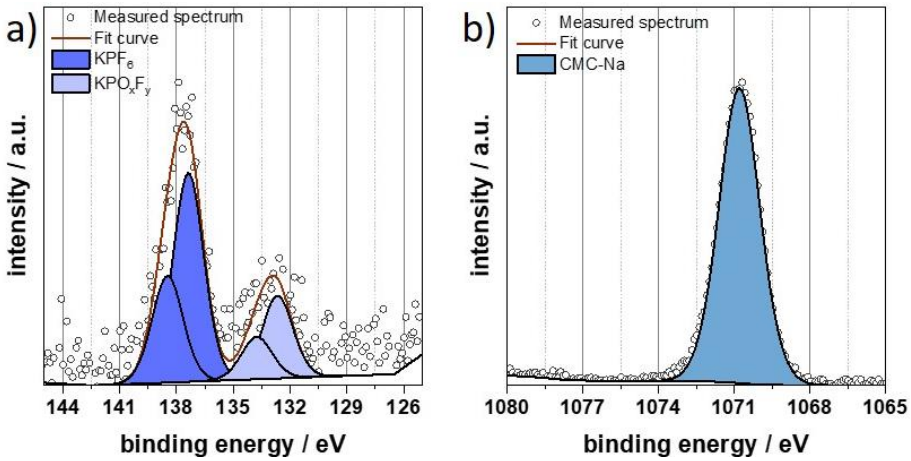

Figure A 31. a)P2p; b) Na1s spectra of Full cell graphite electrode cycled 10 cycles in 750 mM KPF_6 EC:DEC electrolyte

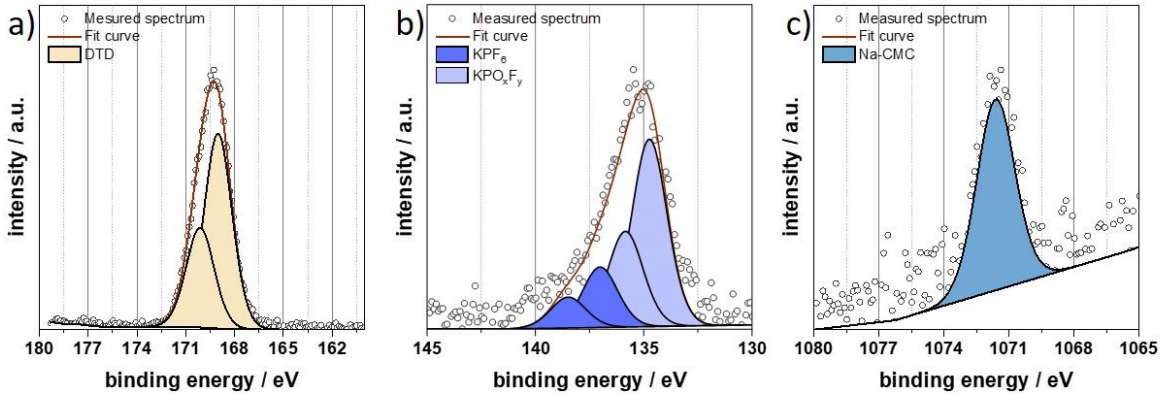

Figure A 32. a)S2p; b)P2p; c)Na1s spectra of Full cell graphite electrode cycled 10 cycles in 750 mM KPF_6 EC:DEC 1 wt. % DTD electrolyte

Table A4. The atomic concentrations found of individual CEI components by XPS

Sample		KFF OCV 0 wt. % DTD	KFF 1c 0 wt. % DTD	KFF 10c 0 wt. % DTD	KFF OCV 1 wt. % DTD	KFF 1c 1 wt. % DTD	KFF 10c 1 wt. % DTD
Element	Bond	Atomic %					
C1s	sp^2-C / C-C	30.95	16.23	18.41	25.95	20.85	25.97
	sp^3-C / -CH-	7.87	11	12.9	7.05	5.03	5.68
	CN	13.08	9.94	10.86	7.61	6.38	8.36
	-CO-	3.78	6.79	5.55	6.31	10.7	4.19
	-(C=O)OR	2.59	3.33	4.7	2.65	2.79	1.44
	CF2	3.38	5.22	4.94	5.49	4.71	3.72
	KFF $K2p_{3/2}$	4.73	3.41	1.65	3.89	2.24	2.85
	PB $K2p_{3/2}$	0.86	1.07	1.35	0.91	0.56	0.57
F1s	R-CF					2.29	2.23
	PVDF	13.55	1.94	1.65	12.95	10.72	15.63
	KF		0.79	1.35		0.88	
N1s	CN	11.15	9.21	8.04	5.85	4.55	7.7
	O=C-N	1.81	2.11	2.56	1.15	1.48	0.81
	NO2	0.63	0.55	0.56	0.44	0.38	0.42
O1s	C-O	1.17	1.82	4.25	4.56	6.41	10.87
	C=O	4.34	5.4	7.7	11.54	15.53	4.96
	Fe-O	0.42		0.63			0.43
P2p	KPF6	1.13	0.6	0.49	1.29	0.6	1.03
		0.33		0.7	0.5	0.7	0.8
S2p	DTD				1.85	3.21	2.34

Table A5. The atomic concentrations found of individual SEI components by XPS

Sample		Gr OCV 0 wt. % DTD	GR 1c 0 wt. % DTD	Gr 10c 0 wt. % DTD	Gr OCV 1 wt. % DTD	Gr 1c 1 wt. % DTD	Gr 10c 1 wt. % DTD
Element	Bond	Atomic %					
C1s	sp^2-C / C-C	45.21	18.99	11.21	22.8	2.31	6.18
	sp^3-C / -CH-	10.62	10.73	11.47	19.59	6.3	7.6
	-CO-	3.51	6.75	7.59	5.51	7.94	10.3
	-(C=O)OR	8.11	6.05	4.17		3.95	1.64
	Carbonates		2.86	4.57	7.18	1.66	0.57
	$K2p_{3/2}$	2.03	11.92	13.6	3	17.67	4.61
F1s	KPF6	5.51	6.22	4.73	1.43	8.32	9.65
	KF		2.09	2.85		4.61	5.48
Na1s							
	Na-CMC	1.34	9.26	7.97	0.96	0.56	0.46
O1s	Na-KLL	0.56	0.66	2.27			
	C-O	5.39	3.81	3.42	10.86	5.13	7.91
	C=O	9.15	2.78	10.76	22.75	14.78	26.52
	Carbonate	7.77	16.73	14.18		15.34	7.85
	K-O					2.11	
P2p	KPF6	0.77	0.94	0.86	1.43	1.15	2.7
			0.2	0.34	0.59	1.14	0.8
S2p	DTD				0.28	6.28	7.71

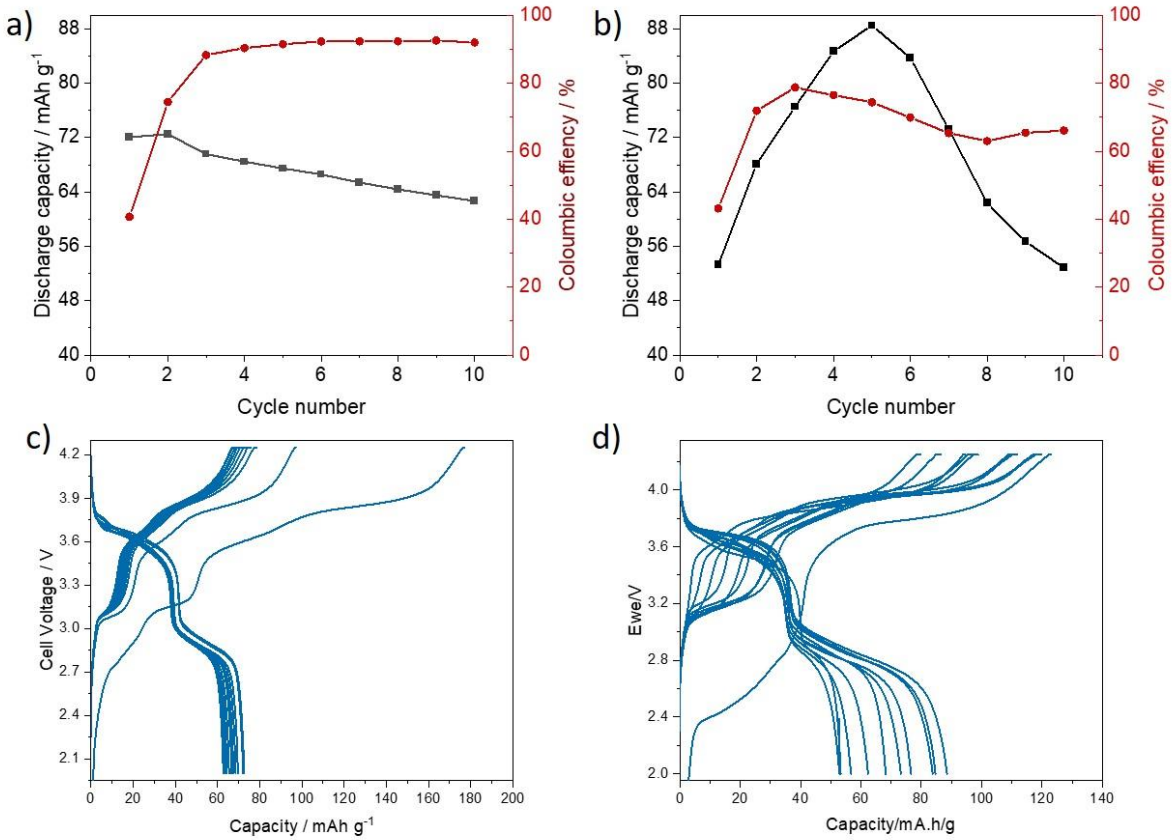

Figure A 33. Two electrode cell data for KFF/graphite full cells a) discharge capacity and C.E. of 0 wt. % DTD; b) discharge capacity and C.E. of 1 wt. % DTD c) cycling curves of 0 wt. % DTD ; d) cycling curves of 1 wt. % DTD

Contributions of co-authors and other researchers

Chapter 6 is based on scientific publication “How Reference Electrodes Improve Our Understanding of Degradation Processes in Half and Full Cell Potassium-Ion Battery Setups”, at *Electrochemica Acta* (Volume 513, 10 February 2025, 145551). The planning, organisation and conception of the presented work, as well as all included electrochemical experiments and preparations, were conducted by Iurii Panasenko supervised by Fabian Jeschull. Interpretation of electrochemical data was supported by Monika Bäuerle.

In **Chapter 7**, the planning, organisation and conception of the chapter, as well as the electrochemical and XPS experiments and their interpretation, were conducted by Iurii Panasenko under the supervision of Fabian Jeschull. Christian Njel, Vanessa Trouillet and Leonie Wildersinn provided assistance with the XPS measurements. Additionally, Leonie Wildersinn contributed to the data interpretation process.